Compliance Characterization and Specification for Surgical Continuum Robots via Modeling, Control, and Design

By

Patrick L. Anderson

Dissertation

Submitted to the Faculty of the

Graduate School of Vanderbilt University

in partial fulfillment of the requirements

for the degree of

DOCTOR OF PHILOSOPHY

in

Mechanical Engineering

January 31, 2021

Nashville, Tennessee

Approved:

Robert J. Webster III, Ph.D.

Nabil Simaan, Ph.D.

Eric J. Barth, Ph.D.

Michael I. Miga, Ph.D.

Fabien Maldonado, M.D.

To Trannie,

my wife and best friend who has supported

me with abiding love, prayer, and laughter.

ACKNOWLEDGMENTS

This dissertation would not have been possible without the help, support, and guidance of many people. First and foremost, I would like to thank God, the Creator of all things, for the opportunity to complete this work. During my undergraduate days at Calvin College, I was often reminded that "every square inch" of this world belongs to God, and that every vocation is worth redeeming and using for His glory here on earth. While I doubt Abraham Kuyper had surgical robotics in mind with this concept, it is nevertheless my hope that this dissertation would glorify Him and that it would further the development of life-saving medical technologies.

Trannie Anderson—my wife, best friend, and source of boundless energy—deserves a huge amount of credit for the existence of this dissertation. She has been with me since my first semester in graduate school and has never stopped encouraging me, celebrating with me on the good days, and bolstering me on the challenging ones. I would not be where I am today without her Godly wisdom and joy.

I would like to thank my advisor, Bob Webster, for his excellent mentorship and support throughout my graduate school career. Not only is Bob a fantastic engineer and thinker, but he also cares deeply about his students and that shows through his efforts to make them better researchers. Bob always goes to great lengths to help his students reach their specific goals. I learned a lot from Bob about how to think about engineering solutions to medical problems, how to frame and present one's ideas, and

how to do work that is impactful to both the academic and medical communities.

My committee members—Bob Webster, Nabil Simaan, Eric Barth, Michael Miga, and Fabien Maldonado—have all played an important role in the shaping of this dissertation. Their feedback, suggestions, and different areas of expertise have made it a better, more complete work.

Vanderbilt is unique in its close relationship and proximity between engineering and medical schools. I would like to thank my clinical collaborators for taking time out of their busy schedules to brainstorm ideas and conduct experiments with me: Fabien Maldonado, Duke Herrell, Smita De, Naren Nimmagadda, Michael Lester, and Nick Kavoussi. I would also like to thank Benoit Dawant, Michael Miga, Michelle Bukowski, and Bill Rodriguez for their roles in making the Vanderbilt Institute for Surgery and Engineering what it is today. I have also benefited from cheerful support from the Department of Mechanical Engineering staff, including Myrtle Daniels, Suzanne Weiss, Jean Miller, Chris Lindsey, Paul Van Wulven, Renee Tomlin, and Sarah Nagy.

I have been exceedingly lucky to work with many wonderful people in the MED Lab, CAOS Lab, and VISE. They have made graduate school fun and energizing, and I have learned so much about life and robotics by working with them every day. I would like to thank the following lab mates, in no particular order: Phil Swaney, Rich Hendrick, Hunter Gilbert, Art Mahoney, Patrick Wellborn, Andria Remirez, Neal Dillon, Loris Fichera, Katy Riojas, Margaret Rox, Josh Gafford, Dave Comber, Ray Lathrop, Michael Siebold, Tayfun Efe Ertop, Max Emerson, Trevor Bruns, Bryn Pitt, James Ferguson, Dominick Ropella, Isuru Godage, Raul Wirz, Ernar Amanov, Josephine Granna, Yue Chen, and Massimo Paradiso. I have also been fortunate to work with several undergraduate students: Matthew Medlock, Jacob Gloudemans, Jacob Rogatinksy, Alyson Chason, Michael Beans, Keaton Scherpereel, and Dominick Jiang. I would also like to thank members of the other mechanical engineering labs

at Vanderbilt (especially the CREATE, STORM, and ARMA labs) and the labs comprising the Vanderbilt Institute for Surgery and Engineering for creating an outstanding and unique research environment at Vanderbilt. I'm especially thankful for the friendship of Andres Martinez, Erik Lamers, and Patrick Wellborn, with whom I spent endless hours doing homework, working on projects, and studying for prelims.

The work in this dissertation is collaborative by nature, and it would not have happened without the help of several specific people. Art Mahoney had a huge influence on my graduate school career. While a postdoc at Vanderbilt, he taught me how to write academic papers, coached me through Cosserat rod modeling and linear algebra, and took a personal interest in my success. Art and I started working together on the multi-needle robot described in Chapter 2 when he invited me, a brand new and unproven graduate student, to help him with his idea for a new type of flexible robot. He played a major role in its development and the results of the chapter. Ron Alterovitz and Alan Kuntz were also key collaborators on this project.

Rich Hendrick taught me a great deal about concentric tube modeling and elastic instability. We worked together to develop the algorithm described in Chapter 3 and the simulation results of the chapter are also found in his dissertation. In addition, Margaret Rox helped design, carry out, and analyze the instability avoidance and stiffness tuning experiments.

The research in Chapter 4 would not have been possible without the collaborative efforts of Josh Gafford and Caleb Rucker. Josh and Caleb have been a constant sounding board for the steerable sheath ideas in the chapter. In addition, Josh worked directly on the handle control box and printed circuit board. Caleb also deserves recognition for his assistance with laser machining at his lab at The University of Tennessee-Knoxville.

Funding engineering and medical research is an expensive endeavor; the National Institutes of Health and the National Science Foundation have supported me finan-

cially in many ways. I am thankful for the opportunity to be an NSF Graduate Research Fellow and participate in an NIH Training Grant to learn about the intersection of surgery and engineering (many thanks to Michael Miga for running this program). These funding sources provided me with many opportunities to learn and grow as a researcher. I would also like to acknowledge the NIH for funding research projects that I worked on in the MED Lab, as well as the Vanderbilt University Discovery Grant program and Vanderbilt Institute for Surgery and Engineering Seed Grant program for supporting the early development of the research in Chapter 2.

My family has been incredibly supportive of me throughout my graduate school career and as I've settled in Nashville, far from my home state of Michigan. I would especially like to thank my parents, Brett and Jane Anderson, for their continuing support of my goals and dreams, their Godly encouragement, their interest in my research, and their willingness to get on planes or sit in cars for hours on end to visit me. I could not imagine a more loving set of parents and friends.

I am thankful for the support and love shown to me by all of my friends, but I would like to give a special shoutout to my friends Daniel and Wendy Paulson, who have been my two closest friends since my freshman year in college. I am thankful every day for their friendship, as they have been there for me every step of the way in my academic career, and that we call the same city home. Phil Swaney also deserves unique thanks for his friendship and mentorship to me. Phil invited me to his church, The Village Chapel, a few short weeks after I first started working in the MED Lab. I kept attending church at TVC and met Trannie there a few months later; Phil unknowingly orchestrated one of the most important moments of my life, and I will always be thankful for that. Phil has always gone the extra mile to ensure that I am thriving in my work, personal life, and walk with Christ.

TABLE OF CONTENTS

LIST OF TABLES

LIST OF FIGURES

Chapter 1

Introduction

1.1 Motivation

Surgery has been revolutionized in the last century by the advent of minimally invasive access to the body. Minimally invasive surgery (MIS) has many benefits to the patient, including lower morbidity, smaller incisions, less blood loss, and shorter hospital stays (e.g., see [9, 10, 11]). As surgeons sought to make procedures less invasive, new tools were needed to make such procedures possible. Whereas traumatic open surgeries with large incisions allow surgeons to use their hands to enter the patient and manipulate tissue, this access is impossible when operating through small incisions or natural orifices.

The MIS procedures that are discussed in this dissertation can be divided into two categories: laparoscopy and endoscopy. Laparoscopy consists of straight, rigid tools that are inserted into open body cavities through trocars. Typically, a rigid endoscope is inserted through a separate trocar for third-person visualization of the surgical field. Laparoscopic tools can easily achieve triangulation—the tools angle towards the surgical site, forming a relatively wide, ergonomic triangle that enables easier control because the eyes are naturally between the hands and the tools meet at the center. However, they typically have limited dexterity and suffer from a fulcrum effect: they must be moved in the opposite direction of desired motion due to the pivot point at the trocar [12]. Endoscopy consists of a rigid or flexible endoscope with working channel(s) for tools (e.g., graspers, needles, electrosurgery, etc.) and fiberoptic or digital visualization at the tip. Endoscopes typically have levers on the handle for tendon-actuated deflection of the distal tip. This allows scopes to be steered through natural orifices or lumens in the body. Steerable catheters also fall

into this category. Endoscopy is limited by the dexterity of the tools passed through the working channel, which typically can only be inserted straight out from the tip of the endoscope and axially rotated. The axes of these instruments are always aligned, resulting in limited lateral dexterity and no triangulation.

Surgical tools play an important role in minimally invasive surgery. MIS procedures create many challenges for the surgeon, including decreased dexterity, visualization, and feeling at the surgical site. Without the ability to physically touch the surgical site with their own hands and use fine motor skills to carry out tasks, surgeons must now rely on the tools themselves to accomplish their intended motions. In MIS, there is a intermediary between the surgeon and the patient or surgical site—this intermediary is the surgical device. With open surgery, success depends purely on surgical skill and the surgeon has direct access to the surgical site. Now, in addition to the surgeon's abilities, success is limited by the inherent capabilities (i.e., access, dexterity, and controllability) of the intermediate device. The input motions of the surgeon outside the body (e.g., moving the handle of a laparoscopic grasper or deflecting the lever of an endoscope) are converted by the tool into useful task space motions inside the body. Therefore, a fundamental limitation of minimally invasive surgery is that success hinges on devices that have the ability to carry out surgeon's intent and provide both the access and dexterity that they need.

Surgical robots have been developed over the last several decades to overcome the shortcomings of manual tools for MIS. Robots enable physicians to perform minimally invasive procedures with unprecedented accuracy, dexterity and precision by providing better dexterity and 3D visualization, while eliminating the fulcrum effect and hand tremors [13]. For example, the most successful commercial surgical robot is Intuitive Surgical's da Vinci robot, which augments laparoscopy with miniature, dexterous "wrist" joints at the distal ends of straight, rigid tools. This approach renews a certain amount of hand-like dexterity to the surgeon. The da Vinci robot has now been used

on over six million patients across the world [14]. Despite the advantages it brings to surgeons, the da Vinci robot (and other laparoscopy-style surgical robots) cannot be used in many types of MIS. Its straight, rigid tools, while much less invasive than open surgery incisions, cannot follow curved passageways in the body (e.g., the digestive tract, lung airways, ventricles, etc.) that can only be accessed with manual endoscopes and catheters. In addition, while laparoscopic tools with 8–12 mm ports (or 25 mm for single-port access) for are much less invasive than open surgery incisions, further miniaturization of tools and reduced incision size is still desirable (and necessary for some procedures).

Unfortunately, manually controlling thin flexible tools can be even more challenging than rigid tools. With a rigid tool, there is a clear mapping between hand position outside the patient and tool end effector position inside the body. With a flexible tool like an endoscope, this is not the case and tip control often depends on knobs and levers on the handle. Therefore, there is strong motivation to bring the benefits of robotic control, precision, and dexterity to flexible surgical tools. In this context, the importance of flexible tools that serve as skillful, easy to control, dexterous intermediates for surgeons is even greater because existing devices are that much more difficult to use. Not only is the kinematic motion of flexible tools sometimes unintuitive, but flexible tools can also behave in unexcepted ways when interacting with tissue. While their innate bending is an advantage for traversing long, narrow passageways and small ports, this compliance must be understood and mentally accounted for when using manual flexible tools for cauterizing, cutting, and retracting tissue.

1.2 Continuum Robots for Minimally Invasive Surgery

Due to the restrictions of robotic or manual rigid laparoscopic approaches to surgery and the challenges of manually controlling flexible tools, much surgical robotics research has focused on developing a category of flexible robots called continuum robots.

These types of robots can reach around anatomical obstacles, safely interact with the environment, follow curved, narrow lumens in the body, and provide end effector dexterity.

A continuum robot is broadly defined as "*an actuatable structure whose constitutive material forms curves with continuous tangent vectors*" [15]. This definition distinguishes continuum robots—continuously flexible robots—from hyper-redundant robots made up of many discrete rigid links. There are many types of surgical continuum robots that have been developed for a wide variety of surgical applications; while a comprehensive list is outside the scope of this dissertation (see [15] for more details), we will briefly review several of the main types and structures. Finally, this section presents related work in the field of continuum robotics research as it pertains to the primary subjects of this work.

In recent years, continuum robot systems are starting to move from purely academic research to commercial development by medical device companies (see Figure 1.1). Hansen Medical, founded in 2002, developed the Sensei robotic catheter for endoscopic procedures. Hansen was later acquired by Auris Health, Inc., which was in turn recently purchased by Ethicon, a division of Johnson & Johnson, for $3.4 billion [16]. The Auris Monarch system is initially targeting bronchoscopy for diagnosing lung cancer [3]. Intuitive Surgical is also developing a robotic endoscope for biopsy called the Ion system. In addition, Intuitive has developed a single port system whose manipulators have rigid-link bending sections similar to continuum devices [17]. The Medrobotics Flex (which also does not technically fall into the continuum robot definition above, as it is made up of many rigid links, but behaves like a continuum robot) is a robotic system that can be deployed through curved passageways in a follow-the-leader fashion. Originally developed by Choset et al. for cardiac applications, it is now being commercialized for general natural orifice procedures such as transoral and transanal surgery [18]. Titan Medical, Inc. is commercializing a bimanual single port

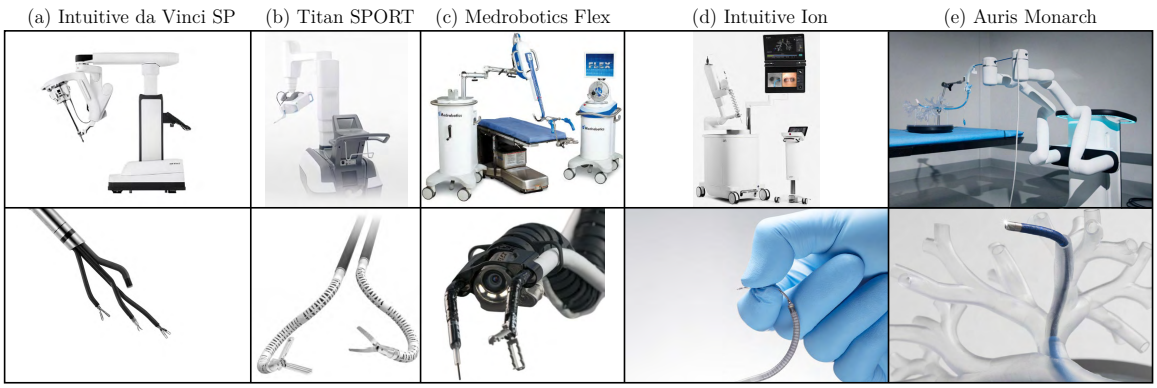

Figure 1.1: A selection of robotic systems undergoing active commercialization that utilize continuum robots or aspects of continuum-like behavior. The top row shows the robotic systems and the bottom row shows close-up images of the end effectors. (a) Intuitive da Vinci SP (Single Port) system ©2019 Intuitive Surgical, Inc. (b) Tital SPORT system (images courtesy of [1]). (c) Medrobotics Flex system for natural orifice surgery (images courtesy of [2]). (d) Intuitive Ion system for bronchoscopy ©2019 Intuitive Surgical, Inc. (e) Auris Monarch system for bronchoscopy (images courtesy of [3]).

robot with continuum manipulators licensed from the multi-backbone robot research of Simaan et al. [19, 20, 1]. It is clear that the field of continuum robotics is generating significant investment from medical device companies and that this type of technology is poised to make a major impact on surgery.

Single-backbone robots, such as the Auris Monarch and Intuitive Surgical Ion, consist of an elastic backbone (e.g., tube or rod) that supports the overall structure and is then deflected by actuation elements (see Figure 1.2(a)). Actuation methods for continuum robots include tendons [21], magnetic fields such as those generated by a magnetic resonance imaging (MRI) scanner [22] or external magnet [23], shape memory alloys [24], pneumatics [25], concentric superelastic tubes [26, 27], and flexible push-pull rods [28].

Multi-backbone robots have multiple elastic elements along the length of the robot that are pushed and pulled to deflect the robot (see Figure 1.2(d)). These elastic elements (often rods or tubes) can be constrained by disks and run in parallel to the robot's tip [29]; like single-backbone robots, they can consist of multiple segments in series. These robots have been intensively studied and applied to problems such

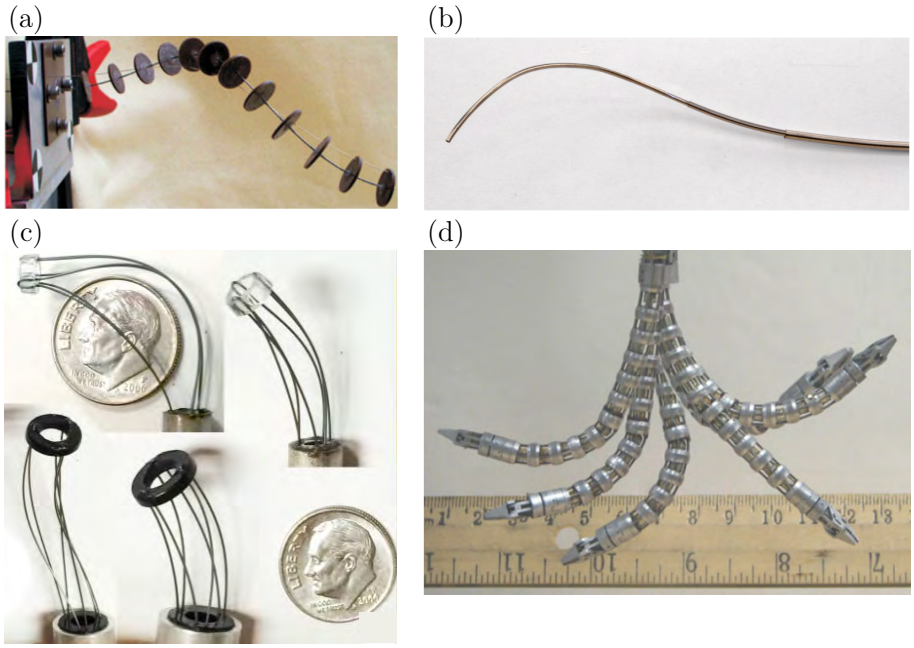

Figure 1.2: Examples of different types of surgical continuum robots. (a) Single-backbone tendon-actuated robot [4]. (b) Concentric tube robot with three nested tubes [5]. (c) Parallel continuum multi-backbone robot with general rod paths [6]. (d) Overlay of multi-backbone continuum robot exploring its workspace [7].

as intrinsic force sensing [30] and hybrid force-motion control [31]. Recently this concept has been studied using backbones that are not constrained between the disks at the end of each section, and instead follow general paths (see Figure 1.2(c)) [32]. This creates a flexible parallel robot that is in some ways analogous to the rigid-link Stewart-Gough platform [33]. Parallel continuum manipulators can apply greater forces than their serial continuum counterparts with the ability to maneuver around obstacles [32]. Efficient model computation [6], robotic teleoperation [34], general intermediate constraint models [35], elastic stability [36], actuation force sensing [37], and stiffness control [38] have been studied. Chapter 2 of this dissertation presents a new type of multi-backbone robot with parallel tubes that enter the body from different body entry points, rather than through a single port, and are joined together inside the body.

Concentric tube robots (CTRs), also known as active cannulas, are composed of

precurved elastic tubes (often made of superelastic Nitinol) nested inside of each other (see Figure 1.2(b)). By rotating and translating the bases of the tubes, complex three dimensional space curves can be created. CTRs are easy to miniaturize to the order of 1–3 mm in diameter. CTRs can be utilized as robot manipulators or pass through tissue or curved lumens (e.g., bronchial tree or vasculature) as steerable needles. Since their invention [26, 27], the continuum robotics community has produced a wealth of research into modeling [39, 40], control [40, 41], and design [42, 43, 44]. They have been proposed for surgical applications in the lungs [45], brain [42, 46, 47], prostate [44], heart [48], and nasal cavities [41], among others. For a thorough review of CTRs, see [49]. Chapter 3 of this dissertation presents a new control method for CTRs that utilizes recent modeling advancements.

Oliver-Butler et al. have developed a hybrid continuum robot that incorporates the use of concentrically arranged tubes, push-pull actuation like that of multi-backbone robots, and notched-tube bending used in miniature dexterous wrists for continuum robots. Swaney et al. created asymmetric cutouts in thin-walled Nitinol tubing, which shifts the neutral bending plane of the tube away from the centerline toward the remaining material; significant distal curvature is achieved when a single tip-attached tendon is pulled [50, 51]. Utilizing the concept of tube stiffness asymmetry, Oliver-Butler et al. nested two notched tubes inside of each other with opposing solid spines and fastened them together at the tip [52]. With this design, the tubes can be pushed and pulled with respect to one another to create bi-directional bending. Like precurved concentric tube robots, this form of concentric tube robot has an open lumen for clinical tools and can be miniaturized to small scales [53]. This concept also makes use of the push-pull backbone actuation of multi-backbone robots. Chapter 4 of this dissertation utilizes this design concept for a flexible endoscopy system with triangulated manipulators.

While different types of continuum robots have many design challenges, perhaps

the most fundamental shared challenge is the need for mathematical models that describe their shapes. Such models are necessary for both design and control of the robots. Regardless of their structure or intended use, continuum robots are flexible and form different curved shapes when actuated. For some continuum robots (e.g., CTRs), the mapping between actuator values and end effector pose is extremely unintuitive. Even for simple, single-backbone continuum robots that form constant curvature arcs, models are an important aspect of designing the robot with the appropriate workspace and stiffness for the surgical task. In the remainder of this chapter, we will review related work in continuum robot modeling, as well as how it pertains to sensing, control, and design. These areas of research are essential to creating intelligent, intuitive tools for surgeons that do not inhibit their skills but rather enhance their access and dexterity in hard-to-reach areas of the body. Continuum robots rely on mathematical models to predict behavior and inform design and control in order to serve as useful intermediaries between surgeons and patients.

1.2.1 Continuum Robot Modeling

Mathematical models are essential for designing and controlling continuum robots. Broadly speaking, these models can be purely kinematic, describing the geometric behavior of the flexible device and resulting curved shape, or mechanics-based, which utilize mechanics principles in addition to kinematics to incorporate forces and torques. From a kinematics model perspective, most approaches can be categorized as constant curvature or variable curvature models. For a review of constant curvature modeling of continuum robots, see [54]. In brief, the constant curvature model describes the robot as a piecewise series of curved segments, each of which has a constant curvature over the length of the segment. The mapping from these arc parameters to the tip pose of the robot is independent of the architecture or actuation method of the particular robot at hand; it can be expressed in terms of Dehavit-Hartenburg

(D-H) parameters, Frenet-Serret frames, integral representations, or exponential coordinates, all of which produce equivalent results [54]. In Chapter 4, we model each curved segment of the flexible tubes forming steerable sheaths as a constant curvature arc, and we employ constant curvature relationships to understand the bending behavior of the laser machined tubes.

In many cases, the curved segments of the robot can be closely approximated as constant curvature arcs in this way. However, variable curvature models have been developed to handle cases which clearly cannot be represented with the constant curvature model [40, 4, 32]. These models use nonlinear differential equations to describe changes in position and orientation of the robot backbone; the equations are solved by integrating in arc length from base to tip.

Mechanics-based models work together with kinematic frameworks to capture the material behavior of the robot. Energy-based methods use principles such as energy minimization or virtual work to describe material behavior. For example, energy minimization methods have been used to develop concentric tube robot models [55, 56], while the principle of virtual work has been used model the statics of multi-backbone robots, which can be used for redundancy resolution and wrench sensing [29, 30]. Another popular method for modeling continuum robots are classical elasticity theories that describe the mechanics and deformation of long, elastic rods. In particular, Cosserat rod models have been employed to describe several types of continuum robots, including concentric tube robots [40, 39], tendon-actuated robots [4], and parallel continuum robots [32, 37]. The Cosserat rod model uses a set of nonlinear differential equations to describe the propagation of forces and moments along the backbone of the robot [57]. These equations are coupled to variable curvature differential equations using constitutive material laws that relate internal forces and moments to changes in backbone shape, and then solved subject to various boundary conditions [15]. Cosserat rod theory is used to model the multi-needle robot in Chap-

ter 2 and the concentric tube robot in Chapter 3. Mechanics-based models can also provide a means for understanding and analyzing non-intuitive robot behavior. For example, models were essential for describing the elastic instability behavior of concentric tube robots [58, 59] and parallel continuum robots [36] and predicting when the behavior will occur in configuration space.

Not only are models critical for controlling continuum robots, but they are also the gateway for characterizing and utilizing their compliant behavior. The innate flexibility of continuum robots can be a benefit when passing through a tortuous lumen, but a challenge to overcome when interacting with tissue. The compliance of a continuum device depends on the materials used, the robotic structure, the actuation methods, and its configuration in the body at any point in time. Throughout the work in this dissertation, models will be used to better understand the stiffness characteristics of these devices and then leverage that understanding to specify desired properties in the design process or during control.

1.2.2 Shape Sensing and Parameter Estimation

Continuum robots are inherently flexible, which means that the models described previously are shape approximations with varying degrees of accuracy. A model will never be a perfect representation of the shape of the robot; this is especially true in unknown environments like the human body. When continuum robots interact with the anatomy and apply forces to tissue, they deflect and their backbone shape changes. In addition, uncertainty in the shape of the robot can result from unmodeled effects (e.g., friction) or uncertainty in the system inputs (e.g., base pose of the robot relative to the workspace, robot parameters and dimensions, etc.).

Sensors can be incorporated into the design of the robot itself or the clinical workflow in order to reduce uncertainty in the model's estimate of the backbone shape. Clinically relevant sensors include electromagnetic tracking sensors [60], opti-

cal tracking systems [61], and fiber Bragg-grating (FBG) sensors [62, 63]. Commonly used clinical imaging modalities can also be treated as sensor observations, such as ultrasound [64], magnetic resonance imaging (MRI) [65], X-rays [66], and computed tomography (CT) [67]. All sensing modalities are noisy and are therefore subject to uncertainty as well. This has motivated the use of statistical methods for incorporating sensor information, because one can account for the degree of noise in the measurement itself [68, 69, 70, 71, 72].

The key related work for Chapter 2 of this dissertation is a statistical sensor fusion framework developed by Mahoney et al. [73]. This work uses an extended Kalman filter for estimating the complete kinematic and mechanic state of a continuum robot, rather than just the backbone shape. By using sensor observations to update the full state, including internal forces and moments, tip loads and other parameters can be estimated. The framework also leverages classical estimation techniques to compute the covariance matrix in addition to the robot state and uses that covariance to optimize sensor placement. A similar extended Kalman filter approach was employed for deflection-based force sensing in [72]. Other intrinsic force sensing work includes extracting curvature information from imaging for steerable catheters [71] and actuation force sensing for multi-backbone robots [30, 74].

1.2.3 Kinematic Control and Redundancy Resolution

Surgical continuum robots are generally controlled either by surgeon teleoperation via a haptic device, or by steering along a pre-defined path. For the applications and robotic systems in this dissertation, we will largely focus on teleoperation scenarios. In this paradigm, the surgeon gives an input with a haptic device which can be interpreted as an desired directional velocity and angular velocity. The controller uses this input to solve for the actuation values needed to carry out the desired tip motion.

In the context of surgical continuum robots, the inverse kinematics problem can be assumed to be quasi-static; even though the robot is in motion, the masses of continuum robots at MIS-scale are small enough that dynamics effects can be ignored (this assumption has been made for CTRs and multi-backbone robots, for example [39, 40, 29]). A common solution to the inverse kinematics problem is the resolved rates approach [75]. Resolved rates is often used for manipulators with difficult-to-solve inverse kinematics (many continuum robots fall into this category). Resolved rates is a differential approach to inverse kinematics that uses the robot's Jacobian to solve for instantaneous joint velocities that will carry out a desired end effector velocity. Differential inverse kinematics control has been explored for multi-backbone robots [76, 77] and concentric tube robots [41, 40, 78], among others.

In some cases, the robot will have more actuation degrees of freedom than are required for the desired task. For instance, a three-tube concentric tube robot has six actuation degrees of freedom (rotation and translation of each tube); if only the tip position is commanded, then this is a three degree-of-freedom task and the robot has *redundant* degrees of freedom. Redundancy resolution encompasses methods for utilizing these extra degrees of freedom to accomplish secondary goals while simultaneously carrying out the primary task.

Redundancy resolution has been employed in the control of surgical continuum robots to accomplish a variety of secondary objectives. For example, it has been used to reduce actuation forces of tendon-actuated [21] and variable diameter continuum robots [79]. Simaan used a redundant backbone in a multi-backbone robot to avoid buckling [29]. Bajo et al. applied redundancy resolution to a multi-backbone robot to avoid joint limits using gradient projection and a singularity-robust weighted pseudoinverse [77]. Sarli et al. used redundancy resolution to minimize visual occlusion from the robot in the field of view when working in confined spaces [80]. Controllers for hyper-redundant robots (very similar to continuum robots but distinguished based

on the definition in [15]) have been developed that simultaneously command both end effector pose and backbone shape [81, 82]. Yip et al. used a model-less control approach to minimize tendon forces in tendon-actuated continuum robots to reduce the risk of buckling [83]. Joint limit avoidance has been implemented using redundancy resolution as well, such as the tendon-actuated continuum robot with rolling joints by [84]. Edelmann et al. used redundancy to improve stability of magnetically controlled continuum catheters [85]. In this case, the secondary goal was to minimize the least negative eigenvalue of the catheter tip stiffness matrix. Leibrandt et al. resolved concentric tube robot redundancy by penalizing columns of the Jacobian based on joint limits and anatomical collisions, while moving toward more stable configurations [86]. Khadem et al. sought to avoid CTR instability with a gradient projection method in which the secondary control goal was to reshape a force-velocity manipulability ellipsoid toward a sphere to ensure that the Jacobian is full rank [87]. These final two examples are the most similar prior work to the new algorithm we present in Chapter 3 that incorporates stiffness tuning and instability avoidance goals for concentric tube robots during path-following and teleoperation.

1.2.4 Dexterity and Tool Triangulation in Endoscopy

Continuum robots are good candidates for flexible endoscopic surgery due to their inherent flexibility, allowing them to pass through the endoscope working channels or serve as a steerable replacement for the endoscope itself. In either case, they have the potential to improve the dexterity of manual endoscopic tools, which can typically only be inserted and retracted. Because of this, tool triangulation is a significant challenge during endoscopic surgery compared to laparoscopy in terms of ergonomics, workspace coverage, and tissue manipulation [88, 12]. Tools without any distal deflection cannot be angled towards each other at the surgical site because their axes are always aligned with the working channel. To perform lateral tool

movements, the surgeon must move the whole endoscope tip which constantly changes the field of view. This makes it very difficult to use two instruments independently, because both instruments will be moved at the same time by the scope. Advanced endoscopic procedures are easier to perform when the surgeon can handle tissue with two instruments at once. For example, countertraction (where one instrument holds and applies tension to tissue while the second tool cuts the tissue) is very difficult when the instruments have no triangulation and cannot be controlled dexterously and independently [89, 90].

Many different approaches have been taken to improving dexterity and triangulation in flexible endoscopy. For a complete review of academic and commercial work in this area, see [91, 92]. These approaches can be divided into three main categories: endoscope tip add-ons, mechanical articulation systems, and robotic systems. Since add-on devices (i.e., devices that are mounted on the distal end of the endoscope) are not continuum devices, we will not focus on them in this discussion; examples include the Apollo OverStitch suturing device [93] and the shape memory alloy-actuated device designed by Gafford et al. [94]. We also exclude systems that only provide enhanced scope navigation rather than tool dexterity. Since it is pertinent to the contributions of Chapter 4, we will include a review of bimanual continuum robots that achieve triangulation in single port surgery, which is similar to rigid endoscopy.

Mechanical articulation systems are typically specialized endoscopes with mechanical structures at their tips that separate tools from the centerline of the scope and then triangulate them. Examples include the Anubiscope (which has also been roboticized [95, 96]), whose wing-like tip opens upon deployment to separate the tools, EndoSamurai [92], Direct-Drive Endoscopic System (DDES) [97], and the articulating system by Okamoto et al. [98].

Robotic systems have been designed for endoscopic tool dexterity using a variety of architectures (both continuum and rigid links). The CYCLOPS has a deploy-

able peripheral scaffold made from either an inflatable or rigid-link mechanism that controls instruments via tendons [99, 100]. The Master and Slave Transendoluminal Robot (MASTER) has two tendon-sheath-actuated manipulators passed through a modified endoscope [101, 102, 103]. This system is being commercialized as Endo-Master for ESD applications. The Highly Versatile Single-Port System (HVSPS) uses elbow joints to triangulate two continuum bending sections made from hinged rigid links [104]. This is a similar concept to the recently released da Vinci SP (Single Port) Surgical System [17]. The Single Port lapaRoscopy bImaNual roboT (SPRINT) also has manipulators with a series of rigid links that can be individually actuated to achieve dexterity and triangulation [105]. The Hansen Medical ViaCath system used an articulating overtube design, but the instruments produced low lateral forces [106]. The shoulder joint has external actuation, while the elbow and wrist have on-board actuation, which raises questions about future sterilizability. Lau developed a flexible robotic system for gastrointestinal procedures that uses a tendon-sheath actuation system [107]. As previously described, the Medrobotics Flex robot is conceptually similar to a continuum robot and has flexible instruments that can be deflected to achieve better triangulation [18].

Several robotic systems use continuum robots to provide dexterity in single port surgery or rigid endoscopy. Xu and Simaan at Vanderbilt University developed a bi-manual multi-backbone continuum robot for single port surgery called the Insertable Robotic Effectors Platform (IREP) [108, 109, 77, 7, 110]. The IREP uses a parallelo-gram mechanism to deploy and separate the continuum arms and the camera module. This technology was licensed by Titan Medical, Inc., who is actively seeking to com-mercialize the Titan SPORT Surgical System [20, 19]. Xu et al. also developed a single port system with a similar architecture at Shanghai Jiao Tong University called the SJTU Unfoldable Robotic System (SURS) [111]. Rosen et al. designed a single port robot with a bending segment and tendon-driven instrument dexterity [112]. Other

efforts to commercialize single port robots with triangulation capabilities include the TransEnterix SPIDER [113]. While these systems achieve tool triangulation and are capable of precice end effector control, they are completely robotic systems designed for single port surgery or rigid endoscopy rather than flexible endoscopy. See [114] for a complete review of continuum robots for single port and intraluminal surgery.

Concentric tube robots have been deployed through the working channels of rigid and flexible endoscopes to provide dexterity at the surgical site. Hendrick et al. developed a CTR system for transurethral rigid endoscopy [44] and a similar architecture was designed for rigid neuroendoscopy [115] and bronchoscopy [116]. CTRs have also been used in flexible endoscopy (e.g., [46, 117, 118]). However, passing concentric precurved tubes through a long flexible endoscope presents unique challenges, namely the elastic instability behavior previously described which is amplified when using long transmission sections. Eccentric arrangements of CTRs for multi-arm single-port robots have also been suggested [119, 120]. Vandebroek combined a bimanual CTR system for triangulation and macro control with McKibben muscle-actuated bending segments for micro control [121].

Roppenecker et al. developed a 3D-printed overtube system for endoscopic procedures [122]. It consists of a sleeve with flexible arms that can be mechanically or robotically actuated with Bowden cables; instruments are passed through the overtube and deflected by the flexible arms. The distal section of the arms is similar to the notched tubes described in [50] in that they have asymmetric stiffness for unidirectional bending and are tendon-actuated. Various designs for the flexible arms and overall system architecture have been presented [123, 124, 125, 126, 127]. The concept showed promising results during *in vivo* porcine ESD experiments [90]. The overtube system is constructed with selective laser sintering (SLS) 3D-printing, making it an inexpensive, disposable system. One disadvantage of the system is its large diameter since it must pass over the endoscope itself.

While many approaches have been proposed for providing dexterity and instrument triangulation in single-port surgery, some are not good candidates for flexible endoscopy because they rely on rigid links to achieve triangulation or can only pass through rigid endoscopes. In addition, most of the systems described above require specialized adapted endoscopes or replace the endoscope altogether; while this certainly does not prohibit their adoption by surgeons, early adoption is potentially easier if the system integrates with existing standard clinical endoscopes. Another disadvantage of many of these systems is that they have diameters that are much larger than standard endoscopes (even dual channel colonoscopes, which are 12–14 mm). It may also be difficult for some of these systems to achieve the long, flexible deployment necessary for colonoscopy and other gastrointestinal procedures.

1.3 Dissertation Overview and Contributions

The focus of this dissertation is the advancement of model-based design and control approaches for surgical continuum robots, with the overarching goal of providing better minimally invasive tools for surgeons. Such tools are essential for providing greater access and dexterity to surgeons during minimally invasive surgery and typically depend on models for both design and control. Through the methods presented in this dissertation, compliance characteristics of continuum robots can be better understood, designed, and controlled during surgery. The contribution and outline of each chapter are summarized below.

1.3.1 Conception, Modeling, and Sensing for a Multi-Needle Surgical Robot

Chapter 2 entails the development of a new type of surgical robot that combines elements of continuum, parallel, and reconfigurable robotics. The first contribution of this chapter is the concept of the robot itself: it is the first robot of its kind that combines the small size and flexibility of continuum robots with the stiffness of

parallel robots *and* the ability of reconfigurable robots to change topology and adjust properties for changing task requirements. The second contribution is a mechanics-based model for this robot that describes the full state (backbone shape and internal moments and forces) of the robot and derives its Jacobian and compliance matrices. The final contribution is a framework for shape sensing and parameter estimation of multi-needle robots. A series of experiments are performed to evaluate the accuracy of the model itself and the degree to which sensing can improve the model's estimate of the robot shape. We are the first group to propose the concept of this robotic system, which may provide a wealth of research questions for the surgical, continuum, parallel, and reconfigurable robotics communities.

1.3.2 Redundancy Resolution Control Algorithms for Concentric Tube Robots to Incorporate Elastic Stability and Stiffness Goals

Chapter 3 describes a control algorithm for concentric tube robots that leverages redundancy resolution to incorporate elastic stability and stiffness goals. Elastic instability behavior of concentric tube robots, which potentially results in unsafe control inside the patient, has been a subject of much research in recent years. New stability measures can now predict when a robot configuration is unstable. The primary contribution of this chapter is the development of a weighted damped least squares resolved rates motion controller that incorporates these elastic stability metrics. In contrast to other approaches, our method actively moves the robot away from unstable configurations with low computational burden. This approach is analyzed in simulation and then experimentally validated during teleoperation with a real time controller on physical robotic hardware. By enabling safe, stable control of highly curved concentric tube robots, new designs and applications may be possible. A final contribution is the demonstration that the redundancy resolution algorithm can be used to easily incorporate other secondary control goals, such as tip compliance.

1.3.3 Modeling and Design Approaches to Tool Triangulation in Flexible Endoscopy

Chapter 4 describes a hand-held bimanual continuum robot system for flexible endoscopy that uses nested steerable sheaths for independent triangulation and dexterity. Steerable sheaths are a type of continuum manipulator made of concentric tubes that bend due to asymmetric stiffness and push-pull actuation. We contribute an asymmetric serpentine laser-machined patterning approach for creating stiffness asymmetry to enable bending. In addition, we characterize the self-contact behavior of the serpentine pattern and employ it for contact-aided triangulation. This system is the first to use self-contact behavior to triangulate flexible endoscopic tools, which is a major challenge for both manual and robotic endoscopy. In this chapter, we evaluate the sheath kinematics and stiffness, as well as design a robotic handle capable of tip motion scaling and control of each nested sheath. This system is also the first bimanual endoscopic robot that uses steerable sheath manipulators.

Chapter 2

A Continuum, Parallel, Reconfigurable Robotic System for Incisionless Minimally Invasive Surgery

This chapter describes a new type of robot for minimally invasive surgery that combines elements of continuum, parallel, and reconfigurable robotics. This robot consists of multiple thin needles connected to one another with wire loops inside a body cavity, creating a flexible structure that is controlled by robot manipulators outside the body. Needlescopic clinical tools such as chip-tip cameras, biopsy forceps, and ablation probes can then be deployed through the needles. The advantage of such a robot is highly minimally invasive access to the body cavity but with greater tip stiffness and controllability than individual needles.

The primary contributions of this chapter are a mechanics-based model and estimation framework for this new type of surgical robot. The model computes the forward and inverse kinematics for multi-needle robots, as well as the Jacobian and compliance matrices. The estimation framework incorporates sensor information to improve the model's description of the robot's shape, as well as estimate other parameters such as unknown applied loads. Both the model and estimation framework are evaluated experimentally.

The content in this chapter is primarily adapted from a previously published conference paper and journal paper. The model and evaluation presented in this chapter was originally published and presented at the *2016 International Conference on Intelligent Robots and Systems (IROS)* [128]. The estimation framework and evaluation was published in *IEEE Robotics and Automation Letters* entitled "Continuum Reconfigurable Parallel Robots for Surgery: Shape Sensing and State Estimation with Uncertainty," of which I am the first author [129]. This paper was also presented at

the *2017 IEEE International Conference on Robotics and Automation (ICRA)*. The contributions of this chapter also led to the following publications: [130, 131, 132, 133].

2.1 Introduction

Continuum robots are tentacle-like devices with the ability to perform manipulation in confined workspaces reachable through narrow, tortuous pathways [15, 134]. Motivated by applications in exploration [54] and minimally-invasive medicine [15], researchers have developed a variety of continuum devices actuated by tendons [21], backbones [28], concentric tubes [40, 39], and pneumatics [135]. These robots typically consist of serially connected curved sections [134].

When designing continuum robots for manipulation tasks through narrow pathways, a tradeoff is often made between the task's geometric and mechanical requirements. For example, the task's geometry may require a long, thin robot to pass through a small opening, but the mechanics of such a robot typically preclude the application of large tip forces. As described in Chapter 1, this relationship is governed by the choice of backbone structure and actuation method. The challenge of balancing geometric and mechanical requirements motivated the development of continuum manipulators with elastic elements arranged in a parallel architecture. Simaan et al. originally suggested the use of parallel combinations of elastic members to form sections of a continuum robot [28]. Xu and Simaan showed how robots of this type can be used for intrinsic force sensing [30, 74]. Recently this concept has been generalized to use backbones that are not constrained between the disks at the end of each section, and instead follow general paths [32]. This creates a flexible parallel robot that is in some ways analogous to the rigid-link Stewart-Gough platform [33]. Parallel continuum manipulators can apply greater forces than their serial continuum counterparts and have the ability to maneuver around obstacles [32]. Efficient model computation [6], robotic teleoperation [34], general intermediate constraint models

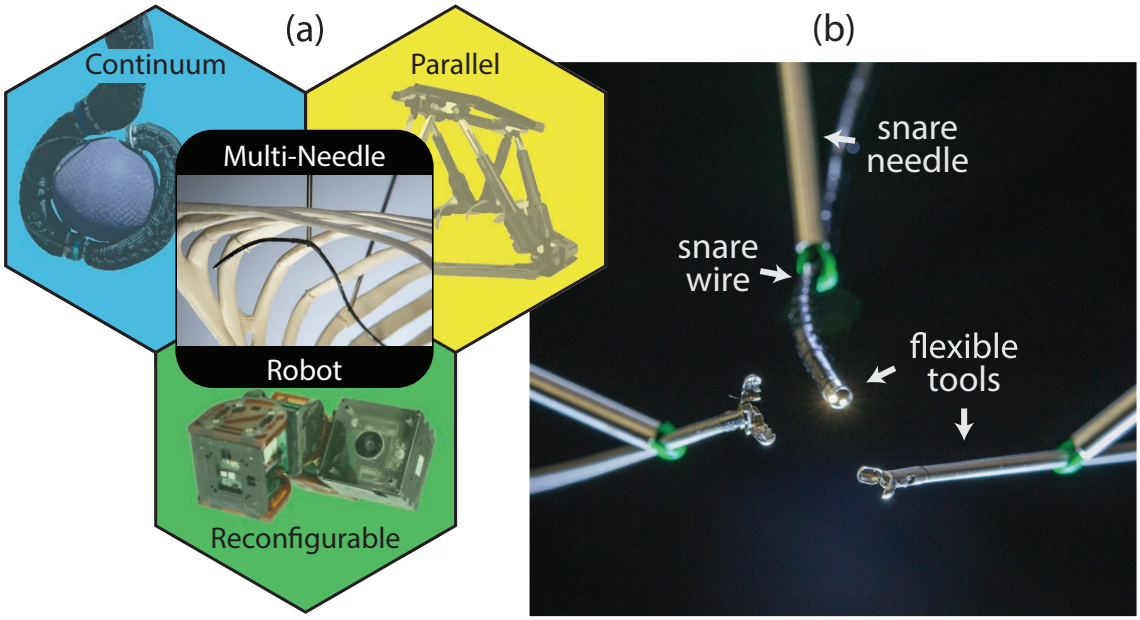

Figure 2.1: (a) This chapter proposes a new surgical multi-needle robot concept combining aspects of continuum, parallel, and reconfigurable robotics. (b) The working end of a multi-needle robot for minimally-invasive surgery that can be assembled with two flexible forceps for manipulation, a thin flexible endoscope for visualization, and three snare needles that can grasp and assist in manipulating the forceps and scope with the ability to reconfigure.

[35], elastic stability [36], actuation force sensing [37], and stiffness control [38] have been studied. Similarly, Yang et al. proposed a parallel continuum Delta robot in which each leg is made up of a multi-backbone continuum structure [136].

For most tasks, a continuum robot will only be required to intermittently apply large tip forces. The required forces also typically vary in direction and magnitude and cannot be fully characterized *a priori*. Any fixed (i.e., non-reconfigurable) design must compromise with respect to device diameter, stiffness, and workspace. Indeed, task-based design problems involve finding the optimal tradeoff of these properties, but all cannot be optimized simultaneously. Formal design methods for continuum robots often incorporate planning [45] and numerical optimization [137], resulting in highly task-optimized devices. It is challenging to design continuum robots (and robots, in general) for tasks whose requirements change. This has motivated the development of self-reconfigurable robotic systems that alter their physical morphology to adapt

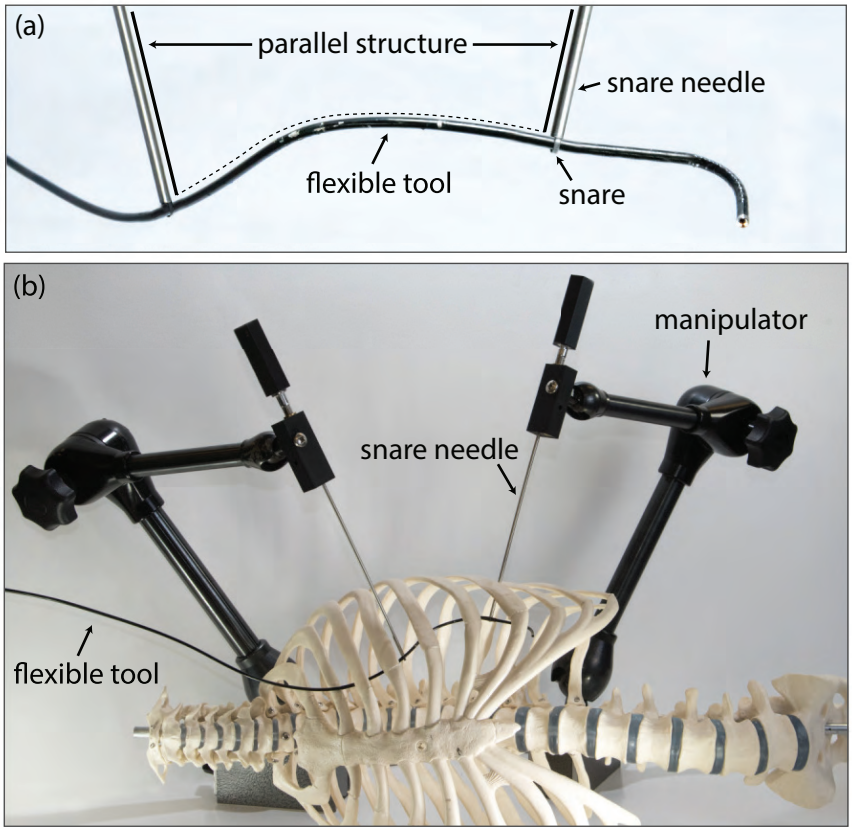

Figure 2.2: (a) Multi-needle robots assemble parallel structures inside a patient's body that can be (b) controlled outside the body using robot manipulators.

to new circumstances or changing task requirements [138, 139]. Reconfigurability removes the need to compromise on performance during the design process—one robot can assemble itself into multiple designs. One example of a reconfigurable robot for surgical applications is a system for gastrointestinal procedures consisting of rigid modules that, when assembled, form a continuum-like structure [140].

This chapter describes a new class of robot system consisting of elastic elements that form closed kinematic chains with reconfigurable morphology. These robots lie at the intersection of continuum, parallel, and reconfigurable robotics (Figure 2.1(a)). In minimally-invasive medicine, a multi-needle robot can be assembled into parallel structures inside the human body. The robot consists of several needle-diameter flexible tools, as well as a set of hollow needles through which wire snare loops are

deployed (Figures 2.1(b) and 2.3). The system is assembled inside the patient by snaring the flexible tools with the wire loops, forming a parallel structure (Figure 2.2). The parallel structure can be actuated by manipulating the snare needles and tool outside the patient's body using robot manipulators. The multi-needle robot concept is well-suited for a robotic approach because the required motions of the robot manipulators to achieve the desired motion of the surgical instrument inside the body are physically well-defined but not necessarily intuitive. Figure 2.1(b) shows the working end of a multi-needle system consisting of three snare needles that control two flexible forceps for manipulation and a 2.5 mm diameter flexible endoscope for visualization. Note that the flexible tools could instead be made up of flexible needle-diameter tubing such as Nitinol through which various clinical tools are deployed. Because of this, we will also refer to the flexible tool as a "tool needle" to go along with the "snare needle(s)."

Key aspects of this concept are that the flexible tool and snare needles are inserted percutaneously, which reduces invasiveness (no sutures are required for diameters 3 mm [141]). The multi-needle concept takes the benefits of continuum robots (e.g., their small size makes them favorable for minimally-invasive therapy [15]) and combines them with the benefits of parallel robots (e.g., their rigid structure [33]). Multi-needle systems also take the benefits of reconfigurable robots [139] with the unique ability to reconfigure their parallel structures inside the patient's body in a way that selectively adjusts their properties (e.g., workspace, stiffness, etc.) to meet changing task requirements. The multi-needle robot's parallel structure, its ability to reconfigure, and its ability to deploy inside the body without incisions, make it a unique concept within the surgical robotics community.

This chapter addresses several key modeling advancements for multi-needle robots. First, we present a mechanics-based large-deflection model that uses Cosserat rod theory to capture the large deflections capable of thin flexible needles. In addition, the

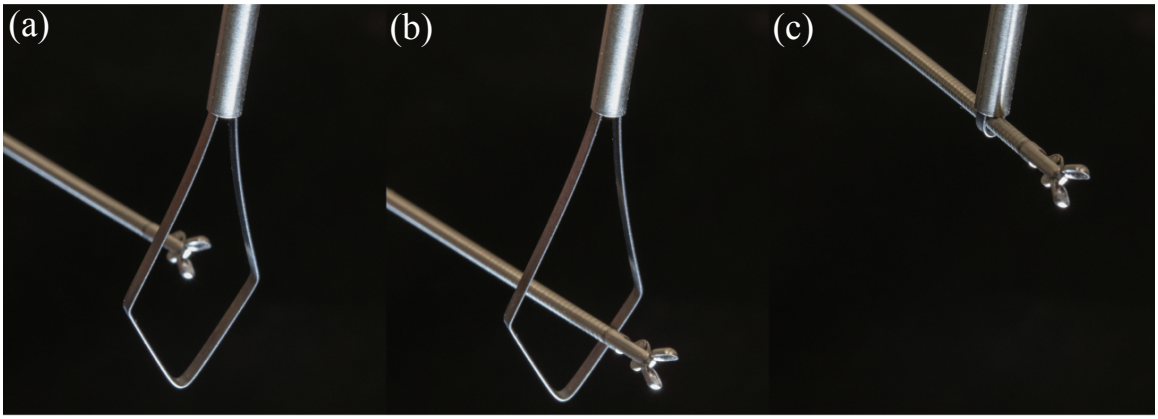

Figure 2.3: Multi-needle robots are assembled by (a) percutaneously inserting a needle and deploying a snare, (b) navigating the flexible tool through the open snare loop, (c) and tensioning the snare. Parallel structures that consist of multiple tools and snare needles can be assembled inside the body this way.

reconfigurability of multi-needle robots is investigated by exploring different morphological arrangements of snare needles. This chapter also addresses the problem of integrating sensing with these large-deflection models in order to determine the robot's configuration when an external load or other disturbance is applied. This estimation framework uses an extended Kalman filtering approach and is capable of estimating unknown robot parameters.

2.2 Medical Motivation

There are a variety of clinical scenarios—both diagnostic and therapeutic—where the reconfigurability, stiffness modulation, and small diameter entry points of multi-needle systems are desirable. Early work on this system has focused on closed-chest lung and pleural procedures, which present unique technical challenges due to the constraints of the rib cage. While some surgical robots have focused on a single-port approach, the large diameter required for many single-port robots (e.g., the da Vinci SP single-port robot has a 25 mm cannula) may be better suited for abdominal and natural orifice procedures. When passing tools through the chest wall between the ribs, however, tool diameter becomes a more pressing concern. The 8–15 mm ports used

for Video Assisted Thoracoscopic Surgery (VATS), which can be performed manually or robotically, can damage nerves running along the rib cage; as many as 1 in 3 patients experience chronic, long-term chest wall pain after VATS [142, 143, 144, 145]. Thoracic surgeons and pulmonologists are strongly motivated to use small diameter tools to prevent nerve damage or spreading of the ribs.

The multi-needle robot concept could provide access to the entirety of the lung cavity while maintaining dexterity and adapting stiffness as needed for palpation and tissue manipulation. These traits are critical to both the diagnosis and therapy of lung cancer. New approaches to lung cancer diagnosis and treatment are urgently needed because of its prevalence and high mortality rate (150,000 deaths in the United States each year [146]), as well as how challenging lung cancer is to diagnose and treat with current instrumentation. For example, it is extremely challenging to localize subsurface tumors [147]. While it is possible to use continuum manipulators with intrinsic force sensing to palpate tissue to localize tumors (e.g., [30, 74, 70]), an inherent tradeoff exists. To maximize the signal-to-noise ratio in intrinsic force sensing, low stiffness is desirable. However, high stiffness is desirable for applying forces to tissue during interventional procedures. In closed-chest lung procedures, the reconfigurability of multi-needle manipulators enables the robot to increase or decrease its stiffness when advantageous. Many currently available biopsy and therapy devices are highly thin and flexible, such as chip tip cameras, biopsy forceps and needles, ultrasound catheters, and ablation probes. However, they typically are only used in lumens because their flexibility and low stiffness make them difficult to control in an open cavity from outside the body. With the multi-needle system, all of these minimally invasive tools could be employed and controlled.

Multi-needle robots may be an important diagnostic tool for other types of lung and pleural diseases as well. In the United States, 1.5 million people suffer from pleural effusions each year [148]. A pleural effusion is the collection of excess fluid in

the pleural space around the lungs, which can be life-threatening if the cause is not determined and corrected. To determine the cause, doctors typically analyze fluid drained from the effusion, but this is inconclusive in 26% of patients [149, 150]. This means that the underlying cause of the pleural effusion is not effectively diagnosed for 390,000 patients each year. Making matters worse, for over 100,000 of these patients, the underlying cause of the pleural effusion is cancer [151, 152, 153, 154, 155]. Patients for whom the underlying cause of the pleural effusion is undiagnosed are usually simply observed over time, despite the fact that their survival rates plummet if the underlying cause is lung cancer. The 5-year survival rate of stage III and IV lung cancer patients is only 15%, compared to 80% at stage I [156, 157]. Thus, it is essential to know as early as possible which 1 in 4 non-diagnosed pleural effusion patients has cancer, and definitive diagnosis requires biopsy. The multi-needle system is a minimally invasive alternative to surgical biopsy via VATS. The needlescopic approach could potentially provide pulmonologists with direct visualization and biopsy of the entire pleural space.

The multi-needle system could also be used for therapeutic procedures. One example that we have explored is pleurodesis, which prevents lung collapse by intentionally introducing an irritant (e.g., talc powder) that causes the visceral pleura and parietal pleura to adhere to one another through scar formation [133]. Pleurodesis is used for patients with recurrent spontaneous pneumothoraces or pleural effusions, or who have had a first lung collapse and work in jobs in which subsequent collapses could be catastrophic (e.g., as an airplane pilot). Patients suffering a spontaneous lung collapse have a 20% chance of recurrence after their first episode, 60% after the second, and 80% after the third [158]. It is also the most common treatment for malignant pleural effusions [159]. Pleurodesis is improved by an even distribution of powder applied to the surface of the pleurae [160]; it can fail if there is a "patchy distribution of talc" [161], and fails up to 57% of the time when attempted using an indwelling

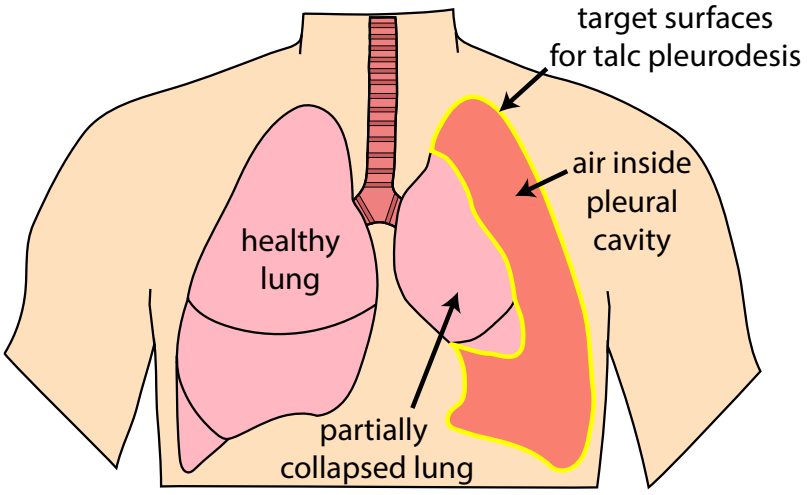

Figure 2.4: Pleurodesis prevents recurrent pneumothorax (collapsed lung) by using chemical agents (e.g., talc powder) to irritate and adhere the pleural surfaces outlined in yellow. Pleurodesis is one example of a potential therapeutic clinical application for multi-needle robots.

pleural catheter that cannot be actively aimed inside the body [159]. If the physician wishes to aim the powder delivery tube, the alternative approach is thoracoscopic surgery, which requires larger incisions to admit endoscopes and other tools [162]. While aiming the powder for complete coverage is important, there is a limit to the amount that should be delivered. In a study of talc pleurodesis safety, the application dose was 8 g of powder, on average [163]. High talc doses (200 mg of powder per kg of patient weight, which is 12.4 g for an average patient weight of 62 kg) have been shown in rabbit studies to be associated with extrapleural talc deposition [164]. This highlights the need for efficient spreading of talc powder within the pleural space: the goal is to cover as much of the interior surface as possible with a standard dose size, without using more powder than necessary.

Multi-needle robots may also be useful in abdominal procedures. In the past several years, surgeons have developed a number of "micro-laparoscopic" or "needle-scopic" procedures [165]. The objective of these procedures is to use small diameter (<3 mm) tools to reduce postoperative pain, recovery time, and scarring. Ports for

tools of this size do not require suture closure after the procedure. However, current needlescopic techniques are challenging for surgeons to perform due to the inherent flexibility of tools of this diameter [166]. Multi-needle robots offer the potential to enhance stiffness in needlescopic techniques without requiring larger port diameters.

Other applications where the multi-needle robot approach may be beneficial include fetal surgery, where small tools are needed due to the size of the anatomy and to reduce the (currently significant) risk of complications like fetal membrane rupture [167]. Similarly in neonatal surgery, small diameter instruments are preferable to adult-sized tools [168]. Both applications would benefit from robotic dexterity [168].

In the context of incisionless laparoscopic surgery in the abdomen or chest, it will most likely be advantageous to create a bimanual multi-needle system with two "hands" for the surgeon as shown in Figure 2.5. Some of the applications described previously, such as exploration and biopsy for pleural effusions or powder spraying for pleurodesis, may only require one hand (i.e., two needles and robot manipulators). For VATS procedures, however, more tissue manipulation is required and a wider array of surgical tools are used (e.g., graspers, electrocautery, etc.).

2.3 Mechanics-Based Model for Multi-Needle Robots

This section derives and evaluates the Cosserat rod model used to describe the kinematics of a multi-needle robot. The model is the basis for the sensing and control work presented later in this chapter and is a primary contribution of this dissertation. The model can be used to control the robot during surgery, optimize the robot's design, and analyze its properties and behavior.

We use a notation where matrices are written in bold, upper-case, upright font (e.g., $\mathbf{M}$), vectors are written in bold, lower-case, standard font (e.g., $\boldsymbol{v}$), and scalars are written in upper- and lower-case standard font (e.g., E, s). We use $\mathcal{N}(\boldsymbol{m}, \Sigma)$ to denote a Guassian random distribution with mean vector $\boldsymbol{m}$ and covariance matrix

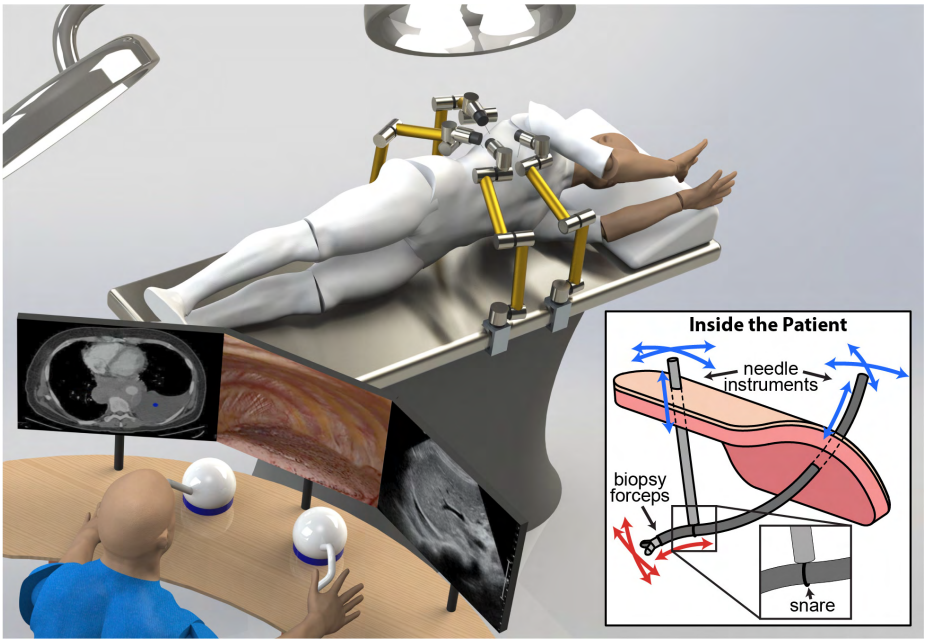

Figure 2.5: Conceptual rendering of a bimanual multi-needle system for incisionless lung surgery. The surgeon uses haptic devices at a console to control the tip of each multi-needle structure. Each multi-needle structure is made up of two flexible needles that are connected inside the chest cavity with a snare loop (inset).

Σ. Many variables in this dissertation are functions of a scalar arc length parameter s. At times, we use subscript notation for compactness to denote s as a function argument. For example, if $\boldsymbol{x}$ is a function of s, then it can be written as $\boldsymbol{x}_s$ rather than $\boldsymbol{x}(s)$.

Note that we assume the multi-needle robot model is quasi-static, which is assumed for other flexible robot models (e.g., concentric tube robots [40, 39] and flexible multi-backbone robots [29]).

2.3.1 Kinematics of Cosserat Rods

We model each member of the parallel structure as an unshearable and inextensible Cosserat rod with a state vector that contain states defining its material position $\boldsymbol{p}(s) \in \mathbb{R}^3$, material orientation represented as a unit quaternion $\boldsymbol{q}(s) \in \mathbb{H}$, internal force $\boldsymbol{n}(s) \in \mathbb{R}^3$, and internal moment $\boldsymbol{m}(s) \in \mathbb{R}^3$. The states vary as a function of

scalar arc length s along the rod's body, measured from a proximal reference.

The rod's position, orientation, internal force, and internal moment propagate in arc length according to

$$\begin{aligned} \boldsymbol{p}' &= \boldsymbol{q}\boldsymbol{e}_3\boldsymbol{q}^{-1} & \boldsymbol{q}' &= \frac{1}{2}\boldsymbol{q}\boldsymbol{u} \\ \boldsymbol{m}' &= \boldsymbol{n} \times \boldsymbol{p}' - \boldsymbol{l} & \boldsymbol{n}' &= -\boldsymbol{r} \end{aligned} \tag{2.1}$$

where $\boldsymbol{u} \in \mathbb{R}^3$ is the angular rate-of-change of the rod's body reference frame expressed in the body frame, $\boldsymbol{r} \in \mathbb{R}^3$ and $\boldsymbol{l} \in \mathbb{R}^3$ are externally applied distributed forces and moments per unit rod length, and $'$ indicates derivative with respect to arc length s. We assume that $\boldsymbol{r} = \boldsymbol{0}$ and $\boldsymbol{l} = \boldsymbol{0}$ in this chapter.

The internal moment can be related to the angular rate of change by a linear constitutive law of the form

$$\boldsymbol{m} = \boldsymbol{q}\left[\mathbf{K}_m\left(\boldsymbol{u} - \boldsymbol{u}^*\right)\right]\boldsymbol{q}^{-1} \tag{2.2}$$

where $\mathbf{K}_m = \mathrm{diag}(EI, EI, JG)$ maps bending and torsion to internal moment, E is the Young's modulus, G is the shear modulus, I is the second moment of area about the body $\boldsymbol{e}_1$ and $\boldsymbol{e}_2$ axes, and J is the polar area moment about the body $\boldsymbol{e_3}$ axis. The vector $\boldsymbol{u}^*$ is the rod's precurvature in its undeformed state as represented in the rod's undeformed body frame. For example, $\boldsymbol{u}^* = \boldsymbol{0}$ for a straight rod.

2.3.2 Kinematic Model Formulation

As previously stated, the multi-needle system consists of multiple flexible elements, each of which is modeled as a Cosserat rod. The state of the system $\boldsymbol{x}$ is constructed by packing the rod states of each element of the parallel structure into a single vector

$$\boldsymbol{x} = \begin{bmatrix} \boldsymbol{x}_t & \boldsymbol{x}_1 & \dots & \boldsymbol{x}_n \end{bmatrix}^{\mathsf{T}} \tag{2.3}$$

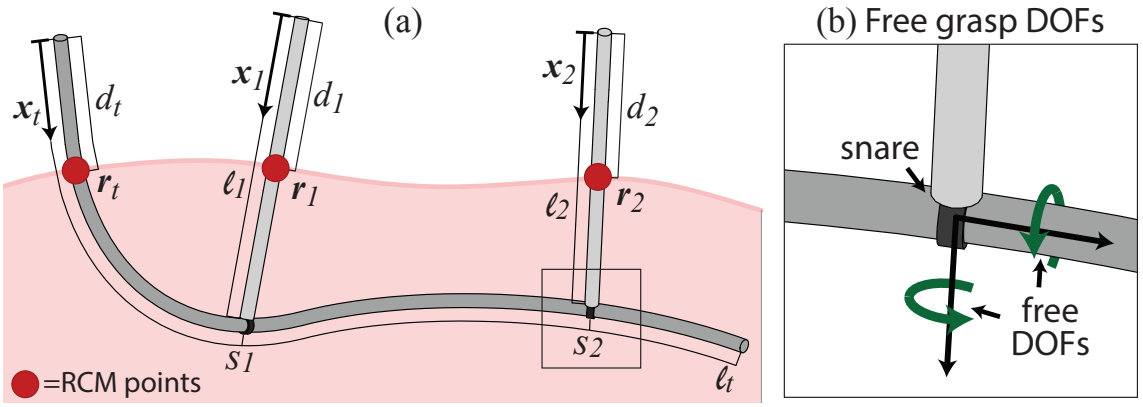

Figure 2.6: (a) A mechanics-based model predicts the arc length states of the flexible tool $\boldsymbol{x}_t$ and snare needles, $\boldsymbol{x}_1$ and $\boldsymbol{x}_2$. The snares grasp the tool at the tool's arc length s_1 and s_2. Remote centers of motion (RCM) of the tool and each snare is enforced at the RCM points $\boldsymbol{r}_t$, $\boldsymbol{r}_1$, and $\boldsymbol{r}_2$. (b) The unconstrained degrees of freedom permitted by the standard snare-grasp constraints expressed in Equation (2.11). In the full grasp constraint (Equation 2.12), there are no free degrees of freedom at the grasp point.

where $\boldsymbol{x}_t$ is the Cosserat-rod states of the flexible tool (i.e., backbone position and orientation, and internal force and moment) and $\boldsymbol{x}_1 \dots \boldsymbol{x}_n$ are the Cosserat-rod states of the snare needles. Note that the state vector for each element $\boldsymbol{x}_i$ is a column vectors, but we express them in the form of (2.3) for compactness. Therefore, the size of $\boldsymbol{x}$ is $13(n+1) \times 1$ for n snare needles. The same notation convention is used for the state derivative and constraint vector.

The state vector $\boldsymbol{x}(s)$ is a function of the arc length parameter s, which is defined so that $s = 0$ is at the proximal end of the flexible tool and $s = \ell_t$ at the distal end of the flexible tool (ℓ_t and ℓ_i are the lengths of tool and i^{th} snare needle, respectively). The tool and snare needle Cosserat-rod states are packed into $\boldsymbol{x}$ so that the corresponding physical location on the tool and snares at arc length s is located at a distance of $\ell_t - s$ from the flexible tool's distal end.

The propagation of the state vector in arc length s is governed by the arc length derivative vector

$$\boldsymbol{x}' = \begin{bmatrix} \boldsymbol{x}_t' & \boldsymbol{x}_1' & \dots & \boldsymbol{x}_n' \end{bmatrix}^{\mathsf{T}} = \boldsymbol{f}(\boldsymbol{x}, s) \tag{2.4}$$

The arc length derivatives of the flexible tool and the i^{th} snare needle rod states are defined piecewise in arc length as

$$\boldsymbol{x}_t'(s) = \begin{cases} \begin{bmatrix} \boldsymbol{p}_t' & \boldsymbol{q}_t' & \boldsymbol{m}_t' + \boldsymbol{\alpha} & \boldsymbol{n}_t' + \boldsymbol{\beta} \end{bmatrix}^{\mathsf{T}}, & \text{if } 0 \leq s \leq \ell_t \\ \mathbf{0}, & \text{otherwise} \end{cases} \tag{2.5}$$

$$\boldsymbol{x}_i'(s) = \begin{cases} \begin{bmatrix} \boldsymbol{p}_i' & \boldsymbol{q}_i' & \boldsymbol{m}_i' & \boldsymbol{n}_i' \end{bmatrix}^{\mathsf{T}}, & \text{if } s_i - \ell_i \leq s \leq s_i \\ \mathbf{0}, & \text{otherwise} \end{cases} \tag{2.6}$$

and are given by the Cosserat-rod equations (2.1), where s_i is the grasp location of the i^{th} snare (Figure 2.6(a)) and $\boldsymbol{\alpha}$ and $\boldsymbol{\beta}$ are defined in Section 2.3.4. The differential equation (2.4) is defined on the arc length interval $\begin{bmatrix} s_{\min} & s_{\max} \end{bmatrix}$ with endpoints defined as

$$s_{\min} = \min\left\{0, s_1 - \ell_1, \ldots, s_n - \ell_n\right\} \quad \text{and} \quad s_{\max} = \ell_t, \tag{2.7}$$

where $s_1 \ldots s_n$ are the snare grasp point locations measured from the tool's base, and ℓ_t and $\ell_1 \ldots \ell_n$ are the lengths of the tool and snare needles, respectively.

2.3.3 Needle Pose and Tip Load Constraints

A set of geometric and mechanic constraints governs the kinematics of multi-needle systems. When solving the forward and inverse kinematics, we will solve for initial conditions of the state vector $\boldsymbol{x}$ that satisfy the constraints when the differential equations (2.4) are integrated.

First, we encode the system inputs as a constraint on the initial pose where $\boldsymbol{p}_{td}$ and $\boldsymbol{q}_{td}$ represent the desired initial position and quaternion of the flexible tool at arc length $s_{\min}$, and $\boldsymbol{p}_{id}$ and $\boldsymbol{q}_{id}$ represent the desired initial position and quaternion of

the i^{th} snare needle at arc length $s_{\min}$. These constraints are given as

$$\boldsymbol{c}_{tu}(s_{\min}) = \begin{bmatrix} \boldsymbol{p}_t - \boldsymbol{p}_{td} & \text{initial tool position} \\ \log\left(\boldsymbol{q}_t \boldsymbol{q}_{td}^{-1}\right) & \text{initial tool quaternion} \end{bmatrix} = \mathbf{0} \tag{2.8}$$

$$\boldsymbol{c}_{iu}(s_{\min}) = \begin{bmatrix} \boldsymbol{p}_i - \boldsymbol{p}_{id} & \text{initial snare position} \\ \log\left(\boldsymbol{q}_i \boldsymbol{q}_{id}^{-1}\right) & \text{initial snare quaternion} \end{bmatrix} = \mathbf{0}. \tag{2.9}$$

Second, we assume that the system is quasistatic which leads to constraints that enforce the force and moment at the tool's distal end to be balanced with any tip applied force $\boldsymbol{f}$ or moment $\boldsymbol{t}$, represented by the tip constraint

$$\boldsymbol{c}_t(\ell_t) = \begin{bmatrix} \boldsymbol{m}_t - \mathbf{t} & \text{tip moment-free} \\ \boldsymbol{n}_t - \boldsymbol{f} & \text{tip force-free} \end{bmatrix} = \mathbf{0}. \tag{2.10}$$

2.3.4 Snare Grasp Conditions and Constraints

The snare needles apply forces and moments to the tool needle at their respective grasp points. Proper modeling assumptions concerning this interaction are key to producing an accurate mechanics model of the entire multi-needle system. Here, we will describe two different approaches to describing the grasp behavior; these will be called the "standard" and "full" grasp conditions.

In both conditions, grasping the flexible tool with the i^{th} snare at arc length location s_i creates a state constraint that relates the components of the flexible tool state $\boldsymbol{x}_t(s_i)$ to the components of the snare needle's state $\boldsymbol{x}_i(s_i)$. We approximate the geometric grasp interaction as a position constraint that enforces the tip of the needle to be coincident with the tool and an orientation constraint that enforces the needle and tool shafts to be orthogonal.

The primary difference between the "standard" and "full" grasp conditions lies in how forces and moments are propagated at the grasp location. The standard grasp

assumes that the snare grasp cannot support moments in the $\boldsymbol{p}_t'$ and $\boldsymbol{p}_i'$ directions (i.e., the "Free DOFs" illustrated in Figure 2.6(b)), which is enforced by two constraints on the snare needle's moment $\boldsymbol{m}_i$. The geometric and wrench constraints can be represented for each of the n needles at arc length s_i as

$$\boldsymbol{c}_i(s_i) = \begin{bmatrix} \boldsymbol{p}_t - \boldsymbol{p}_i & \text{tip coincidence} \\ \boldsymbol{p}_t' \cdot \boldsymbol{p}_i' & \text{shaft orthogonality} \\ \boldsymbol{p}_i' \cdot \boldsymbol{m}_i & \text{needle shaft moment} \\ \boldsymbol{p}_t' \cdot \boldsymbol{m}_i & \text{tool shaft moment} \end{bmatrix} = \mathbf{0}. \tag{2.11}$$

The full grasp constraint assumes that there is a rigid interaction between the snare needle and tool needle at the grasp point. In other words, the orientation of snare needle tip is constrained such that there is a rigid body rotation between the snare tip and the tool needle backbone orientation at arc length s_i. This results in a grasp constraint given as

$$\boldsymbol{c}_i(s_i) = \begin{bmatrix} \boldsymbol{p}_t - \boldsymbol{p}_i & \text{tip coincidence} \\ \mathbf{R}_t^{\mathsf{T}}(s_i)\mathbf{R}_i(\ell_i)\mathbf{R}_x - \mathbf{I}_{3\times 3} & \text{tip rotation} \end{bmatrix} = \mathbf{0} \tag{2.12}$$

where $\mathbf{R}_x \in SO(3)$ is the rotation in the $\begin{bmatrix} -1, 0, 0 \end{bmatrix}^{\mathsf{T}}$ direction by 90°, $\mathbf{I} \in \mathbb{R}^{3x3}$ is the identity matrix, $\mathbf{R}_t(s_i)$ is the orientation of the flexible tool at the grasp arc length s_i, and $\mathbf{R}_i(\ell_i)$ is the orientation of the snare needle at its tip.

The grasp conditions also inform how the force and moment applied by the snare needles to the tool at the grasp points and any applied point moments $\boldsymbol{t}_j$ and point forces $\boldsymbol{f}_j$ (for $j = 1 \dots m$), located at arc lengths s_j, are propagated in arc length.

The derivative propagation terms in (2.10) are defined as

$$\boldsymbol{\alpha}(s) = \sum_{i=1}^{n} \mathbf{G}_i(s)\boldsymbol{m}_i\delta(s_i - s) + \sum_{j=1}^{m} \boldsymbol{t}_j\delta(s_j - s) \tag{2.13}$$

$$\boldsymbol{\beta}(s) = \sum_{i=1}^{n} \boldsymbol{n}_i\delta(s_i - s) + \sum_{j=1}^{m} \boldsymbol{f}_j\delta(s_j - s) \tag{2.14}$$

where $\delta(s)$ is the Dirac delta function. For the standard grasp constraint, $\mathbf{G}_i(s) = \mathbf{I}_{3\times3} - \mathbf{A}_i\mathbf{A}_i^{\dagger}$, where $\mathbf{A}_i(s) = \begin{bmatrix}\boldsymbol{p}_t'(s) & \boldsymbol{p}_i'(s)\end{bmatrix}$ and † denotes the Moore-Penrose pseudoinverse. Equation (2.13) ensures that only the moment applied by each needle about the directions perpendicular to the tool and needle shafts is propagated toward the tool's distal end. It also propagates any external moments at arc lengths s_j. Equation (2.14) propagates the point forces applied to the tool by the snares, as well as external forces, toward the tool's distal end. For the full grasp constraint, $\mathbf{G}_i(s) = \mathbf{I}_{3\times3}$ because moments in all directions can be supported by the full grasp and must be propagated.

It is worth noting that both the standard and full grasp constraints are assumptions. For the standard grasp constraint, the free motion about the needle shaft is a good assumption if the coefficient of friction between the snare and the tool is low, but it is certainly possible to use materials that have higher frictional interaction for these components. As noted in Section 2.4.3, the assumption that the snare needle and tool needle meet at a 90° angle may not be a good assumption when the snare needle diameter is much smaller than the tool needle diameter. In such cases, it may be useful to use shape sensing estimation to account for the actual angle between the needles. This concept is explored in Section 2.4.3. When making the full grasp constraint assumption, we add a plastic tip to the snare needles that extends over the tool needle and ensures a rigid attachment.

Note that the standard grasp conditions are assumed in the model evaluation and sensing work presented in this chapter (see [128, 129]), while the full grasp conditions

are assumed in later motion planning and design optimization work (see [130, 131]). The choice of grasp condition, as well as unmodeled behavior at the grasp point, has a significant effect on the tip pose and shape of the robot (see Section 2.4.5).

2.3.5 Body Wall Fulcrum Constraints

Surgical robots that penetrate the skin perform remote-center motion (RCM) around a fulcrum, located at the body wall, that prevents the robot from pulling the patient's skin by minimizing the entry point's spatial motion [169].

An element of the multi-needle system can perform remote-center motion around a virtual center. A member of the parallel structure passes through an RCM point $\boldsymbol{r}$ if there exists an arc length d on its body such that the constraint

$$\boldsymbol{c}_{rcm} = \boldsymbol{p}(d) - \boldsymbol{r} = \boldsymbol{0} \tag{2.15}$$

is satisfied as the multi-needle robot moves, where $\boldsymbol{p}(d)$ is the backbone position of the member at arc length d.

We denote the RCM points of the tool and snares to be $\boldsymbol{r}_t$ and $\boldsymbol{r}_1, \ldots, \boldsymbol{r}_n$, respectively, with the arc length position where the tool and snares intersect their RCM points denoted as d_t and $d_1, \ldots, d_n$. The RCM constraint (2.15) can be incorporated into the kinematics framework for the flexible tool and each of the snare needles by augmenting the system state $\boldsymbol{x}$ with the scalar arc lengths d_t and $d_1, \ldots, d_n$, and augmenting (2.16) with a constraint of the form (2.15) for the tool and each of the snare needles.

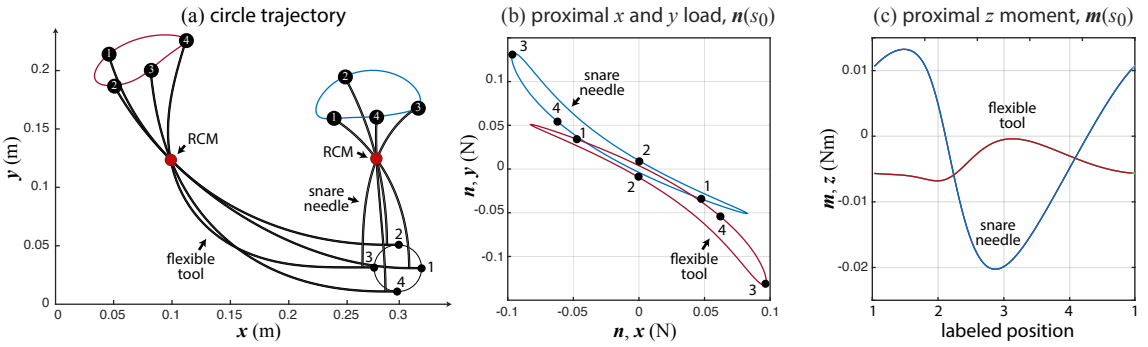

Figure 2.7: (a) The end-effector of a simulated single-snare multi-needle robot follows a 2 cm radius circle trajectory in the $\boldsymbol{x}$-$\boldsymbol{y}$ plane while performing remote-center motion. A curve showing the proximal position of the flexible tool and snare needle as the end-effector follows the circular trajectory is shown, with four configurations shown. (b) The proximal tension cycle of the flexible tool and snare needle, which only lies in the $\boldsymbol{x}$-$\boldsymbol{y}$ plane, required for the tool's end-effector to follow the circle trajectory. (c) The proximal moment of the flexible tool and snare needle, which is only about the $\boldsymbol{z}$ axis, shown in time.

2.3.6 Forward and Inverse Kinematics

All tool and snare constraints are packed into the vector $\boldsymbol{c}$, which is a function of the full state at multiple arc lengths:

$$\boldsymbol{c} = \begin{bmatrix} \boldsymbol{c}_{tu} & \boldsymbol{c}_t & \boldsymbol{c}_{1u} & \boldsymbol{c}_1 & \dots & \boldsymbol{c}_{nu} & \boldsymbol{c}_n \end{bmatrix}^{\mathsf{T}} = \boldsymbol{0}. \tag{2.16}$$

Following the convention of the state vector $\boldsymbol{x}$, the individual constraints are column vectors but are expressed in this form for compactness; the complete constraint vector $\boldsymbol{c}$ in (2.16) is therefore a column vector. The forward kinematics of the parallel structure can be found by piecewise integrating (2.4) on the arc length interval $s_{\min}$ to $s_{\max}$ with initial conditions $\boldsymbol{x}(s_0) = \boldsymbol{x}_0$. The initial condition vector $\boldsymbol{x}_0$ is packed with a vector of inputs $\boldsymbol{u}_0$, which are the initial positions and orientations of the tool and snare needles' proximal ends. The initial conditions are also packed with a vector $\boldsymbol{v}_0$ containing the initial internal moments and forces of the tool and snare needles at their proximal ends, which are unknown *a priori* and must be solved for in order to satisfy the constraints (2.16). Given the known inputs $\boldsymbol{u}_0$, we solve the forward

kinematics using a numerical optimization routine that finds the unknowns $\boldsymbol{v}_0$ that minimize $\|\boldsymbol{c}\|$. This method also assumes that the grasp arc length is known for each snare needle.

The inverse kinematics can be computed by augmenting the constraint vector (2.16) with a constraint on the tool's distal pose at arc length ℓ_t, of the form

$$\boldsymbol{c}_{inv}(\ell_t) = \begin{bmatrix} \boldsymbol{p}_t - \mathbf{P} \\ \log\left(\boldsymbol{q}_t \mathbf{Q}^{-1}\right) \end{bmatrix} = \mathbf{0} \tag{2.17}$$

where $\mathbf{P}$ and $\mathbf{Q}$ denote the desired position and orientation, respectively. In this formulation of the inverse kinematics, the vector $\boldsymbol{v}_0$ of unknowns includes the proximal pose of the tool and snare needles along with the proximal internal moments and forces. The RCM constraint (2.15) is typically utilized when solving the inverse kinematics. The same numerical optimization method can be used to solve the inverse and forward kinematics.

Figure 2.7(a) shows the distal end of a hypothetical single-snare robot, with the tool and snare constructed out of Nitinol tubing (Table 2.1), following a circular trajectory in the $\boldsymbol{x}$-$\boldsymbol{y}$ plane with its heading pointing in the $\boldsymbol{x}$ direction and with RCM constraints illustrated. The necessary proximal tool and snare needle poses are computed by solving the inverse kinematics using the constraint (2.17). The tool and snare needle work in concert to position and orient the end-effector as shown. In all configurations, the tool and snare needles are antagonistic in that their proximal loads, which lie in the $\boldsymbol{x}$-$\boldsymbol{y}$ plane, balance one another (Figure 2.7(b)). The proximal moments of the tool and snare needles lie in the $\boldsymbol{z}$ axis (Figure 2.7(c)).

As noted in prior literature, the forward and inverse kinematics of elastic parallel and serial continuum manipulators may have more than one solution [32], where multiple vectors $\boldsymbol{v}_0$ satisfy the constraints (2.16). This can occur in "buckled" configurations where multiple static equilibrium solutions exist that locally minimize the

system's elastic potential energy (see Figure 2.8(a)). In this case, each of the buckled configurations can be found from the kinematic equations by appropriately selecting $\boldsymbol{v}_0$. Elastic instability has been observed in other continuum devices, including concentric tube robots [58, 59] and parallel continuum robots [36], and has been explored for a robotic manipulation system that holds Kirchhoff elastic rods on both ends [170].

2.3.7 Computing the Jacobian and Compliance Matrices

The Jacobian and compliance matrices relate changes in the inputs $\boldsymbol{u}_0$ and the applied tip wrench $\boldsymbol{w}_\ell$ to changes in the state $\boldsymbol{x}$ at every arc length [171]. They can be found using the state derivative with respect to the initial conditions $\boldsymbol{x}_0$, which is denoted as $\mathbf{X}(s) = \partial \boldsymbol{x}(s)/\partial \boldsymbol{x}_0$, and is the solution of the differential equation

$$\mathbf{X}' = \mathbf{F}\mathbf{X} \tag{2.18}$$

where $\mathbf{X}(s_0) = \mathbf{I}$ and $\mathbf{F}(\boldsymbol{x}, s) = \partial \boldsymbol{f}(\boldsymbol{x}, s)/\partial \boldsymbol{x}$. See Appendix A for the derivation of $\mathbf{F}(\boldsymbol{x}, s)$ sub-matrices.

The time derivative of the state $\dot{\boldsymbol{x}}$ at any arc length and the constraint $\dot{\boldsymbol{c}}$ can be expressed as functions of the time derivative of the initial conditions $\dot{\boldsymbol{x}}_0$ and the applied tip wrench $\dot{\boldsymbol{w}}_\ell$ in the form

$$\dot{\boldsymbol{x}} = \mathbf{X}\dot{\boldsymbol{x}}_0 = \mathbf{X}_u\dot{\boldsymbol{u}}_0 + \mathbf{X}_v\dot{\boldsymbol{v}}_0 \tag{2.19}$$

$$\dot{\boldsymbol{c}} = \mathbf{Y}\dot{\boldsymbol{x}}_0 + \mathbf{W}\dot{\boldsymbol{w}}_\ell = \mathbf{Y}_u\dot{\boldsymbol{u}}_0 + \mathbf{Y}_v\dot{\boldsymbol{v}}_0 + \mathbf{W}\dot{\boldsymbol{w}}_\ell \tag{2.20}$$

which can be split into contributions from time-varying inputs $\dot{\boldsymbol{u}}_0$ and unknowns $\dot{\boldsymbol{v}}_0$, where $\dot{}$ denotes the derivative with respect to time, and where $\mathbf{Y} = \partial \boldsymbol{c}/\partial \boldsymbol{x}_0$ and $\mathbf{W} = \partial \boldsymbol{c}/\partial \boldsymbol{w}_\ell$. The matrices $\mathbf{X}_u = \partial \boldsymbol{x}/\partial \boldsymbol{u}_0$ and $\mathbf{X}_v = \partial \boldsymbol{x}/\partial \boldsymbol{v}_0$ can be computed from $\mathbf{X}$, and the matrices $\mathbf{Y}_u = \partial \boldsymbol{c}/\partial \boldsymbol{u}_0$ and $\mathbf{Y}_v = \partial \boldsymbol{c}/\partial \boldsymbol{v}_0$ can be computed from $\mathbf{Y}$ (see

Table 2.1: Parameters of the multi-needle device for Section 2.3.8 model evaluation experiments.

	Tool	**Snare 1**	**Snare 2**	**Units**
Outer Diameter	1.02	3.00	3.00	mm
Inner Diameter	0.84	2.30	2.30	mm
Length	475	157	153	mm
Young's Modulus	50	180	180	GPa
Poisson's Ratio	0.33	0.305	0.305	–
Grasp-Point Location	–	207	434	mm

Appendix A).

The constraint $\boldsymbol{c}$ must always remain satisfied regardless of how the system inputs and tip wrench vary. Assuming the constraint is already satisfied, this implies that $\dot{\boldsymbol{c}} = \mathbf{0}$. Setting (2.20) equal to $\mathbf{0}$, solving for $\dot{\boldsymbol{v}}_0$, and substituting the result into (2.19) produces the relationship

$$\dot{\boldsymbol{x}} = (\mathbf{X}_u - \mathbf{X}_v \mathbf{Y}_v^{\dagger} \mathbf{Y}_u)\dot{\boldsymbol{u}}_0 - (\mathbf{X}_v \mathbf{Y}_v^{\dagger} \mathbf{W})\dot{\boldsymbol{w}}_\ell \tag{2.21}$$

$$= \mathbf{J}\dot{\boldsymbol{u}}_0 + \mathbf{C}\dot{\boldsymbol{w}}_\ell \tag{2.22}$$

where the $\mathbf{J}$ is the Jacobian and $\mathbf{C}$ is the compliance matrix. The Jacobian and compliance are important for implementing resolved rates control and for analyzing robot properties and behavior.

2.3.8 Experimental Model Evaluation

We performed experiments to verify the kinematic model described in Section 2.3.2 by creating a multi-needle device with two stainless steel snare needles and a superelastic Nitinol tube for the tool. Table 2.1 lists the system's parameters. The snares were constructed out of 1.52 mm wide, 0.28 mm thick superelastic Nitinol strip, and were tightened by hand.

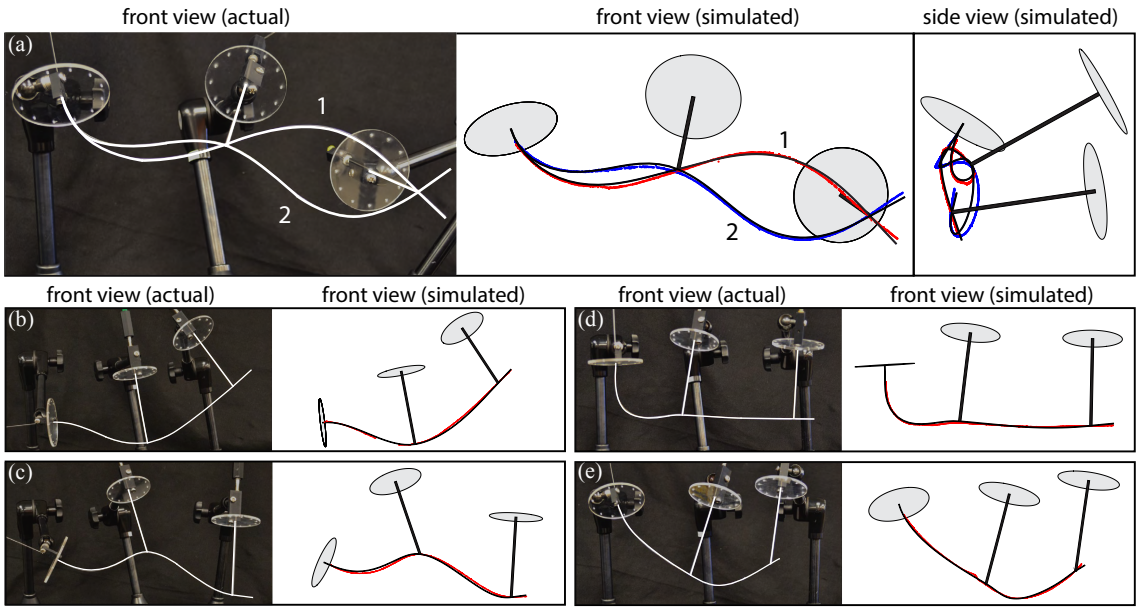

Figure 2.8: Five configurations compare the ground-truth magnetic tracker measurements of the tool's backbone position to that predicted by the model of Section 2.3.2. Configuration (a) demonstrates the potential for multiple tool configurations for the same inputs, both found by the model. In all configurations, a photo of the experimental setup is shown on the left with the simulation results and overlaid tracker data on the right. The tool and the snares are highlighted in white for visibility.

A Northern Digital Inc. Aurora tabletop electromagnetic tracking system with a hand-held measurement probe was used to localize the base positions and orientations of the flexible tool and the snare needles. We measured the grasp-point location of each snare on the tool by hand. Ground-truth measurements of the tool's backbone position were taken by manually sliding a 0.3 mm diameter electromagnetic sensor through the tool with the device placed in five configurations and comparing it to the backbone position predicted by the model of Section 2.3.2. The ground-truth measurements are plotted on top of the predicted backbone position for all five configurations in Figure 2.8.

Figure 2.8(a) shows an example of a snare needle and tool proximal configuration where the system's kinematic equations have more than one solution as described in Section 2.3.6. In this example, there are two solutions which are shown. The mechanics-based model can predict the system states, even if there are multiple so-

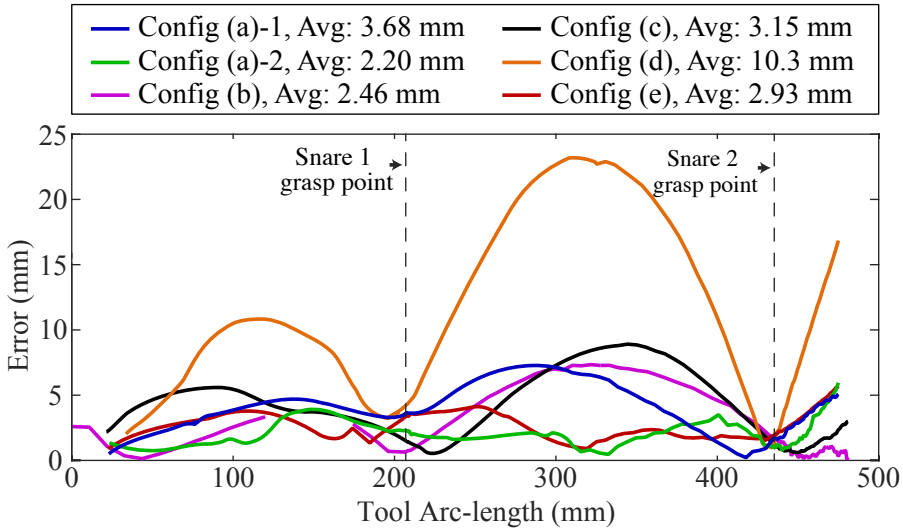

Figure 2.9: Backbone error (2.23) measured between the mechanics-based model and the raw tracker data for each configuration shown in Figure 2.8. Error is shown as a function of the flexible tool's backbone arc length, with average backbone error in the legend. The arc length locations (Table 2.1) where the snares grasp the tool are shown.

lutions, by appropriately selecting the initial moment and load (which are unique) at the proximal ends of the tool and snare needles. Our numerical method was able to find both solutions by starting from two different initial values of the vector $\boldsymbol{v}_0$. The two solutions are plotted alongside their corresponding ground-truth measurements in the front and side views of Figure 2.8(a).

Figure 2.9 shows the ground-truth error between the predicted tool backbone curve and the raw data obtained with the electromagnetic tracker for each of the configurations presented in Figure 2.8. The error $e(s)$ was computed at arc length s as

$$e(s) = \min_k \|\boldsymbol{p}_t(s) - \boldsymbol{p}_k^*\| \tag{2.23}$$

where $\boldsymbol{p}_t$ is the predicted backbone curve and $\boldsymbol{p}_k^*$ is a raw data point indexed by integer $k = 1, \ldots, N$ and N is the number of gathered data points.

The average error for each configuration is shown in the legend of Figure 2.9. The average error for all configurations except (d) was less than 4 mm. In the case of

configuration (d), the average error was 10.3 mm, which we expect was caused by unmodeled static friction at the interface of the snare needles and flexible tool. Static friction was dominated by the flexible tool's internal moments and forces in the other configurations. When scaled by the shortest snare's length, the normalized error of configuration (d) was 6.7%.

Figure 2.9 shows that the flexible tool's backbone error decreases near arc lengths where the snare needles grasp the tool. This is a result of the snare needle's stiffness preventing it from deflecting under the loads applied by the flexible tool. The model predicts the deflection, but using stiffer needles reduces uncertainty. This can be exploited by placing multiple grasp points along the flexible tool's body, as Figure 2.9 illustrates, to reduce the uncertainty of the predicted tool backbone curve by preventing errors at the proximal end from propagating down the tool's body. Multi-needle robots share this property with continuum [32] and rigid-link parallel robots, whose structure prevents error in the individual joints from producing an amplified error at its end effector [33].

2.3.9 Reconfiguring a Multi-Needle Robot

Reconfiguration can be used to change the properties of a multi-needle robot to satisfy changing application requirements; this distinguishes the system from other types of parallel continuum robot devices. Here our system shares several key challenges with reconfigurable and parallel robot systems, notably the challenge of determining the optimal configuration/design for a given task.

The system can be configured into a variety of morphologies in which the complexity increases with the number of flexible tools and snares. Figure 2.10 shows some possible arrangements with one tool and from one to three snare needles. There are many possible morphologies whose utility varies depending on the task. A morphology like "5" could be used to control the flexible tool's body along with its tip,

while a morphology like that of "6", where one snare grasps another, could be used to decrease a snare needle's compliance or exploit mechanical advantage.

The tip compliance of needle-diameter continuum robots often makes manipulation tasks challenging. Reconfiguring the system could be useful for adjusting the flexible tool's compliance as the task requirements change. In this section, we use two example configurations to explore the singular values and input singular vectors of the compliance matrix $\mathbf{C}_{\boldsymbol{fp}}(s)$, which maps small changes in the applied tip force $\boldsymbol{f}$ to small changes in the tool's backbone position $\boldsymbol{p}_t(s)$ and could be useful in determining how to reconfigure the system. The compliance matrix $\mathbf{C}_{\boldsymbol{fp}}(s)$ is the upper-right 3×3 sub-matrix of the system compliance matrix $\mathbf{C}(s)$, which is computed as described in Section 2.3.7, and is a function of arc length s along the tool's backbone.

The singular values and input singular vectors are obtained from the singular value decomposition

$$\mathbf{C}_{\boldsymbol{fp}}(s) = \mathbf{U}(s)\mathbf{\Sigma}(s)\mathbf{V}(s)^{\mathsf{T}} \tag{2.24}$$

where $\mathbf{U} = \begin{bmatrix}\boldsymbol{u}_1 & \boldsymbol{u}_2 & \boldsymbol{u}_3\end{bmatrix}$ and $\mathbf{V} = \begin{bmatrix}\boldsymbol{v}_1 & \boldsymbol{v}_2 & \boldsymbol{v}_3\end{bmatrix}$ are unit-less orthonormal matrices whose columns are the "output" and "input" singular vectors, respectively. The diagonal of the matrix $\mathbf{\Sigma}$ contains the singular values, σ_1, σ_2, and σ_3, ordered from largest to smallest and with units m/N.

The input singular vectors, $\boldsymbol{v}_1$ and $\boldsymbol{v}_2$ indicate the directions of applied tip force that produce the largest and second-largest backbone position displacement, i.e., the directions of most and second-most compliance. The singular values σ_1 and σ_2 indicate the magnitude of the compliance. Figures 2.10(b) and 2.10(c) show the compliance input singular directions $\boldsymbol{v}_1$ and $\boldsymbol{v}_2$ of configurations "2" and "3", respectively, plotted at every arc length of the tool's backbone and scaled by their corresponding singular values. Figure 2.10(d) shows the the largest compliance singular value σ_1 for both configurations plotted as a function of backbone arc length.

It may be tempting to reduce the compliance by regrasping the flexible tool with

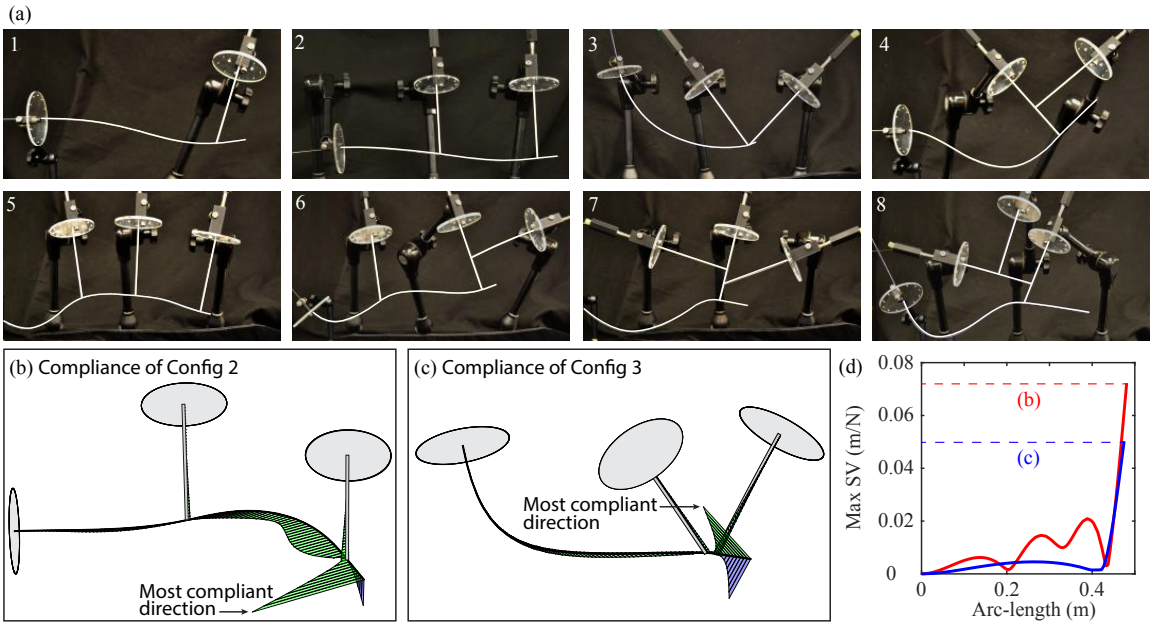

Figure 2.10: (a) Eight possible morphologies of a multi-needle robot consisting of one flexible tool and one to three snare-needles. (b)-(c) The most and second-most compliant directions of configurations "2" and "3" indicated by the input singular vectors of the backbone-position compliance matrix, scaled by their corresponding singular values. (d) The largest compliance singular value for configurations "2" and "3" plotted as a function of tool backbone arc length. The horizontal dashed lines indicate the value of the tip compliance singular value.

needles that are much stiffer than the tool. However, using snare needles that are much stiffer than the flexible tool they manipulate reduces the system's ability to control tip orientation independently of the tip position. This is because the tool and snare needles work in concert to position and orient the tip, i.e., the tool bends the snare needles and vice versa as shown in the example of Figure 2.7(a). When the snare needles are much stiffer than the tool, then the pose of the distal-most snare dominates the pose of the tip. This effect can be observed in the Jacobian's condition number. We anticipate that the compliance of a snared-tool system can be decreased without affecting the ability to control the tip pose by increasing the number (but not the stiffness) of snare needles.

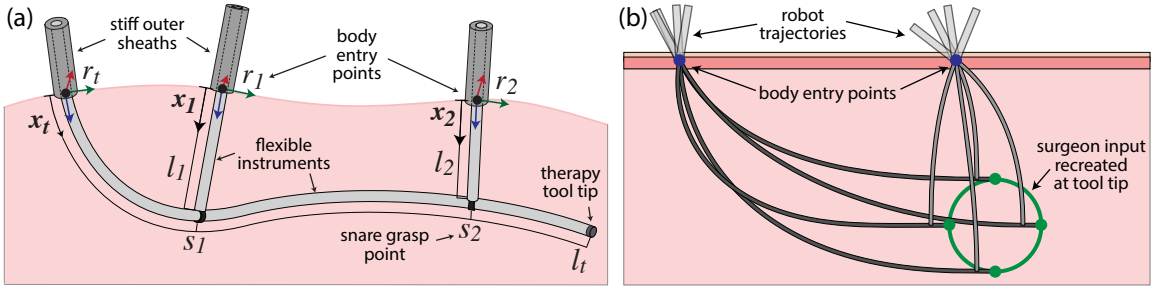

Figure 2.11: (a) Variable needle length modeling approach. (b) Simulated end effector control using the variable needle length model inverse kinematics.

2.3.10 Variable Length Needle Model

The body wall remote-center-of-motion constraints are an important aspect of the multi-needle robot from clinical, implementation, and design standpoints. Clinically, the RCM point is where the needle interacts with the tissue; since the multi-needle robot is motivated by the need for a highly minimally invasive approach, the needles must pass exactly through the RCM point in order to minimize pulling on the tissue at the body wall and prevent nerve injury. From a practical implementation standpoint, the previously described model can require the bases of the robot manipulators holding the needles to move large distances in space in order to accomplish the desired kinematic motions (see Figure 2.7). It may be desirable to reduce these motions as much as possible to limit the robot workspace size required around the patient, as well as to reduce the chance of collisions between the robot manipulators. Finally, the RCM points of the needles are a key design variable for optimizing the workspace of a multi-needle robot [131].

Because the body wall RCM point is so critical, we developed an alternative model formulation that allows the robot manipulators to sit directly at the RCM point and insert the needle into the body from the body wall, rather than deliver it from open space and have it curve through the RCM point. Not only does this reduce the motions required of the robot manipulators, but it also allows us to enforce the RCM

point in the software controlling the robot manipulators in addition to the kinematic model of the multi-needle robot.

To accomplish this, we append an additional variable to the state $\boldsymbol{x}_t$ of the tool needle and to $\boldsymbol{x}_i$ of each snare needle for the needle's length inserted into the body. The needle length is no longer fixed but can be controlled with a linear actuator from outside the body. The needle is covered by a stiff outer sheath outside the body, as shown in Figure 2.11 (i.e., we assume that it does not bend or twist outside the body). The actuation variables for the model are therefore the orientation of the needles outside the body (as controlled by the robot manipulators) and the insertion lengths of the needles. This model is utilized in [130, 131].

2.3.11 Tendon-Actuated Robot Comparison Study: Manipulability and Stiffness

A primary motivation for the development of the multi-needle robot concept is the potential stiffness advantages over some types of serial continuum manipulators. In the context of thoracic surgery, higher manipulator stiffness is advantageous for tisue manipulation, such as applying retraction and cutting forces. In order to contextualize the kinematic and stiffness performance of a multi-needle robot with respect to currently utilized manipulators, we performed a study comparing a multi-needle robot to a tendon-actuated robot with comparable dimensions. A tendon-actuated robot exhibits similar behavior to clinical tools such as flexible endoscopes with bending tips, making it a suitable analog for this study.

We designed the simulated multi-needle robot and tendon-actuated robot to have similar properties and configurations. The multi-needle robot consisted of two Nitinol tubes, each of which had an outer diameter of 1.016 mm and an inner diameter of 0.8382 mm; the tool needle was 200 mm long, while the snare needle was 100 mm long. Similarly, the backbone of the tendon-actuated robot consisted of a 200 mm long Nitinol tube with the same outer and inner diameter dimensions. It had 6

tendons equally spaced around the backbone at a radius of 4 mm.

The multi-needle robot was arranged such that the tip of the tool needle was orientated approximately 90° from its entry port. Therefore, the base of the snare needle was oriented parallel to the base of the tool needle and its base was positioned 140 mm from the base of the tool needle. The snare needle grasped the tool needle 10 mm from its tip and the fully constrained grasp assumptions were used. Similarly, the tendon-actuated robot was actuated such that it formed a curve with a 90° tip angle. In addition to the tension that could be applied to each tendon, the tendon robot was allowed to pivot about its base and insert/retract along its axis through the base point. This motion is analogous to a remote-center-of-motion body entry point such as the chest wall or abdomen wall, where the robot can rotate about and pass through the body entry point.

We computed the Jacobian and compliance matrix for each robot; the multi-needle robot matrices were found using the equations in Section 2.3.7, while the tendon-actuated robot matrices were computed using finite differencing and the tendon robot Cosserat rod model derived in [4]. We then computed the singular value decomposition for the Jacobian position and rotation submatrices (these were computed separately due to the difference in units), as well as the singular value decomposition for the compliance submatrices mapping change in force to change in tip position.

Using these results, we computed the position and rotation manipulability for each robot, where manipulability is defined as the product of the singular values of the Jacobian singular value decomposition (this metric measures the volume of the kinematic manipulability ellipsoid and is equivalent to the Jacobian's determinant) [172]. We also computed the inverse condition number, which is defined as

$$\frac{1}{\kappa} \equiv \frac{\sigma_{min}}{\sigma_{max}} \tag{2.25}$$

where σ_{max} is the maximum singular value and σ_{min} is the minimum singular value [172]. The inverse condition number is bounded between 0 and 1 and gives a measure for the isotropy of the manipulability and should be sought to be maximized.

The results of the comparison study can be found in Table 2.2. We found that both the position and rotation manipulability were higher for the multi-needle robot in this configuration. While the position manipulability was 4.6 times higher than the tendon-actuated robot, the rotation manipulability was 10.7 times higher than the tendon-actuated robot. The inverse condition number was comparable for the position kinematic ellipoid, but the rotation ellipsoid was much closer to isotropic for the tendon-actuated robot (0.712 vs. 0.083). Overall, the multi-needle robot exhibited better dexterity characteristics than the tendon-actuated robot.

In addition, the multi-needle robot was 11 times less compliant in the most compliant direction of each robot and 43 times less compliant in the least compliant direction of each robot. This demonstrates the significant stiffness benefits for the multi-needle robot when compared to a tendon-actuated robot with similar dimensions and configuration. In summary, this study motivates the use of multi-needle robots in surgical applications for their improved stiffness characteristics compared to their serial continuum manipulator counterparts. While it is important to acknowledge that this is an example study (there are countless combinations of robot architectures, dimensions, and configurations to compare), it nevertheless demonstrates the benefit of the parallel needle structure.

Given these results, it is also important to consider the effects of surgical forces on a multi-needle robot with these dimensions and configuration. In a study of electrocautery forces, Gafford et al. found that a maximum interaction force of 0.4 N was required to perforate porcine stomach [94]. Other studies have characterized suturing forces and found that typically less than 0.5 N is required when suturing liver tissue [173]. Using these benchmarks, we can estimate the deflection of the multi-needle end

Table 2.2: Dexterity and stiffness comparison of a multi-needle robot and tendon-actuated robot of similar dimensions.

Matrix	**Parameter**	**Tendon Robot**	**Multi-Needle Robot**
Position Jacobian	σ_{max}	1.012	1.225
	σ_{min}	0.131	0.162
	μ	0.026	0.127
	$1/\kappa$	0.130	0.133
Rotation Jacobian	σ_{max}	1.405	12.436
	σ_{min}	1.000	1.037
	μ	1.877	19.981
	$1/\kappa$	0.712	0.083
Position-Force Compliance	σ_{max}	1.950	0.175
	σ_{min}	0.044	0.001

effector in its most and least compliant directions. In this configuration, a force of 0.5 N would result in 87.5 mm of deflection if applied in the most compliant direction, but only 0.52 mm of deflection if applied in the least compliant direction. This demonstrates the importance of modeling and characterizing the compliance behavior of the robot so that this information can be integrated into the controller when performing surgical tasks. When performing an electrosurgical task, for example, it would be beneficial for the robot to change its shape (or even reconfigure grasp points) so that the applied force is aligned with its stiffer directions. It should also be noted that the example configuration, with the parallel structure formed in a single plane, makes it especially compliant in lateral directions.

This example also illustrates the potential benefits of reconfiguring the robot to achieve different compliance behavior. If a second snare needle also grasps the tool needle 5 mm behind the first grasp point (and the snare needle bases are spaced 40 mm apart laterally so that the needles form an approximately triangular truss shape), then the maximum compliance singular value is reduced to 0.0126 $^{\mathrm{m}}/_{\mathrm{N}}$. This represents a 92.8% decrease compared to the robot with a single snare needle and

would result in a deflection of only 6.3 mm given a force of 0.5 N. This demonstrates how the overall arrangement of the needles—and the use of additional incisionless needles in parallel—can influence the stiffness of the robot.

Finally, the design of the robot's individual needles should be considered in light of the desired surgical tasks. If the original single-snare robot had a snare needle with an outer diameter of 2.032 mm rather than 1.016 mm (with a corresponding doubling of wall thickness for an inner diameter of 1.676 mm), the maximum singular value of the position-force compliance submatrix decreases to 0.0153 $^{\mathrm{m}}/_{\mathrm{N}}$, compared 0.175 $^{\mathrm{m}}/_{\mathrm{N}}$ in the original design. If both needles had an outer diameter of 2.032 mm, the maximum singular value would be 0.0141 $^{\mathrm{m}}/_{\mathrm{N}}$, meaning that the robot with larger tubes would be 12.4 times less compliant than the original design. In this case, a force of 0.5 N in the most compliant direction would only result in a deflection of 7.1 mm. Interestingly, we see that the tip stiffness is significantly impacted by the dimensions of the snare needle for this particular configuration of actuator values and grasp point arc length. It is clear that tube dimensions are a critical aspect of future design algorithms for multi-needle robots.

2.4 Sensing and Estimation Framework

This section examines the problem of state estimation for multi-needle robots and was originally published in [129]. Our work is motivated by the fact that the needle-diameter continuum elements that make up the structure are continuously flexible and a physician will want to know the structure's shape for safe operation near sensitive tissue in the presence of uncertainty. Uncertainty can result from unmodeled friction or uncertainty in the tool and snare needles' base poses relative to the workspace (i.e., system inputs). Adding sensors to the system can reduce uncertainty, even though sensor observations can be subject to uncertainty themselves. Sensors that can be used with continuum robots are also appropriate for the multi-needle concept. Clin-

ically relevant sensors include electromagnetic tracking sensors [60], optical tracking systems [61], and fiber Bragg-grating sensors [62]. In the remainder of this section we extend concepts originally developed for continuum robots in [73] to multi-needle systems that enable powerful classical estimation techniques to be used to reason about a multi-needle system's state in the presence of uncertainty.

2.4.1 Statistical State Estimation for Multi-Needle Structures

The model (2.4) and constraints (2.16) developed in Section 2.3 are approximations that are subject to uncertainty. Uncertainty in the system is modeled with zero-mean additive process noise $\boldsymbol{q}_s$ and constraint noise $\boldsymbol{w}$ as

$$\boldsymbol{x}' = \boldsymbol{f}(\boldsymbol{x}, s) + \boldsymbol{q}_s \quad \text{and} \quad \boldsymbol{c} = \boldsymbol{w}, \tag{2.26}$$

where $\boldsymbol{x}'$ is the state derivative (2.4), $\boldsymbol{q}_s \sim \mathcal{N}(\mathbf{0}, \mathbf{Q}_s)$ and $\boldsymbol{w} \sim \mathcal{N}(\mathbf{0}, \mathbf{W})$. The covariance $\mathbf{W}$ is a block-diagonal matrix packed with covariances of the tool and snare constraints.

Uncertainty can be reduced by using sensors, even though they are also subject to uncertainty in the form of sensor noise. The goal of statistical state estimation is to infer the most likely state of a multi-needle system at all arc lengths s given uncertain sensors and models. Formulating a multi-needle system's kinematics in the form of (2.26) enables decades' worth of estimation techniques to be immediately applicable to the state estimation problem for multi-needle devices.

We model sensors as discrete observations along the body of a multi-needle structure at arc lengths $o_1 \dots o_m$. Noisy sensor observations $\boldsymbol{y}_{o_i}$ at discrete arc lengths o_i are given by the random process

$$\boldsymbol{y}_{o_i} = \boldsymbol{h}_{o_i}(\boldsymbol{x}_{o_i}) + \boldsymbol{z}_{o_i}, \tag{2.27}$$

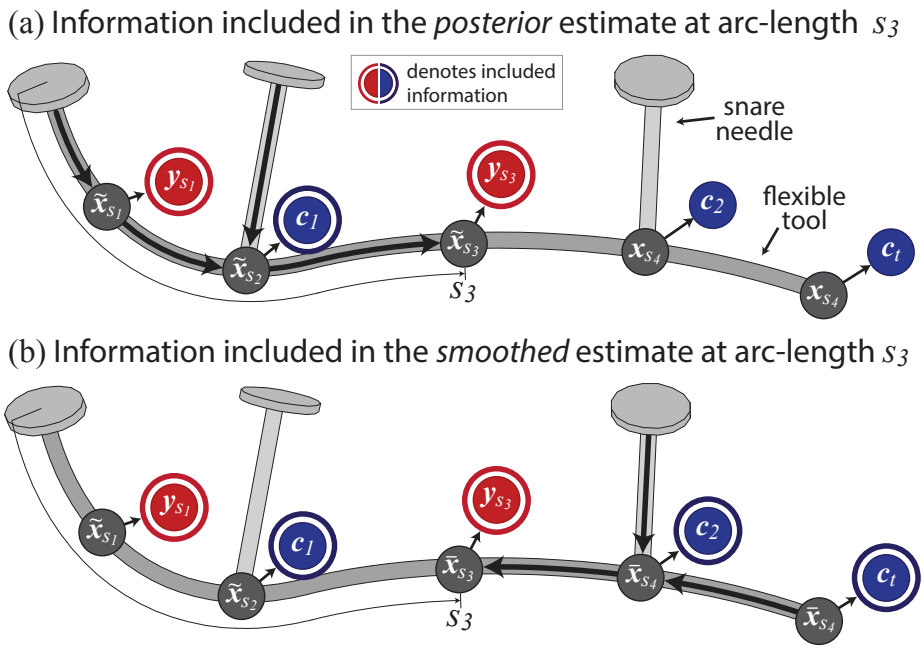

Figure 2.12: An illustration of the information incorporated in (a) the *posterior* state estimate generated by the Kalman-Bucy filter at arc length s_3, and (b) the *smoothed* estimate generated by the Rauch-Tung-Striebel smoother at arc length s_3. Sensor observations are denoted by $\boldsymbol{y}_i$. Constraints $\boldsymbol{c}_i$ are handled by the Kalman-Bucy filter as sensor observations.

where the function $\boldsymbol{h}_{o_i}$ models the sensor and $\boldsymbol{z}_{o_i} \sim \mathcal{N}(\mathbf{0}, \mathbf{Z}_{o_i})$ is zero-mean random noise with covariance $\mathbf{Z}_{o_i}$. Sensor covariances can typically be found experimentally.

The statistical estimate at arc length s that incorporates all available model and sensor information is referred to as the *smoothed* estimate, denoted by $\mathcal{N}(\bar{\boldsymbol{x}}_s, \bar{\mathbf{P}}_s)$ with expected value $\bar{\boldsymbol{x}}_s$ and covariance $\bar{\mathbf{P}}_s$. The smoothed estimate is computed by forward integrating (in arc length s) the extended form of the Kalman-Bucy differential equations and then backward integrating the extended form of the Rauch-Tung-Striebel (RTS) smoothing differential equations.

The Kalman-Bucy equations produce the *posterior* estimate of a multi-needle system's state, denoted by $\mathcal{N}(\tilde{\boldsymbol{x}}_s, \tilde{\mathbf{P}}_s)$, which is the statistical state estimate given the boundary constraints and sensor observations on the arc length interval $\begin{bmatrix} s_{\min} & s_{\max} \end{bmatrix}$ (see Figure 2.12(a)). The Kalman-Bucy differential equations that give the *posterior*

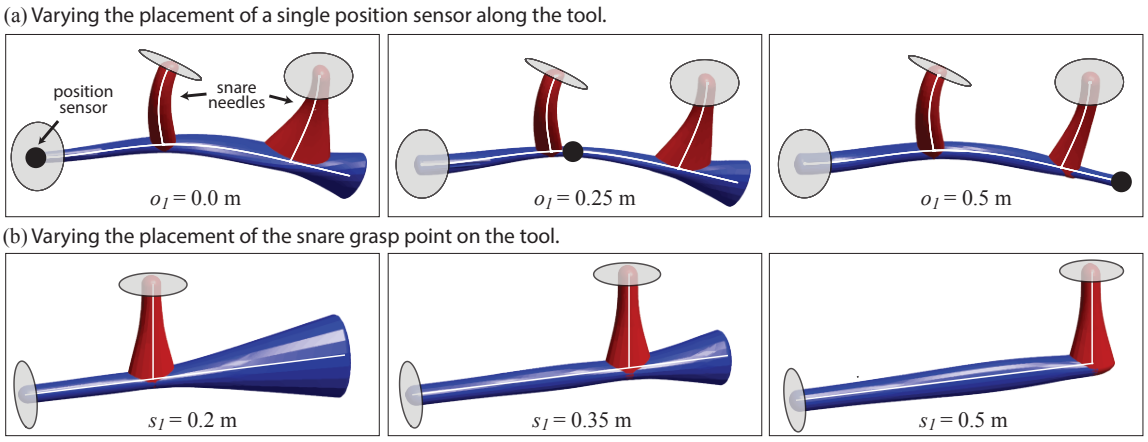

Figure 2.13: (a) A simulated two-snare multi-needle structure is shown with an overlaid depiction of the smoothed position covariance as a single position sensor is moved down the length of the flexible tool. The position covariance represents the position uncertainty of the tool and snares. The placement of the sensor dramatically changes the smoothed estimate's position uncertainty. (b) A simple multi-needle structure with one snare is shown with an overlaid depiction of the smoothed position covariance as the snare and its grasp point are translated along the tool's backbone. The snare configuration has a clear effect on the smoothed estimate's position uncertainty, which may influence how a multi-needle system is reconfigured. Note that this figure was generated with uncertainty in the snare grasp-point location on the tool's body.

state estimate are

$$\tilde{\boldsymbol{x}}'_s = \boldsymbol{f}(\tilde{\boldsymbol{x}}_s, s) \tag{2.28}$$

$$\tilde{\mathbf{P}}'_s = \mathbf{F}_s\tilde{\mathbf{P}}_s + \tilde{\mathbf{P}}_s\mathbf{F}_s^\mathsf{T} + \mathbf{Q}_s \tag{2.29}$$

with initial conditions $\tilde{\boldsymbol{x}}_{s_{\min}}$ and $\tilde{\mathbf{P}}_{s_{\min}}$, and where $\mathbf{F}_s = \partial\boldsymbol{f}(\boldsymbol{x}_s, s)/\partial\boldsymbol{x}_s$. The initial conditions represent the initial state belief. In this case, $\tilde{\boldsymbol{x}}_{s_{\min}}$ contains the initial registration of the base pose of each element as well as estimated values for other appended parameters (see Section 2.4.3).

A Kalman update is performed at each constraint arc length $s_1 \ldots s_n$ and at each sensor observation $o_1 \ldots o_m$ during the forward integration. In the case of a sensor

observation $\boldsymbol{y}_{o_i}$ at arc length o_i, the extended Kalman update equations are given by

$$\tilde{\mathbf{S}}_{o_i} = \tilde{\mathbf{H}}_{o_i}\tilde{\mathbf{P}}^{-}_{o_i}\tilde{\mathbf{H}}^{\mathsf{T}}_{o_i} + \mathbf{Z}_{o_i} \tag{2.30}$$

$$\tilde{\mathbf{K}}_{o_i} = \tilde{\mathbf{P}}^{-}_{o_i}\tilde{\mathbf{H}}^{\mathsf{T}}_{o_i}\tilde{\mathbf{S}}^{-1}_{o_i} \tag{2.31}$$

$$\tilde{\boldsymbol{x}}^{+}_{o_i} = \tilde{\boldsymbol{x}}^{-}_{o_i} + \tilde{\mathbf{K}}_{o_i}\left(\boldsymbol{y}_{o_i} - \boldsymbol{h}_{o_i}(\tilde{\boldsymbol{x}}^{-}_{o_i})\right) \tag{2.32}$$

$$\tilde{\mathbf{P}}^{+}_{o_i} = (\mathbf{I} - \tilde{\mathbf{K}}_{o_i}\tilde{\mathbf{H}}_{o_i})\tilde{\mathbf{P}}^{-}_{o_i}, \tag{2.33}$$

where $\hat{\mathbf{H}}_{o_i} = \partial \boldsymbol{h}_{o_i}(\boldsymbol{x})/\partial \boldsymbol{x}$ and $\mathbf{Z}_{o_i}$ is the covariance of the noisy sensor observation. The $^{-}$ and $^{+}$ symbols denote the state estimate before and after the update. In the case of a constraint $\boldsymbol{c}_i$, the sensor observation $\boldsymbol{y}_{o_i}$ and covariance $\mathbf{Z}_{o_i}$ in equations (2.30)–(2.31) are replaced by the expected constraint value $\mathbf{0}$ and the constraint's covariance, and $\hat{\mathbf{H}}_{o_i}$ is replaced with $\partial \boldsymbol{c}_i/\partial \boldsymbol{x}$.

The second step in the estimation process produces the *smoothed* estimate $\mathcal{N}(\bar{\boldsymbol{x}}_s, \bar{\mathbf{P}}_s)$ by integrating the RTS differential equations from the tip to the base arc lengths. The RTS differential equations are given by

$$\bar{\boldsymbol{x}}'_s = \boldsymbol{f}(\bar{\boldsymbol{x}}_s, s) + \mathbf{Q}_s\tilde{\mathbf{P}}^{-1}_s\left(\bar{\boldsymbol{x}}_s - \tilde{\boldsymbol{x}}_s\right) \tag{2.34}$$

$$\bar{\mathbf{P}}'_s = \left(\mathbf{F}_s + \mathbf{Q}_s\tilde{\mathbf{P}}^{-1}_s\right)\bar{\mathbf{P}}_s + \bar{\mathbf{P}}_s\left(\mathbf{F}_s + \mathbf{Q}_s\tilde{\mathbf{P}}^{-1}_s\right)^{\mathsf{T}} - \mathbf{Q}_s \tag{2.35}$$

with initial conditions $\bar{\boldsymbol{x}}_\ell = \tilde{\boldsymbol{x}}_\ell$ and $\bar{\mathbf{P}}_\ell = \tilde{\mathbf{P}}_\ell$. The *smoothed* estimate incorporates all sensor and constraint information on the interval $\left[s_{\min}\ \ s_{\max}\right]$ (see Figure 2.12(b)).

Figure 2.13(a) shows an illustration of the smoothed position covariance (a sub-matrix of $\bar{\mathbf{P}}_s$) of a simulated two-snare multi-needle structure with a position sensor placed at three locations on a 0.5 m-long flexible tool. The sensor's placement has a substantial effect on the system's position covariance. The sensor's placement along the flexible tool's body changes how informative the sensor is about the entire structure's shape. This can be observed when contrasting the position covariance of the

distal snare when the sensor is placed at the flexible tool's base ($o_1 = 0.0\,\mathrm{m}$) with the distal snare's position covariance with the sensor placed at the tool's tip ($o_1 = 0.5\,\mathrm{m}$). The information that a sensor provides depends on the sensor's noise covariance $\mathbf{Z}_{o_i}$ (smaller being more informative) and the mechanical structure of the multi-needle system (determined by the state matrix $\mathbf{F}_s$).

Along with sensor observations, a multi-needle system's configuration also has an important effect on its position covariance. Figure 2.13(b) shows an illustration of the smoothed position covariance of a multi-needle structure with one snare needle grasping the flexible tool at three different grasp points. Here, there are no sensor observations, making the smoothed covariance a function of the initial uncertainty in the system's inputs (the tool and snare base poses, as well as the grasp arc length). As illustrated, grasping the flexible tool at its tip ($s_1 = 0.5\,\mathrm{m}$) reduces the system's overall position uncertainty despite the same initial uncertainty in the tool and snare base poses. This is a result of the multi-needle system's parallel structure and is an advantage, shared with their rigid-link parallel counterparts [33], over serial continuum and rigid-link manipulators.

Figure 2.13(b) also illustrates that some multi-needle configurations are more information-rich than others (this was also observed for concentric tube robots [73]). When selecting how a multi-needle system should be reconfigured to meet changing application requirements, the system covariance will be an important consideration.

2.4.2 Observability Requirements

Designers of sensing systems for continuum robots must decide what sensors to use and where to place them. There are many considerations that must be made when selecting what sensors to use (e.g., size, cost, etc.). Although we do not address the advantages and disadvantages of the many sensing methods available to designers, the statistical state estimation methods of Section 2.4.1 require that the sensors be

chosen and placed so that the multi-needle system's states are "observable." This condition is satisfied when any perturbation that preserves the system's constraints can be detected in the sensor observations. This condition can be guaranteed by analyzing the rank of the system's observability matrix

$$\mathbf{O}(\boldsymbol{x}_{s_{\min}}) = \begin{bmatrix} \mathbf{Y}_{o_1}^{\mathsf{T}} & \dots & \mathbf{Y}_{o_m}^{\mathsf{T}} \end{bmatrix}^{\mathsf{T}} \tag{2.36}$$

in which $\mathbf{Y}_{o_i} = \partial \boldsymbol{h}_{o_i}(\boldsymbol{x}_{o_i})/\partial \boldsymbol{x}_{s_{\min}}$. If the observability matrix $\mathbf{O}(\boldsymbol{x}_{s_{\min}})$ has full rank, then the states can be locally estimated. Designers should select the number of sensors, types (i.e., position sensors, force sensors, etc.), and placements that make the observability matrix full rank.

2.4.3 Inferring Parameters from Observations

The power of the framework (2.28)–(2.35) as a tool for general estimation can be demonstrated by extending it to estimate general parameters. A parameter vector $\boldsymbol{d}$ can be inferred from noisy sensor observations and an uncertain model by augmenting the state vector $\boldsymbol{x}$ with vector $\boldsymbol{d}$ as

$$\boldsymbol{x} = \begin{bmatrix} \boldsymbol{x}_t & \boldsymbol{x}_1 & \dots & \boldsymbol{x}_n & \boldsymbol{d} \end{bmatrix}^{\mathsf{T}}, \tag{2.37}$$

where the arc length derivative of the parameter is $\boldsymbol{d}' = \mathbf{0}$ and augments the state derivative equation (2.4) in the same manner. The Kalman filter and smoother implicitly estimate the parameter $\boldsymbol{d}$ by the parameter's effect on the linearized state matrix $\mathbf{F}_s$.

Parameter estimation is a useful tool to remove the effects of non-zero-mean systematic uncertainty on the filter and smoother equations. For example, we found that the orthogonality assumption in the snare grasp constraint (2.11) can be relaxed by

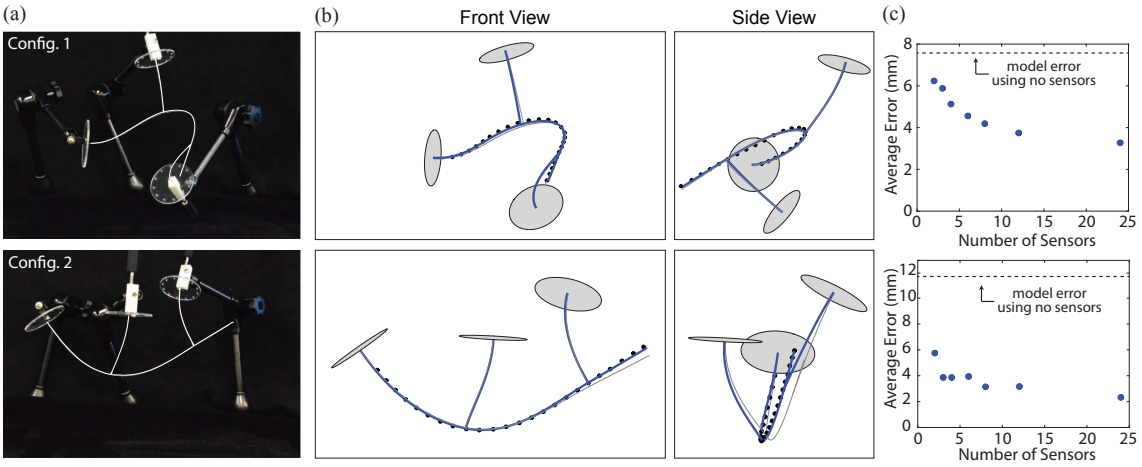

Figure 2.14: (a) The experimental multi-needle structure was placed into two configurations. The snare needles and flexible tool are traced for clarity. (b) Two views of the kinematic model (grey) and smoothed state estimate (blue) are plotted on top of 24 data points obtained with the electromagnetic tracker. (c) The average backbone position error (2.23) is shown as a function of the number of uniformly-spaced sensor observations incorporated into the smoothed estimate. The average error was computed from 100 samples and the standard deviation is smaller than the plot points.

re-expressing it as

$$\boldsymbol{p}'_t \cdot \boldsymbol{p}'_i - d_i = \mathbf{0} \tag{2.38}$$

and then estimating the parameter vector $\boldsymbol{d} = \begin{bmatrix} d_1 & \dots & d_n \end{bmatrix}^\mathsf{T}$. This approach is applied in Section 2.3.8.

Parameter estimation can also be used to estimate applied loads. Discrete applied forces $\boldsymbol{f}_j$ and moments $\boldsymbol{t}_j$ at known arc length s_j are incorporated into the kinematic model of Section 2.3 through equations (2.13) and (2.14). A force $\boldsymbol{f}_j$ at arc length s_j can be estimated by augmenting the multi-needle system state with the force $\boldsymbol{f}_j$ and updating the linearized state matrix $\mathbf{F}_{s_j}$ at arc length s_j accordingly.

Other parameters that can be estimated include system calibration properties (e.g., grasp-point location, rod stiffness, etc.). Many parameters can be estimated as long as the requirements for observability are satisfied.

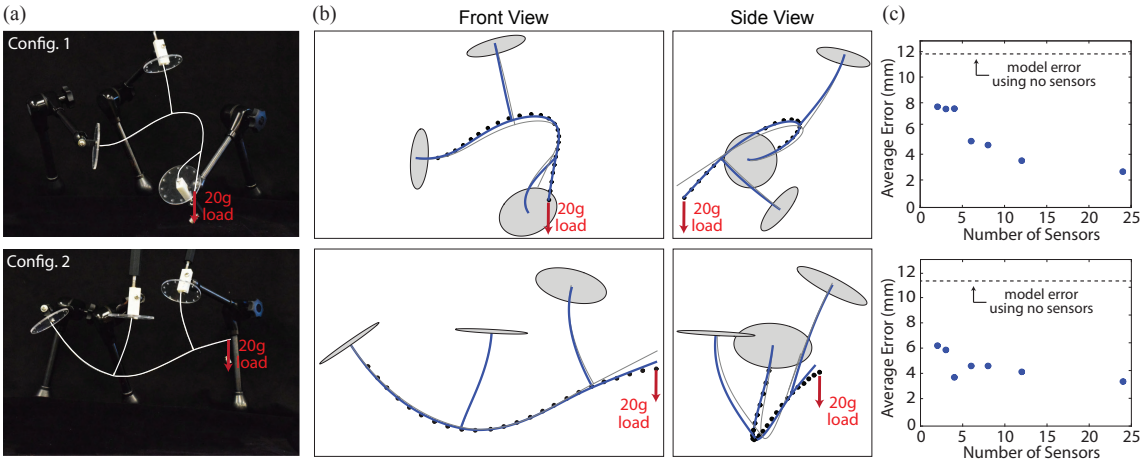

Figure 2.15: (a) The experimental multi-needle structure was placed into two configurations with a 20 g load applied 5 mm from the tool's tip. The snare needles and flexible tool are traced for clarity. (b) Two views of the kinematic model (grey) and smoothed state estimate (blue) are plotted on top of 24 data points obtained with the electromagnetic tracker. (c) The average backbone position error (2.39) is shown as a function of the number of uniformly-spaced sensor observations incorporated into the smoothed estimate. The average error was computed from 100 samples and the standard deviation is smaller than the plot points.

2.4.4 Estimation Framework Experimental Validation

The estimation framework presented in Section 2.4.1 was applied to a multi-needle device consisting of a flexible tool and two snare needles. The tool and snare needles were constructed out of Nitinol tubing (ID = 0.97 mm, OD = 1.27 mm, $E = 50$ GPa, $\nu = 0.33$). The lengths of the tool, first snare, and second snare were 500 mm, 154 mm, and 153 mm, respectively. The snare loops were made of 0.508 mm wide, 0.2794 mm thick Nitinol strip and were tensioned manually. The multi-needle structure was placed into two different static configurations using articulated holders (Figure 2.14(a)). The arc length grasp point locations for the first and second snare needles were 200 mm and 400 mm, respectively. The base poses of the tool and snare needles were localized by rigid registration using a Northern Digital, Inc. Aurora electromagnetic tracking system and a set of fiducial points arranged on clear acrylic disks. The acrylic fiducial disks were placed at the base of the flexible tool and both

snare needles. Six points on each disk were localized using a hand-held sensor probe.

The covariance of the tracker was measured to be isotropic with a standard deviation of 1 mm. The covariance of the base position and orientation (represented with a quaternion) was then found using the known geometry of the acrylic fiducial disks and the measured tracker covariance using the results of [174]. The estimation process was performed with no process noise (i.e., $\mathbf{Q}_s = \mathbf{0}$) and the grasp covariance pseudo-measurement was estimated *a priori*. In all experiments, the grasp constraint was relaxed to allow the snare needle axes and flexible tool axis to violate the perpendicularity constraint as described in Section 2.4.3. The numerical values of the base position and orientation covariances and the constraint covariances are given in Appendix B.

In both configurations, the shape of the flexible tool was measured using a 0.3 mm-diameter electromagnetic 5-DOF sensor at 24 uniformly-spaced positions separated in arc length by 20 mm. Figure 2.14(b) shows the raw tracker data plotted on top of the kinematic model presented in Section 2.3 and the estimated position generated by the Kalman smoother presented in Section 2.4.1 using all 24 data points. The accuracy of the model and smoothed estimate was measured by computing the average tool backbone error at all 24 sensor locations as

$$e(s_k) = \|\boldsymbol{p}_t(s_k) - \boldsymbol{p}_k^*\| \tag{2.39}$$

where $s_k = \big[0.04, \ldots, 0.5\big]$ are the 20 mm-spaced arc lengths where sensor data was collected, $\boldsymbol{p}_t$ is the tool backbone position (in the model case) or the smoothed tool backbone position estimate $\bar{\boldsymbol{p}}_t$ (in the smoothed case), and $\boldsymbol{p}_k^*$ is the measured tool backbone position. Figure 2.14(c) shows the average error of the smoothed estimate and the model after 100 trials, plotted as a function of the number of sensor observations on the flexible tool's backbone that were incorporated into the smoothed

estimate. This demonstrates how additional sensor observations improve the overall position estimate (given by the average error). However, it also shows that adding more sensors has diminishing returns in terms of error reduction; the designer should choose the number of sensors to balance accuracy with the complexity and cost of more sensors.

There is great interest in the continuum robotics community to use continuum devices as manipulators that can estimate the forces they are applying to their environment [74, 30, 72, 175, 176]. Elastic continuum devices are unique compared to their rigid serial-link counterparts in that they are intrinsically compliant devices, where their physical displacement can be used as an indicator of the applied forces [74, 30]. In the case of multi-needle systems, performing manipulation with the flexible tool will result in applied loads to the flexible tool's tip. If there is *a priori* knowledge that a force is being applied, but the force's magnitude and direction is unknown, then the applied force and shape can be simultaneously estimated (see Section 2.4.3).

Figure 2.15 shows the results of simultaneous force and shape estimation for the same configurations as Figure 2.14, but with an applied load created by a 20 g mass hung 5 mm from the flexible tool's tip. We anticipate that position accuracy will be critical for surgical tasks, even under applied loads during manipulation. Figure 2.15(c) shows the average backbone position error (2.39) (over 100 trials) of the smoothed estimate and the model (without any sensor observations).

The estimated applied load with no load present and with a 20 g load present is shown in Figure 2.16 for the configurations of Figure 2.14(a) and Figure 2.15(a), respectively, as a function of the number of sensor observations incorporated in the smoothed estimate. In the case of no actual load applied, the estimator reports almost no applied load (at most less than 6.5×10^{-7} N for both configurations) as shown in Figure 2.16(a). When the 20 g load is applied 5 mm from the tip of the flexible tool, the estimate under-reports the true load (Figure 2.16(b)). In an analysis of observability

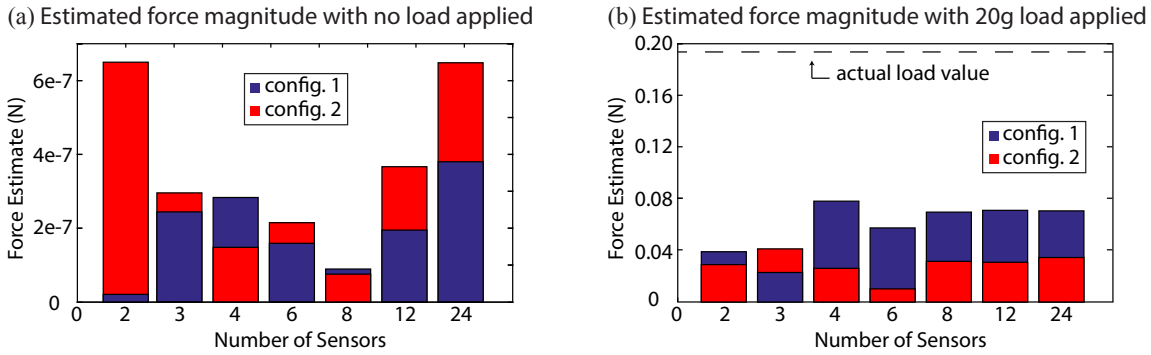

Figure 2.16: (a) The estimated applied load with no actual load present for the configurations shown in Figure 2.14(a), as a function of the number of sensor observations incorporated in the smoothed estimate. The estimator correctly reports there is virtually no load present when no load is actually applied. (b) The estimated applied load when a 20 g load is applied for the configurations of Figure 2.15(a), as a function of the number of sensor observations incorporated in the smoothed estimate. In an observability study and sensitivity study, we found that large uncertainty in the snare grasps can preclude the accurate estimation of applied load; uncertainty must be reduced through improved modeling or design, or through adding new sources of information to the system (e.g., force sensors at the base of each tube to measure actuation forces).

(see Section 2.4.2) we found that applied loads at the tip of the flexible tool are very difficult to distinguish from the parameters used to relax the orthogonality constraint at the grasp locations (see Section 2.4.3). This indicates that uncertainty in the grasp constraints precludes the accurate estimation of tip load. Future multi-needle systems that make use of force sensing must reduce uncertainty in the grasp constraints either through improved modeling or mechanical design. Note that despite under-reporting the tip-load magnitude, the estimate does correctly identify that no load is present when there is, in fact, no load applied.

It is clear that the force estimation accuracy of these experimental results is quite limited, particularly in comparison to force sensing results with other continuum robot systems. For example, Xu et al. used a multi-backbone robot to sense forces via the secondary backbones with an average error of 0.34 g and standard deviation of 0.83 g [30]. Black et al. also used actuation-based force sensing with a parallel continuum robot; the average error was 0.23 N (8% of the applied load) [37]. Similar

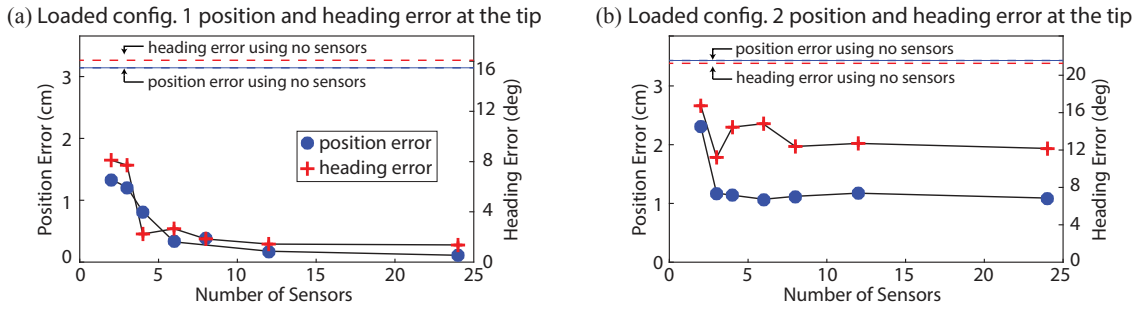

Figure 2.17: (a) The average *tip* position and *tip* heading error of the kinematic model with no sensors and the smoothed estimate measured at the tip of configuration 1 with a 20 g applied load, plotted as a function of the number of sensor observations incorporated in the smoothed estimate. (b) The average position and heading error of configuration 2 with the same load. In both examples, the state estimator does not know the direction or magnitude of the load. This demonstrates the estimator's ability to estimate the multi-needle system's shape even in the presence of an unknown load. The average error is computed with 100 samples and the standard deviation is too small to display.

methods could be explored for the multi-needle system and the estimation framework presented here.

We anticipate that the accuracy of the flexible tool's *tip* position and heading estimates will be critical for manipulation tasks, particularly for surgical tasks where the surgeon may not be able to directly observe the tool tip. Figure 2.17 shows the average position error (over 100 samples) of the smoothed estimate measured at the tool tip for varying number of sensor observations with the multi-needle structure configured in the two configurations shown in Figure 2.15(a). In addition, Figure 2.17 reports the average angle (over 100 samples) between the measured heading obtained by the magnetic tracker system at the tool's tip and the heading reported by the smoothed estimate and kinematic model (without any sensor observations). Note that tip position and heading was inferred by the state estimator from observations knowing the location of the applied force (5 mm from the tip) but without knowing the true magnitude or heading of the applied load. This is representative of the knowledge that a multi-needle system would have if the tip is being used for manipulation tasks.

2.4.5 Sensing and Estimation Discussion

The smoothed covariance matrix $\bar{\mathbf{P}}_s$ indicates the expected uncertainty of the system's state estimates, given known uncertainty in the model and sensor observations. As illustrated by Figure 2.13(a), varying the placement of sensor observations changes the smoothed covariance. After the requirements for observability are ensured, the smoothed covariance matrix $\bar{\mathbf{P}}_s$ can be used to reduce the uncertainty of a multi-needle system's state estimates. A task-specific covariance-based metric is introduced for this purpose in [73]. This ultimately turns the problem of selecting where to place sensor observations into an optimization problem. Since the sensor observation covariances are typically known in advance, actual sensor observations are not required to obtain the smoothed covariance matrix during the computation of the metric. The smoothed covariance can be computed before sensor data is collected, enabling sensor optimization during the system design process. We expect that this approach can also be applied to sensing systems for multi-needle structures, and will result in sensor placements that exploit the multi-needle structure to gain as much state information as possible.

A unique aspect of the multi-needle concept is that the parallel structures can be reconfigured in the body into entirely different topologies [128]. In this chapter, the state estimation techniques assume that the topology—the arrangement in which the snares grasp the tool or one another—is known *a priori*. If this is not the case, then the kinematic model cannot be solved and the statistical state estimation cannot be performed. Future work will focus on discovering the topology of a multi-needle system from sensor observations without *a priori* knowledge. Modular self-reconfigurable robots face a similar problem, which becomes more challenging as the number of modules is increased [139]. We anticipate that for many medical applications, a multi-needle system will likely consist of no more than two snares with a total of four possible topologies.

In both experimental loaded configurations, the smoothed estimate showed a significant improvement in tip position error. For a system with four sensors, configuration 1 had a 74% improvement in tip error (Figure 2.17(a)) and configuration 2 had a 66% improvement in tip error (Figure 2.17(b)). Such accuracy improvements are likely to be important in some clinical applications. We view this robot as a general-purpose concept that can be applied to a variety of thoracic and abdominal procedures (see [128] and Section 2.2 for additional discussion). Depending on the context, the required accuracy will vary. For example, when the robot is teleoperated, the surgeon can compensate for relatively large errors (1 cm errors are within the field of view of chip-tip cameras such as the minnieScope™-XS by Enable, Inc. when positioned at least 0.5 cm away from the tool tip), whereas higher accuracy will be required when the robot performs autonomous motions. We leave determining specific required accuracy thresholds to future work in which the basic multi-needle concept is applied in specific procedures. Future approaches to designing multi-needle structures should take the accuracy requirements of the clinical task into consideration while selecting sensor placements and determining how multi-needle systems should be reconfigured.

As discussed previously, the estimation framework significantly underestimated the applied tip load in both system configurations and an observability study found that the tip load is difficult to distinguish from other estimated parameters. To further characterize this discrepancy between the applied tip load and the estimated tip load in Section 2.4.4, we performed a sensitivity analysis on the assumptions made in the kinematic model. In particular, we examined the effect of the grasp conditions, the tip load, and the assumed material properties of the component tubes on the tip position of the flexible tool in the experimental configurations of Section 2.4.4.

First, we used finite differencing to compute three Jacobian matrices relating changes in grasp conditions to the tip position of the robot. The first matrix relates

changes in the grasp heading (the angle between the snare needle and tool needle, which is assumed to be 90°). Due to the small amount of surface contact area between the two tubes, it is easy for this angle to change depending on the system configuration. In addition, tip loads that bend the tip of the tool can cause the grasp angle assumption to be incorrect. There is one grasp heading parameter per grasp point as seen in (2.11).

The second matrix relates changes in the supported grasp moments. In the experiments, we assumed that the grasp joint does not support moments about either tube axis (i.e., the standard grasp constraint). From experimental experience, we find that it is likely that some degree of moments are supported about both axes, due to friction between the snare wire and tool needle; in addition, the tautness of the snare wire prevents the tool needle from rotating freely about the snare needle axis. Since there are two grasp points, there are four grasp moment parameters, as seen in (2.11).

The third Jacobian matrix relates changes in the arc length along the tool needle at which the snare grasps the tool. This parameter is subject to measurement error, and there is one arc length parameter per grasp point in the system. For the effect of the tip load, we again used finite differencing to compute the necessary Jacobian by perturbing the applied tip load $\boldsymbol{f}$ in (2.10).

We computed the singular value decomposition of each parameter's Jacobian matrix to analyze the relative effect of the parameters on the tip position. The results of this study are summarized in Table 2.3, in which σ_1 is the maximum singular value and σ_{min} is the minimum singular value. These results show that the tip position of the tool needle is most sensitive to the supported grasp moment parameters for both configurations. For Configuration 1, the grasp arc length has the next largest effect on tip position; for Configuration 2, the tip load has the next largest effect. We also investigated the effect of the assumed Young's modulus and Poisson's ratio of Nitinol (since both of these properties have acceptable ranges published by manufacturers),

Table 2.3: Tip load estimation sensitivity study. This study demonstrates that the conditions at the snare grasp points have a significant impact on the modeled tip position of the robot. In particular, the tip position is highly sensitive to whether moments are supported by the grasp joint.

Matrix	**Parameter**	**Configuration 1**	**Configuration 2**
Grasp Heading Jacobian	σ_1	0.062	0.065
	σ_{min}	0.034	0.020
Grasp Moment Jacobian	σ_1	2.475	8.511
	σ_{min}	0.094	0.131
Grasp Arc Length Jacobian	σ_1	1.134	0.582
	σ_{min}	0.861	0.082
Tip Load Jacobian	σ_1	0.593	1.096
	σ_{min}	0.041	0.021

but these effects were negligible compared to the modeling parameters even at the upper and lower bounds of these properties.

Given the sensitivity of the tip position to the grasp conditions and the uncertainty of how these conditions truly behave, we explored re-computing the estimation results with a higher covariance for the grasp update step (recall that the grasp update equations are considered to be a "sensor" that provides information to the estimation framework). Using higher covariance values means that we are much less certain about the information that is added at this step. While this approach did result in higher tip load estimates that were closer to the true physical load, the results were very sensitive to the choice of initialization values for the covariance matrix $\tilde{\mathbf{P}}_{s_{\min}}$, as well as the covariance values for the sensor updates. This limitation was also noted in a similar study on concentric tube robot force estimation [177]. In addition, while the force estimates improved, the backbone position estimates saw an increase in error.

The results of this sensitivity study demonstrate how unknown changes in assumed modeling parameters can have a significant impact on the shape of the robot. These effects make it challenging to successfully estimate tip loads via position sensing in the

presence of sources of modeling error that may have a larger effect on tip position than the tip load itself. As such, there are two important considerations to improve load estimation in future experiments. First, a better modeling approach or mechanical design for the grasp point conditions is essential for accurate modeling. It is clear that any supported moment about the axes of the needles plays a major role in the shape of the overall system. One such method is to design fully constrained grasp points that support fully moments about all three axes. This could be done through mechanical tips on the snare needle that surround and support the tool needle, as suggested in Section 2.3.4 and Equation (2.12).

The other possibility for improving the force estimation capabilities of these devices is to incorporate sources of information in the framework that are not strictly position-based. Other sources of information might provide better estimates than tip deflection alone. For example, we could integrate force and torque sensors into the tube base holders. This would provide the estimation framework with information about the actuation loads and torques that are being applied to the tubes at their proximal ends. Actuation-based force sensing has been successfully utilized in both parallel continuum robots [37] and multi-backbone robots [30, 178]. We could also include orientation measurements from the electromagnetic tracker, which would provide information about the needle's tangent vector. This approach was used in [177]; in that work, an interative approach was used so that the force estimate could converge over a long period of time, which may prove useful for this application as well. It may also be useful to measure forces and torques applied by the snare wires themselves. When using the unconstrained grasp condition, measuring the torque of each snare wire would provide feedback about the moments being applied at the grasp point. The force feedback of the snare wire would also be valuable during reconfiguration to determine when the snare has released and re-grasped the tool needle.

2.5 Future Work and Conclusions

The multi-needle robot concept is a novel approach to minimally-invasive medicine that reduces invasiveness by increasing the number of instruments that enter the body (in contrast to single-port approaches) while decreasing the diameter of each instrument down to that of a needle, requiring no incisions. These systems are excellent candidates for a robotic approach since the necessary motion of the snare needles and flexible tool outside the body is nonintuitive, particularly in the presence of body-wall fulcrum (i.e., RCM) constraints. This is demonstrated by the example trajectory of Figure 2.7. Here, we discuss some of the future research questions relating to the system; in particular, we focus on those at the intersection of continuum, parallel, and reconfigurable robotics.

Reconfiguration is a unique aspect of this concept that makes it particularly versatile as a robotic system. An open problem that multi-needle robots share with reconfigurable robots is that of planning when and how to reconfigure as task requirements change. Planning for reconfigurable robots includes both planning for individual components and planning the connectivity of the reconfigurable parts [138]. In the context of multi-needle robots in the operating room, the planning problem includes both planning the motion of the system inside the body while incorporating anatomical and safety constraints, and determining what configurations the system should form itself into based on the surgeon's needs (e.g., what forces are needed at the tool tip). The ability of the parallel structure to reconfigure from stiff to compliant configurations could be important for surgical applications that require localizing tumors via palpation (e.g., in the lung or liver). Further explorations of the effect of reconfiguration on stiffness and manipulability are necessary.

The planning problem is highly related to the problem of designing a system in that the choices made during the design process (e.g., how many snare needles to use and the relative stiffnesses of the tool and snares) directly affects the configurations it

can achieve. When designing serial continuum robots for manipulation in constrained environments, the geometry of the application guides the selection of the continuum robot's shape and mechanical design [42]. Kuntz et al. used the model presented in this chapter to develop a motion planning algorithm for multi-needle robots [130]. This motion planning algorithm was then employed in a design optimization scheme to select the needle body entry points and grasp locations that maximize visible anatomy [131]. In the future, these approaches can be used to optimize other aspects of multi-needle designs (e.g., tube stiffnesses and lengths) and create teleoperation frameworks that integrate motion planning. In addition, planning should be integrated with reconfiguration to determine the robot assembly configuration that can best carry out a given task.

As with rigid-link and continuum parallel robots, determining the workspace of a multi-needle robot is challenging [33]. Its workspace depends on the configurations that the robot can achieve and the elasticity of its members. One contributing factor to the limits of the workspace is the possibility of buckling in extreme configurations. Recent work in continuum robotics shows that elastic instability can be understood [59, 58, 36], actively avoided by planning [179], eliminated through design [180, 181], and avoided during real-time control with redundancy resolution (Chapter 3). We anticipate that the much of this work for continuum robots will also be applicable to multi-needle robots and can be used to inform the design and reconfiguration planning processes.

One of the first key tasks in future multi-needle system research is to design and build new robotic systems with the clinical workflow in mind. The first prototype versions shown in this chapter were designed with an emphasis on simple construction and debugging, with large open hardware that is easy to take apart and fix. Future actuation systems should be designed to be smaller and more compact, with consideration of the system's integration into a clinical setting. For example, we will

determine the best method of installing the robot manipulators in the operating room (e.g., multiple arms mounted to a single base, or each manipulator mounted to its own base). In the case of the variable needle length modeling approach, the needles could be held by RCM actuators that control needle orientation and insertion, rather than large robot manipulators. Future experiments will be conducted in the context of a dynamic surgical environment, requiring the system to change the grasp point location dynamically to accomplish different tasks. We will use testing in surgical environments to determine whether the estimation accuracy is sufficient for various clinical tasks. These experiments will also be used to validate the quasi-static modeling assumption. Another important consideration is the user interface for controlling the tool tip. In our early robot prototypes, we have teleoperated the system using a haptic device. In a clinical setting, the surgeon will have visual guidance via a chip-tip camera, which will allow for compensation of small estimation errors. This control scheme could also integrate motion planning to avoid local minima during teleoperation; the level of autonomous control in this scenario could be varied.

Clinical workflow and system integration will be important for addressing potential limitations and disadvantages of the multi-needle approach. Using multiple needles, each of which must be inserted at a particular known or tracked location on the chest wall and then attached to the actuation system, may increase setup time early in the procedure compared to a single-port approach. Setup may be particularly challenging or lengthy if the needle assembly process inside the chest cavity is difficult to perform in a surgical environment. We will perform extensive testing to identify the best methods for inserting and assembling the needles inside the closed chest.

This chapter has described the concept, modeling, and sensing of a new type of surgical robot. Multi-needle robots have the potential to give surgeons incisionless access to the chest cavity with the stiffness needed to manipulate flexible, needle-sized tools in open space. In this chapter, we have presented a mechanics-based

model for the multi-needle structure, including the forward and inverse kinematics and the Jacobian and compliance matrices. It was shown that the model can also be formulated such that the base position of each needle is fixed at the body entry point and the needle is inserted through and oriented about this remote center of motion. We also presented and evaluated a statistical estimation approach to shape sensing and parameter estimation.

Chapter 3

Elastic Stability-Aware Redundancy Resolution for Concentric Tube Robots

In this chapter, we present an algorithm for safely and intelligently controlling concentric tube robots. The control approach utilizes a new metric for the elastic stability phenomenon demonstrated in this type of robot and employs the metric to avoid unstable robot configurations while accomplishing different tasks. Other goals can also be incorporated into the redundancy resolution framework, such as locally optimizing robot tip stiffness.

The contributions of this chapter are a resolved rates control approach that uses redundancy resolution to locally optimize stability at each control loop cycle, requires no pre-planned path information, and has low computational burden. This algorithm actively moves the robot away from unstable configurations when the robot is close to snapping by utilizing a stability metric previously derived from first principles. We validate this instability control method on a physical concentric tube robot prototype and conduct real-world, real-time teleoperation and trajectory following experiments. We also demonstrate the ability to achieve other secondary control objectives, such as the changing the tip compliance of the robot.

The content of this chapter is adapted from a journal paper entitled "Exceeding traditional curvature limits of concentric tube robots through redundancy resolution" that is accepted to *The International Journal of Robotics Research*, of which I am the first author. The concept and preliminary simulation work in this chapter was first presented at the *2017 IEEE International Conference on Robotics and Automation (ICRA) C4 Surgical Robotics Workshop* [182]. The algorithm and simulations are also described in Chapter 4 of Dr. Richard Hendrick's dissertation [183], who was a collaborator on this work.

3.1 Introduction

Concentric tube robots have garnered considerable interest in the continuum and surgical robotics communities in recent years. They can achieve bending and elongation via the elastic interactions of their nested, precurved tubes (see Figure 3.1), effects which are desribed by mechanics-based models [39, 40]. These devices have been applied to a number of minimally invasive surgical applications because of their small diameter and dexterity. For a review of concentric tube robotics research and applications, see [49].

Despite many recent advancements in design, modeling, control, and practical applications, concentric tube robots have thus far been limited to maximum curvatures far below the theoretical upper limit provided by Nitinol's maximum recoverable strain. Yet higher curvatures are often desirable, because they enable the robot to work in smaller, more constrained spaces. The reason concentric tube robots have been limited to curvatures far below the maximum recoverable strain limit of the material is that highly curved tubes, when nested within one another and axially rotated, store torsional elastic energy. If the tubes rotate too far, they will exhibit an elastic instability, rapidly releasing this energy and "snapping" from one configuration to another. This snapping effect has recently been studied from design [181, 42, 184, 180] and modeling [58, 59] perspectives. Actuator motions likely to create snapping can now be predicted, and metrics for stability have been derived. Not only is the snapping motion potentially dangerous to the patient during surgery, but it also is uncontrollable from the surgeon's perspective. As described in Chapter 1, intuitive control behavior is essential to the success of continuum robots in minimally invasive surgery. If the robot does not behave as the surgeon dictates with the haptic device or other controller, then the surgeon will be unable to trust the performance of the robot. The goal of natural control is that the surgeon controls the robot without needing to think; rather, they move their hand left when they want the tip to go left,

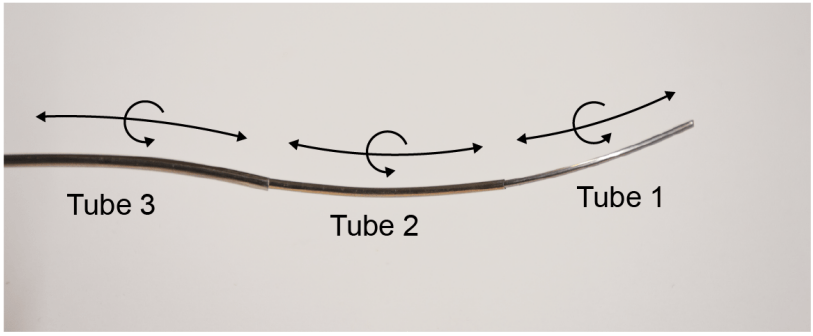

Figure 3.1: Three-tube concentric tube robot. Each nested tube can independently translate and rotate. Concentric tube robots with highly curved tubes can "snap" from one configuration to another due to rapidly released torsional energy. Real-time control schemes must be developed that prevent these elastic instabilities from occurring during teleoperation.

and the robot accomplishes the movement. Unstable snapping movements distract from this control paradigm. Therefore, elastic stability-aware control methods are necessary for both patient safety and surgeon ease of use so that concentric tube robots are effective tools for MIS.

To date, elastic stability-aware control has primarily been achieved in an *a priori*, motion planning sense. An early metric for stability was torsional windup [179], which has been used in planning stable paths [42]. Gilbert et al. devised a relative elastic stability metric and used it to produce stability maps for planning purposes [58]. These examples of stability-aware planners do not run rapidly enough to avoid snapping during real-time teleoperation. The goal of this work is to integrate instability avoidance into a real-time controller so that a user can control the robot safely.

Real-time control of concentric tube robots has been an important research topic in recent years. Several methods involve precomputation of the robot's forward kinematics or path plans; the inverse kinematics can then be solved online at each time step using root-finding methods [40] or a local inverse kinematics solver such as damped least squares [185]. Local Jacobian-based methods seek to solve the inverse kinematics online with no need for precomputation. For example, Burgner et al. proposed a

weighted damped least squares (WDLS) approach that incorporates tracking, damping, and joint limit goals [41]. This is an efficient Jacobian-based approach that can be solved at each time step with low computational burden. Other examples of Jacobian-based damped least squares control of concentric tube robots include [186, 78]. Our proposed approach in this work uses a similar WDLS approach to [41] that also incorporates instability avoidance and stiffness goals.

Online inverse kinematics methods have also been used for instability avoidance. Leibrandt et al. explored rapid, online motion planning for concentric tube robots while integrating elastic stability into the framework [187, 188]. While it has been shown that it is possible to compute these replanning approaches rapidly enough for use in real-time control via parallelized computing, they are computationally intensive and often require some *a priori* knowledge of the environment and/or the desired path. Implementation of these approaches typically requires multi-core parallel computing or graphical processing unit (GPU) computing methods. In contrast, the redundancy resolution approach we present in this paper is computationally inexpensive and requires no *a priori* information. Of course, the tradeoff for these advantages is that a redundancy resolution approach like ours makes no claims of global optimization to a desired final path—it will only locally optimize among competing objectives at each time step—but it is useful for teleoperation when anatomical constraints are not accurately known and/or the user's intended path is not known *a priori*. The ability of our method to move the robot away from unstable configurations is also an advantage over the rapid planning method in [188]; if the user enforces a particular trajectory, it is possible that the online inverse kinematics solver cannot escape local minimum due to the formulation of the stability constraint. Leibrandt et al. also used the online inverse kinematics solver to integrate dexterity goals; the dexterity measure penalizes columns of the Jacobian based on joint limits, anatomical collisions, and configuration stability [86]. Since we employ a computationally efficient Jacobian-based approach,

the controller moves the robot away from instability using knowledge of each joint's effect on the robot's stability. This is a noted limitation of [86] that arises from the high computational cost of the rapid planning GPU approach. Additional extensions in this paper beyond the work of [86, 188] include the integration of stiffness objectives, and experimental evaluation on a physical robot prototype. A final distinction is our use of a stability metric derived from first principles [58], whereas Leibrandt et al. used a torsional windup stability metric [179].

Khadem et al. employed a redundancy resolution approach to integrating instability avoidance into an online concentric tube robot controller [87]. They used a gradient projection method in which the secondary control goal is to reshape a force-velocity manipulability ellipsoid toward a sphere to ensure that the Jacobian is full rank. Our method uses a stability metric that is derived from first principles which enables the controller to enforce an exact stability threshold. In addition, our use of a WDLS redundancy resolution formulation enables the controller to override user trajectories that will make the robot unstable, whereas null-space methods must always satisfy the primary tracking task even when that task could cause instability. An additional advantage of our approach is that it pushes the system away from instability, whereas approaches that seek to iteratively maximize manipulability, like that of Khadem et al., can sometimes push the system toward instability.

It is also desirable to control the stiffness of a concentric tube robot in real time, based on application requirements. Recognizing this, Mahvash and Dupont proposed the first stiffness controller for concentric tube robots [176]. They used a deflection model to control the robot tip stiffness, based on real-time measurements of tip location made with a magnetic tracking coil. In some applications, it may be advantageous to keep an open lumen in the concentric tube robot for surgical instruments or suction/injection, rather than consuming it with such a tracking coil, and image-based tip position sensing may be unavailable or insufficiently accurate. Yet control

of tip mechanical impedance may still be useful, such as to enable the robot to gently interact with delicate tissues or forcefully interact with tissue (as must occur when a needle is being driven through tissue), as has been shown in the past with tendon-operated and multi-backbone continuum robots (e.g., see [189, 31]). One method for controlling tip stiffness is to examine its unified force-velocity manipulability ellipsoid [190, 87]. In these works, the controller seeks to reshape the force-velocity manipulability ellipsoid in order to increase its force application capabilities. Our approach seeks to optimize stiffness using the compliance matrix at the tip of the robot (although different metrics could easily be incorporated into the framework). Compliance control has also been utilized for multi-backbone robots: Goldman et al. designed a compliant motion controller to minimize interaction forces during insertion [178], while Bajo and Simaan used a hybrid motion/force controller to command both tip motion and interaction forces [31]. Both of these approaches estimate the external wrench by measuring backbone actuation forces, whereas the approach in this chapter does not require additional sensor measurements.

The redundancy resolution framework we present in this chapter enables both stiffness tuning and instability avoidance. Redundancy resolution has previously been applied to other kinds of continuum robots to accomplish a variety of objectives. For example, controllers for hyper-redundant robots have been developed that simultaneously command both end effector pose and backbone shape [81, 82]. Redundancy resolution has also been used to reduce actuation forces of tendon-actuated [21, 83] and variable diameter continuum robots [79], avoid buckling in multi-backbone continuum robots [29], improve stability in magnetically controlled continuum catheters [85], avoid joint limits in multi-backbone robots [77] and robots with multiple rolling joints [84], and reduce visual occlusion of the endoscope field of view [80].

Toward the goal of enabling higher curvatures than have traditionally been used in continuum robot prototypes (i.e., to facilitate the stable use of robots with elastic

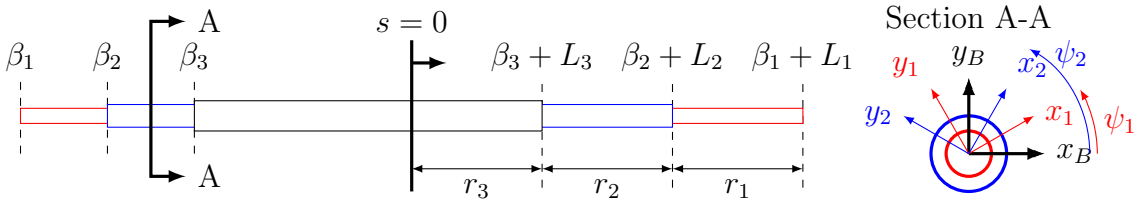

Figure 3.2: Key control variables of a concentric tube robot. The robot's shape has been straightened for clarity. The actuation unit grasps each tube at arc length β_i. The constrained exit point of the robot is marked at arc length $s = 0$. The section view A-A depicts the centerline Bishop frame and the material-attached frames of tubes 1 and 2, with angles ψ_1 and ψ_2 labeled. The controller presented here controls the translation variables $r_i = \beta_i + L_i$, which are the exposed lengths of each tube, and the rotation variables ψ_{iL}, which are the tube distal tip rotations.

instabilities in their workspaces) while also achieving stiffness objectives, we present a new redundancy resolution technique in this chapter. Our approach makes several contributions with respect to existing literature. Compared to rapid planning and parallelized kinematics approaches, our approach has low computational burden by locally optimizing stability (and/or stiffness) at each servo cycle with an efficient Jacobian-based WDLS method. Our method also requires no *a priori* knowledge of the planned path. We use a stability metric derived from first principles which exactly defines when a robot is stable or unstable, as well as how far a given configuration is from instability. Our redundancy resolution approach is formulated with the joint-specific relationship of configuration to stability and uses this knowledge to actively move the robot away from instability only when necessary. A preliminary version of some results in this chapter was presented in conference workshop form in [182]. Extensions in this chapter beyond the results in [182] include more extensive simulation results, the integration of stiffness objectives into the framework, and experimental results on a physical robot prototype.

3.2 Redundancy Resolution Algorithm

To achieve redundancy resolution with multiple control objectives for concentric tube robots, we use a weighted damped least squares control strategy. This section describes the objective function and resulting update law that incorporate instability avoidance and stiffness tuning objectives into resolved rates control.

3.2.1 Choice of Joint Space

In this work, we use the mechanics-based model of concentric tube robots described in [39, 40]. See [58] for a concise form of the equations. We use a notation where matrices are written in bold, upper-case, upright font (e.g., $\mathbf{M}$), vectors are written in bold, lower-case, standard font (e.g., $\boldsymbol{v}$), and scalars are written in lower-case standard font (e.g., s). The simulations and experiments in this chapter use a three-tube, six-degree-of-freedom concentric tube robot (see Figure 3.2). Such a robot has a joint space $\boldsymbol{q}$ given by,

$$\boldsymbol{q} = \begin{bmatrix} \psi_{1L} & \psi_{2L} & \psi_{3L} & r_1 & r_2 & r_3 \end{bmatrix}^{\mathsf{T}}, \tag{3.1}$$

where ψ_{iL} is the angle between the material frame of the i_{th} tube and a Bishop frame $\mathbf{R}_B$ at the tip of the robot, and r_i is the exposed length of each tube, or

$$\begin{aligned} r_1 &= \beta_1 + L_1 - \beta_2 - L_2 \\ r_2 &= \beta_2 + L_2 - \beta_3 - L_3 \\ r_3 &= \beta_3 + L_3 \end{aligned} . \tag{3.2}$$

The inner, middle, and outer tubes correspond to subscripts 1, 2, and 3, respectively.

We use tip angles $\boldsymbol{\psi}_L$ as joint variables here because they correspond to a unique configuration of the robot, which enables us to solve a single differential equation to determine the shape of the robot, rather than performing a shooting method on the differential equation, as would be needed if base angles were used. Note that after

Table 3.1: Concentric tube robot model and redundancy resolution nomenclature

$\boldsymbol{a}$	Bold typeface for vectors
$\mathbf{A}$	Bold, upright typeface for matrices
n	Number of tubes in concentric tube robot
$\boldsymbol{p}_B(s)$	Position of backbone Bishop frame at arc length s
$\mathbf{R}_B(s)$	Rotation matrix of backbone Bishop frame at arc length s
$\psi_i(s)$	Angle between the material frame of tube i and $\mathbf{R}_B$
ψ_{iL}	Angle between the material frame of tube i and $\mathbf{R}_B$ at tube tip
$\psi_{i\beta}$	Angle between the material frame of tube i and $\mathbf{R}_B$ at tube base
β_i	Arc length where tube i is held
L_i	Total length of tube i
r_i	Exposed length of tube i
β	$\min_i\{\beta_i\}$
L	$\max_i\{\beta_i + L_i\}$
$\theta_i(s)$	Relative tube angle $\psi_i - \psi_1$ at arc length s
$\mathbb{S}$	Elastic stability measure derived in [58]
$\boldsymbol{q}$	Joint vector
H	Weighted damped least squares cost function
$\mathbf{J}$	Robot Jacobian
$\mathbf{W}_i$	Weighting matrix

solving the initial value problem differential equation, the base angles $\boldsymbol{\psi}_\beta$ are known and can be commanded to the actuators. Furthermore, if base angles are used, the robot's configuration is not guaranteed to be uniquely specified, and can depend on actuation history [181, 58].

Throughout this paper, we use the elastic stability measure proposed in [58]. We give this stability measure the symbol $\mathbb{S}$, a scalar that is positive when the robot configuration is stable and negative when the robot configuration is unstable. Physically, the robot goes unstable when there is a direction in the solution space in which the robot can move to a lower energy state. This is identified mathematically by a negative eigenvalue of the second variation operation of the energy functional of the robot's twist angles. See [58] for a complete derivation and evaluation of the metric.

3.2.2 Redundancy Resolution Framework

During resolved rates teleoperation, the surgeon commands a desired trajectory, which is converted to a desired task space velocity $\dot{\boldsymbol{x}}_d \in \mathbb{R}^{m\times 1}$. The robot's Ja-

cobian $\mathbf{J} \in \mathbb{R}^{m \times n}$ maps instantaneous joint velocities $\dot{\boldsymbol{q}} \in \mathbb{R}^{n \times 1}$ to instantaneous task space velocities: $\mathbf{J}\dot{\boldsymbol{q}} = \dot{\boldsymbol{x}}_d$. Note that we use the hybrid Jacobian [172] throughout this chapter, with the desired task space velocity specified in the robot's base frame coordinates.

To control a concentric tube robot to track a sequence of desired tip coordinates, we use the weighted damped least squares framework [191], into which we previously incorporated tracking, damping, and joint limits [41]. In this work, we use the same tracking, damping, and joint limit goals as Burgner et al.; our contribution to this framework is the addition of instability avoidance and desired stiffness as additional objectives within this algorithm.

The damped least squares framework defines a cost function and applies weights to these potentially competing objectives. The cost function H, using the notation from [41], is given as

$$H = \frac{1}{2}\Big((\mathbf{J}\dot{\boldsymbol{q}} - \dot{\boldsymbol{x}}_d)^{\mathsf{T}}\mathbf{W}_0(\mathbf{J}\dot{\boldsymbol{q}} - \dot{\boldsymbol{x}}_d) + \sum_{i=1}^{p}(\dot{\boldsymbol{q}} - \boldsymbol{v}_i)^{\mathsf{T}}\mathbf{W}_i(\dot{\boldsymbol{q}} - \boldsymbol{v}_i)\Big)\,, \tag{3.3}$$

where $\mathbf{W}_i$ are non-negative symmetric weighting matrices. The first term penalizes any $\dot{\boldsymbol{q}}$ which does not follow the surgeon's command, while subsequent terms can be used to damp high velocities (if $\boldsymbol{v}_i$ is set to zero), to penalize joint configurations that are near joint limits, or to encourage joint velocities in the direction of the gradient $\boldsymbol{v}_i$ of some objective function. The necessary condition for $\dot{\boldsymbol{q}}$ to minimize H is found by setting $\partial H/\partial\dot{\boldsymbol{q}} = 0$ and can be shown to be

$$\dot{\boldsymbol{q}} = \Big(\mathbf{J}^{\mathsf{T}}\mathbf{W}_0\mathbf{J} + \sum_{i=1}^{p}\mathbf{W}_i\Big)^{-1}\Big(\mathbf{J}^{\mathsf{T}}\mathbf{W}_0\dot{\boldsymbol{x}}_d + \sum_{i=1}^{p}\mathbf{W}_i\boldsymbol{v}_i\Big)\,. \tag{3.4}$$

In this chapter, we will use a cost function and update law with standard tracking, damping, and joint limit avoidance terms that will be augmented with novel instability

avoidance and stiffness tuning terms. The cost function is given by

$$H = \frac{1}{2}\Big(\underbrace{(\mathbf{J}\dot{\boldsymbol{q}} - \dot{\boldsymbol{x}}_d)^{\mathsf{T}}\mathbf{W}_0(\mathbf{J}\dot{\boldsymbol{q}} - \dot{\boldsymbol{x}}_d)}_{\text{Tracking}} + \underbrace{\dot{\boldsymbol{q}}^{\mathsf{T}}\mathbf{W}_D\dot{\boldsymbol{q}}}_{\text{Damping}} + \underbrace{\dot{\boldsymbol{q}}^{\mathsf{T}}\mathbf{W}_J\dot{\boldsymbol{q}}}_{\substack{\text{Joint Limit} \\ \text{Avoidance}}} + \underbrace{(\dot{\boldsymbol{q}} - \boldsymbol{v}_i)^{\mathsf{T}}\mathbf{W}_i(\dot{\boldsymbol{q}} - \boldsymbol{v}_i)}_{\text{Secondary Goal}} \Big) , \quad (3.5)$$

which can again by minimized by setting $\partial H/\partial \dot{\boldsymbol{q}} = 0$. The resulting instantaneous joint velocity vector that minimizes H is

$$\dot{\boldsymbol{q}} = \Big(\mathbf{J}^{\mathsf{T}}\mathbf{W}_0\mathbf{J} + \mathbf{W}_D + \mathbf{W}_J(\boldsymbol{q}) + \mathbf{W}_{\mathbf{i}}(\boldsymbol{q})\Big)^{-1}\Big(\mathbf{J}^{\mathsf{T}}\mathbf{W}_0\dot{\boldsymbol{x}}_d + \mathbf{W}_{\mathbf{i}}(\boldsymbol{q})\boldsymbol{v}_i\Big) . \quad (3.6)$$

We will examine each term in this cost function and resulting update law in subsequent subsections. In particular, the instability avoidance and stiffness tuning terms are an important contribution of this work. The gains used in the algorithm are summarized in Table 3.3.

Tracking

The first term in the cost function (3.5) penalizes joint velocities $\dot{\boldsymbol{q}}$ that differ from those specified by the surgeon. The desired task space velocity is calculated using the current tip position $\boldsymbol{p}_{tip}$ given by the kinematic model and the desired tip position $\boldsymbol{p}_{des}$ from the surgeon interface:

$$\begin{aligned} \boldsymbol{e} &= \boldsymbol{p}_{des} - \boldsymbol{p}_{tip} \\ \dot{\boldsymbol{x}}_{des} &= v_{mag}\frac{\boldsymbol{e}}{\|\boldsymbol{e}\|} \end{aligned} \quad (3.7)$$

where v_{mag} is a piecewise continuous function of the magnitude of $\boldsymbol{e}$ given by

$$v_{mag} = \begin{cases} v_{min} & \|\boldsymbol{e}\| \leq e_{min} \\ v & e_{min} < \|\boldsymbol{e}\| < e_{max} \\ v_{max} & \|\boldsymbol{e}\| \geq e_{max} \end{cases} . \tag{3.8}$$

where

$$v = \frac{v_{max} - v_{min}}{e_{max} - e_{min}}\big(\|\boldsymbol{e}\| - e_{max}\big) + v_{max} \tag{3.9}$$

We also set a converged radius ρ, so that if $\|\boldsymbol{e}\| < \rho$, $\dot{\boldsymbol{x}}_{des} = 0$. The control gains for selecting the task space velocity are found in Table 3.2. The tracking weighting matrix is defined as

$$\mathbf{W}_0 = \alpha_0 \mathbf{I}_{3\times 3}, \tag{3.10}$$

where α_0 is a proportional tracking gain. Note that if tracking in a certain direction is more important than others, the elements of this weighting matrix could be adjusted accordingly by using a higher gain for these directions.

Damping

The second term in the cost function (3.5) penalizes high joint velocities $\dot{\boldsymbol{q}}$, adding numerical damping. The damping term has a weighting matrix defined by

$$\mathbf{W}_D = \alpha_D \begin{bmatrix} b_R \mathbf{I}_{3\times 3} & \mathbf{0} \\ \mathbf{0} & b_T \mathbf{I}_{3\times 3} \end{bmatrix} , \tag{3.11}$$

where α_D is an overall proportional damping gain, b_R is a rotational damping gain, and b_T is a translational damping gain. We distinguish b_R and b_T due to the different rotation and translation units.

Table 3.2: Control gains used for selecting the desired task space velocity $\dot{\boldsymbol{x}}_{des}$.

Parameter	**Symbol**	**Value**	**Units**
Maximum Task Space Velocity	v_{max}	100.0	$^{\text{mm}}/_{\text{s}}$
Minimum Task Space Velocity	v_{min}	13.0	$^{\text{mm}}/_{\text{s}}$
Maximum Velocity Error	e_{max}	5.0	mm
Minimum Velocity Error	e_{min}	1 .0	mm
Converged Radius	ρ	1.0 $\times 10^{-5}$	mm

Joint Limit Avoidance

The third term in the cost function (3.5) penalizes joint velocities $\dot{\boldsymbol{q}}$ that violate joint limits. Here, we define joint limits based on the exposed length of each tube. For each tube, we define a minimum and maximum exposed length, $r_{i,min}$ and $r_{i,max}$. In the simulations and experiments that follow, we make the choice to prevent a given tube from being retracted beyond the tip of the tube surrounding it, meaning that all $r_{i,min}$ must be greater than zero. Note that this joint limit definition could be relaxed if desired; it is not an intrinsic part of the algorithm. Specifically, we set all $r_{i,min}$ to 1 mm and all $r_{i,max}$ to 40 mm for the simulation studies. For the robotic experiments, we define the maximum limits based on the robot actuation unit travel limits. To avoid these joint limits, we define a joint limit penalty function as

$$J(\boldsymbol{r}) = \sum_{i=1}^{3} \frac{1}{4} \frac{(r_{i,max} - r_{i,min})^2}{(r_{i,max} - r_i)(r_i - r_{i,min})} \ . \tag{3.12}$$

which was inspired by results in [192]. We then define a weighting matrix as,

$$\mathbf{W}_J(\boldsymbol{q}) = \alpha_J \ \text{diag}\big(1 + |\nabla J_{\boldsymbol{q}}|\big) \tag{3.13}$$

where

$$\nabla J_{\boldsymbol{q}} = \begin{bmatrix} 0 & 0 & 0 & J_{r_1} & J_{r_2} & J_{r_3} \end{bmatrix} \ , \tag{3.14}$$

Table 3.3: Control gains. Note that joint units are in radians and meters, so what appear as large gains are reasonable, considering task space and translational joint velocities here are in the $^{\text{mm}}/_{\text{s}}$ range.

Parameter	**Symbol**	**Value**
Tracking Proportional Gain	α_0	1.0×10^8
General Damping Proportional Gain	α_D	0.1
Nominal Translation Damping	b_T	5.0×10^8
Nominal Rotation Damping	b_R	$(180/2\pi)^2$
Joint Limit Damping Proportional Gain	α_J	20.0
Stability Proportional Gain	$\alpha_{\mathbb{S}}$	10.0
Compliance Proportional Gain	$\alpha_{\mathbf{C}}$	300
Compliance Weight	$k_{\mathbf{C}}$	1000

$J_{r_i} = \partial J / \partial r_i$, and α_J is a proportional joint limit avoidance gain. We do not enforce rotational joint limits, so the first three elements of $\nabla J_{\boldsymbol{q}}$ are zero. With this strategy, the joint limit avoidance term dominates the cost function when a joint value r_i approaches its limits.

Instability Avoidance

When resolving redundancy to avoid elastic instability, the final term in the cost function (3.5) (i.e., the secondary goal) is designed to dominate the cost function when the robot configuration approaches instability as given by the metric $\mathbb{S}$, derived in [58]. We define an instability avoidance weighting matrix as

$$\mathbf{W}_{\mathbb{S}} = \Big(\exp\Big(\frac{1}{\mathbb{S} - \mathbb{S}^*} \Big) - 1 \Big) \mathbf{I}_{6\times 6} \ , \tag{3.15}$$

in which each diagonal element approaches infinity as $\mathbb{S}$ approaches the stability threshold $\mathbb{S}^*$. In such cases, we want the update law to command joint velocities that

move the robot away from unstable configurations. To do so, we define

$$\boldsymbol{v}_{\mathbb{S}} = \alpha_{\mathbb{S}} \frac{\partial \mathbb{S}}{\partial \boldsymbol{q}} = \alpha_{\mathbb{S}} \nabla \mathbb{S}_{\boldsymbol{q}} \; . \tag{3.16}$$

By choosing the proportional gain $\alpha_{\mathbb{S}} > 0$, the system will ascend the stability gradient when the instability avoidance term dominates the cost function, moving the robot to a more stable configuration. We numerically compute the stability gradient $\nabla \mathbb{S}_{\boldsymbol{q}}$ using centered finite difference (translational step = 0.01 mm, rotational step = 0.05 °). When computing this gradient, we take advantage of our choice of joint variables (see Section 3.2.1). Controlling tip angles and solving the kinematic model as an initial value problem with a single differential equation improves computational speed.

The instability avoidance weighting matrix (3.15) is designed such it does not impact the control law (3.6) when the robot's stability $\mathbb{S}$ is far from the stability threshold $\mathbb{S}^*$. In these cases, the diagonal elements of $\mathbf{W}_{\mathbb{S}}$ are nearly zero. The closer the stability metric is to the threshold, the more the instability avoidance term dominates the control law, causing the controller to steer the robot toward more stable configurations. This approach does not seek to continually maximize stability; rather, instability avoidance is only employed when necessary, allowing the controller to use as much of the stable configuration space as possible. Note that when this term is used in the remainder of the chapter, we will refer to (3.6) as the "instability avoidance control law."

Stiffness Tuning

When resolving redundancy to tune stiffness, we set a stiffness-based secondary goal in the cost function (3.5). To accomplish this, we make use of the concentric tube robot's compliance matrix $\mathbf{C} \in \mathbb{R}^{6\times6}$, which maps a tip wrench $\boldsymbol{\omega} \in \mathbb{R}^{6\times1}$ to a tip deflection $\boldsymbol{\delta} \in \mathbb{R}^{6\times1}$ as $\mathbf{C}\boldsymbol{\omega} = \boldsymbol{\delta}$ (see [171]). In surgical scenarios, it is common for

the robot to experience tip loads; therefore, we will utilize $\mathbf{C}_{\boldsymbol{fp}}$, which is the top left 3×3 submatrix of $\mathbf{C}$ that maps a force $\boldsymbol{f}$ to a position deflection $\boldsymbol{\delta_p}$.

While a variety of stiffness objectives can be defined based on this tip stiffness matrix, in the simulations that follow we simply use the maximum singular value of $\mathbf{C}_{\boldsymbol{fp}}$, for which we use the symbol $\sigma_{\mathbf{C}}$. More precisely, we have that

$$\mathbf{C}_{\boldsymbol{fp}} = \mathbf{U}\boldsymbol{\Sigma}\mathbf{V}^{\mathsf{T}} \tag{3.17}$$

and define $\sigma_{\mathbf{C}}$ as

$$\sigma_{\mathbf{C}} \triangleq \max\Big(\mathrm{diag}(\boldsymbol{\Sigma})\Big) \; . \tag{3.18}$$

This means that when $\sigma_{\mathbf{C}}$ is maximized, the system will attempt to achieve configurations with maximal compliance in its most compliant direction. On the other hand, when $\sigma_{\mathbf{C}}$ is minimized, the system will attempt to achieve configurations with minimal compliance in its most compliant direction. Alternative metrics for stiffness tuning include minimizing tip deflection (if the applied load vector is known), optimizing stiffness in a particular direction (e.g., axial or lateral stiffness, which could be beneficial for different applications), or incorporating the isotropy of the compliance matrix via the inverse condition number. The inverse condition number may be useful as a complement to the singular value approach to ensure that the controller does not send the robot to configurations that are ill-conditioned, with very high compliance in one direction but low compliance in other directions.

We define a compliance weighting matrix as

$$\mathbf{W}_{\mathbf{C}} = k_{\mathbf{C}}\mathbf{I}_{6\times 6} \; . \tag{3.19}$$

In order to maximize or minimize $\sigma_{\mathbf{C}}$, we define a joint space velocity vector $\boldsymbol{v}_{\mathbf{C}}$ as

$$\boldsymbol{v}_{\mathbf{C}} = \alpha_{\mathbf{C}} \frac{\partial \sigma_{\mathbf{C}}}{\partial \boldsymbol{q}} = \alpha_{\mathbf{C}} \nabla \sigma_{\mathbf{C}} \tag{3.20}$$

which points along the positive gradient of $\sigma_{\mathbf{C}}$ if the user defines $\alpha_{\mathbf{C}} > 0$ and along the negative gradient of $\sigma_{\mathbf{C}}$ if the user defines $\alpha_{\mathbf{C}} < 0$. This will command joint velocities that make the robot more (or less) compliant in its most compliant direction. We compute $\partial \sigma_{\mathbf{C}} / \partial \boldsymbol{q}$ numerically using the same centered finite difference parameters as Section 3.2.2. Unlike the instability avoidance term in the control law, which changes in magnitude based on proximity to the stability threshold, the compliance optimization term seeks to always move the robot into more (or less) compliant configurations due to the constant gain $k_{\mathbf{C}}$ used to compute the weighting matrix $\mathbf{W}_{\mathbf{C}}$. Note that when this term is used in the chapter, we will refer to (3.6) as the "stiffness tuning control law."

3.3 Simulations

We tested our redundancy resolution algorithm for both instability avoidance and stiffness tuning in simulation to verify its effectiveness, analyze its impact on the robot's behavior, and tune the control gains. This section first describes the instability avoidance simulations, followed by the stiffness tuning simulations.

3.3.1 Instability Avoidance Simulations

To test our elastic stability-aware redundancy resolution algorithm, we simulated the real-time control of a three-tube concentric tube robot made of superelastic nitinol tubes ($E = 50\,\text{GPa}$, $\nu = 0.33$, see Table 3.4 for tube dimensions) along a desired trajectory. In this simulation, we used the gain parameters given in Tables 3.3 and 3.2, as well as a minimum stability threshold of $\mathbb{S}^* = 0$.

Table 3.4: Tube parameters used in the simulations. Each undeformed tube has an initial straight section, followed by a tip section with constant curvature.

	Tube 1	**Tube 2**	**Tube 3**	**Units**
Outer Diameter	1.1	1.4	1.7	mm
Inner Diameter	1.0	1.3	1.6	mm
Total Tube Length	150.0	100.0	50.0	mm
Straight Tube Length	100.0	60.0	25.0	mm
Precurvature	30.0	30.0	30.0	m^{-1}

Desired Trajectory

During teleoperation, the desired input velocities are those commanded by the surgeon. Here, to create an example trajectory to use in simulation, we chose a helix wrapping around a torus, as shown in Figure 3.3. The equations defining the desired tip position were

$$\boldsymbol{p}_{des} = \begin{bmatrix} \big(R + r\cos(N_T\theta)\big)\cos(\theta) \\ \big(R + r\cos(N_T\theta)\big)\sin(\theta) \\ r\sin(N_T\theta) + z_{off} \end{bmatrix}, \tag{3.21}$$

where the torus' major radius (R) was 15.0 mm, its minor radius (r) was 3.0 mm, the number of helix turns (N_T) was 5, the offset from the x-y plane (z_{off}) was 55.0 mm, and $\theta \in [0, 2\pi)$. The robot's home position was given by $\boldsymbol{\psi}_L = \mathbf{0}$ and $r_1 = r_2 = r_3 = 20\,\mathrm{mm}$. We used a total simulation time of 10 s with a step time of 5 ms and implemented a standard resolved rates scheme in which the desired tip velocities were calculated using the error vector between the current position and desired position at each time step.

Simulation Results

We performed the simulation both with (the "stability-aware" case) and without (the "stability-unaware" case) the instability avoidance term included in the cost function and control law. In Figure 3.4(a), we show the stability metric and tracking error

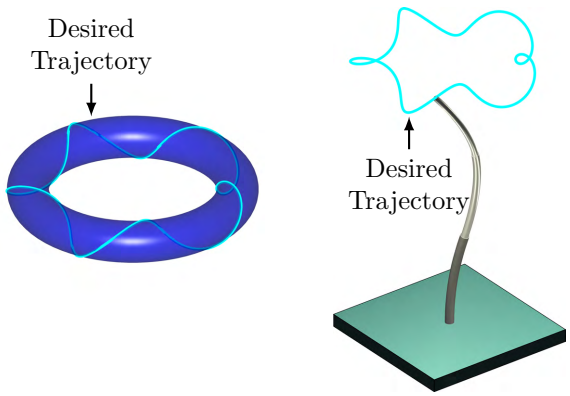

Figure 3.3: (Left) Desired trajectory of a helix wrapping around a torus. (Right) Simulated concentric tube robot following the desired trajectory.

throughout the entire trajectory for the stability-unaware case. Due to the high curvature of the tubes and the commanded trajectory, the robot snaps twice. The controller has no knowledge of this instability nor does it have a way to avoid it. Based purely on the kinematic model, the robot appears to be tracking well from the controller's perspective. However, the physical robot is in a different local minimum energy solution than the local minimum energy solution assumed by the controller, due to the uncontrolled snapping. As soon as the stability metric first crosses to $\mathbb{S} < 0$, the robot snaps to a configuration far away and tracking is lost.

Figure 3.4(b) shows that using the instability avoidance control law enables the robot to avoid instabilities while maintaining good tracking ($\sim$1 mm) in task space. Note that the error along the chosen trajectory is due to the dynamic trajectory and high damping; the error quickly reduces to < 0.01 mm when regulating a constant desired tip position. At the beginning of the trajectory, stability moves toward zero, but unlike Figure 3.4(a), the instability avoidance term causes the robot to move to a more stable configuration while continuing to track the desired trajectory.

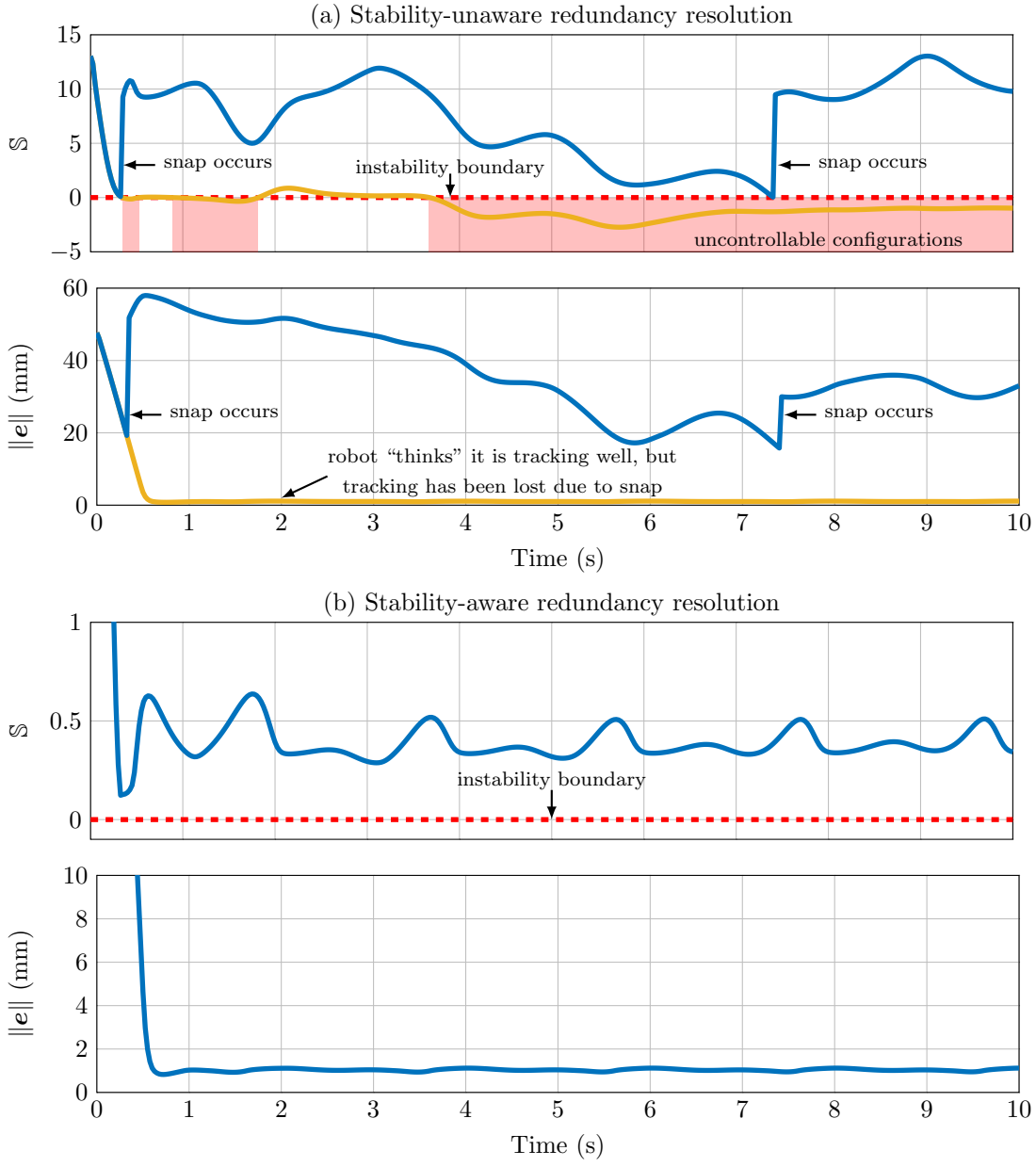

Figure 3.4: (a) When the control law is stability-unaware, the robot's stability crosses to $\mathbb{S} < 0$ and it snaps to a new configuration. Based on the kinematic model alone, tracking appears to be good, but tracking of the physical robot has been lost. (b) When the controller is stability-aware, the entire trajectory is stabilized. When $\mathbb{S}$ approaches zero, the robot moves away from the unstable configuration while still tracking the trajectory.

Computing the Robot's Post-Snap Configuration

In order to generate the simulated unstable robot trajectory, we calculated the new physical configuration of the robot in cases where the robot snaps. This was necessary for finding the results of Figure 3.4(a). The key idea behind this problem is that, when the robot is in an unstable configuration, there are multiple configurations in model space (and therefore multiple sets of tip angles $\boldsymbol{\psi}_L$) corresponding to the same base rotational angles $\boldsymbol{\psi}_\beta$. When the robot snaps, the current modeled tip angles are unstable, and the physical solution must be found. To find the new, post-snap configuration, one must search the tip angle space for a configuration corresponding to the same base angles $\boldsymbol{\psi}_\beta$. Note that the relative tube angles affect stability, not the absolute angles, so the search for the new configuration is done in the relative angle space and then converted back to absolute angles. We define the relative joint angles as $\theta_i = \psi_i(s) - \psi_1(s)$.

When the stability of the robot in the simulation goes to 0, we use MATLAB's `fzero` function to find the exact relative tube angles $\boldsymbol{\theta}_{L,unstable}$ at the edge of the unstable configuration space. This point is shown by the yellow"before snap" points in Figure 3.5. Once this unstable configuration is found, we calculate the unique relative base angles $\boldsymbol{\theta}_\beta$ using the kinematic model. Then, we use MATLAB's `fsolve` function to find another set of relative tip angles $\boldsymbol{\theta}_{L,stable}$ that produce the same relative base angles as the unstable solution.

Because the relative joint space is wrapped from 0 to 2π radians we must convert the new relative tip angles to absolute angles. To do so, we first assume a configuration of $\boldsymbol{\psi}_{L,guess} = \left[0,\, \theta_{2L,stable},\, \theta_{3L,stable}\right]^\mathsf{T}$. Solving the kinematic model returns absolute base angles that have the same relative angles but are offset from the original absolute base angles by $\Delta\boldsymbol{\psi}$. We then add this offset to the tip angle guess to get the new,

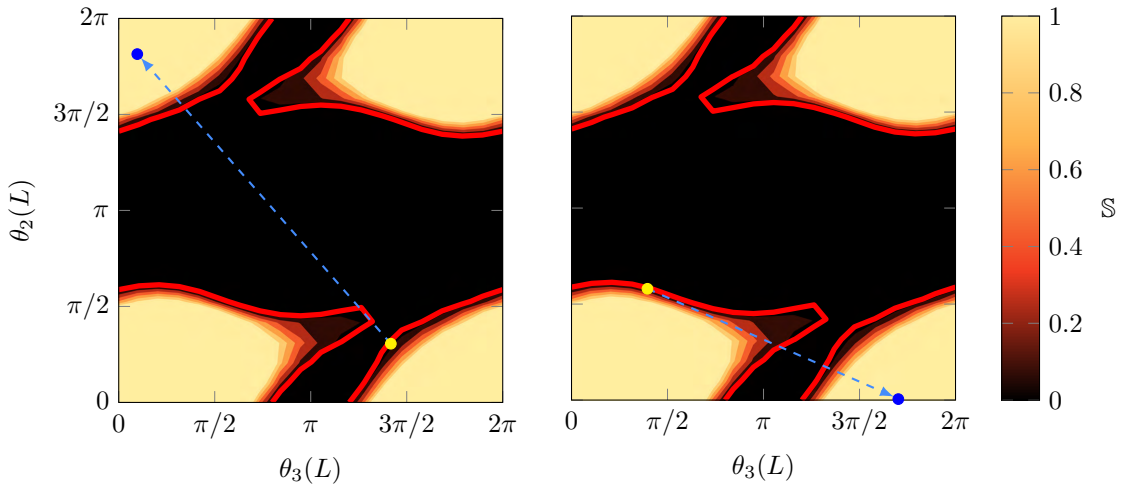

Figure 3.5: These plots show the relative tip angle configuration space of the simulated three-tube concentric tube robot. The colormap depicts the stability measure $\mathbb{S}$, truncated from 0 to 1. The red line is the boundary of the unstable region. When the robot hits this boundary at the yellow dots, it snaps. The new configuration it reaches after the snap can be found by searching the configuration space for a set of relative tip angles that produces the same relative base angles at the actuators (blue dots). Note that the shape of the unstable region can change substantially based on tube translation variables.

stable configuration:

$$\boldsymbol{\psi}_{L,stable} = \begin{bmatrix} 0 & \theta_{2L,stable} & \theta_{3L,stable} \end{bmatrix}^{\mathsf{T}} + \Delta\boldsymbol{\psi}. \tag{3.22}$$

The new robot configuration is shown by the blue "after snap" points in Figure 3.5. This approach could potentially be used in a physical system to "recover" tracking should a snap occur.

Effect of Instability Avoidance

When using the weighted damped least squares approach for redundancy resolution, there are several interacting variables (damping, joint limit avoidance, tracking, and instability avoidance) which interact in a nonlinear manner. Selecting gains can be challenging and the performance of the algorithm can be sensitive to these gain selections. There was one analysis tool that proved particularly useful towards selecting

these gains. If we define the 6×6 inverted matrix from (3.6) as $\mathbf{A}$, then we can re-express this update law as

$$\dot{\boldsymbol{q}} = \underbrace{\mathbf{A}\mathbf{J}^{\mathsf{T}}\mathbf{W}_0\dot{\boldsymbol{x}}_d}_{\dot{\boldsymbol{q}}_T} + \underbrace{\mathbf{A}\mathbf{W}_{\mathbb{S}}(\boldsymbol{q})\boldsymbol{v}_{\mathbb{S}}}_{\dot{\boldsymbol{q}}_{\mathbb{S}}} , \tag{3.23}$$

and it becomes clear that the joint velocity $\dot{\boldsymbol{q}}_T$ is related to tracking, and the joint velocity $\dot{\boldsymbol{q}}_{\mathbb{S}}$ is related to instability avoidance. We can compare the norm of these two competing joint velocities to better understand which term is dominating the simulation. Figure 3.6 shows the relative norm of these joint velocities, or

$$\phi_{\mathbb{S}} = \frac{\|\dot{\boldsymbol{q}}_{\mathbb{S}}\|}{\|\dot{\boldsymbol{q}}_{\mathbb{S}}\| + \|\dot{\boldsymbol{q}}_T\|} \tag{3.24}$$

for both rotational ($\phi_{\mathbb{S},\boldsymbol{\psi}_L}$) and translational ($\phi_{\mathbb{S},\boldsymbol{r}}$) joint velocities for the simulation. As is clear from the figure, when $\mathbb{S}$ is low, the effect of $\dot{\boldsymbol{q}}_{\mathbb{S}}$ becomes more prominent. In addition, there appears to be an oscillating exchange of control priority from tracking to instability avoidance.

Effect of Stability Threshold

We explored the effect of the stability threshold $\mathbb{S}^*$ on the robot's behavior. We performed the trajectory-following simulation with $\mathbb{S}^*$ chosen as 0.0, 0.1, 0.2, and 0.3. The results of these simulations are shown in Figure 3.7. In each case, the controller tracks well and does not violate the stability threshold. As can be seen in Figure 3.7(Top), the stability trajectories are nearly identical and only differ by an offset in $\mathbb{S}$. The initial tracking response time is slower for higher values of $\mathbb{S}^*$, as shown in Figure 3.7(Bottom).

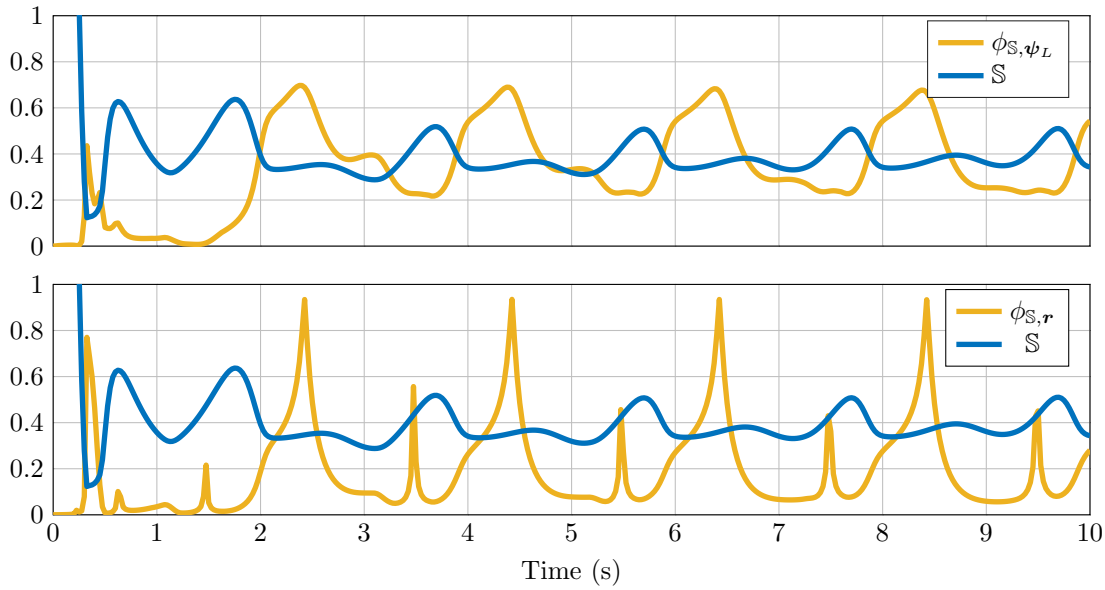

Figure 3.6: (Top) $\phi_{\mathbb{S},\boldsymbol{\psi}_L}$ and $\mathbb{S}$ in time. When stability is low, stabilizing rotational joint velocities become more prominent. (Bottom) $\phi_{\mathbb{S},\boldsymbol{r}}$ and $\mathbb{S}$ in time. When stabilility is low, there are short bursts of stabilizing translational joint velocities.

3.3.2 Stiffness Tuning Simulations

To test our stiffness-tuning redundancy resolution algorithm, we simulated the real-time control of a three-tube concentric tube robot. For this simulation, we used tubes of the same dimensions as Table 3.4 with curvatures of 10, 12, and 22 m^{-1} for tubes 1, 2, and 3, respectively.

Stiffness Tuning with Trajectory Following

First, we optimized $\sigma_{\mathbf{C}}$ while the robot follows the torus trajectory given by (3.21). The results for this redundancy resolution controller are shown in Figure 3.8. The first panel depicts $\sigma_{\mathbf{C}}$ throughout the trajectory with $\alpha_{\mathbf{C}}$ set to 300 (maximize $\sigma_{\mathbf{C}}$), -300 (minimize $\sigma_{\mathbf{C}}$), and 0 (nominal performance). The second panel shows the difference in performance when maximizing or minimizing $\sigma_{\mathbf{C}}$. This shows that the redundancy resolution algorithm is capable of commanding a robot configuration that is nearly four times more compliant (in its most compliant direction) than the least compliant

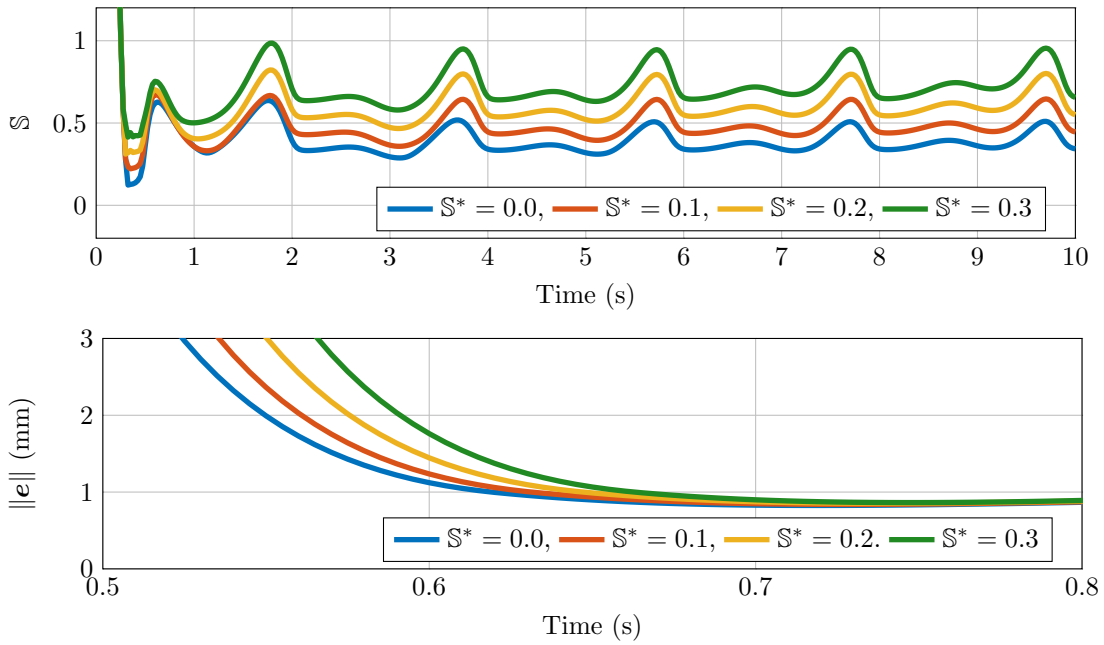

Figure 3.7: (Top) The stability metric $\mathbb{S}$ in time for varying choices of $\mathbb{S}^*$. (Bottom) The tracking error in time for varying choices of $\mathbb{S}$. Note that the time axis is only 0.3 s. The tracking response time is correlated with the choice of $\mathbb{S}$.

case. The third panel shows the tracking error in task space is similar and small for each case ($\sim$1 mm).

It is likely this difference in compliance would be apparent to a surgeon. It has been shown that the peak forces during minimally invasive surgery are around 2 N for suturing skin, around 1 N for suturing muscle, and typically less than 0.5 N for suturing liver tissue [173]. The forces during other tissue interactions (i.e., not driving needles) are typically much less than these. For example, Gafford et al. found that using bipolar cautery tools to perforate layers of porcine stomach produced maximum interaction forces of 0.4 N, with most forces closer to 0.2 N [94]. As a specific example of the potential utility of this control law, consider a 0.5 N force on the tip of the concentric tube manipulator investigated here. In maximum compliance mode, this would generate a deflection of up to 20 mm, and in minimum compliance mode, this would generate a deflection as small as 5 mm. This could very well be the difference between being able to drive the needle and not drive the needle, and the difference

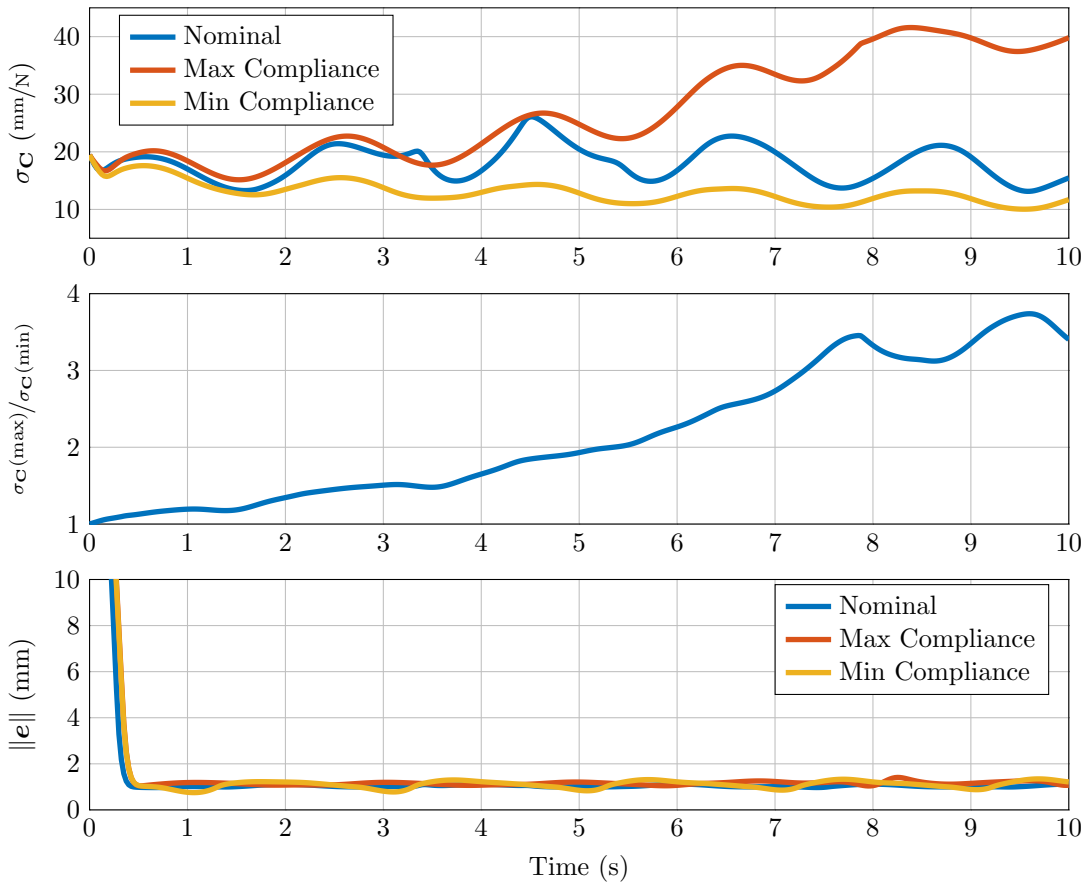

Figure 3.8: (Top) Trajectories of the compliance metric $\sigma_{\mathbf{C}}$ following the path described in (3.21) with the tubes from Table 3.4. For the nominal trajectory, we utilize the control law from (3.4), for the maximum compliance trajectory we utilize the stiffness tuning update law from (3.6) with $\alpha_{\mathbf{C}} = 300$, and the same law for the minimum compliance trajectory with $\alpha_{\mathbf{C}} = -300$. (Middle) The ratio of $\sigma_{\mathbf{C}}$ in the maximum compliance trajectory to $\sigma_{\mathbf{C}}$ in the minimum compliance trajectory. The manipulator becomes nearly four times more compliant by the end of the trajectory, which is likely to be significant in a surgical scenario. (Bottom) All three trajectories have very similar tracking performance.

in deflection would be apparent in the surgeon's field of view.

Stiffness Tuning with Position Regulation

Next, we sought to maximize or minimize $\sigma_{\mathbf{C}}$ while keeping the tip position of the robot at a fixed position in space, which illustrates the degree of stiffness tuning self-motion. We commanded a static tip position at $\boldsymbol{p} = \begin{bmatrix}1, 1, 55\end{bmatrix}^{\mathsf{T}}$ mm, which is near the center of the robot's workspace. The simulation lasted for 40 seconds, where every

10 seconds we changed the goal from maximizing ($\alpha_{\mathbf{C}} > 0$) to minimizing ($\alpha_{\mathbf{C}} < 0$) $\sigma_{\mathbf{C}}$, or vice versa. This is shown in the first panel of Figure 3.9.

The second and third panels of Figure 3.9 show the configuration variable paths that move the robot from compliant configurations to stiff configurations, and vice versa. The translational joint values shown in the third panel make intuitive sense: when maximizing $\sigma_{\mathbf{C}}$, the outer tube nearly fully retracts (r_3 approaches 0 mm), meaning that the exposed length of the robot is almost entirely made up of the middle and inner tubes, which are more flexible. The fourth panel of Figure 3.9 shows $\sigma_{\mathbf{C}}$ throughout the simulation as it is clearly maximized and minimized according to $\alpha_{\mathbf{C}}$. Also, note that the error is not plotted here, but quickly approaches ∼0.1 mm and remains there throughout the trajectory. In this case, a 0.5 N electrosurgical or suturing force applied to the tip of the robot in its most compliant direction would deflect the tip 19.1 mm when the controller is maximizing compliance, but only 7.7 mm when minimizing compliance.

While a maximum deflection of 19.1 mm may seem large, it should be noted that many concentric tube robots used in surgery may be shorter than the robot used in these simulations. The simulation was repeated with a desired tip position of $\boldsymbol{p} = \begin{bmatrix}1, 1, 40\end{bmatrix}^{\mathsf{T}}$ mm (i.e., reducing the cantilevered length by 15 mm), a longer switching time of 40 seconds, and a starting configuration of $r_1 = r_2 = r_3 = 10$ mm. This approach yields a maximum and minimum deflection of 8.3 mm and 2.7 mm, respectively. The robot is 3 times stiffer when minimizing compliance, which is a similar relative difference as the previous simulations, but the predicted deflection is smaller due to the shorter robot length. Also, note that the tip compliance can be further optimized by the controller by increasing the value of α_C. Conducting the experiment with $\alpha_C = 2000$, the predicted maximum and minimum deflection are 10.7 mm and 2.5 mm, respectively. However, this comes at the cost of slightly higher mean tip position error of 1.8 mm.

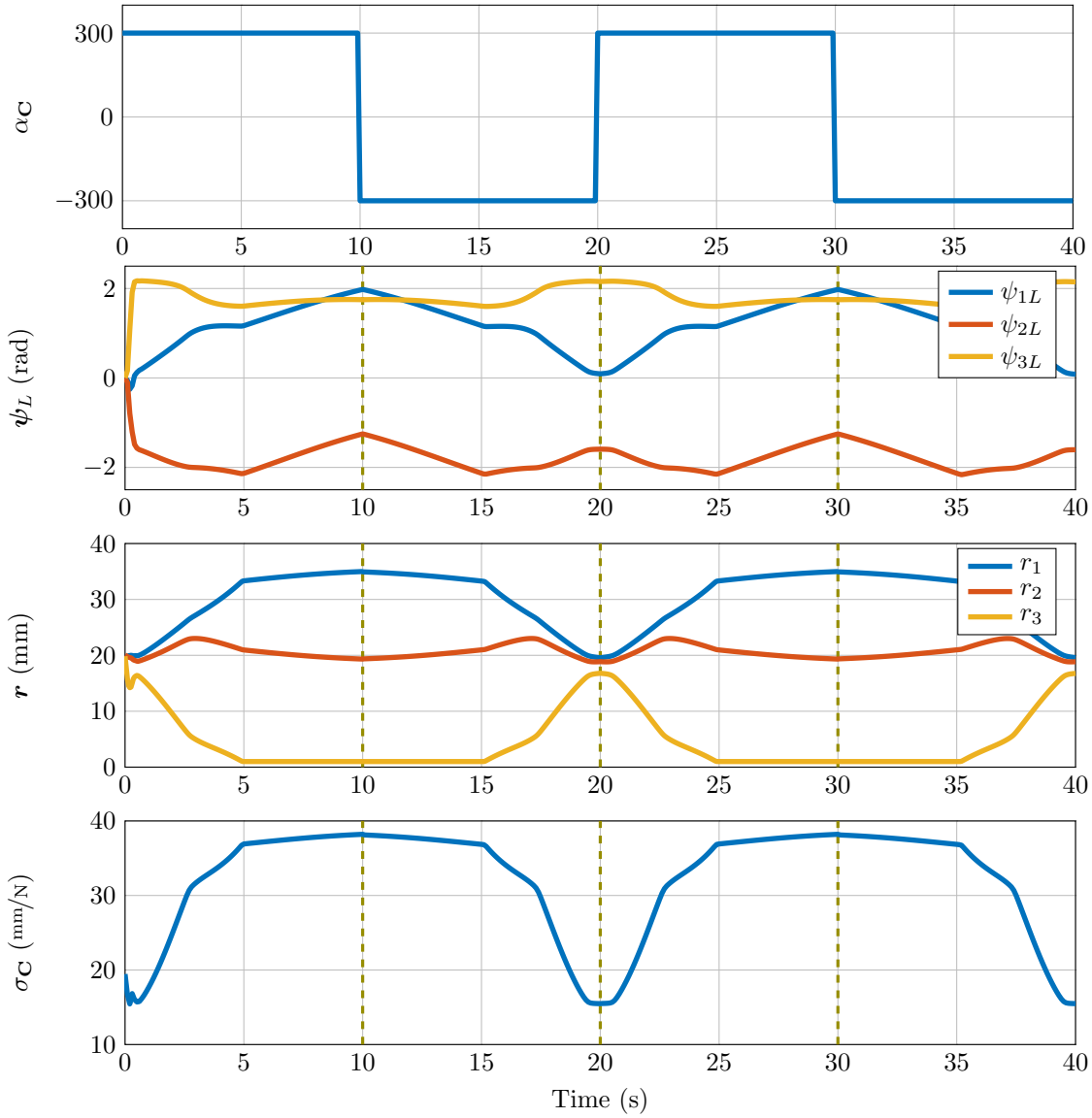

Figure 3.9: These plots show the manipulator tracking a single point at all times. From top to bottom: compliance gain $\alpha_{\mathbf{C}}$, rotational joint trajectories, translational joint trajectories, and compliance metric $\sigma_{\mathbf{C}}$ response. Every 10 seconds, the system switches between maximizing and minimizing the compliance metric. Notice that the inner tube extends and the outer tube retracts to maximize compliance, and the opposite happens to minimize compliance. The tracking error (not shown) goes below 0.1 mm in 0.5 s and remains there.

Finally, the stiffness of the manipulator can also change significantly based on the diameters of the component tubes themselves, as noted in Chapter 2. Increasing the inner and outer diameter of each tube by a factor of 1.25 decreases the maximum and minimum tip deflection to 7.1 mm and 3.1 mm, respectively, when using the original simulation conditions. Creating a robot suitable for different surgical tasks benefits from both design and real-time control considerations.

3.3.3 Elastic Stability and Stiffness Relationship

This work also motivates examining the relationship between elastic stability and stiffness. Because Nitinol is a superelastic material, it will bend but spring back to its original shape when a load is applied and then released. However, when the robot configuration is unstable, an applied load will cause the robot to move to an entirely new configuration, like a spring with a negative spring constant. In other words, we hypothesize that the stiffness of the robot becomes 0 when the stability metric $\mathbb{S}$ becomes 0. To explore this concept, we performed a simulation with the same set of unstable tubes used in Section 3.2 following the torus trajectory. We used the "stability-unaware" controller to allow the robot to reach unstable configurations. We compared the resulting stability metric plot to a plot of $\sigma_{\mathbf{C}}^{-1}$, which is the minimum stiffness singular value of $\mathbf{C}_{\boldsymbol{fp}}$ (i.e., the inverse of the maximum compliance in any direction). Figure 3.10 shows that $\sigma_{\mathbf{C}}^{-1}$ and $\mathbb{S}$ go to zero at the same points in the trajectory (we do not attempt to prove this property, but merely observe it). In fact, the two metrics have similar trajectories throughout the simulation. It is possible that one could ensure a stable robot by maximizing $\sigma_{\mathbf{C}}^{-1}$ rather than $\mathbb{S}$ and achieve a similar result. However, resolving redundancy for stiffness maximization and stability maximization will result in different joint space paths. The concept of relating stability and stiffness can be see in the work of Edelmann et al. which used the redundancy of magnetically-controlled catheters to improve stability [85]. The secondary

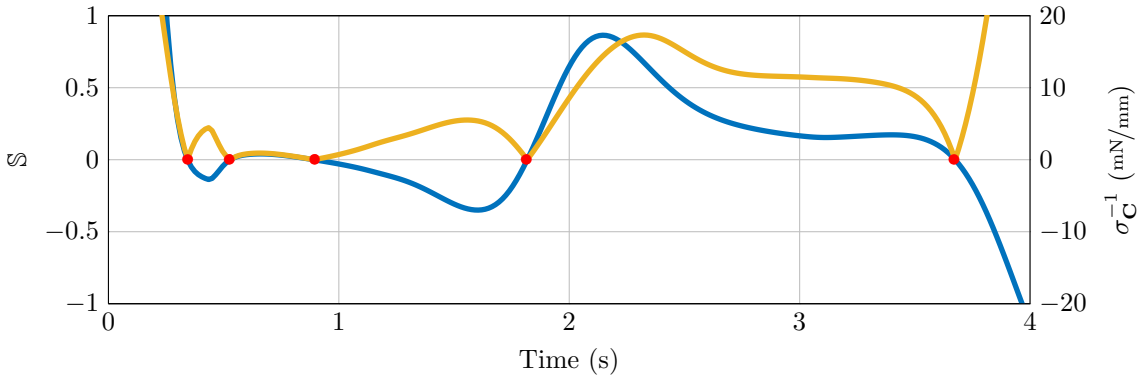

Figure 3.10: The stability metric $\mathbb{S}$ trajectory and the minimum stiffness trajectory for the simulation from Section 3.3.1. The stability metric and the minimum stiffness approach zero simultaneously, as shown with the red dots.

objective was to minimize the least negative singular value of the tip stiffness matrix.

3.4 Experiments

After exploring the ability of the controller to avoid instabilities and tune stiffness in simulation, we conducted experiments to verify performance on physical hardware. This is an important contribution of this chapter, since previous investigations of controllers including stability metrics have been primarily in simulation.

3.4.1 Instability Avoidance Experiments

To evaluate the elastic stability-aware redundancy resolution algorithm on robotic hardware, we performed a series of experiments using a three-tube concentric tube robot. The tube dimensions are listed in Table 3.5. First, we conducted a trajectory following experiment to compare the simulation results to a physical robotic system. Next, we used a teleoperation experiment to demonstrate the use of the redundancy resolution algorithm.

For both experiments, we used the robotic setup shown in Figure 3.11. The desired joint velocities are calculated in (3.6) at each time step of the trajectory following or

Table 3.5: Tube parameters used in the instability avoidance and stiffness tuning robotic experiments. Each undeformed tube has a proximal straight section, with a constant curvature section near its tip.

	Tube 1	**Tube 2**	**Tube 3**	**Units**
Outer Diameter	1.2446	2.0547	2.540	mm
Inner Diameter	1.0287	1.6002	2.2479	mm
Total Tube Length	398.1	284.7	162.3	mm
Straight Tube Length	301.0	200.2	89.96	mm
Precurvature	9.174	10.075	4.794	m^{-1}

teleoperation process. The joint values are converted to motor position commands and sent to the six motors that rotate the tubes and translate the tubes along linear slides. Further information on the design and use of this robot can be found in [41, 193, 194].

Throughout the experiments, the tip position of the robot was tracked using an electromagnetic tracking coil (Aurora, Northern Digital, Inc.) inserted into the inner tube. The tracker data is used for recording purposes only and is not fed back into the controller (i.e., the controller is open loop with respect to the tip position). We set the joint limit $r_{1,min} = 10\,\mathrm{mm}$ to ensure that the tracking coil is not accidentally dislodged from the inner tube during operation.

After shape-setting the tube curvatures using the procedure described in [195], we measured the resulting curvatures and tube lengths (see Table 3.5). We then performed an calibration process to register the base pose of the robot (i.e., the exit point $s = 0$ from the base plate shown in Figure 3.2) to the tracker frame. We moved the robot joints to 82 configurations and recorded the actuator vectors $\boldsymbol{q}$ and corresponding tip positions in the tracker frame. We used MATLAB's `fmincon` function to find the transformation between the tracker frame and the robot base frame by minimizing the total euclidean error between the tip position transformed into the base frame and the tip position found with the forward kinematics model. The pa-

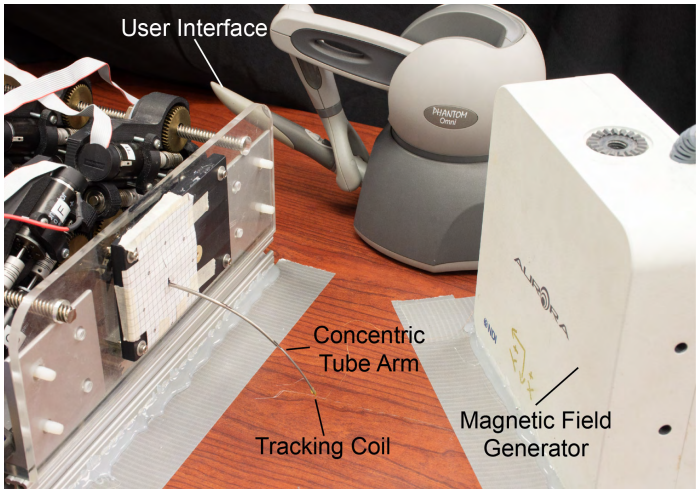

Figure 3.11: Experimental setup. A magnetic tracking coil was embedded in the tip of the three tube concentric tube manipulator, which was tracked by the magnetic field generator (Aurora, Northern Digital, Inc.).

rameters for the optimization routine were the position vector of the transformation, the ZYX Euler rotation angles, and the torsional and bending stiffness of each tube.

Trajectory Following Experiment

We had the robot follow a helix trajectory similar to the simulations described in Section 3.3.1, with the parameters $R = 28\,\text{mm}$, $r = 12\,\text{mm}$, $N_T = 2$, and $z_{off} = 110\,\text{mm}$, and a total time of $50\,\text{sec}$. We completed the trajectory 3 times with and without the instability avoidance control law. For each trial, the robot began at the home configuration $\boldsymbol{\psi}_L = \mathbf{0}$ and $r_1 = r_2 = r_3 = 20\,\text{mm}$. From the home configuration, the robot was commanded to the first point of the trajectory ($x = 40\,\text{mm}$, $y = 0\,\text{mm}$, $z = 110\,\text{mm}$) using the instability avoidance control law; this was done so that the robot began at the trajectory in the same configuration whether or not the instability avoidance term would be used for that particular trial. Once the robot tip reached the first point in the trajectory, it stopped for 10 seconds before following the trajectory; here, we jostled the tubes to remove small static frictional effects that may have built up during the transition between the home configuration and the initial trajectory

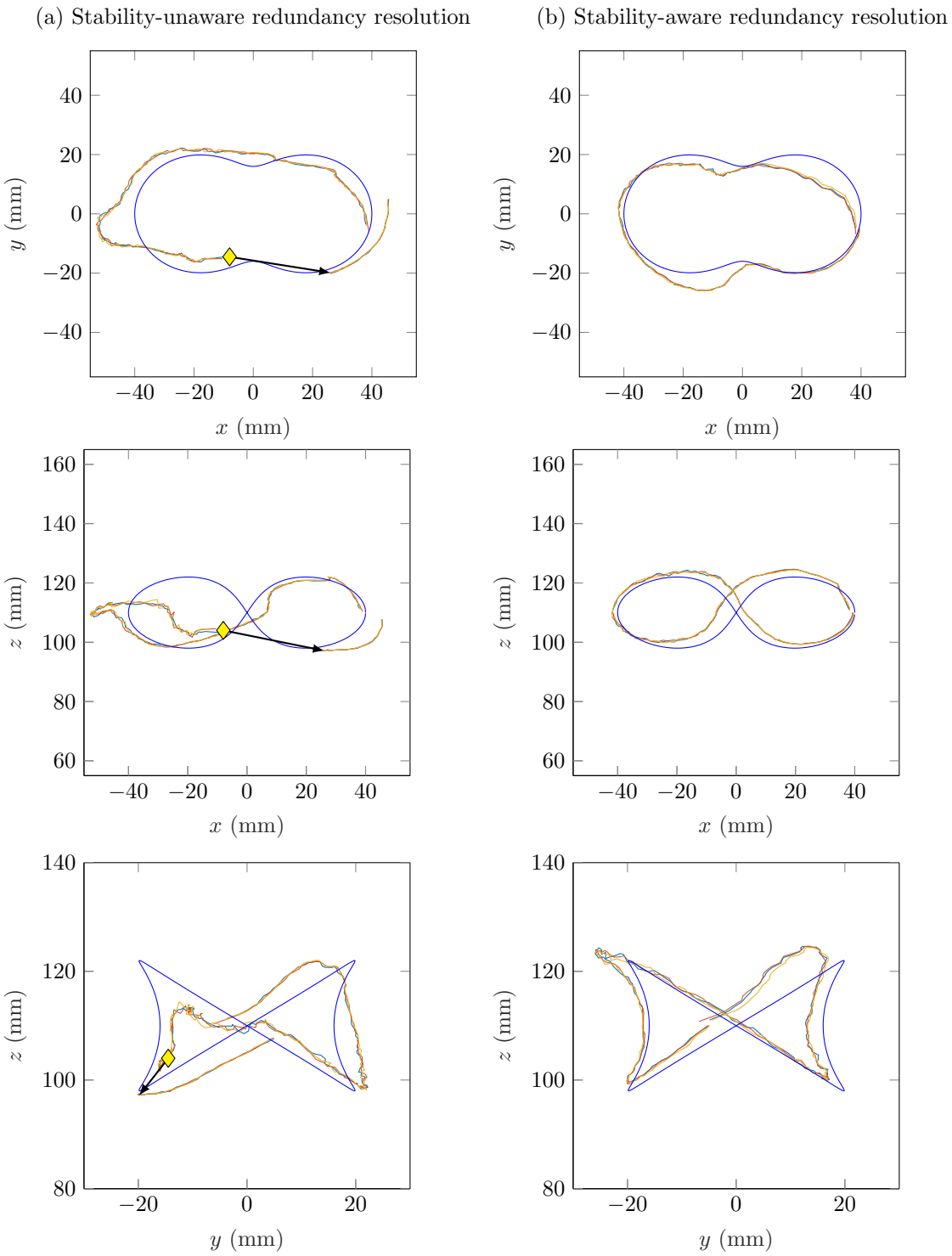

Figure 3.12: These plots show the spatial results of the trajectory following experiment in three planar views ($N = 3$ trials for each controller). The blue curve is the desired trajectory. (a) Without awareness of elastic stability, the robot snaps while attempting to follow the trajectory. The snapping points are marked with yellow diamonds and the post-snap position is at the tip of the black arrow. (b) With instability avoidance, the robot tracks the trajectory and remains stable.

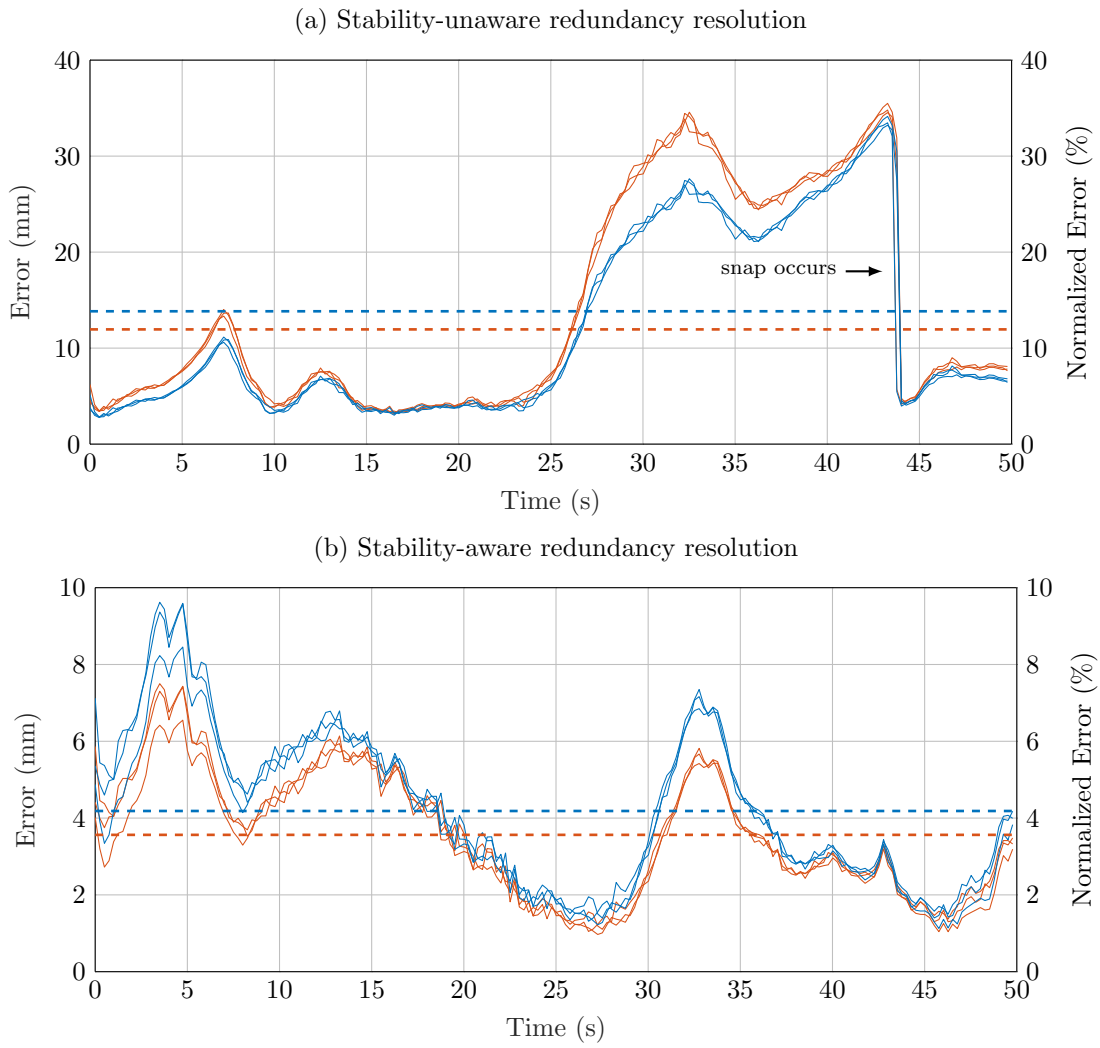

Figure 3.13: Trajectory following tracking error and normalized error with (a) the stability-unaware controller and (b) the stability-aware controller. Without instability avoidance, the robot undergoes an uncontrolled snap. With instability avoidance, the robot both tracks the trajectory and remains stable. The error is shown in blue, and the normalized error is shown in red, while the mean error and mean normalized error are shown with horizontal dashed lines of the same colors.

configuration. This again was to ensure uniformity between trials.

During the experiments, the magnetic tracker recorded data at a rate of 40 Hz, and the robot positions were set to update at a loop rate of 125 Hz. The tracking output produced approximately 2000 data points. The tracking output was then transformed from the tracker frame to the robot's base frame using the calibrated transformation between the two frames. Taking the euclidean norm between the desired trajectory and sensor data provides the trajectory following error at each time step.

As seen in Figure 3.12(b), the robot does not snap when using the instability avoidance control law. However, without the control law (Figure 3.12(a)), the robot exhibits poor tracking and snaps. Snap points are marked with yellow diamonds and the post-snap position is at the tips of the black arrows.

The tracking errors are shown in time in Figure 3.13. We performed these experiments with a stability threshold $\mathbb{S}^*$ of 0.5. The mean error and mean normalized error are shown for the stable and unstable cases as horizontal dashed lines. The mean error for all data across 3 trials with the elastic stability-aware redundancy resolution was 4.18±1.98 mm. When normalized by the extended arc length of the robot at each time step, the mean error is 3.56±1.58 %. The mean error with elastic stability-unaware redundancy resolution was 13.84±10.95 mm (11.95±9.58 % when normalized by arc length). More importantly, the robot undergoes an uncontrolled snap when the controller does not include the instability avoidance term. Note that these levels of error are excellent considering the intrinsic error in concentric tube robot models. The standard kinematic model for CTRs does not include effects such as friction, tube clearances, and nonlinear material properties. Experimental evaluations of the model report errors of 1.5–3.0% [39] and 2.1% [40] of robot arc length. Thus, our results of 3.56±1.58 % of arc length represent very good tracking.

It is interesting to note that a simulation of this experiment reveals that the stability measure goes below zero twice when not using instability avoidance, but only

one snap occurred during the experimental trials. This is to be expected based on the experiments in [58], which show the stability measure to be generally conservative; i.e., the physical robot generally snaps at a relative angle greater than that predicted by the model due to unmodeled frictional effects.

Teleoperation Experiment

Applying redundancy resolution methods to concentric tube robots to avoid elastic instabilities is motivated by the need for stable control without the significant computational overhead or *a priori* knowledge necessary for path planning. While the trajectory following experiment described above is not "pre-planned" (in the sense that the controller gets a new desired task space velocity at each time step and calculates a joint space velocity based only on that time step, without knowledge of the entire trajectory), it is still worthwhile to validate the algorithm's performance in a teleoperated scenario with a user in the loop and no prescribed trajectory.

The user was instructed to control the tip position of the robot to explore the robot's workspace. This was conducted with and without the instability avoidance control law. The user controlled the robot using a 3D Systems Touch haptic device. The user's commanded tip position was compared to the previous position to compute the desired task space velocity $\dot{\boldsymbol{x}}_{des}$ using (3.7).

Figure 3.14 shows all points that the robot can reach in stable configurations (blue) overlaid with all points that if reached would be unstable (red). Note that there is overlap between the two areas due to the robot's redundancy—many points can be reached in both stable and unstable configurations. The user's teleoperated position time history is overlaid using a black line. With instability avoidance turned off, the user experienced several uncontrolled snaps while moving the manipulator. These snapping points are marked with yellow diamonds in Figure 3.14.

This experiment demonstrates the importance of using the stability metric for

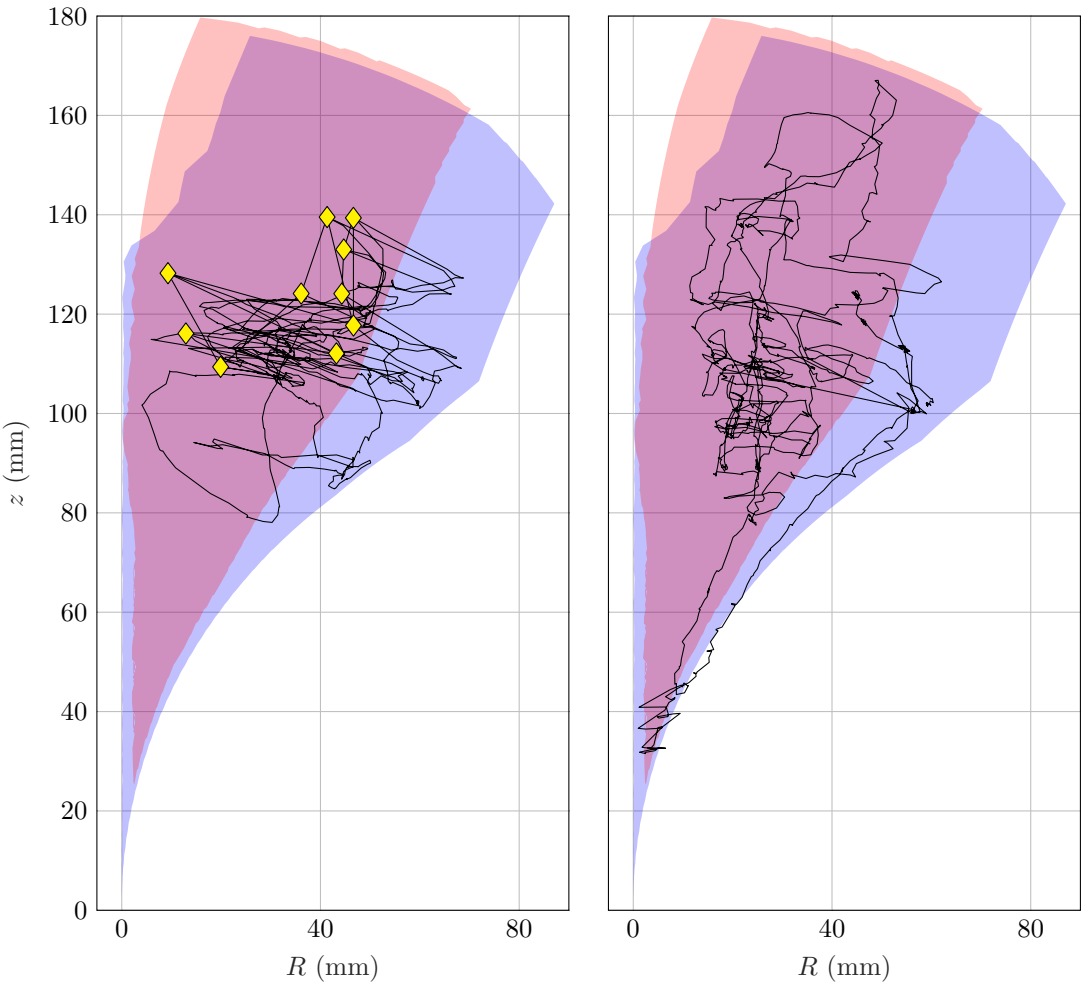

Figure 3.14: Results of the teleoperation redundancy resolution experiment without instability avoidance (left) and with instability avoidance (right). In both cases, the tracked tip data is projected into the (R, z) plane describing the robot's workspace. The red region contains robot configurations that are unstable and physically unachievable, while the blue region contains configurations that are stable. The elastic stability-aware controller allows the user to navigate the robot throughout the workspace without snapping. Without this control law, the robot snaps 10 times, as marked by the yellow diamonds.

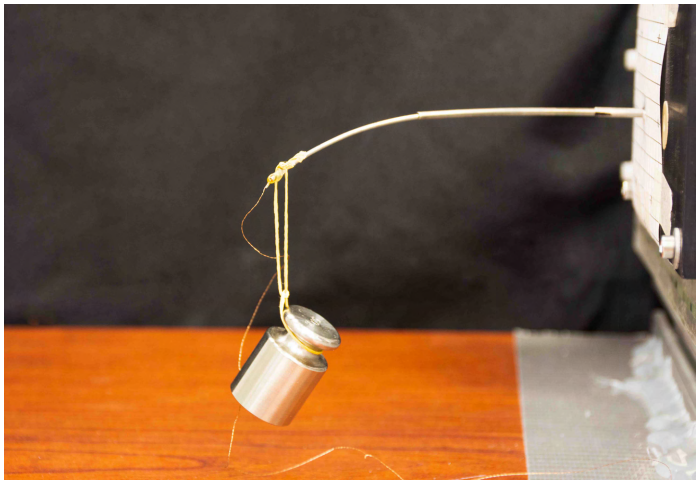

Figure 3.15: Experimental setup for the stiffness tuning redundancy resolution experiment. The robot maximized and minimized compliance while regulating tip position. A 50 g mass was hung from the tip of the robot and the resulting deflection was measured with the electromagnetic tracker.

redundancy resolution in a real-time control scenario on a prototype with highly curved tubes. Without the elastic stability-aware algorithm, the robot cannot be reliably teleoperated throughout much of its workspace.

3.4.2 Stiffness Tuning Experimental Validation

To validate the stiffness tuning approach, we measured the tip deflection of a three-tube concentric tube robot. We used the stiffness tuning control law to first minimize and then maximize the maximum singular value of the compliance matrix $\sigma_{\mathbf{C}}$ while regulating the robot's tip position, as described in the simulations of Section 3.3.2.

The same tube set was used for these experiments as were used in the instability avoidance experiments of Section 3.4.1. The commanded tip position was $\boldsymbol{p} = \begin{bmatrix}50, 0, 100\end{bmatrix}^{\mathsf{T}}$ mm. This is a suitable point for testing compliance, as the direction of $\sigma_{\mathbf{C}}$ in this configuration is approximately aligned with the $\boldsymbol{y}$ axis of the robot base frame (i.e., vertically in the world frame).

To evaluate the tip stiffness of the robot, we hung a 50 g mass approximately 4 mm from the tip of the inner tube (shown in Figure 3.15). We measured the tip position

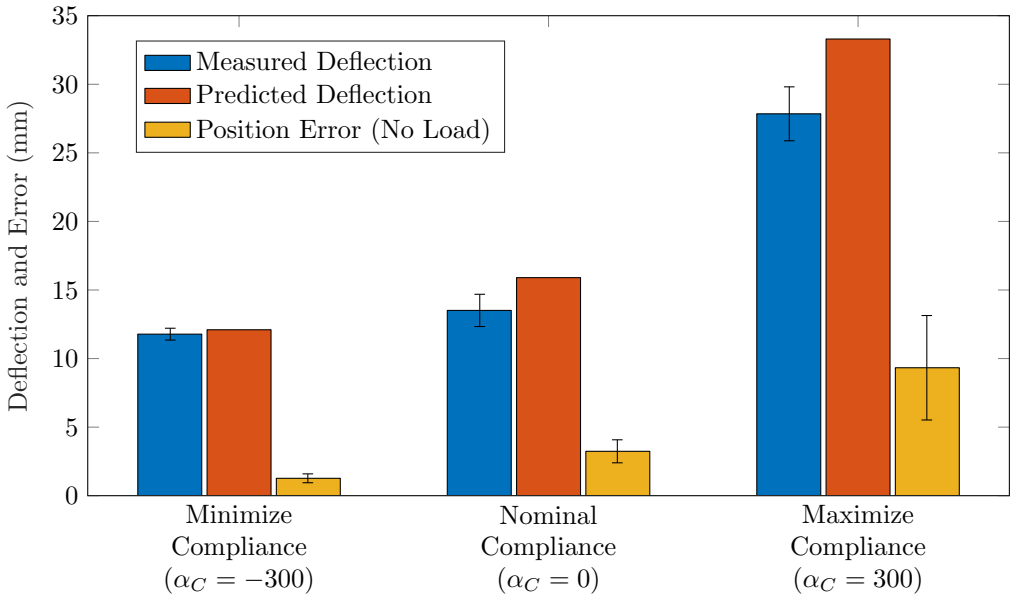

Figure 3.16: Results of the robotic stiffness tuning experiment ($N = 5$ trials). When the compliance metric $\sigma_{\mathbf{C}}$ is minimized, the robot exhibits the least amount of tip deflection under an applied load; when $\sigma_{\mathbf{C}}$ is maximized, it exhibits the highest tip deflection. The measured tip deflections are all close in magnitude to the corresponding theoretical tip deflections in the robot's most compliant direction. Also shown is the tip regulation error in the unloaded cases.

with and without the applied load using the same electromagnetic tracking system as Section 3.4.1 in order to assess the position regulation error and the deflection. These measurements were taken at the nominal configuration ($\alpha_C = 0$), the compliance minimization configuration ($\alpha_C = -300$), and the compliance maximization configuration ($\alpha_C = 300$). The robot was driven to these positions by commanding a constant tip position, changing the value of α_C, and waiting for the motors to stop moving (the ability of the robot to change compliance and maintain tip regulation is dictated by joint limits and the location of the desired position in the workspace). When no further changes in motor positions or $\sigma_{\mathbf{C}}$ were observed, tip position measurements were taken with and without the applied load. This procedure was repeated 5 times and the resulting mean and standard deviation for each configuration were computed.

We compared our experimental results to a simulated robot, using the tip regulation simulation described in Section 3.3.2. The simulated robot achieved a nominal

$\sigma_{\mathbf{C}}$ of 32.4 mm/N, minimized $\sigma_{\mathbf{C}}$ of 24.7 mm/N, and maximized $\sigma_{\mathbf{C}}$ of 67.8 mm/N. Using the nominal, minimized, and maximized $\sigma_{\mathbf{C}}$, an applied load of 50 g produced predicted tip deflections of 15.9 mm, 12.1 mm, and 33.3 mm, respectively, in the robot's most compliant direction. As shown in Figure 3.16, the corresponding measured deflections were 13.5±1.2 mm, 11.8±0.4 mm, and 27.8±2.0 mm. Figure 3.16 also shows the tip regulation error in all three cases, computed as the euclidean norm between the commanded tip position $\boldsymbol{p}$ and the measured tip position with no load applied. The tip error was 3.23±0.84 mm in the nominal configuration, 1.27±0.32 mm in the minimized $\sigma_{\mathbf{C}}$ configuration, and 9.33±3.81 mm in the maximized $\sigma_{\mathbf{C}}$ configuration.

3.5 Future Work and Conclusions

In this chapter, we have proposed a redundancy resolution algorithm for concentric tube robots, and shown that it can be implemented on robotic hardware. This approach is employed using real-time resolved rates control, making it suitable for teleoperation, and utilizes new understanding of elastic stability. Use of this algorithm makes it possible to safely control highly curved concentric tube robots that are capable of maneuvering in tight spaces, thus increasing the realistic design space of these robots.

We have also shown that concentric tube robots can resolve redundancy to tune their compliance. This ability could be used to improve the capabilities of these tools in the hands of surgeons and to allow the user to change the properties of their manipulator on the fly. We have demonstrated this capability with simulations and an example experimental configuration. Future work on redundancy resolution stiffness control of concentric tube robots includes further evaluation of the control scheme's performance with different robot configurations. Different stiffness goals, such as optimizing axial or lateral stiffness, could be explored as well. In addition, user studies could be carried out for the stiffness controller in which the surgeon can select

different stiffness modes during teleoperation when carrying out different surgical tasks. When coupled with intrinsic force sensing, selecting a high compliance control mode may improve performance in palpation tasks; conversely, a low compliance mode may improve performance in a tissue manipulation or needle driving task. Future experiments are necessary to evaluate this approach in both benchtop and clinical models. Improved designs and stiffness modification may one day combine to enable physicians to perform new surgical procedures that cannot be attempted today.

A potential limitation of this approach is that it only locally optimizes the secondary control objective. This means that there is no guarantee that the controller finds the globally optimal solution. For example, during stiffness tuning, the algorithm will seek to maximize tip compliance using local compliance gradient information at each step. After running the controller, there is no guarantee that the final configuration will be the most compliant configuration in the robot's entire configuration space. Another limitation is that the particular compliance metric chosen here does not include any isotropy information, so it is possible for the robot to move into configurations that are ill-conditioned from a compliance perspective. Finally, any weighted damped least squares approach requires careful selection of weighting matrices. The control design process typically involves trial-and-error tuning of damping, tracking, and other control gains for smooth performance with desired behavior.

Relatively little research has been performed on redundancy resolution for concentric tube robots. It would be useful to explore other secondary control goals to integrate into the framework presented in this chapter. For example, redundancy could be utilized to move the robot into configurations that optimize tip manipulability, using the manipulability ellipsoid. Visual occlusion could also be minimized, which has been studied with multi-backbone robots but not explored with CTRs. The algorithm presented in this chapter is easily amenable to different control objectives, making it a useful platform for future concentric tube robot control research.

Chapter 4

A Bimanual Steerable Sheath System with Contact-Aided Triangulation for Flexible Endoscopy: Design, Modeling, and Validation

This chapter describes the design and evaluation of a continuum surgical manipulator system for flexible endoscopy. Steerable sheaths are comprised of flexible, thin-walled, concentrically-arranged tubes. These sheaths are able to achieve distal bending through asymmetric stiffness properties of the constituent tubes themselves. The tubes are attached at their tips and actuated via differential axial motion between the tubes. Tip bending is achieved independently from the shape of the unmodified sections of the tubes; this means that steerable sheaths can be deployed through long, flexible endoscopes. In this way, steerable sheaths are a hybrid robot concept that draws from both concentric tube robots (due to the sheath's concentric tube arrangement) and multi-backbone continuum robots (due to the sheath's push-pull actuation method). Steerable sheaths have an open lumen through which flexible endoscopic instruments can be inserted and controlled.

Since steerable sheaths are actuated by differential axial motion and are not precurved like traditional concentric tube robots, these manipulators can be deployed through flexible endoscopes, broadening the scope of potential surgical applications to curved natural orifices. The steerable sheath system in this chapter is specifically designed for endoscopic submucosal dissection, a challenging surgical procedure in the colon that benefits from coordinated motion of clinical tools to simultaneously manipulate and cut tissue.

The work in this chapter makes several contributions in the context of steerable sheath development, the use of patterned tubes for continuum robots, and research efforts surrounding the medical motivation. The steerable sheath tubes are designed

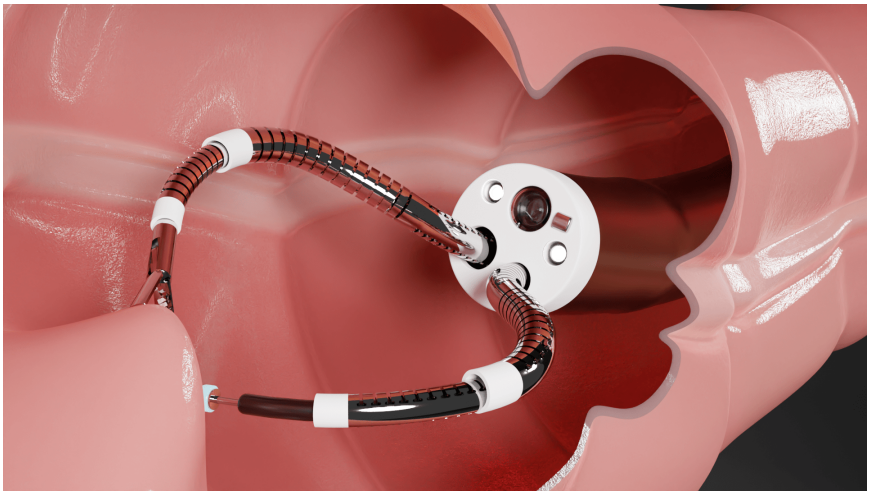

Figure 4.1: This chapter describes the development of a continuum manipulator system for endoscopic submucosal dissection that uses nested steerable sheaths. To achieve triangulation, we deploy two dual-steerable sheath manipulators through a clinical endoscope and use self-contact segments to triangulate instruments. This conceptual rendering shows two setup sheaths aiming the dexterous sheaths towards the center of the workspace. The dexterous sheaths control clinical tools and work together to manipulate tissue during endoscopic submucosal dissection. In this chapter, a new serpentine pattern is used to design the contact-aided triangulation behavior of the setup sheaths.

with a novel serpentine pattern of slotted cutouts that shifts the neutral axis of each tube. This is the first example in continuum robots of an asymmetric serpentine laser-cut pattern of this type that is specifically designed to shift the neutral axis of the tube. It is also the first steerable sheath design that combines tool triangulation with the use of contact-aided joints. The sheath tubes are patterned such that the slot cutouts come into self-contact to stiffen the structure when it is in a triangulated configuration. The overall system described in this chapter is the first research platform for endoscopic submucosal dissection that provides tool triangulation but is deployed through the working channels of a standard clinical colonoscope rather than utilizing a re-engineered robotic endoscope or large overtube system. Finally, it is also the first bimanual endoscopic robot that utilizes steerable sheath manipulators.

4.1 Medical Motivation

The bimanual steerable sheath technology described in this chapter has potential applications in many areas of both rigid and flexible endoscopy. For the purposes of this dissertation, we focus on advanced colonoscopy procedures that require precise instrument control.

One such procedure is endoscopic submucosal dissection (ESD). This technique is used for *en bloc* removal of gastrointestinal lesions for patients with early-stage gastrointestinal cancer (see Figure 4.2) [196]. Early-stage treatment is essential, as these patients have a good prognosis with a 5-year survival rate over 85% [197, 198]. In certain regions of the world, endoscopic resection has become the standard of care for early-stage gastric cancer [197]. ESD is preferable to endoscopic mucosal resection (EMR), in which the lesion is removed with a snare, because ESD results in lower recurrence rates [103]. EMR is also limited by the size of the lesion that can be resected (approximately 20 mm) [197]. During an ESD procedure, the border of the lesion is first marked with electrosurgical tools (see Figure 4.2 for procedure steps). Next, a saline injection is made to elevate the lesion, and an incision is made into the submucosal space. Then, the mucosal layer is circumferentially cut around the margin and the lesion is dissected *en bloc* from the submucosal layer.

ESD is challenging and time-consuming to perform, in part because of the limited dexterity of the instruments [199]. ESD is best performed with two instruments to enable bimanual handling of tissue. In particular, ESD is much easier when the instruments can apply countertraction (i.e., one instrument holds and applies tension to tissue while a second tool cuts the tissue) and when the instruments can reach around large lesions [89, 90]. Current endoscopic instruments have aligned axes and no ability to deflect, resulting in limited lateral dexterity; as seen in Figure 4.2, all control of instruments must be done with the endoscope itself, which constantly moves the field of view and, if using a dual-channel endoscope, moves both instruments at the

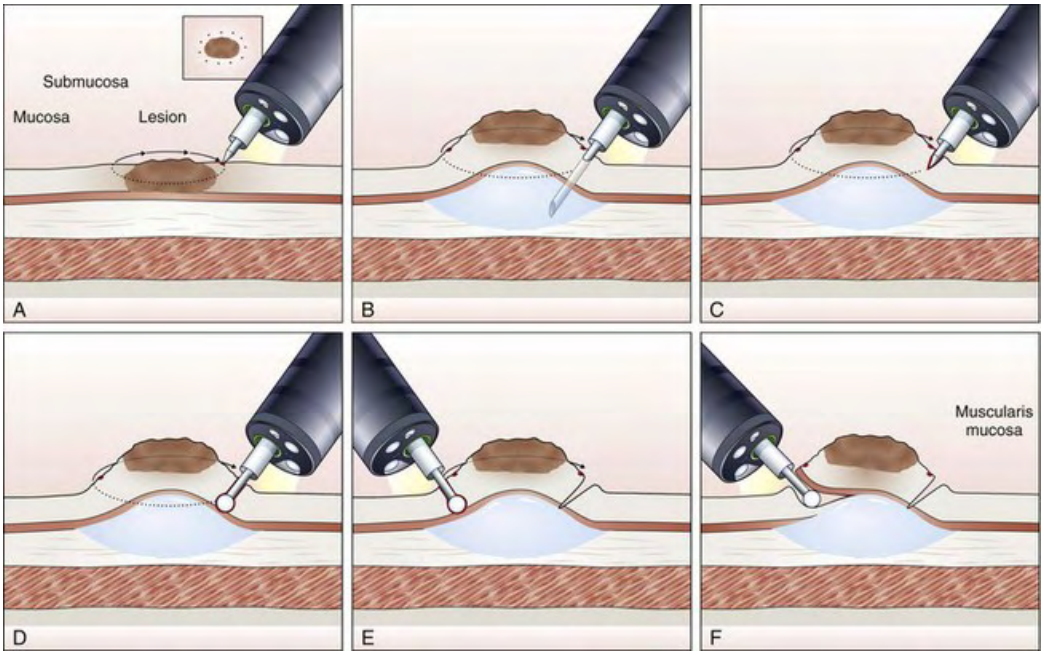

Figure 4.2: Endoscopic submucosal dissection (image from [8]). (a) Lesion margin is marked with electrosurgical tool. (b) Saline is injected into submucosal space to elevate lesion. (c) Incision into submucosal space is made. (d) Side-cutting electrosurgical knife is inserted into incision. (d) Mucosal layer is cut around margin. (e) Lesion is dissected *en bloc* from submucosal layer.

same time. If both instruments move at the same time, countertraction is impossible.

The system described in this chapter provides instrument triangulation and dexterity so that maneuvers like countertraction can be performed more easily than with conventional instruments alone (see Figures 4.1 and 4.3). Triangulation and dexterity are accomplished with steerable sheaths, a technology that uses asymmetric stiffness in nested tubes to create bending. Each tube has a slotted cutout pattern that shifts its neutral bending axis; the tubes are nested and counteraligned with their remaining material backbones opposite each other. By attaching the tube tips and translating the tube bases with respect to each other, the assembled structure bends. This principle is illustrated in Figure 4.3(c). The proposed bimanual system will have two manipulators, each of which is made up of two nested steerable sheath pairs. The first pair of tubes (the "setup sheath") bends into an S-shaped curve to triangulate the instruments. A unique aspect of this setup sheath is that its notches come into

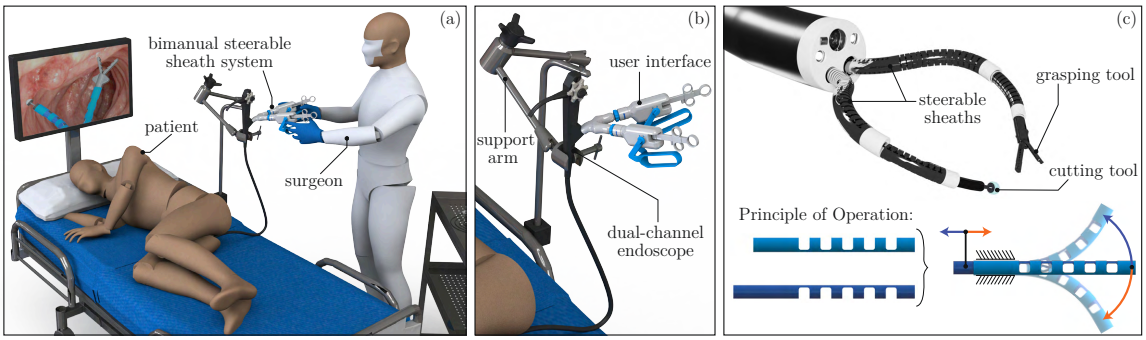

Figure 4.3: System concept: (a) endoscopy suite, where surgeon navigates to the surgical site, mounts endoscope, and deploys steerable sheaths, (b) the bimanual steerable sheath system integrates with standard clinical endoscopes and instruments, and (c) the steerable sheaths offer dexterity at the surgical site. Steerable sheath bending is produced by nested tubes with stiffness asymmetry that are axially pushed and pulled relative to each other. In this work, serpentine patterns are used for the first time as a more robust alternative to rectangular notches.

self-contact to create a stable high-stiffness platform for the second sheath. The second pair of tubes (the "dexterous sheath") passes through the setup sheath and use push-pull actuation to carry out tasks at the surgical site. The system is designed to integrate with standard clinical endoscopes and provide triangulation using only pairs of nested tubes; no external structures or tendons are required, leaving an open lumen for clinical instruments.

4.2 Related Work

4.2.1 Endoscopic Instrument Dexterity and Triangulation

A number of systems attempt to solve the problem of instrument triangulation and dexterity, including distal add-on devices, mechanical articulation systems, and robotic systems [91]. Note that this review excludes systems designed purely for robotic endoscope locomotion. Distal add-on devices are not continuum devices and are thus not within the primary focus of this chapter. Examples of distal add-on devices that specifically enhance dexterity include the Apollo OverStitch suturing device [93] and

the shape memory alloy-actuated device designed by Gafford et al. [94]. Mechanical systems such as the ANUBIScope, EndoSamarai, Direct-Drive Endoscopic System (DDES), and articulating devices by Okamoto et al. have specialized endoscope tips and/or articulating instruments to achieve triangulation [92, 97, 98].

Robotic systems of many different architectures have been developed to provide dexterity in single-port surgery (including rigid and flexible endoscopy). The IREP and SURS robots use multi-backbone continuum manipulators that are deployed using a parallelogram mechanism [110] or a two-segment dual continuum mechanism [111]. These mechanisms separate the "elbows" of the arms and triangulate the manipulators. The IREP technology is licensed to Titan Medical, Inc. and is being commercialized in the Titan SPORT system [20]. A robotic version of the ANUBIScope called the STRAS has also been developed [95, 96]. The Master and Slave TransEndoluminal Robot (MASTER) has two tendon-sheath-actuated manipulators passed through a modified endoscope [101, 102, 103]. This system is being commercialized as the EndoMaster EASE robot for gastrointestinal applications. The Hansen Medical ViaCath system used an articulating overtube design, but the instruments produced low lateral forces [106]. Bimanual concentric tube robots have been developed for rigid endoscopy in the prostate [44], brain [115], fetal surgery [121], and upper airway and bronchoscopy [116], as well as for flexible endoscopy [46, 117, 118]. Precurved concentric tube robots suffer from elastic instability, particularly when built with long, flexible transmissions. The Medrobotics Flex is a steerable robotic endoscope that advances using follow-the-leader motion; it also has mechanically actuated articulating instruments that pass along the outside of the scope [18]. Lau developed a flexible robotic system for gastrointestinal procedures that uses a tendon-sheath actuation system [107].

Roppenecker et al. developed a 3D-printed overtube system for endoscopic procedures that consists of a sleeve with flexible arms that deflect instruments passed

through them [122]. Various designs for the flexible arms and overall system architecture have been presented [123, 124, 125, 126, 127]. The concept showed promising results during *in vivo* porcine ESD experiments [90]. The CYCLOPS has a deployable peripheral scaffold (made from either an inflatable or rigid-link mechanism) that then uses tendons to control instruments [99, 100].

Many of the proposed solutions require specialized endoscopes or replace the standard clinical endoscope entirely, which requires significant capital equipment investment from the hospital and forces physicians to adopt and implement an entirely new workflow. These factors create hurdles for early and widespread adoption. In addition, the overall diameter of these systems are typically much larger than even the largest dual channel colonoscopes (12–14 mm). An additional advantage of the steerable sheath concept is that only the tubes enter the body; there are no other moving parts inside the patient. These tubes can be made from biocompatible materials and could be a disposable unit. Other technologies have many moving parts which makes them more difficult to sterilize.

4.2.2 Notched Tube and Patterned Continuum Devices

Steerable sheaths achieve bending due to stiffness asymmetry designed into nested thin-wall tubes. By removing material from one side of the tube, the neutral bending plane is shifted away from the centerline of the tube. This lowers the required actuation force to bend the tube and increases the achievable curvature. Swaney and York designed a tendon-actuated miniature wrist for continuum robots using this concept [50, 51]. Other examples of tendon-actuated notched-tube devices can be found in [200, 201, 202]. Chitalia et al. designed a tendon-actuated notched-tube robot for rigid neuroendoscopy; they explored different types of notch patterns in the device's two bending sections to achieve tool triangulation.

Oliver-Butler et al. developed a continuum robot that is a hybrid of concentric

tube and multi-backbone robots and uses the notched tube asymmetric stiffness concept for bending [52]. By nesting two notched tubes with opposing backbones and attaching their tips, bidirectional bending is produced by pushing and pulling the tube bases with respect to each other. This robot uses concentrically-arranged tubes like a traditional concentric tube robot to maintain an open lumen for instruments and push-pull actuation like that of multi-backbone continuum robots [110]. Initial prototypes have been used to resect central airway tumors [53]. The work in this chapter builds on this concept.

One notched tube design that is particularly relevant to this work is that of Eastwood et al. [201]. This asymmetrical notched-tube joint utilizes unique cutout patterns to purposefully create self-contact in the notches; it is the first "Contact-Aided Compliant Mechanism" (CCM) to be applied to a notched-tube device. CCMs have been previously employed in a number of robotics and engineering applications, including medical devices [203]. In the context of the notched-tube device, the notch is designed such that a region comes into contact when an external load is applied to the tip. This contact self-reinforces and stiffens the joint, yet the remaining (i.e., non-contacted) portion of the notch allows the joint to still be actuated by the tendon. The shape of the contact region also causes the notch to bend in an elliptical shape rather than a circular arc, resulting in less lateral movement during actuation. Eastwood et al. also designed a contact aided joint for a tendon-actuated notched-tube neuroendoscopic instrument [204]. In this device, the top and bottom of the notch have geared surfaces that mesh together to increase the blocking force.

The steerable sheath system in this chapter also utilizes a contact-aided compliant mechanism to determine a "setup" pose of the robot for improved instrument triangulation and stability. In this case, we employ the contact behavior of an asymmetric serpentine pattern to dictate the fully actuated shape of the setup sheath. It is the first device to combine the concepts of triangulation and contact-aided compliant

mechanisms.

Strategic material removal has been employed in other medical robots as well. For example, patterning tubes with cutouts can increase the ratio of torsional stiffness to bending stiffness in order to reduce the risk of elastic instability in concentric tube robots [205, 206, 184]. Triangular notches were made in Nitinol tubes to create tendon-actuated continuum manipulators for a bimanual single-port system [207]. An asymmetric design with notches alternating on either side of the tube centerline was employed for a tendon-actuated continuum robot with bidirectional bending for removing osteolytic lesions [208, 209]. Notches have been used to reduce bending stiffness in other tendon-actuated contintuum robot designs as well [210, 211, 212]. Vandebroek used pattern-cut Nitinol tubes to create McKibben muscle-actuated bending segments for a single port robot [121]. Many catheter-based and other flexible medical devices also use material cutout patterning to reduce bending stiffness so that the devices can pass through highly curved lumens.

The aforementioned 3D-printed overtube system from Roppenecker et al. utilizes material cutouts for both the overtube that passes over the endoscope and for the flexible arms that control the instruments. The distal section of the arms is similar to the notched tubes described in [50] in that they have asymmetric stiffness for unidirectional tendon-actuated bending. The flexible arms have multiple sections that allow for triangulation. The overtube section utilizes material cutouts to decrease the structure's stiffness.

4.3 Steerable Sheath Design

This section entails the primary contribution of this chapter, which is the design of a steerable sheath system for flexible endoscopy, with a focus on colonoscopy procedures such as endoscopic submucosal dissection. These types of procedures often use a dual-channel colonoscope with multiple tools passed through the scope to the surgical site.

The system consists of a standard dual-channel colonoscope that is mounted to the bed with a passive support arm, two dual-sheaths manipulators (consisting of a setup sheath and dexterous sheath) that are passed through the scope's working channels and controlled via user interface handles, and clinical transendoscopic instruments (e.g., electroknife, grasper, etc.) that are then passed through the open lumens of the sheaths (see Figure 4.3).

Triangulation is an essential but challenging aspect of minimally invasive surgeries involving multiple tools, particularly endoscopic procedures. Tools exit dual-channel endoscopes directly beside and parallel to one another; therefore, the tools must first be spread apart and then their tips must be brought back together to achieve triangulation. Inspired by this concept, we designed manipulators with two sheaths: the proximal "setup sheath" bends away from the centerline of the endoscope and then back toward the centerline to aim the instruments towards the surgical site for triangulation, while the distal "dexterous sheath" uses push-pull actuation for bending to perform tasks. The setup sheath also uses notch self-contact during triangulation to create a stiff platform for the distal sheath and dictate the setup pose at full actuation.

4.3.1 Serpentine Patterned Slotted Tubes for Steerable Sheaths

Steerable sheaths are a form of continuum (i.e., continuously flexible) device made up of two nested, thin-walled tubes that are attached at their tips. Stiffness asymmetry is encoded into the tips of the tubes so that the sheath bends controllably when the tubes are linearly translated with respect to one another. The steerable sheath concept was originally inspired by tendon-actuated miniature wrists developed by York et al. [50] and Swaney et al. [51]. This led to initial sheath modeling development by Oliver-Butler et al. [52] and experimental validation by Rox et al. [53].

The first steerable sheath model made piece-wise constant curvature assumptions [52]. In other words, each notch is modeled as a constant curvature arc followed by

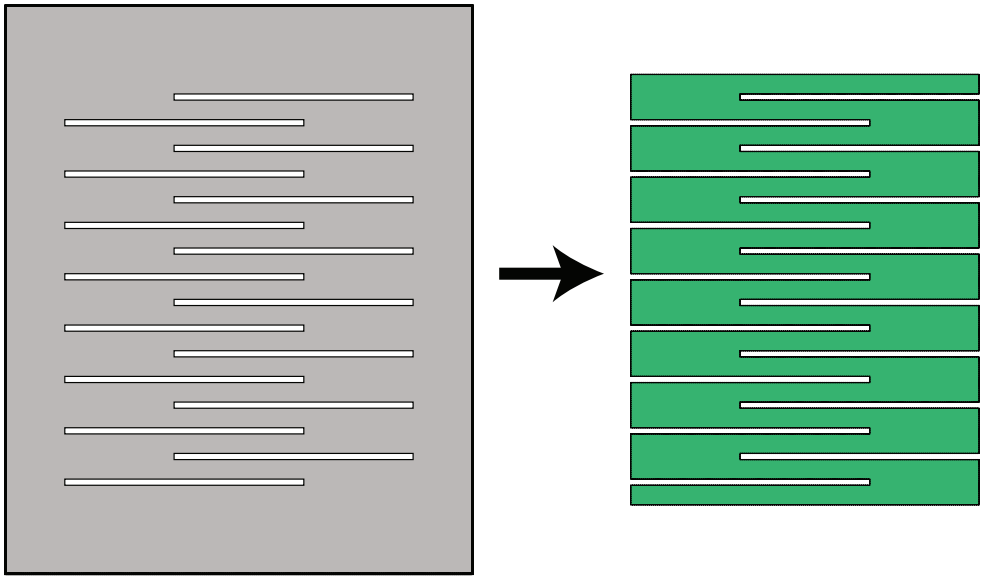

Figure 4.4: Flattened serpentine pattern for material removal via laser cutting. Rather than using aligned rectangular cutouts, the offset slots maintain connected material throughout the tube for better stiffness characteristics.

a rigid section of uncut tube. The model also assumes that each notch has the same geometry and therefore the same deflection angle for a given actuator input. The angle of the end effector is found by simply multiplying the angle of one notch by the total number of notches.

Both tendon-actuated wrists and the first examples of steerable sheaths in the literature used rectangular notch cutouts to create stiffness asymmetry. These cutouts are relatively straightforward to manufacture with milling or wire electrical discharge machining techniques. However, sheaths with long bending segment lengths and rectangular cutouts can suffer from poor torsional stiffness due to the small remaining backbone of solid material that is left over after machining. The length of each cutout is also limited by buckling issues and potentially fragile rings of non-machined tube.

Due to these challenges, we sought out other methods of patterning tubes with cutouts that would shift their neutral bending axes but retain some degree of higher torsional stiffness and less susceptibility to buckling. To this end, we designed a serpentine pattern of slots that selectively removes material to induce bending but

keeps continuous material along the tubes length in addition to the solid backbone (see Figure 4.4). The serpentine pattern consists of thin, offset slots that overlap opposite the solid backbone. When the tube is bent, these slots close much like rectangular notches; however, the slots come into self contact at the two edges of the overlapping region, as shown in Figure 4.5, rather than at a single point directly opposite the solid backbone. An additional benefit of this patterning approach is that the resulting curve is effectively continuously constant curvature; in contrast, notched tube designs are piece-wise constant curvature with solid straight sections between the constant curvature notches. The edges of these solid sections can cause friction on the actuation tendon or inner tube [50].

As discussed previously in Section 4.2.2, serpentine laser-cut patterns are frequently used for flexible and catheter-based medical devices (for example, see the Boston Scientific Fathom guidewire, which uses a serpentine-patterned Nitinol tube [213]). In such devices, the goal of the material removal pattern is typically to introduce axisymmetric flexural compliance with significantly compromising axial and torsional stiffness. This allows devices such as catheters to navigate anatomy while still transmitting axial force and torque from the base of the device to the tip. Since the devices are designed to be equally flexurally compliant in all directions, the patterned cutouts are symmetric about the axis of the tubing. One exception in the literature is the work of Kim et al., in which a serpentine pattern is cut on either side of the tube to make it stiff about one axis but flexible about the other axis for use in a steerable needle [214]. In all of these cases, the neutral axis of the tube remains on its axial centerline. The serpentine pattern utilized in this chapter is unique in its purpose: by patterning asymmetrically and leaving a solid backbone of uncut material, the serpentine pattern shifts the neutral away from the centerline toward the solid backbone. This stiffness characteristic enables the push-pull actuation of the steerable sheath when the tubes are nested and anti-aligned.

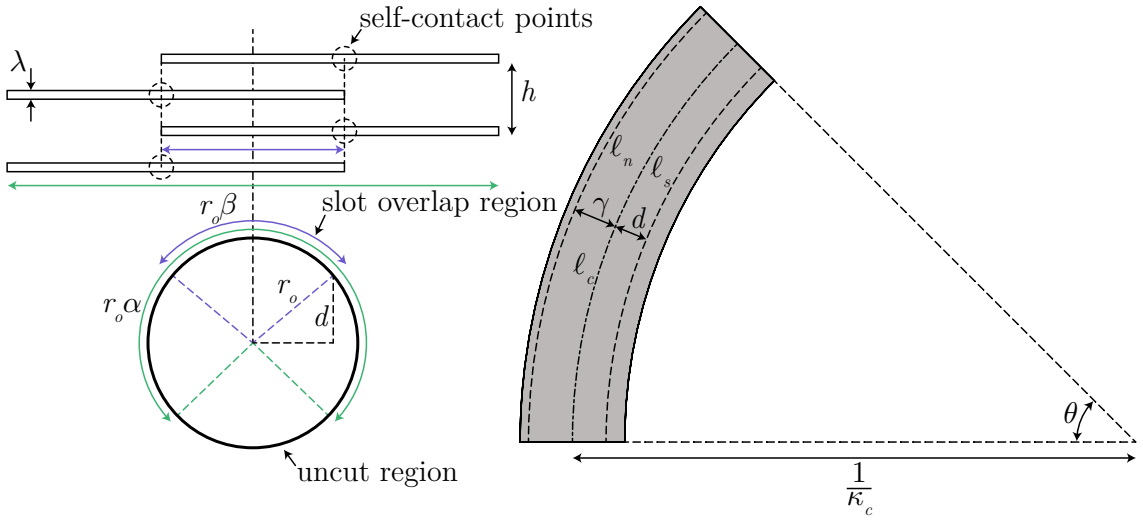

Figure 4.5: Serpentine pattern parameters. The flattened pattern illustrates that the slots come into self-contact at the edges of the overlapping region, which is defined by the angular parameter β. The overall width of the slots is defined by the angle α (with the uncut solid backbone consisting of the angular region $2\pi - \alpha$. The slot sizes are given by the height λ and spacing h. The distance d from the centerline to the contact points can be used to determine the resulting curvature of a given slot height, or vice versa.

In the remainder of this section, we will derive the relationships governing the bending characteristics of a serpentine patterned tube. In doing so, we will relate the slot parameters (slot spacing h, height λ, overlapping angle β, and combined angle α) to the centerline length and curvature of the device when the slots are in self-contact, which are important characteristics for designing a steerable sheath system. The total width of the pattern is given by the angular parameter α, while the tube circumference is uncut in the region of $2\pi - \alpha$, leaving a solid backbone. The dimensions of the backbone relative to the size of the tube impact its stiffness and must be selected such that the tube is not too stiff for actuation but still robust. The backbone dimension also determine the location of the neutral axis with respect to the centerline. The slot overlapping angle β determines how far from the centerline of the tube that the slots come into self-contact. This distance from the centerline is given by

$$d = r_o \cos\left(\frac{\beta}{2}\right), \tag{4.1}$$

where r_o is the outer radius of the tube, as seen in Figure 4.5. Next, we must find the relationship between slot closure and the change in length of the device. Here, we assume that the change in length of the entire length of the sheath is proportional to the change in length for one set of slots. In other words, for each slot spacing h, the maximum change in length for that segment of tube is the height of the slot λ. Therefore, we have

$$\Delta\ell = \frac{\lambda}{h}\ell_n, \tag{4.2}$$

where ℓ_n is the length of the sheath neutral axis. As seen in the right half of Figure 4.5, there are three length parameters all related by the same deflection angle, θ. ℓ_c is the centerline length of the device, and ℓ_s is the length of the device at the serpentine pattern closure points. We have that

$$\ell_s = \ell_n - \Delta\ell = \ell_n - \frac{\lambda}{h}\ell_n = \ell_n\left(1 - \frac{\lambda}{h}\right), \tag{4.3}$$

allowing us to relate these lengths using the common bending angle:

$$\theta = \kappa_n\ell_n = \kappa_c\ell_c = \kappa_s\ell_s = \kappa_s\ell_n\left(1 - \frac{\lambda}{h}\right) \tag{4.4}$$

where κ_n, κ_c, and κ_s are the neutral axis, centerline, and serpentine closure point curvatures, respectively. We use the geometry of the tube to define the relationships between the curvatures:

$$\begin{aligned} \kappa_n &= \frac{1}{r_c + r_o} = \frac{\kappa_c}{1 + \kappa_c\gamma} \\ \kappa_s &= \frac{1}{r_c - d} = \frac{\kappa_c}{1 - \kappa_c d}, \end{aligned} \tag{4.5}$$

where $r_c = 1/\kappa_c$ and γ is the distance from the centerline to the neutral axis. γ is found using the centroid equations for a circular segment as described in [50]. Here, we make an assumption that the uncut solid backbone forms a circular segment,

which is the same assumption made for sheaths with rectangular cutouts [52]. Using these curvature relationships to put (4.3) in terms of the design input κ_c, we find that

$$\frac{\kappa_c}{1-\kappa_c d}\ell_b\left(1-\frac{\lambda}{h}\right)=\frac{\kappa_c}{1+\kappa_c\gamma}\ell_b. \tag{4.6}$$

Rearranging and using (4.1), we find an expression for the slot height λ given the tube dimensions, the other slot design parameters h and β, and the desired shape curvature κ_c:

$$\lambda = h\left(1-\frac{1-\kappa_c r_o\cos\left(\frac{\beta}{2}\right)}{1+\kappa_c\gamma}\right). \tag{4.7}$$

Using this derived relationship, we can calculate the necessary slot height for a desired curvature (given h and β) or solve for any other of the desired parameters if given different inputs. In this chapter, we will design curves for the setup and dexterous sheaths and use these relationships to calculate the slot size for the serpentine patterns.

4.3.2 Designing Dual-Steerable Sheath Manipulators

We will now use this understanding of the serpentine pattern self-contact to design steerable sheaths with contact-aided triangulation. For each sheath, we will design the serpentine pattern parameters such that the slots close at a specific designed curvature of the device. Not only does this method enable us to specify the setup pose of the setup sheath and the deflection range of motion of the dexterous sheath, but slot closure ensures that the sheath does not over-strain during actuation because the curvature is inherently physically limited by design.

Setup Sheath Design with Contact-Aided Triangulation

The driving objectives for the design of the setup sheath are the desired shape and tip pose at its full actuation length (i.e., when all of the slots in the serpentine

pattern are in self-contact). The parameters of the triangulation S-curve and the tip pose were selected based on the requirements for endoscopic submucosal dissection. Several other devices have devised such requirements for other ESD systems. For a distal dexterity add-on device for ESD, Gafford et al. identified a required range of motion for a single tool of 90° (±45°) and a length of 40 mm. The second prototype of the MASTER robot slave manipulators was designed for a flexion/entension range of motion of 180° (±90°) and a length of 41.7 mm [215, 101]. The CYCLOPS scaffold has a deployed length of 61 mm [100]. Based on these prior designs, we constrained the deployed distance of the setup sheath from the tip of the endoscope (in the axial direction) to be between 30 and 60 mm.

The lateral distance between the tips of the two setup sheaths should be 30 mm, as the lesions eligible for ESD are typically between 20 mm and 30 mm in diameter (in one study, the mean lesion diameter was 25.4 mm for standard eligibility criteria and 28.3 mm for extended criteria to include patients with ulcerated morphology) [216]. The setup sheath tips should be on either side of the lesion. We selected a triangulation angle for each sheath of 45° relative to the endoscope axis, which aims the dexterous sheaths toward the center of the workspace within the field of view of the endoscope (maximum depth of field of 100 mm [217]). The setup sheath was also designed with a solid tube segment of 3 mm between the proximal and distal segments of the S-curve. Initial prototypes for S-shaped steerable sheaths showed that a rigid section of tube between the opposed patterns improves the durability in this region. Similarly, 2 mm of solid tube were left at the distal tip of the sheath. These segments are illustrated in Figure 4.6.

Using these dimension ranges and the desired tip pose, we were able to directly calculate the curvature and length of the proximal and distal segments based on the arc length of the total curve (throughout this analysis, we assumed that both segments exhibit constant curvature bending). We selected a total sheath length of

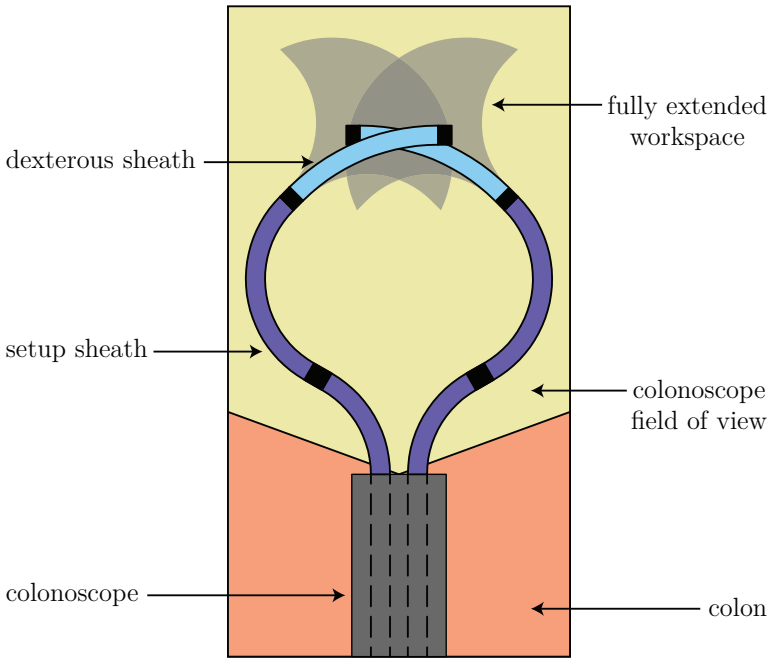

Figure 4.6: Triangulation concept for steerable sheath manipulators using a contact-aided set-up sheath and an independently controlled dexterous sheath. Sheath and scope dimensions are drawn to scale based on the design choices in Section 4.3.2. Black segments of the sheaths indicate solid, uncut sections of tube.

50 mm which, when factoring in the working channel spacing of the dual colonoscope, produces tip positions that are 41 mm from the end of the colonoscope in the axial direction. The desired lengths of the proximal and distal segments are 16.4 mm and 28.6 mm, respectively, and both segments have a desired radius of curvature of 15.6 mm.

In order to calculate the required slot height to accomplish this centerline curvature at the point of slot self-contact, we make assumptions for the angular parameters α and β, as well as the slot spacing h. We selected α to be 270°, which leaves 90° of the circumference of the tube as solid backbone. We selected β to be 100° and h to be 1.0 mm. In the future, rigorous experimental investigation can be made to determine the effects of these parameters on the sheath's mechanical properties.

Using these design choices, we used (4.7) to calculate the necessary slot height to achieve the desired curvatures in the proximal and distal segments: 0.130 mm, which

is within the resolution capabilities of the in-house laser cutter (see Section 4.3.3). Given all the slot dimensions, the slot pattern can be repeated to fill the desired manipulator length.

Dexterous Sheath Design

We designed the dexterous sheaths to have a range of motion of 180° (±90°). We selected a bending section length of 23 mm with a 2 mm solid tip for a total manipulator length of 25 mm. Therefore, the desired radius of curvature is 14.6 mm. Using the same slot spacing and overlapping angle as the setup sheath, we find a necessary slot height of 0.100 mm.

In addition to the serpentine pattern bending section, we designed a transition section immediately proximal to the bending section (Figures 4.7 and 4.9). This transition section is nested within the S-curve of the setup sheath, so it must be highly flexible to minimize its effect on the setup sheath kinematics and actuation force. While there are many examples of different laser-cut patterns to create flexible catheters and other medical devices, we chose a straightforward pattern of alternating slots, which is approximately uniform in bending stiffness in all directions. The dimensions of these slots were selected iteratively based on the desired radius of curvature given by the shape of the setup sheath. The design of the transition section will be an important topic of future work to select a pattern that allows the dexterous sheath to pass smoothly through the setup sheath while retaining as much torsional and axial stiffness as possible. Inspiration can be taken from examples of laser-cut hypotubes used in existing medical devices, as there are many variations of axisymmetric material removal patterns. We could also explore spiral cut patterns, as well as patterns with interlocking tabs such as the flexible outer sheath shown in [204].

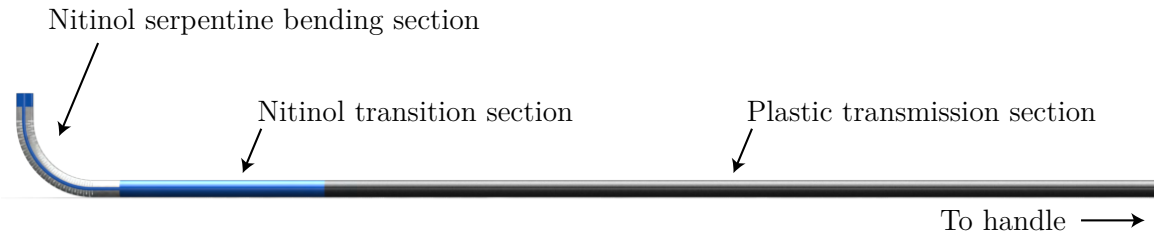

Figure 4.7: The dexterous sheath is made up of three sections. The steerable tip is manufactured cut from Nitinol tubing using the serpentine pattern. The same Nitinol tube has a laser-cut transition section that passes through the S-curve of the setup sheath. The transmission section is made from plastic medical tubing that passes through the working channel of the endoscope to the user interface.

4.3.3 Sheath Manufacturing and Assembly

Due to the long working length of colonoscopes (the Olympus Evis Exera CF-2T160L Dual Channel Colonoscope has a working length of 1680 mm) and the expense of Nitinol, we manufactured only the bending tip of the sheaths from Nitinol. The Nitinol bending tips are then actuated with flexible transmission shafts made of plastic medical tubing that run through the working channel(s) of the endoscope (Figure 4.7). Plastic tubing such as PEEK and Pebax® is commercially available with very thin walls, allowing several tubes to be nested concentrically. Tube dimensions for the setup sheath and dexterous sheath can be found in Tables 4.1 and 4.2, respectively. While the tubes were originally intended to fit through either working channel (3.2 mm or 3.7 mm), we were unable to buy stock tubing with the exact dimensions to nest all of the necessary tubes. As such, the maximum diameter of this prototype is 3.3 mm. Similarly, there was no available plastic tubing in stock to fit over the inner tube of the dexterous sheath bending section but within the outer tube of the dexterous sheath transmission section. Due to this constraint, the innermost plastic transmission tube fits inside the innermost Nitinol tube, which reduces the available lumen for clinical tools. However, in future prototypes, we will order custom plastic tubing extrusions so that the ideal dimensions can be used. Similarly, we could order Nitinol tubing

Table 4.1: Setup sheath tube dimensions and materials.

Tube	OD (mm)	ID (mm)	WT (mm)	Material
Bending Section Outer Tube	2.895	2.667	0.114	Nitinol
Bending Section Inner Tube	2.590	2.438	0.076	Nitinol
Transmission Section Outer Tube	3.302	3.048	0.127	PEEK 381G
Transmission Section Inner Tube	2.921	2.667	0.127	PEEK 381G

Table 4.2: Dexterous sheath tube dimensions and materials.

Tube	OD (mm)	ID (mm)	WT (mm)	Material
Bending Section Outer Tube	2.050	1.900	0.075	Nitinol
Bending Section Inner Tube	1.800	1.620	0.090	Nitinol
Transmission Section Outer Tube	2.337	2.083	0.127	Pebax®
Transmission Section Inner Tube	1.524	1.27	0.127	PEEK 381G

with custom dimensions rather than be limited by the stock lists of suppliers. Due to the high expense of such custom orders, this will be done on future iterations of the device. An additional benefit of custom plastic tubing extrusions is that the tubes will be long enough to pass through the entire length of the colonoscope.

The serpentine patterns were laser machined from the Nitinol tubes with a Q-switched ytterbium pulse fiber laser (Wuhan Raycus Fiber Laser Technologies Co., Ltd.). This 30 W laser system has a fixed pulse width of approximately 100 ns, a pulse frequency of 20 kHz, and uses an f-theta galvo lens to traverse its 175 mm by 175 mm cutting area at a speed of 1000 $^{mm}/_{s}$. The tube is rotated about its long axis with a 3-phase, 1.2 degree step-angle Leadshine Stepper motor and a 1/10,000 microstep driver. Depending on the wall thickness of the tubes, we repeated 30-60 passes of the pattern to fully cut through the wall; to prevent the laser from cutting through the backside of the tube, we inserted a steel mandrel inside the tube during the cutting process. The laser was focused and aligned manually based on a galvonometer preview with a red-dot laser source. After completing the cutting process, we also performed a low-power rastering pass to remove slag and debris

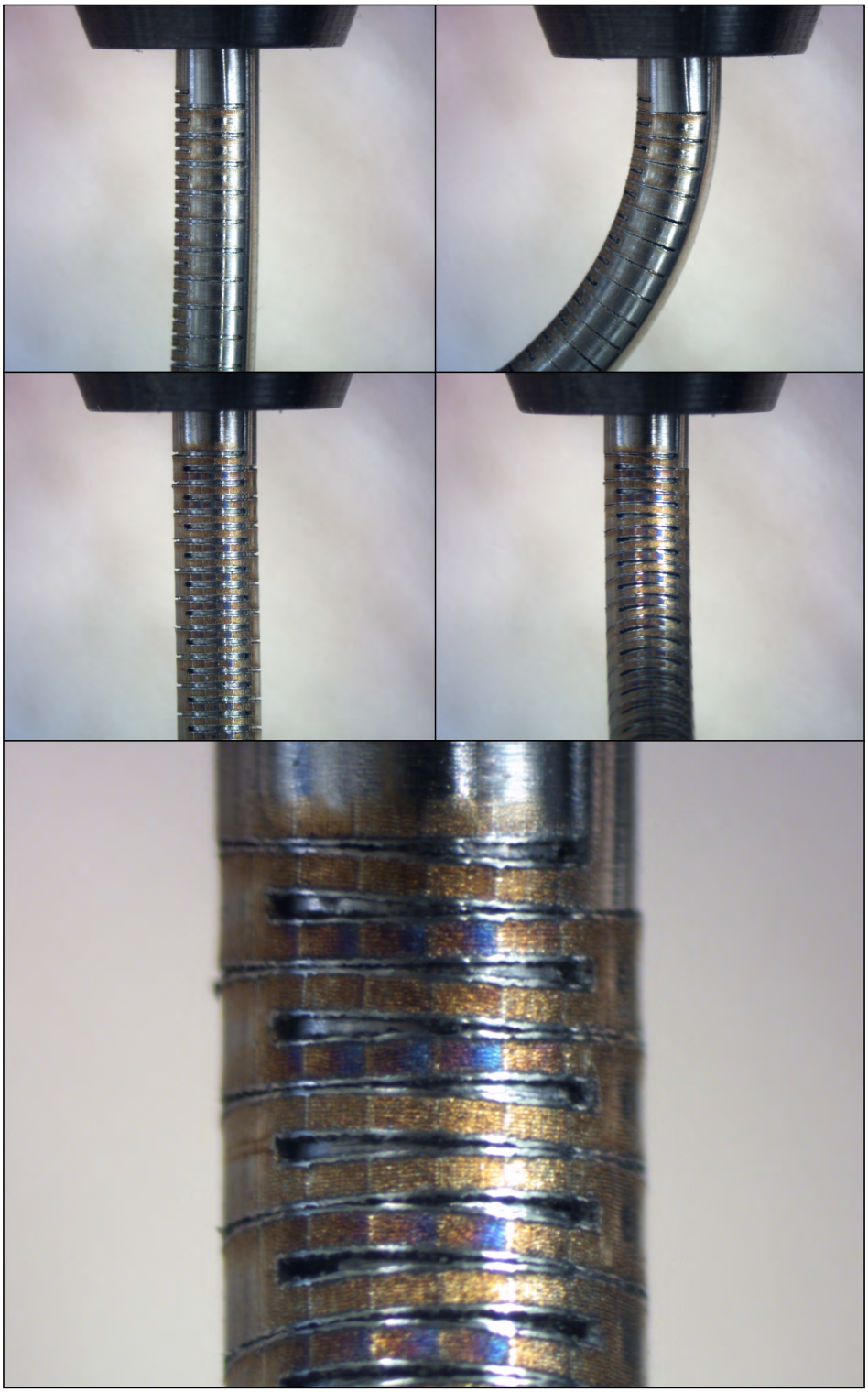

Figure 4.8: Magnified views of the serpentine cutting pattern closing. Top row: Side view of the open (left) and closed (right) notches. Middle row: Top view of the open (left) and closed (right) notches. Bottom row: Magnified top view of the closed notches. Notice how the notches make self-contact at either end of the overlapping region of the serpentine pattern, matching the modeling assumption.

Figure 4.9: Magnified views of the transition section of the dexterous sheath. This section is designed to be highly flexible to pass through the S-curve of the setup sheath.

from the tube. With this manufacturing procedure, we estimate that we can cut a minimum slot size of approximate 0.1 mm. Since the sheaths were manufactured before the final version of the serpentine closure model derived in Section 4.3.1, we used a slot height of 0.120 mm for both sheaths, which was consistent with a prior version of the model. Regardless, due to the limited precision and finishing of the in-house laser machining process compared to professional laser machining, we expect the difference in performance to be relatively minor.

After laser cutting, the tubes were sanded with grits ranging from 400 to 2000 to improve the surface finish. The tips of the bending sections, as well as the transition points from Nitinol to plastic tubing, were glued together with metal bonding cyanoacrylate (Loctite 430 Instant Adhesive). The plastic transmission tubes were glued to their respective actuator and handle components with medical device cyanoacrylate (Loctite 4981 Instant Adhesive). Future versions of the tube prototypes could be electropolished to further improve the surface finish. The entire laser machining and electropolishing process could also be outsourced to a medical device and stent manufacturing company that specializes in cutting and finishing Nitinol (e.g., Pulse Systems). While the most expensive option, contract manufacturing would produce the highest-quality samples with reliable cutting dimensions, excellent surface

finish, and smaller achievable feature dimensions.

Another important area of future work is to characterize the effects of laser machining on the fatigue and failure properties of Nitinol sheaths, particularly when using in-house laser machining processes. Thermal-based material removal processes such as laser machining and wire electrical discharge machining can cause heat-affected zones in Nitinol parts, which can lead to early fatigue and failure [218, 219, 220]. The heat-affected zones, surface roughness, kerf size, and residual stress could be improved through the careful selection of pulse width, cutting speed, and laser frequency, all of which affect the pulse power and resulting cutting characteristics [218, 219, 221]. While we would rely on the expertise of contract manufacturers when outsourcing the laser machined parts, it will be important to fine-tune our in-house processes as well and evaluate the fatigue and failure of sheaths manufactured in-house. This has been demonstrated previously with tendon-actuated Nitinol wrists [51].

4.4 Evaluating the Kinematic and Stiffness Characteristics of Steerable Sheaths

In this section, we describe the experimental evaluation of the steerable sheath prototypes. There are two important components of this experimental testing. First, we determine the actuation characteristics, including the shape of the sheaths and the actuation forces and translations. These results inform the design of the robotic actuator. Second, we evaluate the tip stiffness of the sheaths when subjected to forces in different directions. This simulates the forces sustained during clinical scenarios and determines whether the sheath designs are sufficient for ESD applications.

4.4.1 Metrology Testbed

We designed a custom metrology testbed for experimentally evaluating the kinematics and statics of the steerable sheath prototypes, as shown in Figure 4.10. This testbed, which features a motorized linear stage, load cell, and industrial camera, can be

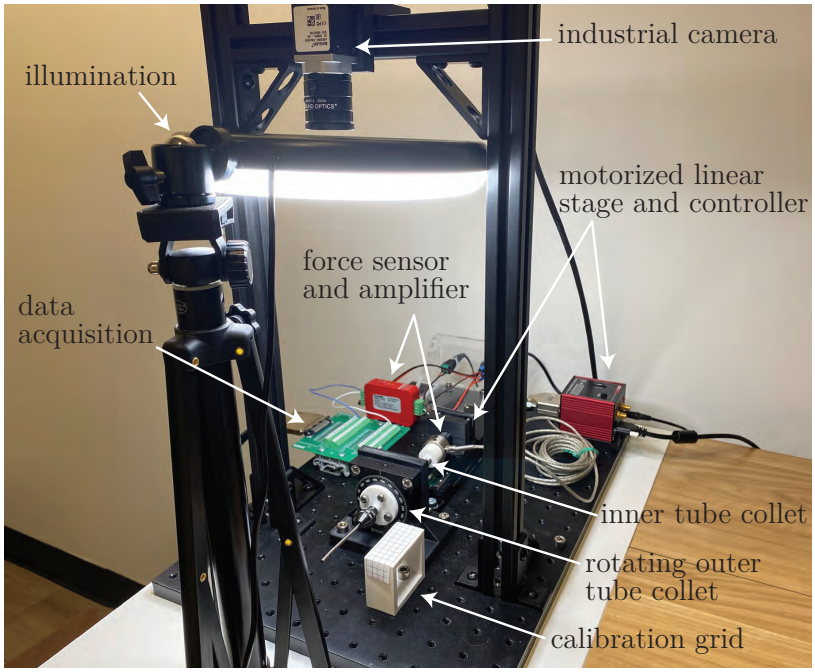

Figure 4.10: Metrology testbed for evaluating the kinematics and statics of steerable sheath prototypes. A motorized linear stage translates the inner tube, while a load cell captures the actuation force and an industrial camera captures the sheath's shape.

used to perform a parametric sweep over the range of possible inner tube actuation displacements while tracking the resulting curved shape of the tubes in space. By post-processing the camera images, we can evaluate both the kinematics of the sheath (particularly the distinct set-up and dexterous segments) and the required actuation forces for each segment. Similar testbeds have previously been used for analyzing the kinematic and mechanical properties of tendon-actuated notched wrists [50, 51, 204].

For linear motion, we use a motorized translation stage with a maximum velocity of 2.4 $^{\text{mm}}/_{\text{s}}$ and minimum repeatable incremental step size of 0.8 μm (MTS50/M-Z8, Thorlabs, Newton, NJ). Two collets grasp the outer and inner tubes of the sheath; the outer tube is fixed in place, while the inner tube is actuated by the linear stage. The outer tube collet is mounted to a manual rotary stage (Thorlabs RP01/M) which allows the plane of the sheath's curve to be adjusted. The inner sheath's collet is attached to a threaded in-line load cell to measure actuation forces. We employ a

Futek LCM300 tension and compression load cell that is rated to 50 lb; the signal is amplified by a Futek IAA100 strain gauge analog amplifier with a voltage output (Futek, Irvine, CA). The voltage signal is acquired with an NI PCI Express 6321 multifunction DAQ device and filtered in a LabVIEW application (NI, Austin, TX).

Images are acquired with a Basler ace 2 Basic USB3.0 area scan camera (Basler a2A2590-60ucBAS, Basler AG, Ahrensburg, Germany). This camera features a 5.0 MP resolution CMOS sensor and a frame rate of 60 frames per second.

4.4.2 Sheath Kinematics Experiments

We conducted actuation experiments for both the setup and dexterous sheaths to determine their range of motion and feasibility for ESD applications based on the desired performance laid out in Section 4.3.2. Using the metrology testbed described in the previous section, the inner tube of each sheath was linearly actuated at 0.1 mm increments, with force data and a camera image collected at each step. 100 samples of the force data output (which runs at 1 kHz) were collected and averaged per step. In each trial, the actuator displacement was increased until there was no visible change in tip position or curvature and the slots appeared to all be closed.

To process the camera images in MATLAB, two points were selected on a 5 mm calibration grid in the image frame and the corresponding real-world distance was given. This measurement calibrates physical units to image pixels. The calibration grid was placed at the same image plane as the sheath to minimize perspective errors in the measurement. Next, points were selected at the base and tip of the sheath to obtain the tip position relative to the base frame of the sheath (this coordinate frame is show in Figure 4.11 and is the same for all experiments in this section). Then, we entered the number of curved segments to evaluate and drew a rectangle for each region of interest. The ROI(s) were converted to grayscale images and thresholding was used to convert from grayscale to binary images. The testbed lighting was set

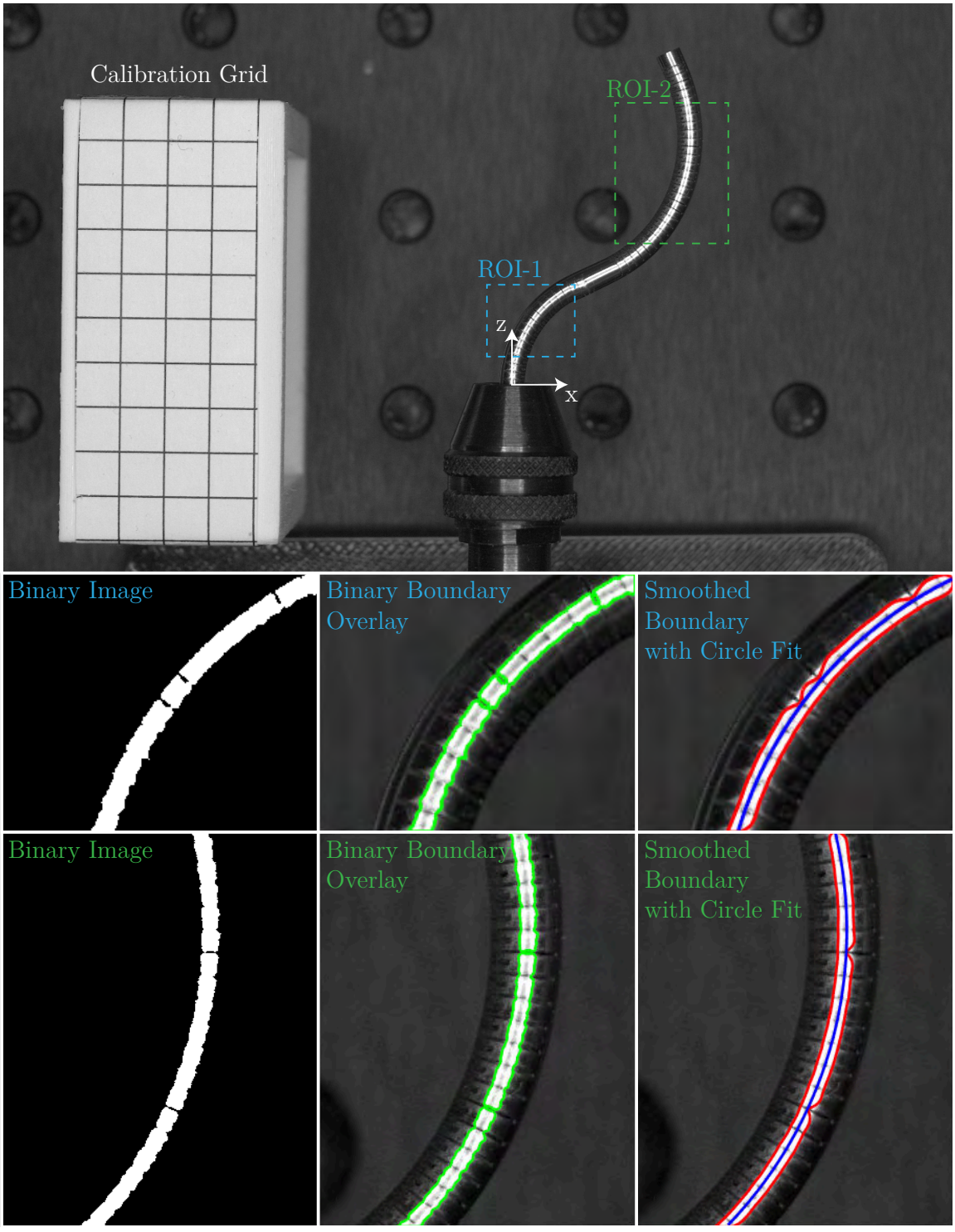

Figure 4.11: Evaluation of the setup sheath kinematics with the metrology testbed. Image pixels are calibrated to physical units using the 5 mm calibration grid. The user selects regions-of-interest which are converted to binary images. The sheath backbone is extracted with thresholding, and circles are fit to the backbone boundary to calculate the curvature of each segment. The coordinate frame for all experiments is shown at the base of the tube at the collet.

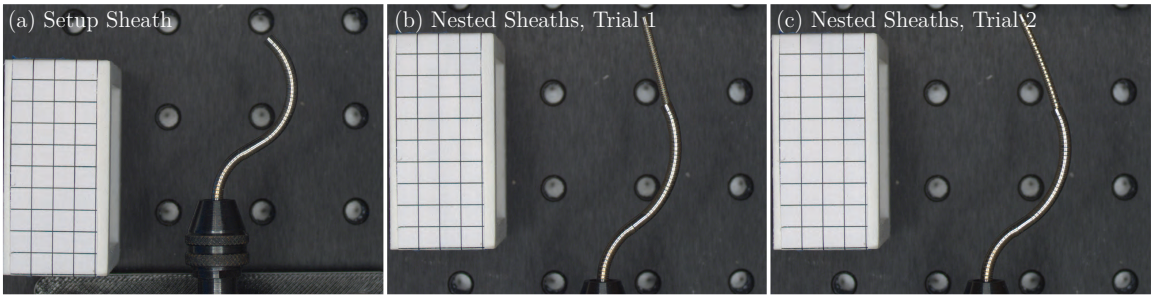

Figure 4.12: Metrology testbed images of setup sheath actuation experiment. Each trial is shown at its final actuated shape.

up such that the bright reflection from the Nitinol tubing was centered on the sheath backbone curve. This allowed the sheath curve to be easily extracted from the image using simple binary thresholding techniques. The boundary of the binary image was obtained and smoothed and the boundary points were used to fit a circle to the curved segment [222]. An example of this image analysis protocol is shown in Figure 4.11.

Setup Sheath Actuation

We conducted the setup sheath actuation experiment three times. The first trial consisted of actuating the setup sheath alone; during the second two trials, the dexterous sheath was nested inside of the setup sheath with the transition section fully overlapping the bending section of the setup sheath. These trials were performed to evaluate the effect of the dexterous sheath transition section on the setup sheath kinematics and quantify any change in required actuation force.

In each case, we measured the curvature of the proximal and distal curved segments of the setup sheath (ROI-1 and ROI-2, respectively, in Figure 4.11) throughout its range of motion, as well as the actuation force and the tip position. Figure 4.13 shows the measured actuation forces for each trial. The trials with the nested dexterous sheath exhibit a steeper slope for the first 4 mm of actuation distance. After this point, frictional effects come into play between the inner tube of the setup sheath and the outer tube of the dexterous sheath, which must slide past one another during

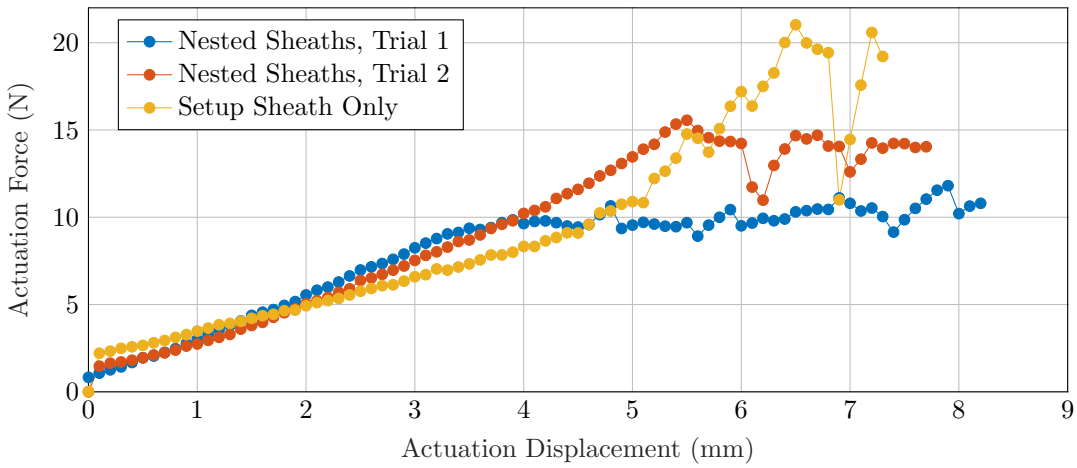

Figure 4.13: Force profiles of the setup sheath during actuation. Two trials were conducted with the dexterous sheath nested inside of the setup sheath; one trial was conducted with the setup sheath alone.

actuation. At several points in the nested sheath trials, we paused the test and moved the dexterous sheath to release any friction between the two sheaths; this can be seen in the drops in force at 6.2 mm and 6.9 mm in Nested Trial 2 in Figure 4.13.

In addition, the nested sheath force profiles show that the force flattens towards the end of the actuation input. While this is somewhat counterintuitive behavior (we might expect the actuation force to increase dramatically when the notches close or when there are high inter-sheath frictional forces), it is likely due to the limitatations of the testbed fixtures. The collets hold the Nitinol tubes at their smooth, unmachined segments, so there is a limit to how much holding force the collets can exert. When there is a high amount of frictional or self-contact force that is preventing the setup sheath from deflection, the instantaneous force when the actuator moves is too high for the collet and it slips. This behavior is shown in Figure 4.14, in which a brief spike in force can be seen before the collet slips and the force reverts to its original value.

The radius of curvature profiles for the proximal and distal segments are shown in Figure 4.15. As is expected in the absence of the nested dexterous sheath, the

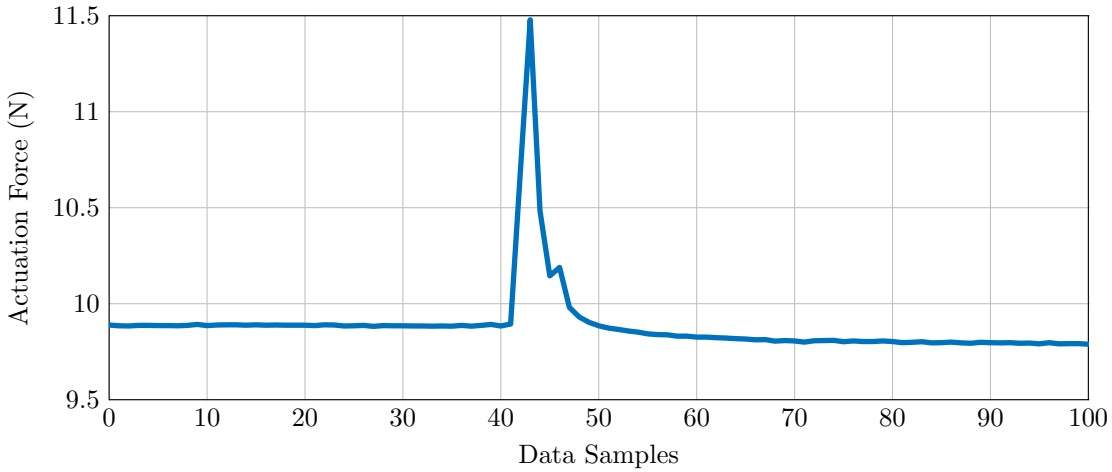

Figure 4.14: Spike in actuation force during Nested Sheath Trial 2 near end of actuation range which likely causes tube collet to slip.

Table 4.3: Sheath actuation experimental results. Minimum measured radius of curvature (mm) of each segment and final tip angle (°), measured from the $\boldsymbol{z}$ axis.

Trial	**Proximal Radius**	**Distal Radius**	**Tip Angle**
Nested Sheaths, Trial 1	15.3	20.7	26.1
Nested Sheaths, Trial 2	13.4	20.2	25.6
Setup Sheath Only	11.2	12.8	45.1
Dexterous Sheath, Trial 1	15.2	–	81.9
Dexterous Sheath, Trial 2	12.2	–	91.2

setup sheath alone achieved a smaller radius of curvature for both segments. The radii for the nested sheath trials were consistent compared to each other, particularly for the distal segment and in the second half of the actuation range. The radius of curvature of both segments trends consistently downward throughout the duration of each trial (with some small jumps when friction was released by hand or incidentally in the course of actuation). The minimum radius of curvature measurements for each segment and trial are summarized in Table 4.3, as well as the measured tip angle in the final configuration.

We also show the spatial trajectory of the tip throughout each trial (Figure 4.16). Once again, the tips of the sheaths follow a similar profile throughout the trajectory,

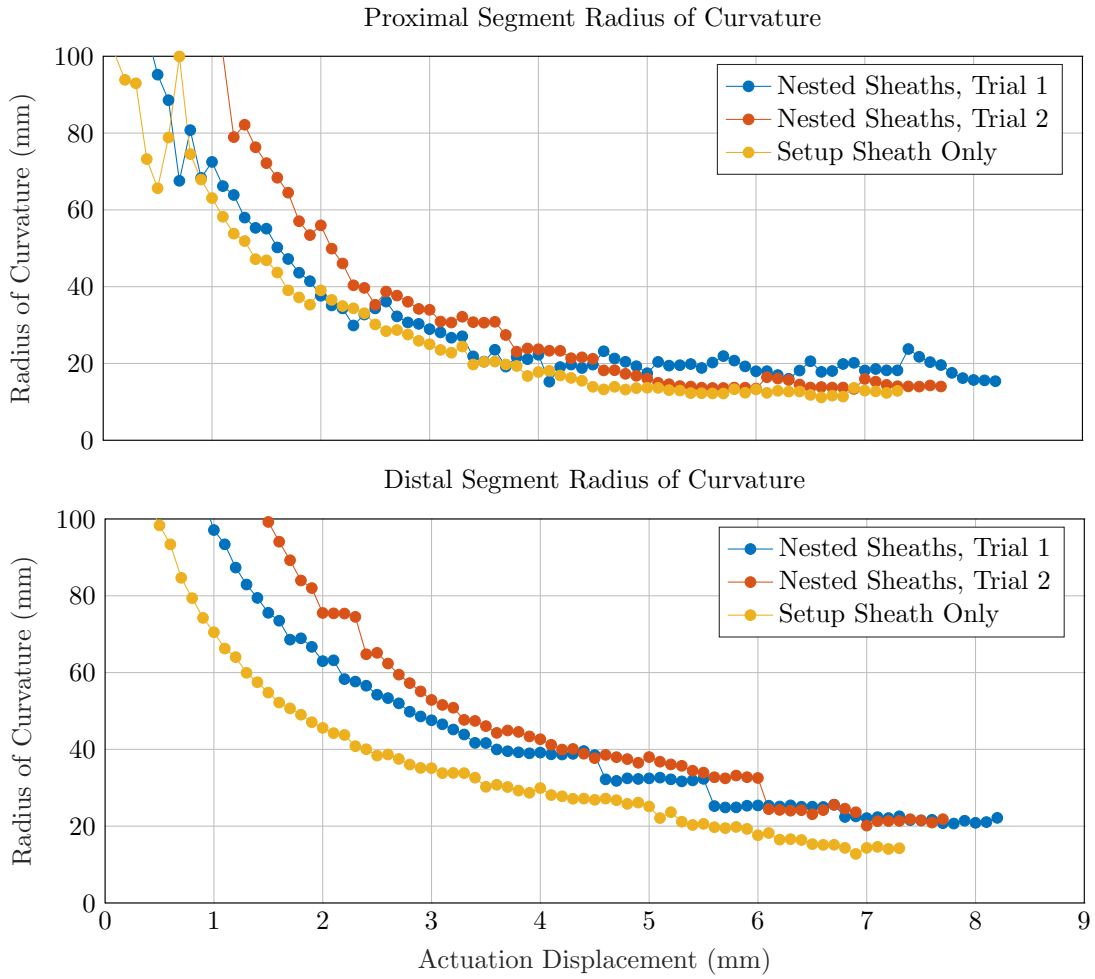

Figure 4.15: Setup sheath radius of curvature throughout actuation experiment. Note that the y-axis is limited to 100 mm for visualization purposes, as the radius of curvature goes to infinity as the sheath straightens.

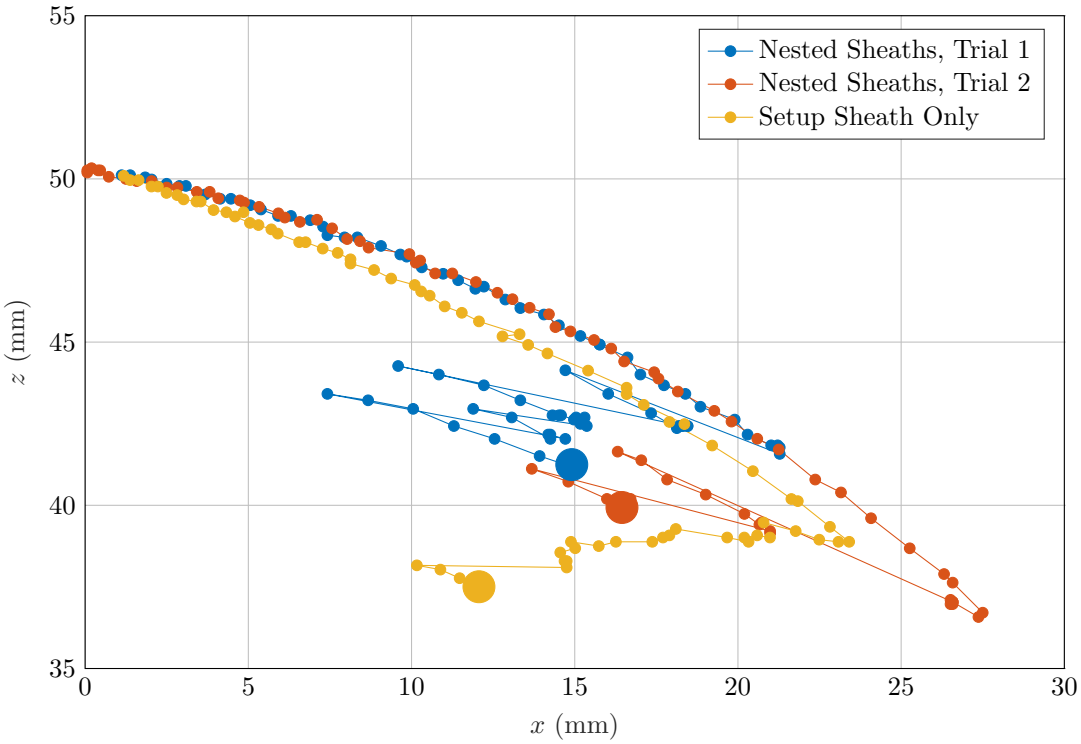

Figure 4.16: Spatial trajectory of the setup sheath tip during the actuation trials. The final point of each trajectory is enlarged.

with more variability over the last few data points, particularly as friction is released and the sheath moves large distances between data points. The final tip position of each trial is enlarged for emphasis.

The spatial trajectory demonstrates the kinematic behavior of the sheath and how this behavior could be employed by the system. Figure 4.17 shows how the shape of the sheath changes over the course of actuation. Theoretically, all of the slots in the proximal and distal segments should close at the same time, since they have identical dimensions. However, we see that the proximal segment reaches self-contact at approximately 4 mm of actuation (frame (e)) and remains relatively unchanged throughout the remainder of the actuation process. The distal segment accounts for the remainder of the sheath motion, independently of the proximal segment. The distal segment likely closes later than the proximal segment because of frictional effects; similar proximal-first bending behavior can be seen in other continuum devices.

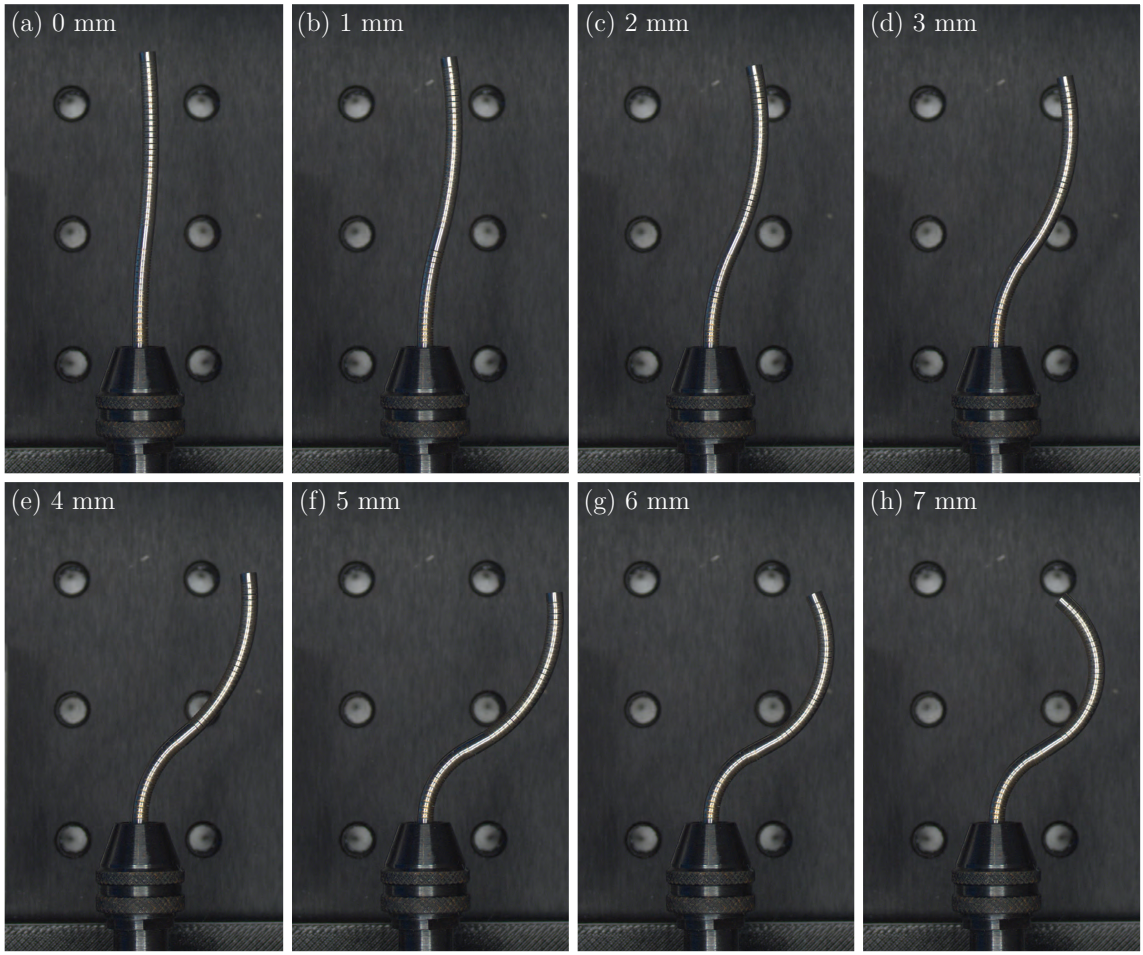

Figure 4.17: Setup sheath space curves at 1 mm actuation increments. Notice how continued actuation from (e) 4 mm to (h) 7 mm varies the tip angle from approximately 0° (straight ahead) to 45° (fully triangulated). The majority of this motion is caused by reducing the radius of curvature of the distal segment, whereas the proximal segment comes into self-contact first and remains relatively fixed after 4 mm. This could be a desirable feature for surgeons to independently adjust the triangulation angle with or without a dexterous sheath.

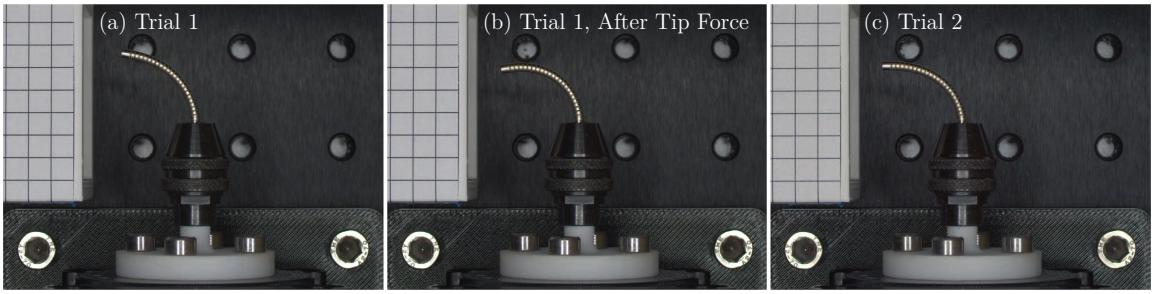

Figure 4.18: Final shapes of the dexterous sheaths after the actuation experiment. Note that while the radius of curvature in Trial 1 was initially higher than that of Trial 2, a small tip force released friction and the resulting shape was similar to Trial 2.

While tip-first bending is a desirable property in many types of surgical continuum robots, the proximal segment-first bending demonstrated here could be used advantageously in several ways. First, it could enable the surgeon to change and select the triangulation angle of the sheath. While the sheath may be less stiff because not all of the notches are closed, the ability to adjust the triangulation angle could be valuable as the surgical environment changes. In addition, one could even create a single-sheath arm for each manipulator of the bimanual system, rather than the dual-sheath system described here. In this paradigm, the proximal segment would close and than the surgeon would use the remaining actuation range to control tools with the distal segment of the S-curve. This would reduce the overall complexity of the system, at the cost of the independent translation and axial rotation afforded by the dexterous sheath with respect to the setup sheath pose. Finally, an additional potential benefit of proximal-first bending of the setup sheath is that the spreading of the distal segment could serve to push surrounding tissue away from the center of the workspace and open up the lumen for better visibility and access.

Dexterous Sheath Actuation

We conducted two trials of the dexterous sheath actuation experiment. As seen in Figure 4.19, the majority of the force profile was very similar for each trial. Slight

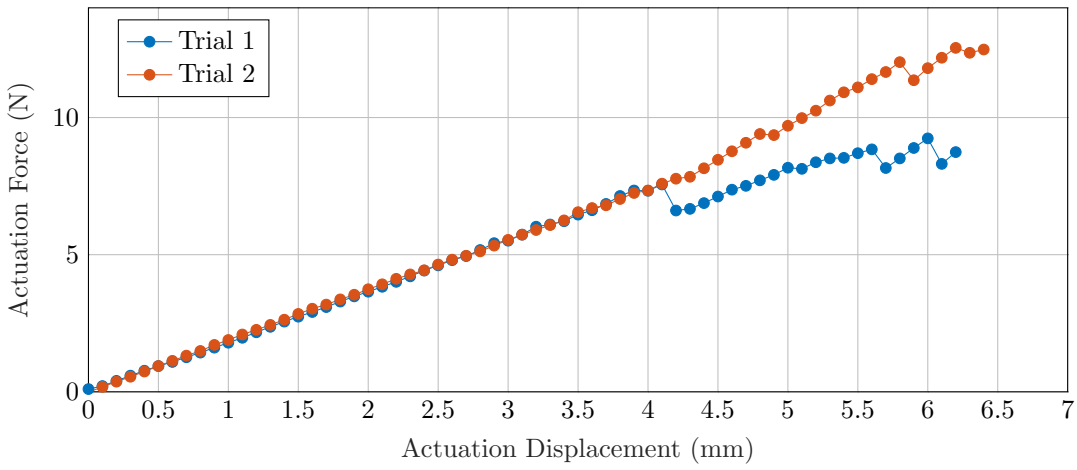

Figure 4.19: Force profile of the dexterous sheath during actuation.

discrepancies arise at 4 mm of actuation, most likely due to the release of friction at this point in Trial 1. Regardless, the slopes of the force profiles remain consistent even after this point. It is also worth noting that after Trial 1, the tip stiffness experiments described in Section 4.4.3 were conducted. When the first tip load was applied to the sheath, the sheath immediately released friction and came to rest in a shape very similar to the final shape of Trial 2. These results are shown in Figure 4.18(a-b). This suggests that friction was preventing the full curvature of the device during Trial 1.

The radius of curvature profiles for each trial are given in Figure 4.20. The slopes and values are very consistent throughout the duration of the actuation displacement, with Trial 2 finishing at a slightly higher curvature as is expected based on the final shape in Figure 4.18(c).

The spatial trajectory of the dexterous sheath tip position is shown in Figure 4.21. Note that the sharp decrease in radius of curvature at the end of Trial 2 (5.9 mm) in Figure 4.20 corresponds to a large change in tip position. In addition, it should be pointed out that the initial "straight" configuration is not completely straight and therefore the x-coordinate is not at zero for the initial data point. This is due to the slight precurvature that is introduced to the tube during the manufacturing process. We believe this is due to heat effects of the laser cutting process.

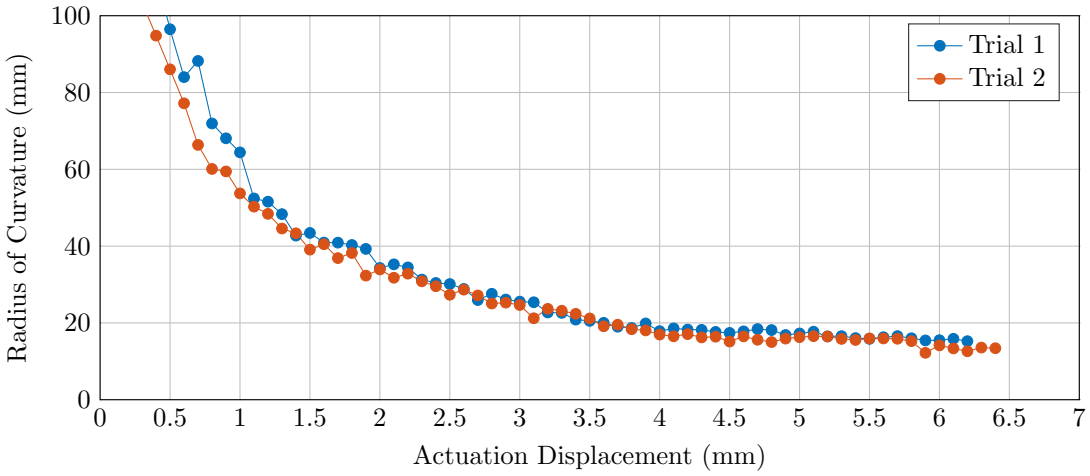

Figure 4.20: Dexterous sheath radius of curvature during actuation experiment. Note that the y-axis is limited to 100 mm for visualization purposes, as the radius of curvature goes to infinity as the sheath straightens.

In future experiments, we will quantify the bi-directional bending angle of the dexterous sheath; the current testbed fixtures only support pulling forces rather than pushing forces. Regardless, it is likely that unidirectional bending will be sufficient for many of the motions during ESD due to the triangulated setup pose. Even if the bending angle is less than 90° in the opposite direction, this may still be enough range of motion to access the surgical workspace.

The actuation experiments in this section demonstrate that the setup sheath successfully reaches a triangulation pose with or without the nested dexterous sheath. Without the nested dexterous sheath, the setup sheath reaches the desired triangulation angle of 45° and would be spaced 29.5 mm from the opposite sheath (in the x-direction) when accounting for the 5.4 mm working channel spacing at the tip of the Olympus endoscope. With the nested sheaths, the triangulation angle for each sheath is approximately 26° and two setup sheaths would be laterally spaced by 35–38 mm. In addition, the dexterous sheath actuation experiments show that the tip angle meets the desired tip angle range of motion of ±90° (Trial 1 had a tip angle of 82°, but the results of Trial 2 suggest that the tip angle and curvature were limited

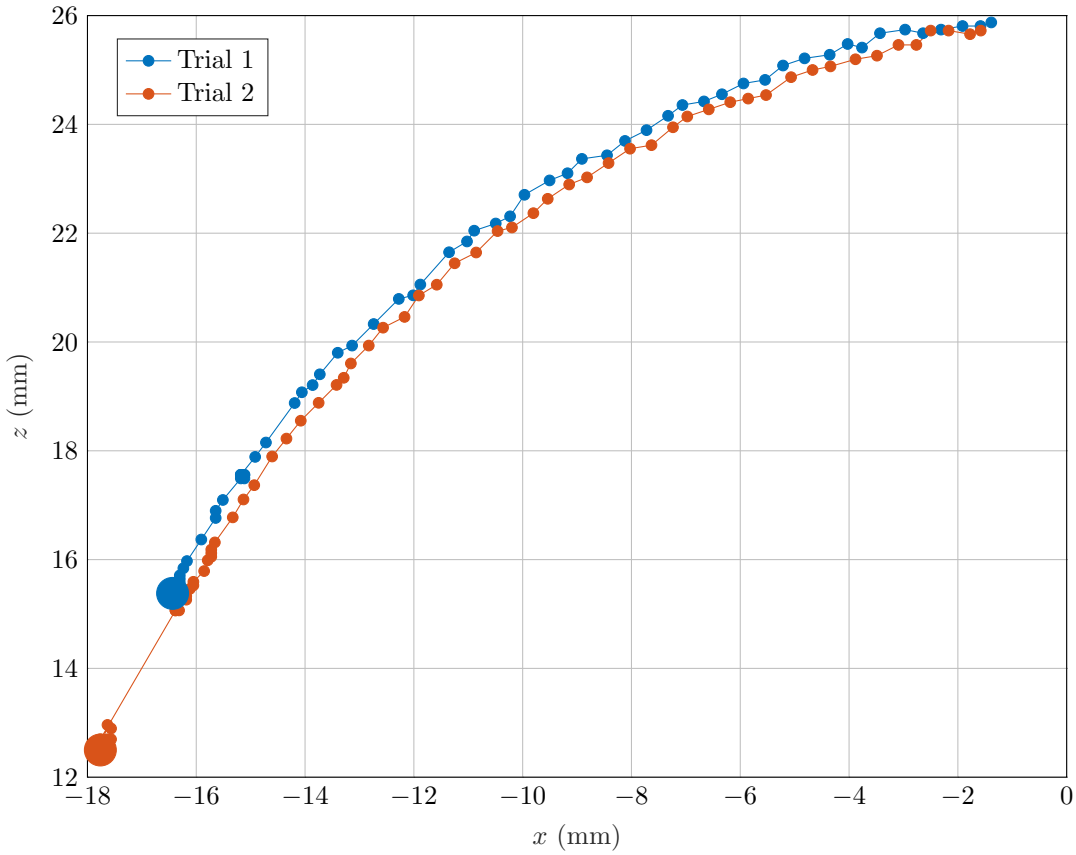

Figure 4.21: Spatial trajectory of the dexterous sheath tip during the actuation trials. The final point of each trajectory is enlarged.

by friction). In summary, the sheath kinematics meet the goals for triangulation and dexterity for ESD procedures.

4.4.3 Tip Stiffness Experiments

We conducted several tip loading experiments to determine the stiffness of the sheaths when subjected to forces in different directions. For each experiment, we applied forces to the tip of the sheath using 3D-printed jigs mounted to a manual linear stage. The stage had a graduated input knob capable of measuring positions with a resolution of 0.01 mm (Velmex A251202-S2.5). Force data was collected with an ATI Nano17 6-Axis Force/Torque Transducer at an effective sampling rate of 62.5 Hz with a resolution of 1/320 N (ATI Industrial Automation). 100 data points were collected and averaged for each translation step. Experiments were stopped when the maximum torque of the sensor was reached (50 N-mm) or when additional displacement could potentially damage the prototype.

Setup Sheath Tip Stiffness

We experimentally evaluated the tip stiffness of the setup sheath when fully actuated and subjected to loads in four different directions: normal to the tip, laterally outward with respect to the base, laterally inward with respect to the base, and transverse with the sheath axially rotated 90° at its base in the testbed collet. See Figure 4.22 for the test setup for each loading scenario. The tip loads were applied in linear increments of 0.1 mm (Normal and Transverse cases) or 0.5 mm (Lateral cases) using the linear slide, and each case was repeated three times.

Figure 4.23 shows the blocking force of the sheath in the four loading configurations. In each case, the mean force is plotted with a linear fit of the data; the error bars show the standard deviation of the force data between the three trials. The stiffness of the sheath in each direction is summarized in Table 4.4. Here we

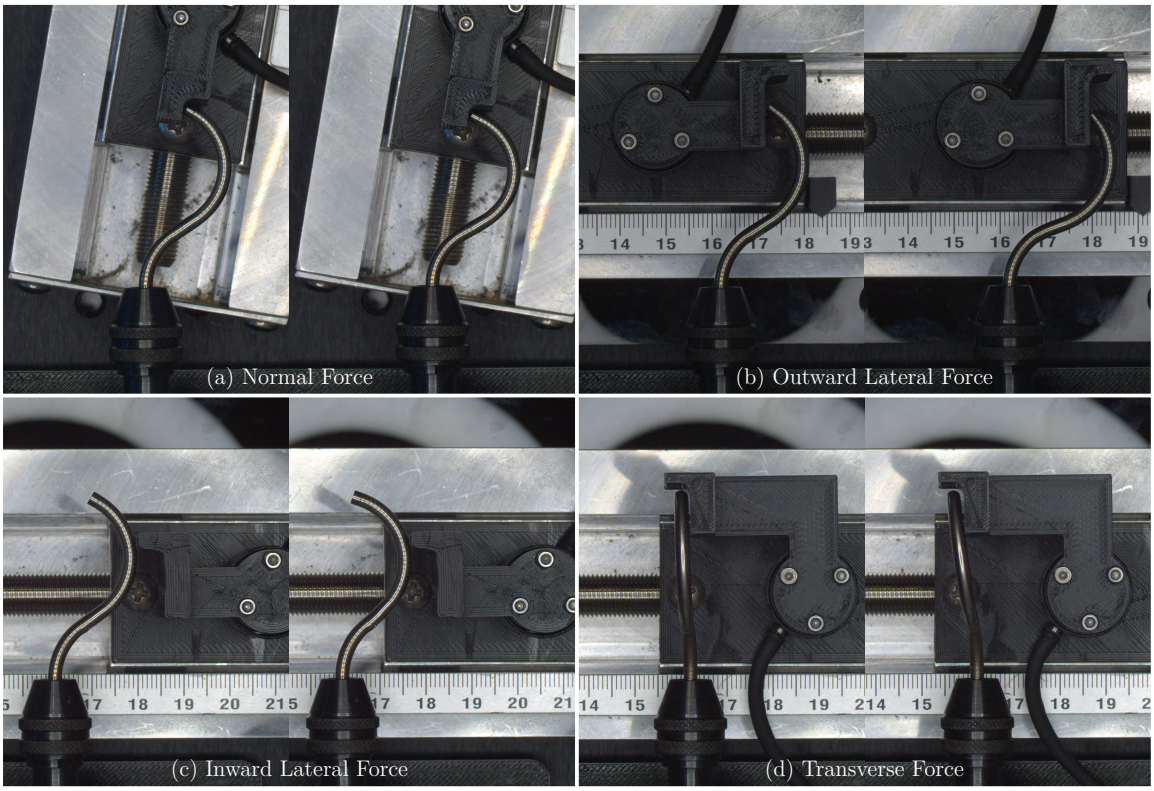

Figure 4.22: Setup sheath tip force experimental setup. Panel (a) shows a force being applied with a linear slide and force/torque transducer in a direction approximately normal to the tip of the sheath. Panels (b) and (c) show the application of an outward and inward lateral force, respectively. Panel (d) shows the application of an transverse force with the setup sheath rotated 90 degrees in the testbed collet.

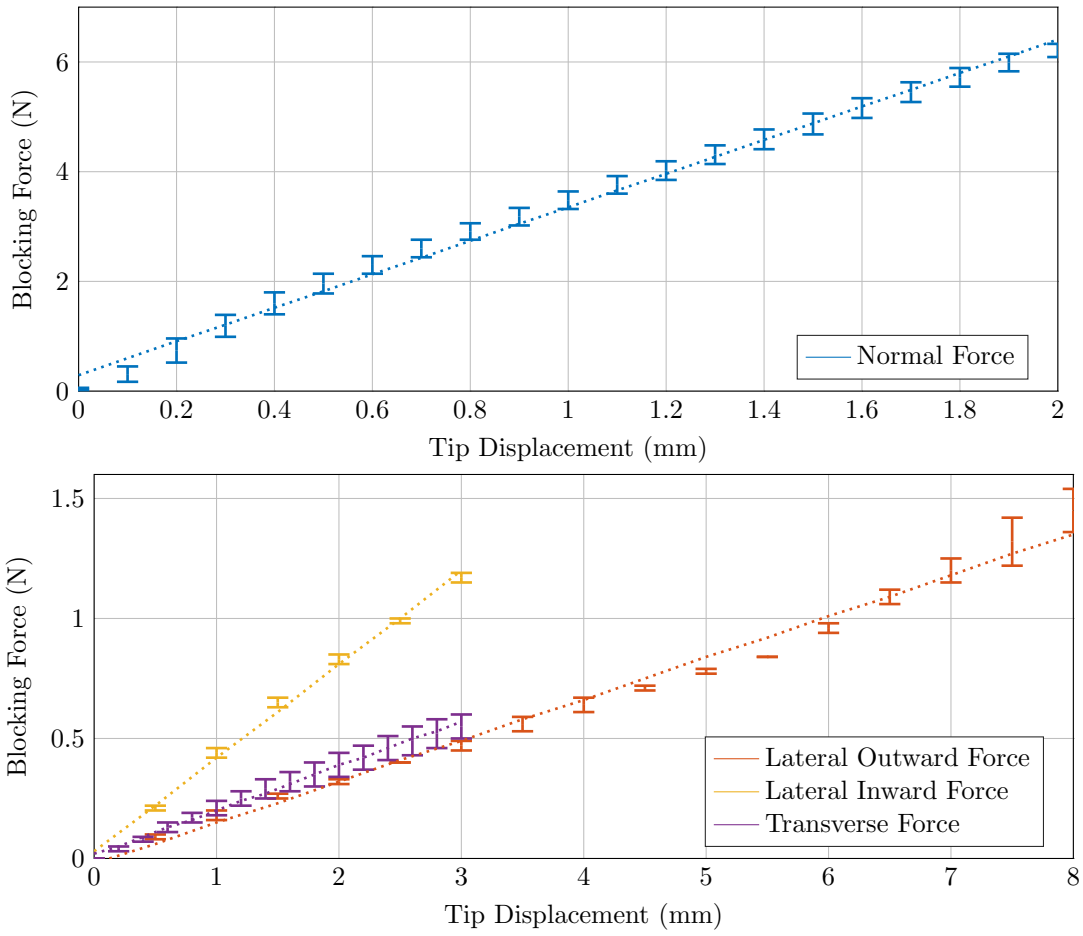

Figure 4.23: Blocking force of the sheath sheath under four different loading directions. Top: force applied normal to the tip. Bottom: force applied in laterally outward, laterally inward, and transverse directions. The stiffness in the normal direction was an order of magnitude higher than the other directions (note the different axes lengths for the top and bottom plots). Error bars show the standard deviation between trials, and linear fit lines to calculate stiffness constants are shown with dotted lines.

Table 4.4: Tip stiffness constants ($^{N}/_{mm}$) of the setup and dexterous sheaths in various force directions.

Force Direction	Setup Sheath	Dexterous Sheath	Dexterous Sheath, Straight
Normal	3.06	1.20	–
Lateral Outward	0.17	1.52	0.052
Lateral Inward	0.39	–	0.053
Transverse	0.18	–	0.081

see that the blocking force in the normal direction is much higher than in the other directions, with a steeper slope. This demonstrates the role of the serpentine pattern slot closure, which limits deflection in this direction by self-contact. The sheath is less stiff in the other directions without the benefits of slot self-contact; in the lateral directions, the force is applied in the direction of self-contact of either the proximal or the distal segments, but not both. Regardless, the sheath should be sufficiently stiff for sustaining tissue interaction forces ($\sim$0.4 N for electrosurgical ablation forces for ESD applications [94]) with relatively small tip displacement (less than 2.5 mm). Finally, it should be noted that the tip stiffness of the setup sheath will be higher when the dexterous sheath is nested inside, so it is likely that the deflection in that case would be even smaller.

Dexterous Sheath Tip Stiffness

We also performed a similar tip blocking force experiment for the dexterous sheath. In this case, we applied tip loads with the same linear slide and force sensor to the fully actuated dexterous sheath. The tip forces were applied at 0.1 mm increments in the direction normal to the sheath tip (towards the base on the sheath), as well as laterally, as shown in Figure 4.24. Each protocol was conducted three times and the resulting average force data and standard deviation are shown in Figure 4.25. The stiffness in each direction can be found in Table 4.4.

In this experiment, the lateral stiffness of the dexterous sheath was higher than

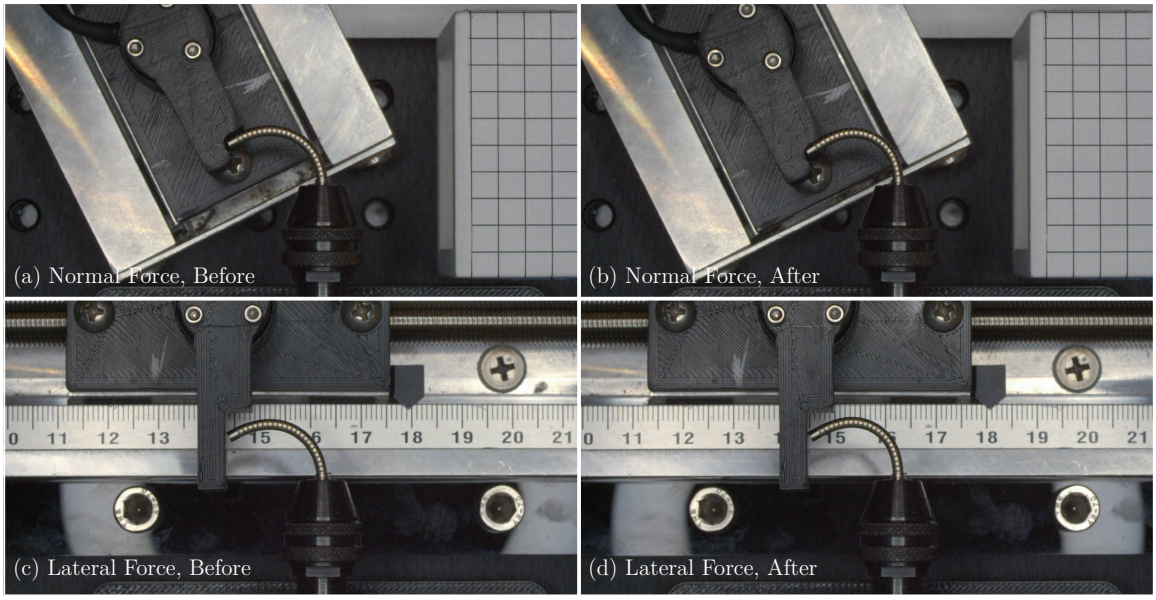

Figure 4.24: Dexterous sheath tip force experimental setup. Panels (a) and (b) show a force being applied with a linear slide and force/torque transducer in a direction approximately normal to the tip of the sheath. Panels (c) and (d) show the application of a lateral force.

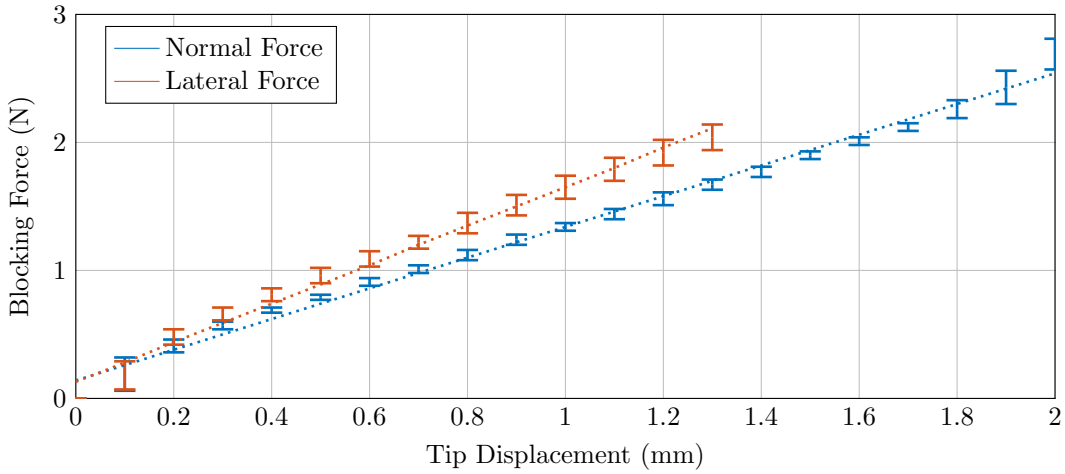

Figure 4.25: Blocking force of the dexterous sheath in the normal and lateral directions. Note that the tip displacement range was limited in the lateral case due to the torque limit of the F/T sensor. Error bars show the standard deviation between trials, and linear fit lines to calculate stiffness constants are shown with dotted lines.

the stiffness in the normal direction. This is because the lateral force pushes the sheath in the direction of self-contact, closing any slots that might still be open, and making the structure stiffer. This occurs because the deflection angle of the fully actuated sheath in this scenario was greater than 90 degrees, as seen in Figure 4.24. Based on the linear fit of the stiffness relationship, 0.4 N of tissue interaction forces in the normal direction would result in a deflection of 0.33 mm, while the same force in the lateral direction would cause the sheath tip to deflect 0.26 mm.

Since the dexterous sheath will interact with tissue in many different configurations, we repeated this experiment with an unactuated sheath (i.e., a straight configuration). The inner and outer tubes were held in place, but not axially displaced relative to each other (see Figure 4.26 for experiment design). We applied loads in the outward lateral, inward lateral, and transverse directions with 0.5 mm linear steps; each trial was conducted once and the results are shown in Figure 4.27. Based on a 0.4 N load (the upper bound electrosurgical force) in the lateral outward, lateral inward, and transverse directions, the sheath would deflect 7.7, 7.5, and 4.9 mm, respectively. These deflections represent the worst-case deflection both in terms of configuration and required electrosurgical force. The straight configuration is less stiff than the actuated configuration because the slots are not in self-contact when the sheath is unactuated.

To further contextualize the blocking force and stiffness profile of each sheath, we can compare these experimental results to the contact-aided joints presented by Eastwood et al. [201, 204]. The contact-aided joint in [201] was found to exhibit a blocking force of 0.1175 N per millimeter of lateral tip deflection in the region of deflection where the joint is in self-contact. This was compared to a stiffness of $0.0736\,{}^{\mathrm{N}}/_{\mathrm{mm}}$ for a rectangular notch. The former case is analogous to the experiments shown here in actuated configurations (where the contact behavior is in question), whereas the latter case is analogous to the straight configuration test of the dexterous

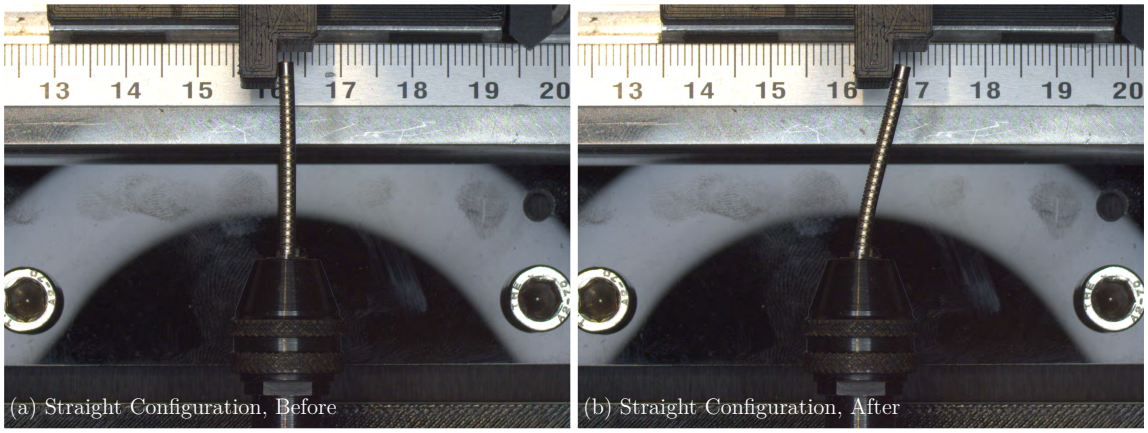

Figure 4.26: Dexterous sheath tip force experimental setup in straight configuration (a) before lateral tip load and (b) after lateral tip load. This experiment gives a lower bound on the dexterous sheath blocking force.

case where the device is not in self-contact. When applying loads in the closing direction of the self-contact slots (the Normal case for the setup sheath and the Normal and Lateral Outward cases for the actuated dexterous sheath), the stiffnesses found in this work are an order of magnitude higher than the contact-aided joint in [201]. This shows the benefit of the triangulation pose that has fully closed slots along the entire length of the setup sheath, whereas the joint in [201] is designed to have range of motion after the point of self-contact.

The geared contact-aided joint in [204] demonstrated a maximum blocking stiffness of approximately 2.3 $^{\mathrm{N}}/_{\mathrm{mm}}$ in its stiffest design and configuration. The fully assembled tool with three geared joints had stiffnesses of approximately 0.2, 0.38, and 0.75 $^{\mathrm{N}}/_{\mathrm{mm}}$ in the with-bending, against-bending, and orthogonal to bending directions (these results are estimated from the force profile data given). These values are of comparable magnitude to the sheaths in this chapter. It is important to note, however, that these comparisons are not meant to prove the superiority of one type of contact-aided joint over another, because the devices are designed for different applications with different lengths and tube dimensions. In addition, the test conditions are not identical in terms of the joint closure, force directions, or experimental methods. For example,

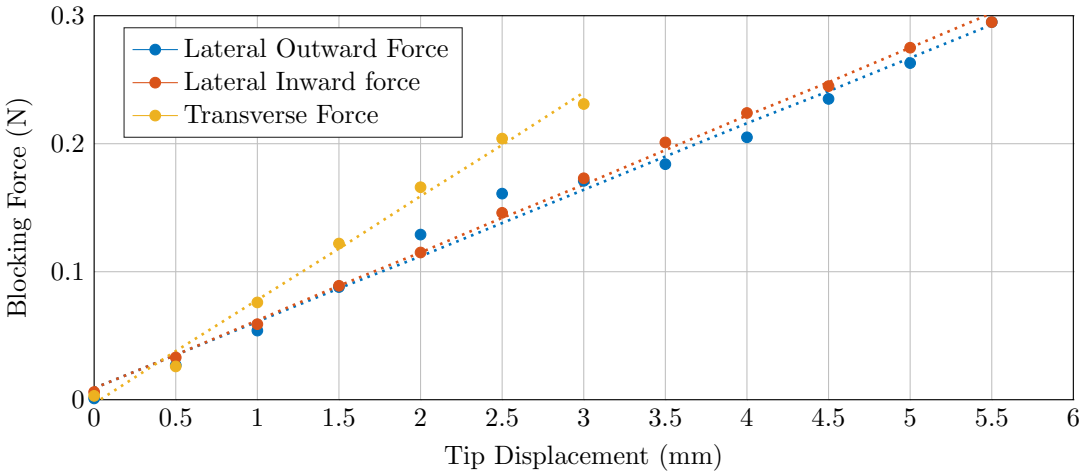

Figure 4.27: Dexterous sheath blocking force in its straight, unactuated configuration. Linear fit lines to calculate stiffness constants are shown with dotted lines.

a tendon-actuated wrist with a length of only 7.66 mm and fully closed rectangular notches was found to have a blocking force of 2 N with 0.25 mm of deflection (8 N/mm).

The blocking force experiments in this section demonstrate that the setup sheath exhibits sufficient stiffness to provide a stable conduit for the dexterous sheath as it interacts with tissue. In addition, the experiments show that the dexterous sheath is sufficiently stiff to interact with tissue with acceptable levels of deflection, given the required forces for performing endoscopic submucosal dissection.

4.5 Handle Design and Evaluation

In this section, we describe the design of a handle to control the each arm of the bimanual steerable sheath system. Each handle can be directly attached to the working channels of standard endoscopes. The endoscope itself is mounted on a passive support arm while the surgeon uses the two handles to allow for stable bimanual control of the instruments (see Figure 4.3).

The handle consists of three sections: a manual slider to actuate the setup sheath, a motorized transmission to actuate the dexterous sheath, and a user interface. Figure 4.28 shows an overview of the handle assembly. While the dexterous sheath could

be controlled with a purely mechanical transmission, the robotic transmission with an attached user interface offers two benefits for future experiments. First, we will be able to use software to tune the gain between the user input and the deflection of the sheath. This will enable us to use the platform for future user studies with surgeons without needing to redesign a mechanical transmission for different gains by changing gear ratios or lead screw pitches, for example. Similarly, by designing the user interface as a separate component that attaches to the transmission, we can explore different user interfaces (e.g., lever inputs, pistol grips, joysticks, etc.) while making use of the same transmission design. This will streamline the design process because we will not need to integrate the transmission components into each user interface design.

4.5.1 Setup Sheath Actuator Design

In this system, the setup sheaths are actuated manually to their triangulated setup poses and then locked in place. The manual actuator consists of an endoscope coupler, a sliding disk, and a transmission coupler (see Figure 4.29(c) and Figure 4.28). The endoscope coupler attaches the sheath handle to the endoscope port. For the Olympus colonoscope that the system was designed to integrate with, each working channel has a ringed port that the coupler fits over. The coupler is secured to the ringed port with set screws. The coupler is angled such that the handles do not interfere with each other. The outer tube of the setup sheath is fixed to the coupler, while the inner tube is fixed to the sliding disk. Both tubes are glued with to their respective actuator components with cyanoacrylate (Loctite 4981 Medical Device Adhesive).

When the sliding disk reaches the full translation distance of the setup sheath, it is locked in place by two snap-fit flexure latches on the coupler. The latches, which are made of 3D-printed nylon, are flexible and can be released by two captive pins or by hand so that the setup sheath can return to its straight configuration. We analyzed

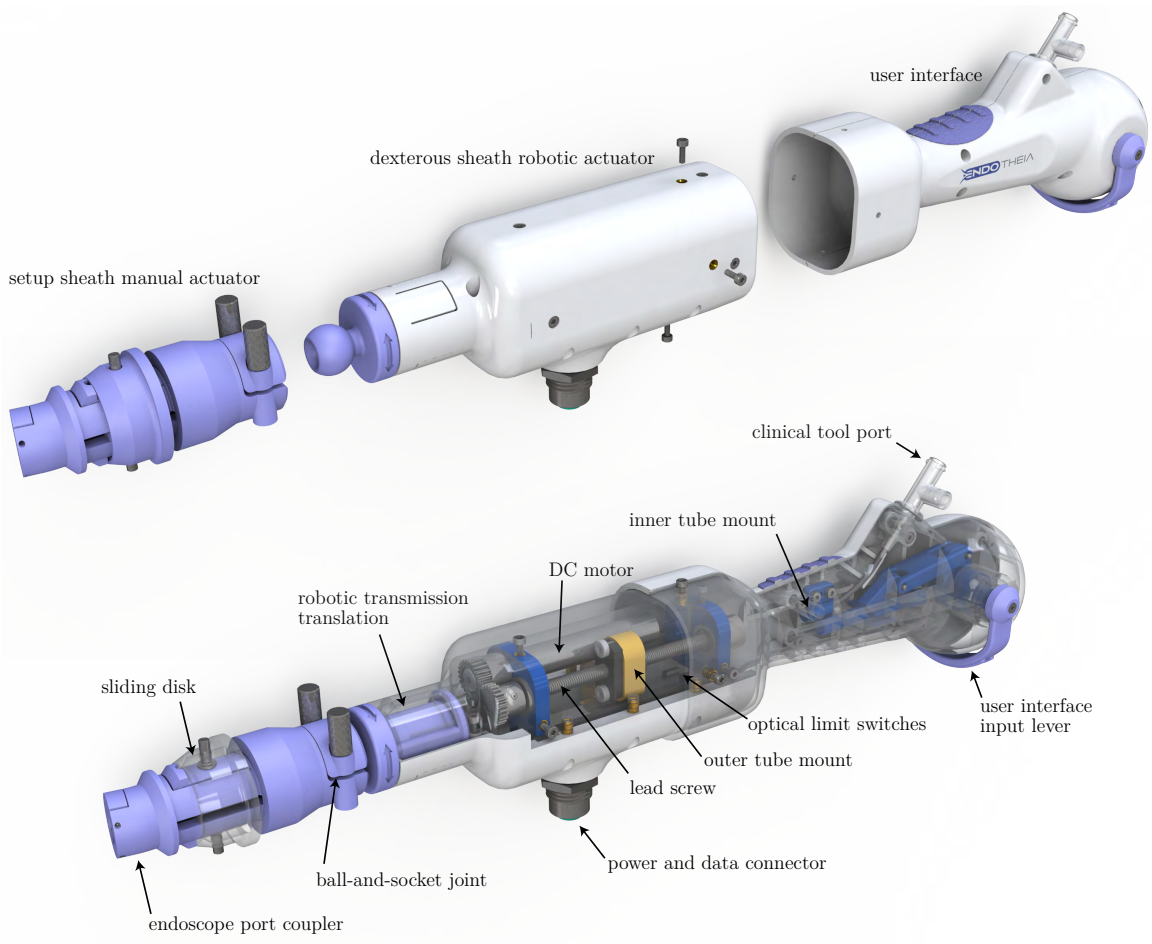

Figure 4.28: Rendering of handle assembly. (Top) Three main sections of the handle, from left to right: setup sheath manual actuator with sliding disk, dexterous sheath robotic actuator, and modular user interface. (Bottom) Individual components of actuators and user interface.

the deflection forces and resulting strain using finite element analysis in Solidworks to ensure that the latches do not over-strain or require unreasonable actuation forces.

In future iterations of the system, the setup sheath actuator could motorized for full position control if user studies show that surgeons prefer to vary the triangulation pose of the setup sheaths. If a single translation position is sufficient and the design of the setup sheath serpentine pattern is finalized, the manual actuator could be replaced by a solenoid with a button or switch to actuate the sheath and automatically enter the setup configuration. The manual actuator was preferable for this design because the actuator translation parameter is easily changed by 3D-printing new components. This makes it simple to adjust the actuator for new setup sheath designs.

The motorized transmission connects to the manual setup sheath actuator with a ball-and-socket joint that allows the user to comfortably angularly reposition the handle, as well as perform gross axial rotation of the dexterous sheath.

4.5.2 Robotic Transmission Design

The modular transmission section of the handle houses a motorized linear actuation system for the dexterous sheath. The handle and transmission utilize the following control scheme: 1) the surgeon uses the input lever to command a tip deflection, 2) the measured rotation of the input handle is mapped to a relative translation between the dexterous sheath tubes, 3) the linear actuator translates the outer sheath tube, and 4) the sheath deflects. With a robotic handle, the mapping between the input and output can be changed in software to adjust the amount of lever deflection that is needed to move the sheath tip.

The outer tube is translated linearly by a lead screw mechanism, as shown in Figure 4.29(a) and Figure 4.28. A brushed DC motor (Maxon DCX 10L EB KL 6V with a 64:1 gearhead and a 128 count-per-revolution encoder) rotates a lead screw (Haydon Kerk, 3/16 in diameter, 0.5 in pitch, with an anti-backlack lead nut); the

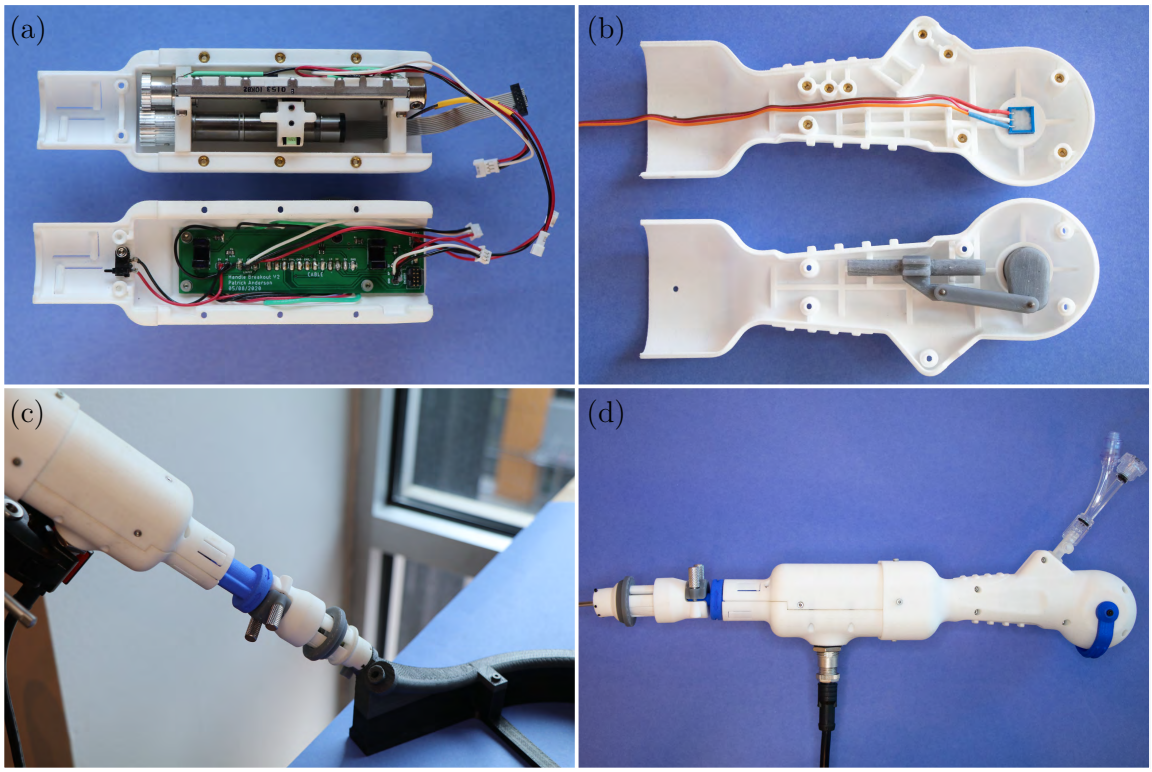

Figure 4.29: Major components of the motorized sheath actuator and user interface. (a) Motorized actuator with DC motor and lead screw mechanism (top) and on-board PCB (bottom). (b) Reverse grip user interface with lever input (lever not shown). Rotary potentiometer reads in surgeon input (top), while a slider-crank mechanism provides resistance for improved feel (bottom). (c) Setup sheath manual actuator and endoscope coupler mounted to mock-colonoscope. (d) Assembled system with manual actuator, motorized actuator, and user interface from left to right.

outer tube is glued to the lead nut carrier that travels along the lead screw. The inner tube of the sheath extends into the user interface, where it is integrated into and fixed in a Luer fitting such that flexible clinical tools can be easily introduced into the handle and deployed through the sheath.

The transmission section also houses an on-board printed circuit board (PCB). This PCB serves as a breakout board for the motor power, motor encoder, linear and rotary potentiometers, and safety limit switches. A linear slide potentiometer is attached to the lead screw carrier; this signal provides absolute position feedback for calibrating the home position of the sheath outer tube. The rotary potentiometer is integrated into the user interface (see Figure 4.29(b)) and reads in the surgeon input. Two optical limit switches are mounted to the on-board PCB at either end of the lead screw assembly. If either limit switch is triggered by the lead nut carrier, then a flag is sent to the control board and motor operation is halted.

Finally, a mechanical plunger limit switch sits at the base of the sheath insertion slider. The entire handle slides along this component (see Figure 4.29(c) and Figure 4.28) to insert and retract the dexterous sheath at the tip of the setup sheath. The limit switch at the base of the slider can be used in software to detect when the dexterous sheath is fully extended. This ensures that the sheath is not actuated while it is retracted inside the setup sheath (or inside of the endoscope working channel, in the case of a single sheath system). Snap-fit flexure latches at either end of the slider housing hold the handle in the extended or retracted position. The latches were designed such that the snap fit push-on force is high enough to hold the handle in place securely, but low enough for the user to push past without significant effort.

Power and data input/output is delivered to the on-board PCB with a circular cable connector integrated into the bottom of the transmission section. The handle is connected with a cable to the control box, which houses a custom PCB for powering and controlling the handles with an Atmega644 microcontroller (Figures 4.31

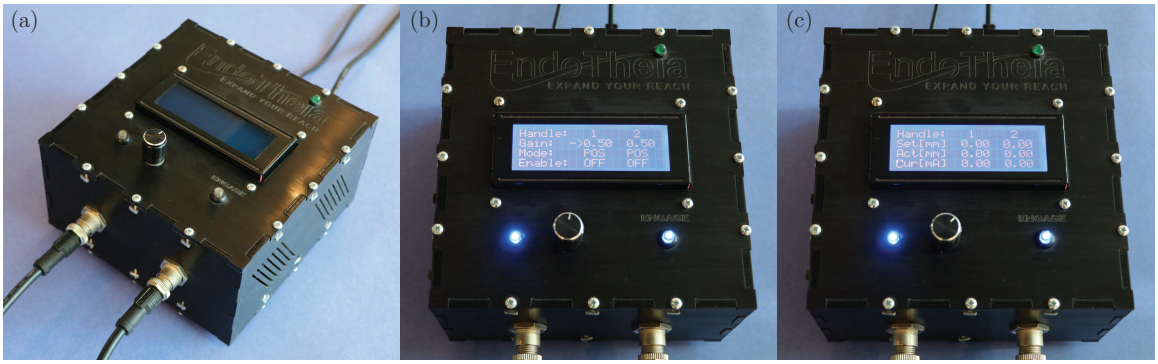

Figure 4.30: (a) Steerable sheath system control box, which houses the handle control board, has connection ports for two handles, and has selection buttons and knobs for the user. Screens are shown for (b) interfacing with the control gains and handle selection and (c) displaying actuator information during operation.

and 4.32). The control box is shown in Figure 4.30. The microcontroller computes PWM motor signals which are sent to two H-bridge brushed motor drivers (Texas Instruments DRV8876), reads the motor encoder signals with a differential line receiver (RS422) and two quadrature decoders (LSI Computer Systems, Inc. LS7366RS), and displays pertinent information to an LCD screen that is integrated into the box. The control box also has an input knob and two buttons for changing control gains, selecting which handle to use, and other functions such as sheath homing. The LCD screen displays these options to the user, as well as the setpoint and actual linear positions of each actuator, as shown in Figure 4.30(b) and (c). The control box connects to a PC via USB cable for programming; 5V DC power is delivered by USB or through a 12V DC barrel jack. Power from the barrel jack is regulated to 6V for the motors and 5V for other components (potentiometers, optical limit switches, etc.). The barrel jack power is required for driving the motors, but other components can be powered by USB alone while programming and debugging.

The controller software implements a state machine with actuation, homing, and calibration states. During the actuation states, we read in rotary potentiometer analog signals and convert them to a linear translation setpoint in millimeters using the desired control gain. We use the motor encoder count and lead screw parameters

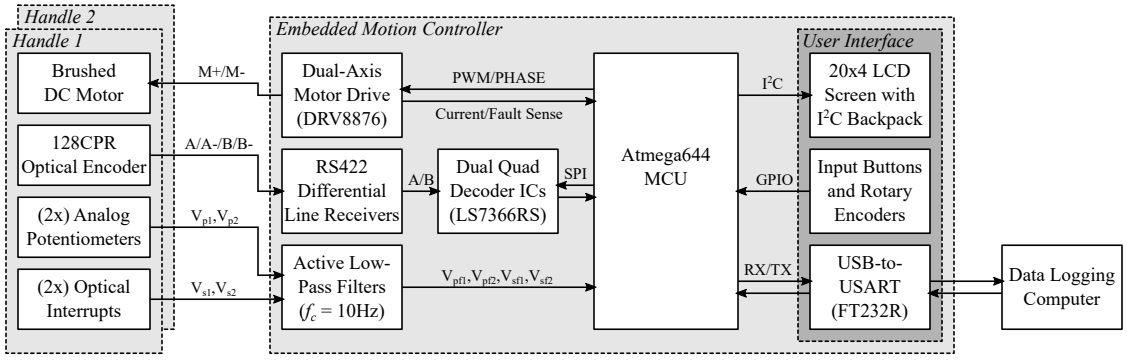

Figure 4.31: Control board block diagram. An Atmega644 microcontroller is used to send motor PWM control signals and receive optical encoder, potentiometer, and limit switch information from each handle. In addition, the control board features a user interface with an LCD screen and user input buttons and a knob.

to compute the actual translation distance of the sheath outer tube from its home position. We use a standard PID controller to compute a PWM signal and direction based on the error between the setpoint and actual linear outer tube mount position. This signal is sent to each H-bridge motor driver.

4.5.3 User Interface Design

An intuitive user interface is essential for ensuring that dexterous endoscopic devices are effective tools for surgeons. Without easy, simple controllability, a dexterous tool may be too difficult for the surgeon to use and therefore lose the advantages that dexterity could potentially bring over straight tools. To this end, we designed a modular user interface connection to the robotic transmission so that we can explore different user interface form factors.

In this work, we designed a user interface with a reverse grip (i.e., the thumb faces toward the user or upright and away from the working channel port) with a thumb input lever (Figure 4.29(b) and (d), Figure 4.28, and Figure 4.33). The user interface sits in the surgeon's palm, while they use their thumb to deflect the lever. We believe this is an intuitive choice for an input method because the deflection of

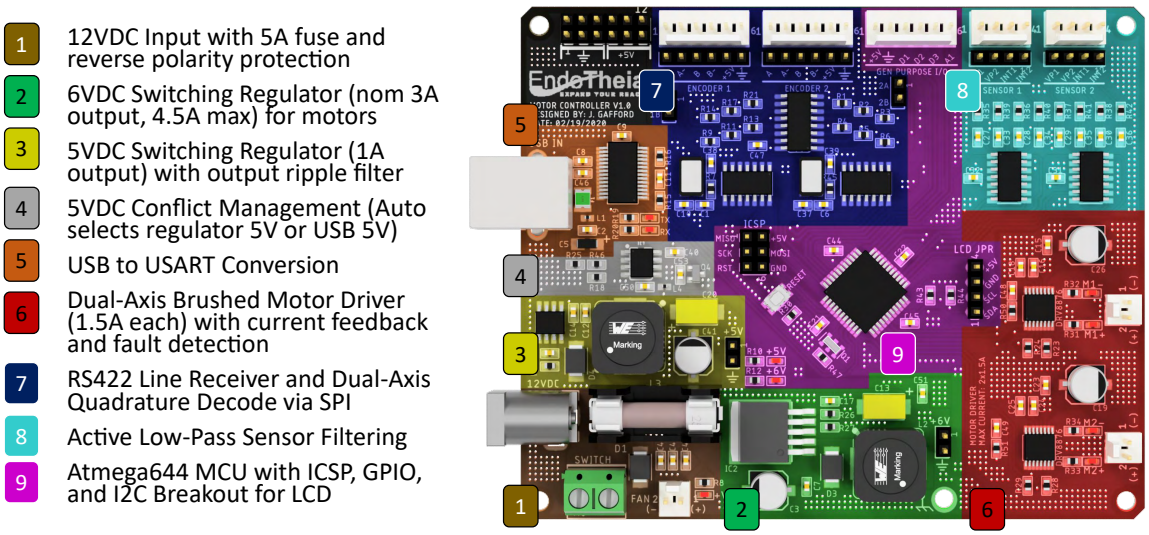

Figure 4.32: Layout of the handle control board.

the lever matches the deflection of the sheath that the surgeon sees. In addition, this grip style matches the technique already employed by endoscopists to operate clinical endoscopes: the endoscope is held upright in the palm and the thump is used to steer the endoscope with levers.

The user interface (in tandem with the robotic transmission section) also allows for gross translation and rotation of the dexterous sheath independently of the setup sheath. These degrees of freedom are accommodated via the interface between the manual setup sheath actuator and the robotic transmission. The user can rotate the entire transmission-user interface assembly about the ball-and-socket joint shown in Figure 4.28, as well as slide along its length to insert and retract the sheath. The ball-and-socket joint also enables the user to comfortably reposition their hand without moving the sheath tip (other than rotating about the long axis of the handle).

There are several other form factors that we can explore in the future, as shown in Figure 4.33. One example is the pistol grip shape that is frequently employed in laparoscopic tools. In this paradigm, we could use a finger trigger input (Figure 4.33(a)) or a thumb joystick input (Figure 4.33(b)). In the latter case, we could also motorize the gross rotational actuation of the dexterous sheath to give the user 2-DOF

Figure 4.33: User interface concepts that can be easily integrated into the existing handle transmission framework. (a) Pistol grip with finger trigger input, (b) pistol grip with thumb joystick input, (c) reverse grip with thumb lever input (current design described in this chapter), (d) forward grip with finger or thumb knob input, and (e) reverse grip with thumb joystick input.

control of the sheath tip via the joystick. Another feasible form factor is a forward grip (in which the thumb faces forward away from the body and toward the working channel of the endoscope) with a thumb or finger knob input (Figure 4.33(d)). Finally, the reverse grip could be employed with a joystick input rather than the lever input (Figure 4.33(e)). With the handle transmission architecture designed in this section, any of these options and more could be explored through rigorous user testing and feedback.

4.5.4 System Performance and User Testing

We assembled the setup and dexterous sheaths with their respective actuators and the user interface handle, as described in the previous sections. Since colonoscopes are too long for the off-the-shelf medical tubing used in the sheaths, we designed a 3D-printed mock-colonoscope for evaluating the system. This experimental setup has approximately the same dual channel dimensions as the Olympus colonoscope (channel dimensions are adjusted to account for 3D printing resolution and tolerances), a curved entry point with ringed ports like the Olympus scope, and a total channel length of 510 mm (see Figure 4.34).

To confirm the setup and workflow of the system, we first deployed the setup sheath through the working channel of the mock-colonoscope and used the coupler to mount the manual actuator to the ringed port. Next, we passed the dexterous sheath through the setup sheath and coupled the robotic transmission to the manual actuator using the ball-and-socket joint. Finally, the setup sheath was actuated into its S-curve shape with the sliding disc, and the user interface lever was employed to deflect the tip of the dexterous sheath via the robotic transmission.

While the overall system architecture and workflow was performed successfully, the achievable deflection of the dexterous sheath was limited compared to the kinematics shown in the metrology testbed actuation experiments or the achievable deflection

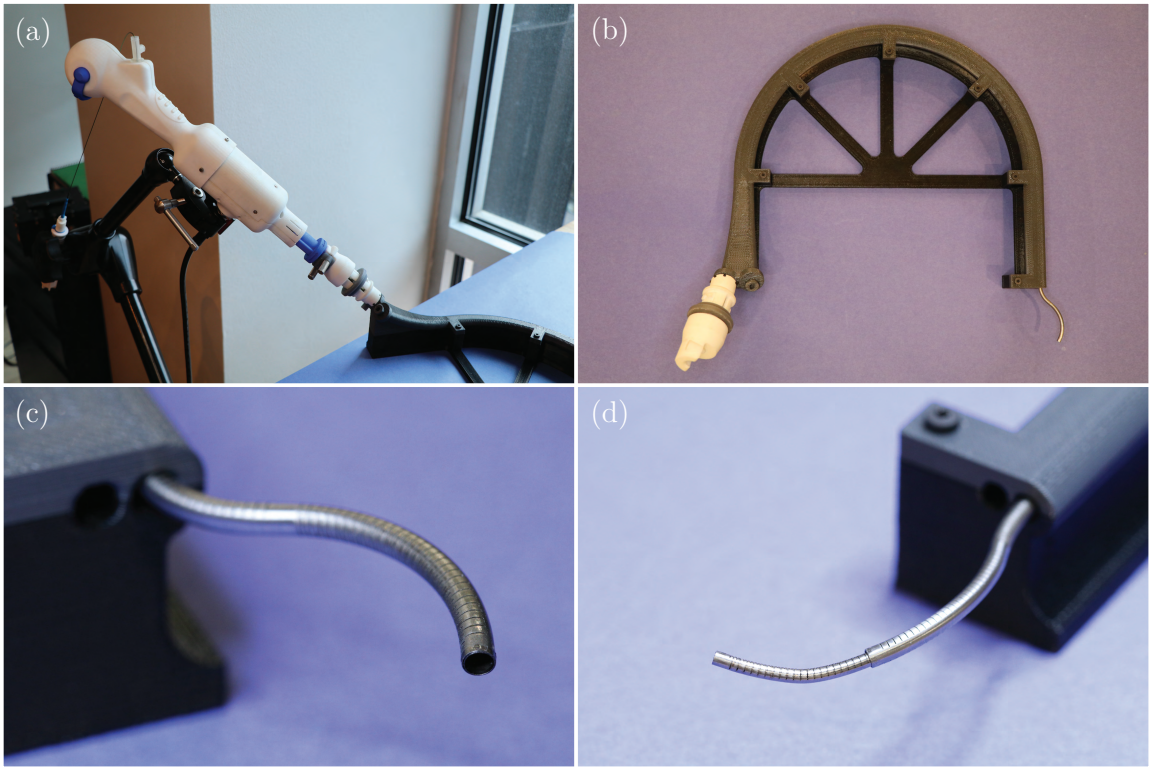

Figure 4.34: (a) Assembled steerable sheath system with mock-colonoscope fixture. (b) Setup sheath deployed through fixture and coupled to colonoscope port. (c) Setup sheath actuated through mock-colonoscope fixture. (d) Dexterous sheath deployed and actuated through setup sheath.

when using the robotic dexterous sheath alone, without passing it through the setup sheath. This is primarily due to two limitations of our available manufacturing and assembly methods.

First, we manufactured the laser-cut serpentine pattern with an in-house laser system that has significantly reduced capabilities compared to professional laser cutting machines. It has a fixed pulse width of approximately 100 ns and an estimated minimum cutting resolution of 0.1 mm, whereas high-end systems use lasers with femtosecond pulse widths and much smaller spot size (e.g., the femtosecond Optec Laser system used in [223] has a spot size of 6 μm). In addition, professional precision Nitinol laser cutting companies (such as the Pulse Systems, Inc. and other companies that produce Nitinol stents) have extensive trade secrets concerning the cutting pa-

rameters and the post-processing steps like electropolishing. In short, professionally laser cut Nitinol tubing has a much smoother surface finish with precise edges and cut lines. In comparison, our in-house prototypes have relatively rough edges, as seen in Figure 4.8. These edges are prone to catching and binding when laser-cut regions slide past each other. This limits the ability of the dexterous transition section to pass smoothly through the S-curve of the setup sheath, therefore limiting the deflection angle range and the ability to rotate or translate the dexterous sheath independently of the setup sheath. We will have future prototypes for user studies professionally laser cut; simultaneously, we can continue to improve our in-house methods and explore finishing processes such as Nitinol-specific electropolishing.

One approach for limiting the interaction between the outer surface of the dexterous transition section with the inner surface of the setup sheath would be to use the robotic transmission to translate the inner tube of the dexterous sheath rather than the outer tube. The downside of this approach is that fixing the inner tube's position makes it simpler to design the user interface to pass clinical tools through the sheath. If the inner tube translates and the outer tube is fixed, a linear bearing or other translating tool interface would have to be designed to accommodate clinical tools as the inner tube moves within the handle. Another approach would be the introduction of a heat-shrink PTFE layer on the outer tube of the dexterous sheath to create a smoother surface to interact with the setup sheath.

The second manufacturing and assembly challenge is the availability of exact tubing sizes for this application, as discussed previously in the chapter. Plastic transmission tubing for the inner tube of the dexterous sheath that would fit between the outer diameter of the inner Nitinol tube and the inner diameter of the outer transmission tube was unavailable, so we were forced to use a tube that fit inside the inner Nitinol tube rather than outside. Because we used this smaller tube, there was a large amount of clearance between the plastic transmission tubes of the dexterous sheath. As such,

the innermost plastic transmission tube can bow slightly when pushed (i.e., when the outer tube is translated backwards). This reduces the amount of translation that occurs at the distal end of the transmission tube where it is attached to the Nitinol tip. In the future, we can order custom plastic tubing with the exact needed dimensions to reduce the amount of clearance between the transmission tubes. In addition, we can explore the use of braid-reinforced tubing to improve the torsional and axial stiffness of the transmission tubing; different steel braiding patterns can significantly change this behavior. Increasing the torsional stiffness will improve the transparency of rotational movements in the handle to rotation of the dexterous sheath about the axis of the setup sheath tip. Increasing the axial stiffness will decrease actuator deadband, as well as reduce the required actuation travel for the robotic transmission. In addition to this material property improvements, it may be useful to model the deadband, friction, and compliance characteristics of the sheath and compensate for these issues in the control system design.

User Study with Control Gain Selection

We performed a user study with an experienced endoscopic surgeon to solicit feedback on the system architecture, workflow, and handle design. In addition, this user study tested the concept of using the control box to iteratively change the gain between the user interface input to dexterous sheath output deflection. For this study, a short dexterous sheath was constructed and positioned in front of a peg board with screws mounted at 10 mm spacing (Figure 4.35(a)). The user was instructed to test the dexterity of the sheath by aiming a clinical Nitinol basket at the screw heads on either side of the workspace (Figure 4.35(b)). For each control gain, the user examined the range of motion, the achievable deflection speed, and the ability to perform fine control of the basket position. We began with a control box gain of 0.5 and adjusted the gain in increments of 0.5 until the user was satisfied with the

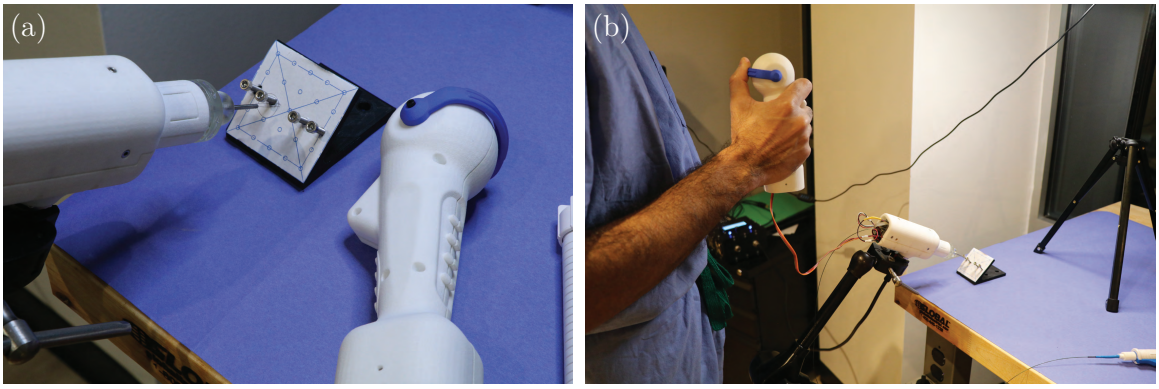

Figure 4.35: User study with control gain selection. An experienced endoscopic surgeon was instructed to test the range of motion, deflection speed, and fine motion control of the dexterous sheath by aiming a Nitinol basket at a pegboard simulating the workspace. The user selected the optimal control gain between the lever input and the output motion. (a) The experiment setup with mounted robotic transmission and pegboard with 10 mm spaced screws. (b) The surgeon completing the user study.

sheath's performance.

The initial gain setting of 0.5 was too low; the full input lever range of motion did not provide adequate sheath deflection to aim the basket across the whole workspace. In addition, the surgeon felt that small input motions for fine motion control did not appear to move the sheath. This could be due to mechanical slop in the lever mechanism and rotary potentiometer, or deadband in the actuator. As the control gain increased, the tip speed and responsiveness and range of motion improved. The surgeon was satisfied with the ability to quickly move across the workspace but also carefully and precisely aim the basket. At the highest control gains, fine motion control was inhibited by the sensitivity to the lever input position. It became challenging to precisely aim the basket. The user found that the preferred control box gain was 2.0. Future work for this system includes a comprehensive control gain study with multiple surgeons and user interface paradigms, but these initial results show promise for the experimental approach and modular user interface concept.

4.6 Future Work and Conclusions

In this chapter, we described the design of a bimanual dual-steerable sheath system for endoscopic submucosal dissection. The setup sheaths presented here are the first continuum manipulators to use contact-aided triangulation for a stiff, stable platform from which to deploy the dexterous sheaths and clinical tools towards the center of the workspace. This approach enables the system to be deployed through the working channels of standard clinical endoscopes rather than requiring a re-engineered robotic endoscope or large overtube structure. We contributed a serpentine laser cut pattern to create asymmetric bending with slots that close when the sheath reaches its triangulated pose. This work is the first example of an asymmetric serpentine pattern designed to shift the neutral axis of a flexible device.

The chapter derived the mathematical relationship between the serpentine pattern and the triangulated shape of the setup sheaths. We experimentally validated the kinematic behavior of both the setup and dexterous sheaths and characterized the blocking force of each manipulator, confirming that both the kinematic and mechanic behavior meets the endoscopic submucosal dissection design goals. Finally, we designed, built, and tested a user interface to manually actuate the setup sheath and robotically control the dexterous sheath.

The steerable sheath system described in this chapter has several interesting areas of future work in the fields of modeling and validation, design, manufacturing, and user testing. From a modeling perspective, further investigation is necessary for validating the serpentine pattern closure model. To do this, prototypes with serpentine patterns spanning the possible slot parameters (height, width, spacing, and overlapping length) would need to manufactured and tested. Not only would this process validate the accuracy of the kinematic model, but it would also further characterize the effects of slot parameters on the stiffness performance of the devices. It would be advantageous to out-source the manufacturing of these prototypes to carefully con-

trol the laser cutting dimensions and tolerances, as well as the surface finish. In the future, we can also explore the use of braid-reinforced plastic transmission tubing for enhanced stiffness properties. Braid-reinforced tubes can be designed with linearly varying stiffness properties to improve actuation performance.

It would also be useful to use finite element modeling to predict the behavior of both the serpentine patterned sections and the flexible transition sections of the sheaths, and compare these results to analytical models. Finite element methods would further our understanding of the mechanics characteristics of the sheaths. Models could also be derived for actuation compensation. By modeling the effects of axial and torsional stretching in the plastic transmission tubes and flexible transition sections of the dexterous sheath, as well as friction and mechanical slack throughout the system, we could compensate for these effects in the control scheme when using a robotic handle. Such analytical models, together with finite element models, could also provide better tools for understanding the effects of the serpentine pattern on the axial stiffness of slotted tubes and the resulting limitations on device stiffness.

From a user study perspective, the modular robotic handle makes it straightforward to explore preferred control gains and input methods. In addition, we could explore alternative (or augmented) methods for triangulating the sheaths. As discussed in Section 4.4.2, the proximal-first bending and resulting spatial trajectory of the setup sheath kinematics could be utilized to vary the triangulation angle during the procedure or to use the distal segment of the setup sheath itself to control the clinical tools in lieu of the distinct dexterous sheath. In contrast, the dexterous sheath could be designed with a serpentine pattern that varies from base to tip to give the sheath tip-first bending behavior. These system architecture decisions should be made after significant user testing and feedback.

In addition to the control gain user studies, experiments should be conducted with surgeons to evaluate the bimanual system in the context of endoscopic submucosal

dissection. This can include phantom studies, *ex vivo* porcine studies, and eventually *in vivo* porcine studies. These experiments will provide valuable information on the behavior of the sheaths and handles during operation, such as the setup sheath triangulation pose, dexterous sheath range of motion, and stiffness characteristics for both sheaths. These experiments will also provide feedback on the clinical workflow when using the steerable sheath system.

In summary, there are many interesting avenues to explore in order to design steerable sheaths that are effective dexterous tools for flexible endoscopy and to evaluate their performance. This system has the potential to bring tool triangulation and dexterity to standard clinical endoscopes and flexible tools so that complex natural orifice surgeries such as endoscopic submucosal dissection are easier to perform.

Chapter 5

Future Work and Conclusions

5.1 Future Work: Multi-Needle Robot for Incisionless Surgery

Chapter 2 described the concept, mechanics-based model, and estimation framework for a new type of multi-needle robot. This robot concept combines aspects of continuum, reconfigurable, and parallel robots for an incisionless approach to thoracic surgery. There are many opportunities for new research on multi-needle robots. One such area is a formal evaluation of teleoperation approaches for the multi-needle robot. Surgeon teleoperation could be combined with motion planning techniques developed by Kuntz et al. [130]. In conjunction with teleoperation, another important aspect of future work is system evaluation in more clinically realistic scenarios, such as phantom studies, and later *ex vivo* studies. These experiments will be critical for informing the design and workflow of the overall system so that the next generation of multi-needle robot prototypes can be designed, built, and tested. Much like the progression of other continuum robotic systems from benchtop prototypes to more clinically-ready devices, frequent evaluation and testing in different models will be critical.

From a robotics research perspective, there are many interesting topics that have been studied in other types of continuum robots that can be explored for multi-needle robots. For example, the elastic stability problems that have been addressed in concentric tube robots [58, 59] and parallel continuum robots [36] have also been observed in multi-needle robots and could be studied so that the behavior can be predicted. Early work on intrinsic force sensing was presented in Chapter 2; this behavior could be leveraged for hybrid force-motion controllers or compliant motion controllers, such as those developed for multi-backbone robots [31, 178]. Further research is required for improving the accuracy of force sensing using multi-needle robots. Finally, the

unique reconfiguration ability of multi-needle robots could be analyzed in order to explore possible configurations for the needles, how reconfiguration affects robot behavior, and how motion planning can be used to decide if and when to reconfigure the needles.

5.2 Future Work: Redundancy Resolution for Concentric Tube Robots

In Chapter 3, we designed and experimentally validated a redundancy resolution algorithm for concentric tube robots to avoid elastic instability and tune stiffness. One avenue of future work related to the studies presented in this chapter would be user studies with a tunable stiffness controller. In our stiffness experiments, we regulated the tip position and evaluated tip stiffness, but we did not evaluate the algorithm's performance during teleoperation or surgical tasks. It would be interesting to give surgeon users the ability to tune their manipulator's tip stiffness while they are asked to perform different types of tasks, as it may impact their performance depending on the stiffness requirements of the task. Similarly, it would be interesting to implement the instability avoidance controller during a clinically relevant phantom, animal, or cadaver study. This would enable us to test its performance in unknown environments.

Redundancy resolution for concentric tube robots in general is an area primed for future work. Many research prototypes have been developed for different clinical applications, which may prompt the need for different secondary control goals to integrate into the framework presented in Chapter 3. Such goals could include maximizing end effector manipulability or minimizing visual occlusion from the manipulator(s).

Instability avoidance redundancy resolution enables concentric tube robots to be designed with higher curvature tubes. This may make it possible to design concentric tube robots for new surgical applications that require highly curved tubes to maneuver in tight spaces. Future work could therefore include exploring new procedures for these robotic systems.

5.3 Future Work: Bimanual Steerable Sheath System with Triangulation

In Chapter 4, we designed a bimanual steerable sheath system for flexible endoscopy that uses self-contact segments to create a stable triangulated platform for instrument dexterity. The primary contributions of this chapter were the use of a serpentine pattern for asymmetric tube stiffness and slot closure, as well as the use of slot closure for stiff triangulation from flexible devices.

The first step of future work following this dissertation will be to experimentally evaluate the performance of the system for endoscopic submucosal dissection in a colonoscope phantom or animal model. In the future, rigorous experimental testing of the sheath and handle should be conducted for different endoscopic surgical tasks and procedures to improve the ergonomics, clinical workflow, and sheath performance when interacting with tissue.

Other avenues of future work include alternative sheath triangulation designs and further validation of the serpentine pattern model derived in this chapter. For example, one could design the setup sheath to have a range of triangulation poses rather than a single pose. One could also experimentally validate the effect of slot dimensions on the kinematic and stiffness behavior of steerable sheaths and also use the model in optimization schemes to design sheaths with desired bending shapes but high stiffness.

Another interesting area of future work for steerable sheaths is a rigorous evaluation of different handle control schemes and user interfaces. In particular, it will be useful to test the number of degrees of freedom given to the surgeon, as there may be a tradeoff between the extra dexterity or workspace provided by more degrees of freedom versus the complexity and mental mapping required when there are more joint to control. Ideally, the user interface will provide intuitive control of the tip of each manipulator without mentally taxing the user. Accomplishing such a control paradigm will require extensive testing of different control methods.

5.4 Conclusions

This dissertation has described the development of design, control, and sensing methods for surgical continuum robots that utilize mathematical models describing the kinematics and mechanics of the robot structures. Through these methods, the compliance characteristics of continuum robots can be better understood, designed, and controlled during surgery.

In Chapter 2, we developed a model and estimation framework for a new multi-needle robot that combines aspects of continuum, parallel, and reconfigurable robotics. The model was experimentally evaluated to demonstrate its accuracy in describing the shape of the flexible needle structure. We also demonstrated that integrating sensors into the robot with a statistical estimation framework can improve the shape estimation of the model even when subjected to unknown applied loads. We also showed that other parameters can be incorporated into the estimation framework; this approach was used to estimate the magnitude of applied loads. This aspect of the work is the first step towards intrinsic force sensing for multi-needle robots.

Chapter 3 contributed a redundancy resolution algorithm for concentric tube robots that uses weighted damped least squares to incorporate instability avoidance and stiffness tuning goals. The algorithm is straightforward to implement using resolved rates and has a low computational burden. We demonstrated the performance of instability avoidance control on a physical robot prototype, successfully controlling potentially unstable robots during teleoperation and trajectory-following without any uncontrolled snapping. This approach has the potential to broaden the design space of concentric tube robots to include more highly curved tubes. Stiffness tuning capabilities of this algorithm were also shown in simulations and physical experiments.

Chapter 4 presented a new design method for steerable sheath continuum robots that leverages self-contact in serpentine patterned tubes to achieve instrument triangulation. A steerable sheath system was design for endoscopic submucosal dissection

that uses a setup sheath as a stiff, triangulated deployment platform for an independently controlled dexterous sheath. The kinematic and stiffness properties of the two sheaths were experimentally validated as sufficient for the desired surgical tasks. In addition, a robotic handle was designed that enables triangulation set-up and then independent control of standard clinical instruments via the dexterous sheath.

In summary, the work in this dissertation seeks to advance the capabilities of surgical continuum robots through model-based design and control. A major goal of these design and control challenges is to characterize and specify compliance properties of the devices so that they are effective tools during surgery. As surgeons seek to make surgery less invasive, they need better minimally invasive tools to carry out surgical tasks in confined spaces and through small ports in the body. Success of these procedures depends on surgical tools that are dexterous and can fit through curved passageways in the body, but can also interact with tissue to accomplish surgical tasks. The continuum robots, design approaches, mathematical models, and control methods presented here are a step toward making such surgical instruments a reality in future operating rooms.

BIBLIOGRAPHY

[1] SPORT Surgical System. https://titanmedicalinc.com/technology/. Accessed: 2019-10-22.

[2] Flex Robotic System and Flex Colorectal Drive. https://www.sages.org/publications/tavac/flex-robotic-system-and-flex-colorectal-drive/. Accessed: 2019-10-22.

[3] Auris Indications for Use. https://www.aurishealth.com/#/indications-for-use. Accessed: 2019-10-22.

[4] D. C. Rucker and R. J. Webster III. Statics and dynamics of continuum robots with general tendon routing and external loading. *IEEE Transactions on Robotics*, 27(6):1033–1044, 2011.

[5] H. B. Gilbert, J. Neimat, and R. J. Webster III. Concentric tube robots as steerable needles: Achieving follow-the-leader deployment. *IEEE Transactions on Robotics*, 31(2):246–258, 2015.

[6] J. Till, C. E. Bryson, S. Chung, A. Orekhov, and D. C. Rucker. Efficient computation of multiple coupled cosserat rod models for real-time simulation and control of parallel continuum manipulators. In *2015 IEEE International Conference on Robotics and Automation (ICRA)*, pages 5067–5074. IEEE, 2015.

[7] J. Ding, R. E. Goldman, K. Xu, P. K. Allen, D. L. Fowler, and N. Simaan. Design and coordination kinematics of an insertable robotic effectors platform for single-port access surgery. *IEEE/ASME Transactions on Mechatronics*, 18(5):1612–1624, 2012.

[8] C. Ryu and Y. Chen. Endoscopic therapy for gastric neoplasms. In *Clinical Gastrointestinal Endoscopy*, pages 425–447. Saunders Elsevier, St Louis (MO), 2012.

[9] Colon Cancer Laparoscopic or Open Resection Study Group and others. Laparoscopic surgery versus open surgery for colon cancer: short-term outcomes of a randomised trial. *The Lancet Oncology*, 6(7):477–484, 2005.

[10] M. Reza, J. Blasco, E. Andradas, R. Cantero, and J. Mayol. Systematic review of laparoscopic versus open surgery for colorectal cancer. *British Journal of Surgery: Incorporating European Journal of Surgery and Swiss Surgery*, 93(8):921–928, 2006.

[11] U. Guller, S. Hervey, H. Purves, L. H. Muhlbaier, E. D. Peterson, S. Eubanks, and R. Pietrobon. Laparoscopic versus open appendectomy: outcomes comparison based on a large administrative database. *Annals of Surgery*, 239(1):43, 2004.

[12] V. Vitiello, S.-L. Lee, T. P. Cundy, and G.-Z. Yang. Emerging robotic platforms for minimally invasive surgery. *IEEE Reviews in Biomedical Engineering*, 6:111–126, 2012.

[13] A. R. Lanfranco, A. E. Castellanos, J. P. Desai, and W. C. Meyers. Robotic surgery: a current perspective. *Annals of Surgery*, 239(1):14, 2004.

[14] Intuitive for Patients. `https://www.intuitive.com/en-us/patients/patients`. Accessed: 2019-10-14.

[15] J. Burgner-Kahrs, D. C. Rucker, and H. Choset. Continuum robots for medical applications: A survey. *IEEE Transactions on Robotics*, 31(6):1261–1280, 2015.

[16] Johnson & Johnson Announces Completion of Acquisition of Auris Health, Inc. `https://www.jnj.com/johnson-johnson-announces-completion-of-acquisition-of-auris-health-inc`. Accessed: 2019-10-22.

[17] J. H. Kaouk, G.-P. Haber, R. Autorino, S. Crouzet, A. Ouzzane, V. Flamand, and A. Villers. A novel robotic system for single-port urologic surgery: first clinical investigation. *European Urology*, 66(6):1033–1043, 2014.

[18] M. Remacle, V. Prasad, G. Lawson, L. Plisson, V. Bachy, and S. Van der Vorst. Transoral robotic surgery (TORS) with the Medrobotics Flex™ System: first surgical application on humans. *European Archives of Oto-Rhino-Laryngology*, 272(6):1451–1455, 2015.

[19] B. Seeliger, M. Diana, J. P. Ruurda, K. M. Konstantinidis, J. Marescaux, and L. L. Swanström. Enabling single-site laparoscopy: the SPORT platform. *Surgical Endoscopy*, pages 1–8, 2019.

[20] Titan Medical Inc. Announces Research Agreement with ARMA Lab at Vanderbilt University. `https://titanmedicalinc.com/titan-medical-inc-announces-research-agreement-with-arma-lab-at-vanderbilt-university/`. Accessed: 2019-10-20.

[21] D. Camarillo, C. Milne, C. Carlson, M. Zinn, and J. Salisbury. Mechanics modeling of tendon-driven continuum manipulators. *IEEE Transactions on Robotics*, 24(6):1262–1273, 2008.

[22] T. Liu, N. L. Poirot, D. Franson, N. Seiberlich, M. A. Griswold, and M. C. Çavuşoğlu. Modeling and validation of the three-dimensional deflection of an

MRI-compatible magnetically actuated steerable catheter. *IEEE Transactions on Biomedical Engineering*, 63(10):2142–2154, 2015.

[23] L. B. Kratchman, T. L. Bruns, J. J. Abbott, and R. J. Webster III. Guiding elastic rods with a robot-manipulated magnet for medical applications. *IEEE Transactions on Robotics*, 33(1):227–233, 2016.

[24] J. H. Crews and G. D. Buckner. Design optimization of a shape memory alloy–actuated robotic catheter. *Journal of Intelligent Material Systems and Structures*, 23(5):545–562, 2012.

[25] G. Chen, M. T. Pham, and T. Redarce. Sensor-based guidance control of a continuum robot for a semi-autonomous colonoscopy. *Robotics and Autonomous Systems*, 57(6-7):712–722, 2009.

[26] R. J. Webster III, A. M. Okamura, and N. J. Cowan. Toward active cannulas: Miniature snake-like surgical robots. In *2006 IEEE/RSJ International Conference on Intelligent Robots and Systems*, pages 2857–2863. IEEE, 2006.

[27] P. Sears and P. Dupont. A steerable needle technology using curved concentric tubes. In *2006 IEEE/RSJ International Conference on Intelligent Robots and Systems*, pages 2850–2856. IEEE, 2006.

[28] N. Simaan, R. Taylor, and P. Flint. A dexterous system for laryngeal surgery. In *2004 IEEE International Conference on Robotics and Automation*, volume 1, pages 351–357. IEEE, 2004.

[29] N. Simaan. Snake-like units using flexible backbones and actuation redundancy for enhanced miniaturization. In *2005 IEEE International Conference on Robotics and Automation*, pages 3012–3017. IEEE, 2005.

[30] K. Xu and N. Simaan. An investigation of the intrinsic force sensing capabilities of continuum robots. *IEEE Transactions on Robotics*, 24(3):576–587, June 2008.

[31] A. Bajo and N. Simaan. Hybrid motion/force control of multi-backbone continuum robots. *The International Journal of Robotics Research*, 35(4):422–434, 2016.

[32] C. E. Bryson and D. C. Rucker. Toward parallel continuum manipulators. In *2014 IEEE International Conference on Robotics and Automation (ICRA)*, pages 778–785. IEEE, 2014.

[33] J.-P. Merlet. *Parallel robots*, volume 128. Springer Science & Business Media, 2005.

[34] A. L. Orekhov, C. B. Black, J. Till, S. Chung, and D. C. Rucker. Analysis and validation of a teleoperated surgical parallel continuum manipulator. *IEEE Robotics and Automation Letters*, 1(2):828–835, July 2016.

[35] A. L. Orekhov, V. A. Aloi, and D. C. Rucker. Modeling parallel continuum robots with general intermediate constraints. In *2017 IEEE International Conference on Robotics and Automation (ICRA)*, pages 6142–6149, May 2017.

[36] J. Till and D. C. Rucker. Elastic stability of cosserat rods and parallel continuum robots. *IEEE Transactions on Robotics*, 33(3):718–733, 2017.

[37] C. B. Black, J. Till, and D. C. Rucker. Parallel continuum robots: Modeling, analysis, and actuation-based force sensing. *IEEE Transactions on Robotics*, 34(1):29–47, Feb 2018.

[38] V. Aloi, C. Black, and C. Rucker. Stiffness control of parallel continuum robots. In *ASME 2018 Dynamic Systems and Control Conference*. American Society of Mechanical Engineers Digital Collection, 2018.

[39] D. C. Rucker, B. A. Jones, and R. J. Webster III. A geometrically exact model for externally loaded concentric-tube continuum robots. *IEEE Transactions on Robotics*, 26(5):769–780, 2010.

[40] P. E. Dupont, J. Lock, B. Itkowitz, and E. Butler. Design and control of concentric-tube robots. *IEEE Transactions on Robotics*, 26(2):209–225, 2010.

[41] J. Burgner, D. C. Rucker, H. B. Gilbert, P. J. Swaney, P. T. Russell, K. D. Weaver, and R. J. Webster III. A telerobotic system for transnasal surgery. *IEEE/ASME Transactions on Mechatronics*, 19(3):996–1006, 2014.

[42] C. Bergeles, A. Gosline, N. V. Vasilyev, P. J. Codd, P. J. del Nido, and P. E. Dupont. Concentric tube robot design and optimization based on task and anatomical constraints. *IEEE Transactions on Robotics*, 31(1):67–84, Feb 2015.

[43] J. Burgner, H. B. Gilbert, and R. J. Webster III. On the computational design of concentric tube robots: Incorporating volume-based objectives. In *2013 IEEE International Conference on Robotics and Automation*, pages 1193–1198. IEEE, 2013.

[44] R. J. Hendrick, C. R. Mitchell, S. D. Herrell, and R. J. Webster III. Hand-held transendoscopic robotic manipulators: A transurethral laser prostate surgery case study. *The International Journal of Robotics Research*, 34(13):1559–1572, 2015.

[45] L. G. Torres, R. J. Webster III, and R. Alterovitz. Task-oriented design of concentric tube robots using mechanics-based models. In *2012 IEEE/RSJ International Conference on Intelligent Robots and Systems*, pages 4449–4455. IEEE, 2012.

[46] E. J. Butler, R. Hammond-Oakley, S. Chawarski, A. H. Gosline, P. Codd, T. Anor, J. R. Madsen, P. E. Dupont, and J. Lock. Robotic neuro-emdoscope

with concentric tube augmentation. In *2012 IEEE/RSJ International Conference on Intelligent Robots and Systems*, pages 2941–2946. IEEE, 2012.

[47] I. S. Godage, A. A. Remirez, R. Wirz, K. D. Weaver, J. Burgner-Kahrs, and R. J. Webster III. Robotic intracerebral hemorrhage evacuation: An in-scanner approach with concentric tube robots. In *2015 IEEE/RSJ International Conference on Intelligent Robots and Systems (IROS)*, pages 1447–1452, Sep. 2015.

[48] N. V. Vasilyev, A. H. Gosline, A. Veeramani, M. T. Wu, G. P. Schmitz, R. T. Chen, V. Arabagi, P. J. Del Nido, and P. E. Dupont. Tissue removal inside the beating heart using a robotically delivered metal mems tool. *The International Journal of Robotics Research*, 34(2):236–247, 2015.

[49] H. B. Gilbert, D. C. Rucker, and R. J. Webster III. Concentric tube robots: The state of the art and future directions. In *Robotics Research*, pages 253–269. Springer, 2016.

[50] P. A. York, P. J. Swaney, H. B. Gilbert, and R. J. Webster III. A wrist for needle-sized surgical robots. In *2015 IEEE International Conference on Robotics and Automation (ICRA)*, pages 1776–1781. IEEE, 2015.

[51] P. J. Swaney, P. A. York, H. B. Gilbert, J. Burgner-Kahrs, and R. J. Webster III. Design, fabrication, and testing of a needle-sized wrist for surgical instruments. *Journal of Medical Devices*, 11(1):014501, 2017.

[52] K. Oliver-Butler, Z. H. Epps, and D. C. Rucker. Concentric agonist-antagonist robots for minimally invasive surgeries. In *Medical Imaging 2017: Image-Guided Procedures, Robotic Interventions, and Modeling*, volume 10135, page 1013511. International Society for Optics and Photonics, 2017.

[53] M. Rox and K. Riojas. Luminal robots small enough to fit through endoscope ports: Initial tumor resection experiments in the airways. In *Hamlyn Symposium on Medical Robotics*, 2018.

[54] R. J. Webster III and B. A. Jones. Design and kinematic modeling of constant curvature continuum robots: A review. *The International Journal of Robotics Research*, 29(13):1661–1683, 2010.

[55] R. J. Webster, III, J. M. Romano, and N. J. Cowan. Mechanics of precurved-tube continuum robots. *IEEE Transactions on Robotics*, 25(1):67–78, Feb 2009.

[56] D. C. Rucker, R. J. Webster III, G. S. Chirikjian, and N. J. Cowan. Equilibrium conformations of concentric-tube continuum robots. *The International Journal of Robotics Research*, 29(10):1263–1280, 2010.

[57] S. S. Antman. Nonlinear plasticity. In *Nonlinear Problems of Elasticity*, pages 603–628. Springer, 1995.

[58] H. B. Gilbert, R. J. Hendrick, and R. J. Webster III. Elastic stability of concentric tube robots: A stability measure and design test. *IEEE Transactions on Robotics*, 32(1):20–35, 2016.

[59] J. Ha, F. C. Park, and P. E. Dupont. Elastic stability of concentric tube robots subject to external loads. *IEEE Transactions on Biomedical Engineering*, 63(6):1116–1128, 2016.

[60] S. Song, Z. Li, H. Yu, and H. Ren. Electromagnetic positioning for tip tracking and shape sensing of flexible robots. *IEEE Sensors Journal*, 15(8):4565–4575, 2015.

[61] K. Wu, L. Wu, and H. Ren. An image based targeting method to guide a tentacle-like curvilinear concentric tube robot. In *2014 IEEE International Conference on Robotics and Biomimetics (ROBIO)*, pages 386–391, Dec 2014.

[62] S. C. Ryu and P. E. Dupont. FBG-based shape sensing tubes for continuum robots. In *2014 IEEE International Conference on Robotics and Automation (ICRA)*, pages 3531–3537. IEEE, 2014.

[63] R. J. Roesthuis, M. Kemp, J. J. van den Dobbelsteen, and S. Misra. Three-dimensional needle shape reconstruction using an array of fiber bragg grating sensors. *IEEE/ASME Transactions on Mechatronics*, 19(4):1115–1126, 2014.

[64] H. Ren and P. E. Dupont. Tubular enhanced geodesic active contours for continuum robot detection using 3d ultrasound. In *2012 IEEE International Conference on Robotics and Automation*, pages 2907–2912. IEEE, 2012.

[65] H. Su, D. C. Cardona, S. Weijian, A. Camilo, G. A. Cole, D. C. Rucker, R. J. Webster III, and G. S. Fischer. A MRI-guided concentric tube continuum robot with piezoelectric actuation: A feasibility study. In *2012 IEEE International Conference on Robotics and Automation*, pages 1939–1945, 2012.

[66] E. J. Lobaton, J. Fu, L. G. Torres, and R. Alterovitz. Continuous shape estimation of continuum robots using x-ray images. In *2013 IEEE International Conference on Robotics and Automation*, pages 725–732. IEEE, 2013.

[67] R. A. Lathrop, D. C. Rucker, and R. J. W. III. Guidance of a steerable cannula robot in soft tissue using preoperative imaging and conoscopic surface contour sensing. In *2010 IEEE International Conference on Robotics and Automation (ICRA)*, pages 5601–5606, May 2010.

[68] A. B. Koolwal, F. Barbagli, C. Carlson, and D. Liang. An ultrasound-based localization algorithm for catheter ablation guidance in the left atrium. *The International Journal of Robotics Research*, 29(6):643–665, 2010.

[69] J. A. Borgstadt, M. R. Zinn, and N. J. Ferrier. Multi-modal localization algorithm for catheter interventions. In *2015 IEEE International Conference on Robotics and Automation (ICRA)*, pages 5350–5357. IEEE, 2015.

[70] S. Sanan, S. Tully, A. Bajo, N. Simaan, and H. Choset. Simultaneous compliance and registration estimation for robotic surgery. In *Robotics: Science and Systems*, 2014.

[71] M. Khoshnam, A. C. Skanes, and R. V. Patel. Modeling and estimation of tip contact force for steerable ablation catheters. *IEEE Transactions on Biomedical Engineering*, 62(5):1404–1415, 2015.

[72] D. C. Rucker and R. J. Webster III. Deflection-based force sensing for continuum robots: A probabilistic approach. In *2011 IEEE/RSJ International Conference on Intelligent Robots and Systems*, pages 3764–3769, 2011.

[73] A. W. Mahoney, T. L. Bruns, P. J. Swaney, and R. J. W. III. On the inseparable nature of sensor selection, sensor placement, and state estimation for continuum robots or "where to put your sensors and how to use them". In *2016 IEEE International Conference on Robotics and Automation (ICRA)*, pages 4472–4478, May 2016.

[74] K. Xu and N. Simaan. Intrinsic wrench estimation and its performance index for multisegment continuum robots. *IEEE Transactions on Robotics*, 26(3):555–561, 2010.

[75] D. E. Whitney. The mathematics of coordinated control of prosthetic arms and manipulators. *Journal of Dynamic Systems, Measurement, and Control*, 94(4):303–309, 1972.

[76] N. Simaan, K. Xu, W. Wei, A. Kapoor, P. Kazanzides, R. Taylor, and P. Flint. Design and integration of a telerobotic system for minimally invasive surgery of the throat. *The International Journal of Robotics Research*, 28(9):1134–1153, 2009.

[77] A. Bajo, R. E. Goldman, L. Wang, D. Fowler, and N. Simaan. Integration and preliminary evaluation of an insertable robotic effectors platform for single port access surgery. In *2012 IEEE International Conference on Robotics and Automation*, pages 3381–3387. IEEE, 2012.

[78] R. Xu, A. Asadian, A. S. Naidu, and R. V. Patel. Position control of concentric-tube continuum robots using a modified jacobian-based approach. In *2013 IEEE International Conference on Robotics and Automation*, pages 5813–5818. IEEE, 2013.

[79] C. Abah, A. L. Orekhov, and N. Simaan. Design considerations and redundancy resolution for variable geometry continuum robots. In *2018 IEEE International Conference on Robotics and Automation (ICRA)*, pages 767–774. IEEE, 2018.

[80] N. Sarli and N. Simaan. Minimal visual occlusion redundancy resolution of continuum robots in confined spaces. In *2017 IEEE/RSJ International Conference on Intelligent Robots and Systems (IROS)*, pages 6448–6454. IEEE, 2017.

[81] G. S. Chirikjian and J. W. Burdick. A modal approach to hyper-redundant manipulator kinematics. *IEEE Transactions on Robotics and Automation*, 10(3):343–354, 1994.

[82] G. S. Chirikjian and J. W. Burdick. The kinematics of hyper-redundant robot locomotion. *IEEE Transactions on Robotics and Automation*, 11(6):781–793, 1995.

[83] M. C. Yip and D. B. Camarillo. Model-less feedback control of continuum manipulators in constrained environments. *IEEE Transactions on Robotics*, 30(4):880–889, 2014.

[84] P. Berthet-Rayne, K. Leibrandt, G. Gras, P. Fraisse, A. Crosnier, and G.-Z. Yang. Inverse kinematics control methods for redundant snake-like robot teleoperation during minimally invasive surgery. *IEEE Robotics and Automation Letters*, 2018.

[85] J. Edelmann, A. J. Petruska, and B. J. Nelson. Magnetic control of continuum devices. *The International Journal of Robotics Research*, 36(1):68–85, 2017.

[86] K. Leibrandt, C. Bergeles, and G.-Z. Yang. Implicit active constraints for concentric tube robots based on analysis of the safe and dexterous workspace. In *2017 IEEE/RSJ International Conference on Intelligent Robots and Systems (IROS)*, pages 193–200. IEEE, 2017.

[87] M. Khadem, J. O'Neill, Z. Mitros, L. da Cruz, and C. Bergeles. Autonomous steering of concentric tube robots for enhanced force/velocity manipulability. In *2019 IEEE/RSJ International Conference on Intelligent Robots and Systems (IROS)*, pages 2197–2204, 2019.

[88] X. Wang and M. Q.-H. Meng. Robotics for natural orifice transluminal endoscopic surgery: a review. *Journal of Robotics*, 2012.

[89] T. Oyama. Counter traction makes endoscopic submucosal dissection easier. *Clinical Endoscopy*, 45(4):375, 2012.

[90] E. Zizer, D. Roppenecker, F. Helmes, S. Hafner, Y. Krieger, T. Lüth, and A. Meining. A new 3d-printed overtube system for endoscopic submucosal dissection: first results of a randomized study in a porcine model. *Endoscopy*, 48(08):762–765, 2016.

[91] J. B. Gafford. *Modular Robotic Systems for Interventional Endoscopy*. Ph.D. dissertation, Harvard University, 2018.

[92] N. Patel, C. Seneci, G.-Z. Yang, A. Darzi, and J. Teare. Flexible platforms for natural orifice transluminal and endoluminal surgery. *Endoscopy International Open*, 2(02):E117–E123, 2014.

[93] S. V. Kantsevoy and P. J. Thuluvath. Successful closure of a chronic refractory gastrocutaneous fistula with a new endoscopic suturing device (with video). *Gastrointestinal Endoscopy*, 75(3):688–690, 2012.

[94] J. Gafford, T. Ranzani, S. Russo, H. Aihara, C. Thompson, R. Wood, and C. Walsh. Snap-on robotic wrist module for enhanced dexterity in endoscopic surgery. In *2016 IEEE International Conference on Robotics and Automation (ICRA)*, pages 4398–4405. IEEE, 2016.

[95] A. De Donno, L. Zorn, P. Zanne, F. Nageotte, and M. de Mathelin. Introducing stras: A new flexible robotic system for minimally invasive surgery. In *2013 IEEE International Conference on Robotics and Automation*, pages 1213–1220. IEEE, 2013.

[96] L. Zorn, F. Nageotte, P. Zanne, A. Legner, B. Dallemagne, J. Marescaux, and M. de Mathelin. A novel telemanipulated robotic assistant for surgical endoscopy: Preclinical application to ESD. *IEEE Transactions on Biomedical Engineering*, 65(4):797–808, 2017.

[97] C. C. Thompson, M. Ryou, N. J. Soper, E. S. Hungess, R. I. Rothstein, and L. L. Swanstrom. Evaluation of a manually driven, multitasking platform for complex endoluminal and natural orifice transluminal endoscopic surgery applications (with video). *Gastrointestinal Endoscopy*, 70(1):121–125, 2009.

[98] Y. Okamoto, R. Nakadate, S. Nakamura, J. Arata, S. Oguri, T. Moriyama, M. Esaki, T. Iwasa, K. Ohuchida, T. Akahoshi, et al. Colorectal endoscopic submucosal dissection using novel articulating devices: a comparative study in a live porcine model. *Surgical Endoscopy*, 33(2):651–657, 2019.

[99] G. P. Mylonas, V. Vitiello, T. P. Cundy, A. Darzi, and G.-Z. Yang. CYCLOPS: A versatile robotic tool for bimanual single-access and natural-orifice endoscopic surgery. In *2014 IEEE International Conference on Robotics and Automation (ICRA)*, pages 2436–2442. IEEE, 2014.

[100] T. J. O. Vrielink, M. Zhao, A. Darzi, and G. P. Mylonas. ESD CYCLOPS: A new robotic surgical system for GI surgery. In *2018 IEEE International Conference on Robotics and Automation (ICRA)*, pages 150–157. IEEE, 2018.

[101] S. Phee, A. Kencana, V. Huynh, Z. Sun, S. Low, K. Yang, D. Lomanto, and K. Ho. Design of a master and slave transluminal endoscopic robot for natural orifice transluminal endoscopic surgery. *Proceedings of the Institution of Mechanical Engineers, Part C: Journal of Mechanical Engineering Science*, 224(7):1495–1503, 2010.

[102] K.-Y. Ho, S. J. Phee, A. Shabbir, S. C. Low, V. A. Huynh, A. P. Kencana, K. Yang, D. Lomanto, B. Y. J. So, Y. J. Wong, et al. Endoscopic submucosal dissection of gastric lesions by using a master and slave transluminal endoscopic robot (MASTER). *Gastrointestinal Endoscopy*, 72(3):593–599, 2010.

[103] P. W. Chiu, S. J. Phee, P. Bhandari, K. Sumiyama, T. Ohya, J. Wong, C. C. Poon, H. Tajiri, K. Nakajima, and K. Y. Ho. Enhancing proficiency in performing endoscopic submucosal dissection (ESD) by using a prototype robotic endoscope. *Endoscopy international open*, 3(05):E439–E442, 2015.

[104] S. Can, C. Staub, A. Knoll, A. Fiolka, A. Schneider, and H. Feussner. Design, development and evaluation of a highly versatile robot platform for minimally invasive single-port surgery. In *2012 4th IEEE RAS & EMBS International Conference on Biomedical Robotics and Biomechatronics (BioRob)*, pages 817–822. IEEE, 2012.

[105] M. Piccigallo, U. Scarfogliero, C. Quaglia, G. Petroni, P. Valdastri, A. Menciassi, and P. Dario. Design of a novel bimanual robotic system for single-port laparoscopy. *IEEE/ASME Transactions On Mechatronics*, 15(6):871–878, 2010.

[106] D. J. Abbott, C. Becke, R. I. Rothstein, and W. J. Peine. Design of an endoluminal notes robotic system. In *2007 IEEE/RSJ International Conference on Intelligent Robots and Systems*, pages 410–416. IEEE, 2007.

[107] K. C. Lau, E. Y. Y. Leung, P. W. Y. Chiu, Y. Yam, J. Y. W. Lau, and C. C. Y. Poon. A flexible surgical robotic system for removal of early-stage gastrointestinal cancers by endoscopic submucosal dissection. *IEEE Transactions on Industrial Informatics*, 12(6):2365–2374, 2016.

[108] K. Xu, R. E. Goldman, J. Ding, P. K. Allen, D. L. Fowler, and N. Simaan. System design of an insertable robotic effector platform for single port access (SPA) surgery. In *2009 IEEE/RSJ International Conference on Intelligent Robots and Systems*, pages 5546–5552. IEEE, 2009.

[109] J. Ding, K. Xu, R. Goldman, P. Allen, D. Fowler, and N. Simaan. Design, simulation and evaluation of kinematic alternatives for insertable robotic effectors

platforms in single port access surgery. In *2010 IEEE International Conference on Robotics and Automation*, pages 1053–1058. IEEE, 2010.

[110] N. Simaan, A. Bajo, A. Reiter, L. Wang, P. Allen, and D. Fowler. Lessons learned using the insertable robotic effector platform (IREP) for single port access surgery. *Journal of Robotic Surgery*, 7(3):235–240, 2013.

[111] K. Xu, J. Zhao, and M. Fu. Development of the SJTU unfoldable robotic system (SURS) for single port laparoscopy. *IEEE/ASME Transactions on Mechatronics*, 20(5):2133–2145, 2014.

[112] J. Rosen, L. N. Sekhar, D. Glozman, M. Miyasaka, J. Dosher, B. Dellon, K. S. Moe, A. Kim, L. J. Kim, T. Lendvay, et al. Roboscope: A flexible and bendable surgical robot for single portal minimally invasive surgery. In *2017 IEEE International Conference on Robotics and Automation (ICRA)*, pages 2364–2370. IEEE, 2017.

[113] A. D. Pryor, J. R. Tushar, and L. R. DiBernardo. Single-port cholecystectomy with the TransEnterix SPIDER: simple and safe. *Surgical Endoscopy*, 24(4):917–923, 2010.

[114] A. Orekhov, C. Abah, and N. Simaan. Snake-like robots for minimally invasive, single-port, and intraluminal surgeries. In *The Encyclopedia of Medical Robotics*, pages 203–243. World Scientific, 2018.

[115] M. F. Rox, D. S. Ropella, R. Hendrick, E. Blum, R. P. Naftel, H. C. Bow, S. D. Herrell, K. D. Weaver, L. B. Chambless, and R. J. Webster III. Mechatronic design of a two-arm concentric tube robot system for rigid neuroendoscopy. *IEEE/ASME Transactions on Mechatronics*, 2020.

[116] J. B. Gafford, S. Webster, N. Dillon, E. Blum, R. Hendrick, F. Maldonado, E. A. Gillaspie, O. B. Rickman, S. D. Herrell, and R. J. Webster III. A concentric

tube robot system for rigid bronchoscopy: A feasibility study on central airway obstruction removal. *Annals of Biomedical Engineering*, pages 1–11, 2019.

[117] P. J. Swaney, A. W. Mahoney, A. Remirez, E. Lamers, B. Hartley, R. Feins, R. Alterovitz, and R. J. Webster III. Tendons, concentric tubes, and a bevel tip: Three steerable robots in one transoral lung access system. In *2015 IEEE International Conference on Robotics and Automation (ICRA)*, pages 5378–5383, 2015.

[118] R. Ponten, C. B. Black, A. J. Russ, and D. C. Rucker. Analysis of a concentric-tube robot design and feasibility for endoscopic deployment. In *Medical Imaging 2017: Image-Guided Procedures, Robotic Interventions, and Modeling*, volume 10135, page 1013514. International Society for Optics and Photonics, 2017.

[119] H. Yu, L. Wu, K. Wu, and H. Ren. Development of a multi-channel concentric tube robotic system with active vision for transnasal nasopharyngeal carcinoma procedures. *IEEE Robotics and Automation Letters*, 1(2):1172–1178, 2016.

[120] Z. Mitros, M. Khadem, C. Seneci, S. Ourselin, L. Da Cruz, and C. Bergeles. Towards modelling multi-arm robots: Eccentric arrangement of concentric tubes. In *2018 7th IEEE International Conference on Biomedical Robotics and Biomechatronics (BioRob)*, pages 43–48. IEEE, 2018.

[121] T. Vandebroek, M. Ourak, C. Gruijthuijsen, A. Javaux, J. Legrand, T. Vercauteren, S. Ourselin, J. Deprest, and E. Vander Poorten. Macro-micro multi-arm instrument for single-port access surgery. In *2019 IEEE/RSJ International Conference on Intelligent Robots and Systems*. IEEE, 2019.

[122] D. B. Roppenecker, A. Meining, G. Horst, H. Ulbrich, and T. C. Lueth. Interdisciplinary development of a single-port robot. In *2012 IEEE International Conference on Robotics and Biomimetics (ROBIO)*, pages 612–617. IEEE, 2012.

[123] D. B. Roppenecker, A. Pfaff, J. A. Coy, and T. C. Lueth. Multi arm snake-like robot kinematics. In *2013 IEEE/RSJ International Conference on Intelligent Robots and Systems*, pages 5040–5045. IEEE, 2013.

[124] M. F. Traeger, D. B. Roppenecker, M. R. Leininger, F. Schnoes, and T. C. Lueth. Design of a spine-inspired kinematic for the guidance of flexible instruments in minimally invasive surgery. In *2014 IEEE/RSJ International Conference on Intelligent Robots and Systems*, pages 1322–1327. IEEE, 2014.

[125] D. B. Roppenecker, L. Schuster, J. A. Coy, M. F. Traeger, K. Entsfellner, and T. C. Lueth. Modular body of the multi arm snake-like robot. In *2014 IEEE International Conference on Robotics and Biomimetics (ROBIO)*, pages 374–379. IEEE, 2014.

[126] Y. S. Krieger, D. B. Roppenecker, J.-U. Stolzenburg, and T. C. Lueth. First step towards an automated designed multi-arm snake-like robot for minimally invasive surgery. In *2016 6th IEEE International Conference on Biomedical Robotics and Biomechatronics (BioRob)*, pages 407–412. IEEE, 2016.

[127] Y. S. Krieger, D. B. Roppenecker, I. Kuru, and T. C. Lueth. Multi-arm snake-like robot. In *2017 IEEE International Conference on Robotics and Automation (ICRA)*, pages 2490–2495. IEEE, 2017.

[128] A. W. Mahoney, P. L. Anderson, P. J. Swaney, and R. J. W. III. Reconfigurable parallel continuum robots for incisionless surgery. In *2016 IEEE/RSJ International Conference on Intelligent Robots and Systems (IROS)*, pages 4330–4336, October 2016.

[129] P. L. Anderson, A. W. Mahoney, and R. J. Webster III. Continuum reconfigurable parallel robots for surgery: Shape sensing and state estimation with uncertainty. *IEEE Robotics and Automation Letters*, 2(3):1617–1624, 2017.

[130] A. Kuntz, A. W. Mahoney, N. E. Peckman, P. L. Anderson, F. Maldonado, R. J. Webster III, and R. Alterovitz. Motion planning for continuum reconfigurable incisionless surgical parallel robots. In *2017 IEEE/RSJ International Conference on Intelligent Robots and Systems (IROS)*, pages 6463–6469, Sep. 2017.

[131] A. Kuntz, C. Bowen, C. Baykal, A. W. Mahoney, P. L. Anderson, F. Maldonado, R. J. Webster III, and R. Alterovitz. Kinematic design optimization of a parallel surgical robot to maximize anatomical visibility via motion planning. In *2018 IEEE International Conference on Robotics and Automation (ICRA)*, pages 926–933, May 2018.

[132] A. W. Mahoney, P. L. Anderson, F. Maldonado, and R. J. W. I. III. More ports = less invasive? a multi-needle robot for lung ablation. In *Hamlyn Symposium on Medical Robotics*, page 35, 2017.

[133] P. L. Anderson, T. E. Ertop, A. Kuntz, F. Maldonado, R. Alterovitz, and R. J. Webster III. Sand blasting inside a patient: A crisp robot for spraying powder inside the chest cavity to preclude lung collapse. In *Hamlyn Symposium on Medical Robotics*, pages 123–124, 2018.

[134] G. Chirikjian. Conformational modeling of continuum structures in robotics and structural biology: A review. *Advanced Robotics*, 29(13):817–829, 2015.

[135] W. McMahan, V. Chitrakaran, M. Csencsits, D. Dawson, I. Walker, B. Jones, M. Pritts, D. Dienno, M. Grissom, and C. Rahn. Field trials and testing of the octarm continuum manipulator. In *2006 IEEE International Conference on Robotics and Automation*, pages 2336–2341, 2006.

[136] Z. Yang, X. Zhu, and K. Xu. Continuum delta robot: a novel translational parallel robot with continuum joints. In *2018 IEEE/ASME International Conference on Advanced Intelligent Mechatronics (AIM)*, pages 748–755. IEEE, 2018.

[137] C. Bedell, J. Lock, A. Gosline, and P. E. Dupont. Design optimization of concentric tube robots based on task and anatomical constraints. In *2011 IEEE International Conference on Robotics and Automation*, pages 398–403. IEEE, 2011.

[138] M. Yim, W.-M. Shen, B. Salemi, D. Rus, M. Moll, H. Lipson, E. Klavins, and G. Chirikjian. Modular self-reconfigurable robot systems [grand challenges of robotics]. *IEEE Robotics Automation Magazine*, 14(1):43–52, 2007.

[139] M. Yim, P. White, M. Park, and J. Sastra. Modular self-reconfigurable robots. In *Encyclopedia of Complexity and Systems Science*, pages 5618–5631. Springer New York, New York, NY, 2009.

[140] K. Harada, E. Susilo, A. Menciassi, and P. Dario. Wireless reconfigurable modules for robotic endoluminal surgery. In *2009 IEEE International Conference on Robotics and Automation*, pages 2699–2704. IEEE, 2009.

[141] F. Ghezzi, A. Cromi, G. Siesto, L. Boni, S. Uccella, V. Bergamini, and P. Bolis. Needlescopic hysterectomy: incorporation of 3-mm instruments in total laparoscopic hysterectomy. *Surgical Endoscopy*, 22(10):2153–2157, 2008.

[142] M. Furrer, R. Rechsteiner, V. Eigenmann, C. Signer, U. Althaus, and H. Ris. Thoracotomy and thoracoscopy: postoperative pulmonary function, pain and chest wall complaints. *European Journal of Cardio-thoracic Surgery: Official Journal of the European Association for Cardio-thoracic Surgery*, 12(1):82–87, 1997.

[143] P. C. Bertrand, J.-F. Regnard, L. Spaggiari, J.-F. Levi, P. Magdeleinat, L. Guibert, and P. Levasseur. Immediate and long-term results after surgical treatment of primary spontaneous pneumothorax by vats. *The Annals of Thoracic Surgery*, 61(6):1641–1645, 1996.

[144] R. J. Landreneau, M. J. Mack, S. R. Hazelrigg, K. Naunheim, R. D. Dowling, P. Ritter, M. J. Magee, S. Nunchuck, R. J. Keenan, and P. F. Ferson. Prevalence of chronic pain after pulmonary resection by thoracotomy or video-assisted thoracic surgery. *The Journal of Thoracic and Cardiovascular Surgery*, 107(4):1079–1086, 1994.

[145] S. T. Kwon, L. Zhao, R. M. Reddy, A. C. Chang, M. B. Orringer, C. M. Brummett, and J. Lin. Evaluation of acute and chronic pain outcomes after robotic, video-assisted thoracoscopic surgery, or open anatomic pulmonary resection. *The Journal of Thoracic and Cardiovascular Surgery*, 154(2):652–659, 2017.

[146] American Cancer Society. Cancer facts & figures 2010. Technical report, American Cancer Society, 2010.

[147] L. Solaini, F. Prusciano, P. Bagioni, F. Francesco, and D. B. Poddie. Video-assisted thoracic surgery (VATS) of the lung. *Surgical Endoscopy*, 22(2):298–310, 2007.

[148] R. W. Light. *Pleural diseases*. Lippincott Williams & Wilkins, 2007.

[149] T. R. Collins and S. A. Sahn. Thoracocentesis: clinical value, complications, technical problems, and patient experience. *Chest*, 91(6):817–822, 1987.

[150] C. M. McDonald, C. Pierre, M. de Perrot, G. Darling, M. Cypel, A. Pierre, T. Waddell, S. Keshavjee, K. Yasufuku, and K. Czarnecka-Kujawa. Efficacy and cost of awake thoracoscopy and video-assisted thoracoscopic surgery in the

undiagnosed pleural effusion. *The Annals of Thoracic Surgery*, 106(2):361 – 367, 2018.

[151] Z. S. DePew and F. Maldonado. The role of interventional therapy for pleural diseases. *Expert Review of Respiratory Medicine*, 8(4):465–477, 2014.

[152] R. Bhatnagar, B. C. Kahan, A. J. Morley, E. K. Keenan, R. F. Miller, N. M. Rahman, and N. A. Maskell. The efficacy of indwelling pleural catheter placement versus placement plus talc sclerosant in patients with malignant pleural effusions managed exclusively as outpatients (IPC-PLUS): study protocol for a randomised controlled trial. *Trials*, 16(1):48, 2015.

[153] C. Hooper, Y. G. Lee, and N. Maskell. Investigation of a unilateral pleural effusion in adults: British Thoracic Society pleural disease guideline 2010. *Thorax*, 65(Suppl 2):ii4–ii17, 2010.

[154] J. M. Porcel, A. Esquerda, M. Vives, and S. Bielsa. Etiology of pleural effusions: analysis of more than 3,000 consecutive thoracenteses. *Archivos de Bronconeumología (English Edition)*, 50(5):161–165, 2014.

[155] R. F. Casal, G. A. Eapen, R. C. Morice, and C. A. Jimenez. Medical thoracoscopy. *Current Opinion in Pulmonary Medicine*, 15(4):313–320, 2009.

[156] The International Early Lung Cancer Action Program Investigators. Survival of patients with Stage I lung cancer detected on CT screening. *The New England Journal of Medicine*, 355(17):1763–1771, October 2006.

[157] M. J. Horner, L. A. G. Ries, M. Krapcho, N. Neyman, R. Aminou, N. Howlader, S. F. Altekruse, E. J. Feuer, L. Huang, A. Mariotto, B. A. Miller, D. R. Lewis, M. P. Eisner, D. G. Stinchcomb, and B. K. Edwards. SEER Cancer Statistics Review, 1975-2006, National Cancer Institute. Bethesda, MD. Available: http://seer.cancer.gov/csr/, 2009.

[158] P. Chan, P. Clarke, F. J. Daniel, S. R. Knight, and S. Seevanayagam. Efficacy study of video-assisted thoracoscopic surgery pleurodesis for spontaneous pneumothorax. *The Annals of Thoracic Surgery*, 71(2):452–454, 2001.

[159] R. Bhatnagar, E. K. Keenan, A. J. Morley, B. C. Kahan, A. E. Stanton, M. Haris, R. N. Harrison, R. A. Mustafa, L. J. Bishop, L. Ahmed, A. West, J. Holme, M. Evison, M. Munavvar, P. Sivasothy, J. Herre, D. Cooper, M. Roberts, A. Guhan, C. Hooper, J. Walters, T. S. Saba, B. Chakrabarti, S. Gunatilake, I. Psallidas, S. P. Walker, A. C. Bibby, S. Smith, L. J. Stadon, N. J. Zahan-Evans, Y. G. Lee, J. E. Harvey, N. M. Rahman, R. F. Miller, and N. A. Maskell. Outpatient talc administration by indwelling pleural catheter for malignant effusion. *New England Journal of Medicine*, 378(14):1313–1322, 2018.

[160] V. Steger, U. Mika, H. Toomes, T. Walker, C. Engel, T. Kyriss, G. Ziemer, and G. Friedel. Who gains most? A 10-year experience with 611 thoracoscopic talc pleurodeses. *The Annals of Thoracic Surgery*, 83(6):1940–1945, 2007.

[161] G. Massard, P. Thomas, and J.-M. Wihlm. Minimally invasive management for first and recurrent pneumothorax. *The Annals of Thoracic Surgery*, 66(2):592–599, 1998.

[162] J.-R. Viallat, F. Rey, P. Astoul, and C. Boutin. Thoracoscopic talc poudrage pleurodesis for malignant effusions: a review of 360 cases. *Chest*, 110(6):1387–1393, 1996.

[163] S. Kolschmann, A. Ballin, and A. Gillissen. Clinical efficacy and safety of thoracoscopic talc pleurodesis in malignant pleural effusions. *Chest*, 128(3):1431–1435, 2005.

[164] J. F. Montes, J. Ferrer, M. A. Villarino, B. Baeza, M. Crespo, and J. García-Valero. Influence of talc dose on extrapleural talc dissemination after talc pleurodesis. *American Journal of Respiratory and Critical Care Medicine*, 168(3):348–355, 2003.

[165] M. Gagner and A. Garcia-Ruiz. Technical aspects of minimally invasive abdominal surgery performed with needlescopic instruments. *Surgical Laparoscopy Endoscopy & Percutaneous Techniques*, 8(3):171–179, 1998.

[166] D. M. Krpata and T. A. Ponsky. Needlescopic surgery: what's in the toolbox? *Surgical Endoscopy*, 27(3):1040–1044, 2013.

[167] J. Deprest, J. Jani, L. Lewi, N. Ochsenbein-Kölble, M. Cannie, E. Doné, X. Roubliova, T. Van Mieghem, A. Debeer, F. Debuck, et al. Fetoscopic surgery: encouraged by clinical experience and boosted by instrument innovation. *Seminars in Fetal and Neonatal Medicine*, 11(6):398–412, 2006.

[168] A. G. Coran, A. A. Caldamone, N. S. Adzick, T. M. Krummel, J.-M. Laberge, and R. Shamberger. *Pediatric Surgery*. Elsevier, Philadelphia, PA, 7 edition, 2012.

[169] R. Taylor, J. Funda, B. Eldridge, S. Gomory, K. Gruben, D. LaRose, M. Talamini, L. Kavoussi, and J. Anderson. A telerobotic assistant for laparoscopic surgery. *Engineering in Medicine and Biology Magazine, IEEE*, 14(3):279–288, 1995.

[170] T. Bretl and Z. McCarthy. Quasi-static manipulation of a Kirchhoff elastic rod based on a geometric analysis of equilibrium configurations. *The International Journal of Robotics Research*, 33(1):48–68, 2014.

[171] D. C. Rucker and R. J. Webster III. Computing jacobians and compliance matrices for externally loaded continuum robots. In *2011 IEEE International Conference on Robotics and Automation*, pages 945–950. IEEE, 2011.

[172] R. M. Murray, Z. Li, and S. S. Sastry. *A Mathematical Introduction to Rootic Manipulation*. CRC Press, 1994.

[173] J. Peirs, J. Clijnen, D. Reynaerts, H. Van Brussel, P. Herijgers, B. Corteville, and S. Boone. A micro optical force sensor for force feedback during minimally invasive robotic surgery. *Sensors and Actuators A: Physical*, 115(2-3):447–455, 2004.

[174] L. Dorst. First order error propagation of the procrustes method for 3d attitude estimation. *IEEE Transactions on Pattern Analysis and Machine Intelligence*, 27(2):221–229, 2005.

[175] W. Wei and N. Simaan. Modeling, force sensing, and control of flexible cannulas for microstent delivery. *Journal of Dynamic Systems, Measurement, and Control*, 134(4):041004, 2012.

[176] M. Mahvash and P. E. Dupont. Stiffness control of surgical continuum manipulators. *IEEE Transactions on Robotics*, 27(2):334–345, 2011.

[177] H. B. Gilbert. *Concentric Tube Robots: Design, Deployment, and Stability*. Ph.D. dissertation, Vanderbilt University, Nashville, TN, 2016.

[178] R. Goldman, A. Bajo, and N. Simaan. Compliant motion control for multisegment continuum robots with actuation force sensing. *IEEE Transactions on Robotics*, 30(4):890–902, Aug 2014.

[179] C. Bergeles and P. E. Dupont. Planning stable paths for concentric tube robots. In *Intelligent Robots and Systems (IROS), 2013 IEEE/RSJ International Conference on*, pages 3077–3082. IEEE, 2013.

[180] J. Ha, F. C. Park, and P. E. Dupont. Achieving elastic stability of concentric tube robots through optimization of tube precurvature. In *2014 IEEE/RSJ International Conference on Intelligent Robots and Systems*, pages 864–870. IEEE, 2014.

[181] R. J. Hendrick, H. B. Gilbert, and R. J. Webster III. Designing snap-free concentric tube robots: A local bifurcation approach. In *2015 IEEE International Conference on Robotics and Automation (ICRA)*, pages 2256–2263. IEEE, 2015.

[182] P. L. Anderson, R. J. Hendrick, and R. J. Webster III. Real-time redundancy resolution for concentric tube robots to avoid elastic instability. In *2017 IEEE International Conference on Robotics and Automation (ICRA) C4 Surgical Robotics Workshop*, pages 1–4, 2017.

[183] R. J. Hendrick. *System Design and Elastic Stability Modeling of Transendoscopic Continuum Robots*. Ph.D. dissertation, Vanderbilt University, 2017.

[184] K. A. X. J. Luo, T. Looi, S. Sabetian, and J. Drake. Designing concentric tube manipulators for stability using topology optimization. In *2018 IEEE/RSJ International Conference on Intelligent Robots and Systems (IROS)*, pages 1764–1769. IEEE, 2018.

[185] L. G. Torres, A. Kuntz, H. B. Gilbert, P. J. Swaney, R. J. Hendrick, R. J. Webster III, and R. Alterovitz. A motion planning approach to automatic obstacle avoidance during concentric tube robot teleoperation. In *2015 IEEE International Conference on Robotics and Automation (ICRA)*, pages 2361–2367. IEEE, 2015.

[186] G. Fagogenis, C. Bergeles, and P. E. Dupont. Adaptive nonparametric kinematic modeling of concentric tube robots. In *2016 IEEE/RSJ International Conference on Intelligent Robots and Systems (IROS)*, pages 4324–4329. IEEE, 2016.

[187] K. Leibrandt, C. Bergeles, and G.-Z. Yang. On-line collision-free inverse kinematics with frictional active constraints for effective control of unstable concentric tube robots. In *2015 IEEE/RSJ International Conference on Intelligent Robots and Systems (IROS)*, pages 3797–3804. IEEE, 2015.

[188] K. Leibrandt, C. Bergeles, and G.-Z. Yang. Concentric tube robots: Rapid, stable path-planning and guidance for surgical use. *IEEE Robotics & Automation Magazine*, 24(2):42–53, 2017.

[189] Y.-J. Kim, S. Cheng, S. Kim, and K. Iagnemma. A stiffness-adjustable hyperredundant manipulator using a variable neutral-line mechanism for minimally invasive surgery. *IEEE Transactions on Robotics*, 30(2):382–395, 2014.

[190] M. Khadem, L. Da Cruz, and C. Bergeles. Force/velocity manipulability analysis for 3d continuum robots. In *2018 IEEE/RSJ International Conference on Intelligent Robots and Systems (IROS)*, pages 4920–4926. IEEE, 2018.

[191] C. W. Wampler II. Manipulator inverse kinematic solutions based on vector formulations and damped least-squares methods. *IEEE Transactions on Systems, Man, and Cybernetics*, 16(1):93–101, 1986.

[192] T. F. Chan and R. V. Dubey. A weighted least-norm solution based scheme for avoiding joint limits for redundant joint manipulators. *IEEE Transactions on Robotics and Automation*, 11(2):286–292, 1995.

[193] P. J. Swaney, H. B. Gilbert, R. J. Webster III, P. T. Russell III, and K. D. Weaver. Endonasal skull base tumor removal using concentric tube continuum

robots: a phantom study. *Journal of Neurological Surgery. Part B, Skull Base*, 76(2):145, 2015.

[194] R. Wirz, L. G. Torres, P. J. Swaney, H. Gilbert, R. Alterovitz, R. J. Webster III, K. D. Weaver, and P. T. Russell III. An experimental feasibility study on robotic endonasal telesurgery. *Neurosurgery*, 76(4):479–484, 2015.

[195] H. B. Gilbert and R. J. Webster III. Rapid, reliable shape setting of superelastic nitinol for prototyping robots. *IEEE Robotics and Automation Letters*, 1(1):98–105, 2016.

[196] T. Gotoda. Endoscopic resection of early gastric cancer. *Gastric Cancer*, 10(1):1–11, 2007.

[197] P. W. Y. Chiu. Novel endoscopic therapeutics for early gastric cancer. *Clinical Gastroenterology and Hepatology*, 12(1):120–125, 2014.

[198] S. Everett and A. Axon. Early gastric cancer in europe. *Gut*, 41(2):142–150, 1997.

[199] J. Lian, S. Chen, Y. Zhang, and F. Qiu. A meta-analysis of endoscopic submucosal dissection and EMR for early gastric cancer. *Gastrointestinal Endoscopy*, 76(4):763–770, 2012.

[200] K. W. Eastwood, H. Azimian, B. Carrillo, T. Looi, H. E. Naguib, and J. M. Drake. Kinetostatic design of asymmetric notch joints for surgical robots. In *2016 IEEE/RSJ International Conference on Intelligent Robots and Systems (IROS)*, pages 2381–2387. IEEE, 2016.

[201] K. W. Eastwood, P. Francis, H. Azimian, A. Swarup, T. Looi, J. M. Drake, and H. E. Naguib. Design of a contact-aided compliant notched-tube joint

for surgical manipulation in confined workspaces. *Journal of Mechanisms and Robotics*, 10(1):015001, 2018.

[202] S. Jeong, Y. Chitalia, and J. P. Desai. Design, modeling, and control of a coaxially aligned steerable (COAST) guidewire robot. *IEEE Robotics and Automation Letters*, 5(3):4947–4954, 2020.

[203] P. A. Halverson, L. L. Howell, and A. E. Bowden. A flexure-based bi-axial contact-aided compliant mechanism for spinal arthroplasty. In *ASME 2008 International Design Engineering Technical Conferences and Computers and Information in Engineering Conference*, pages 405–416. American Society of Mechanical Engineers Digital Collection, 2009.

[204] K. W. Eastwood, A. Swarup, P. Francis, A. N. Alvara, H. Chen, T. Looi, H. E. Naguib, and J. M. Drake. A steerable neuroendoscopic instrument using compliant contact-aided joints and monolithic articulation. *Journal of Medical Devices*, 14(2), 2020.

[205] H. Azimian, P. Francis, T. Looi, and J. Drake. Structurally-redesigned concentric-tube manipulators with improved stability. In *2014 IEEE/RSJ International Conference on Intelligent Robots and Systems*, pages 2030–2035. IEEE, 2014.

[206] D.-Y. Lee, J. Kim, J.-S. Kim, C. Baek, G. Noh, D.-N. Kim, K. Kim, S. Kang, and K.-J. Cho. Anisotropic patterning to reduce instability of concentric-tube robots. *IEEE Transactions on Robotics*, 31(6):1311–1323, 2015.

[207] D. Wei, Y. Wenlong, H. Dawei, and D. Zhijiang. Modeling of flexible arm with triangular notches for applications in single port access abdominal surgery. In *2012 IEEE International Conference on Robotics and Biomimetics (ROBIO)*, pages 588–593. IEEE, 2012.

[208] M. D. Kutzer, S. M. Segreti, C. Y. Brown, M. Armand, R. H. Taylor, and S. C. Mears. Design of a new cable-driven manipulator with a large open lumen: Preliminary applications in the minimally-invasive removal of osteolysis. In *2011 IEEE International Conference on Robotics and Automation*, pages 2913–2920. IEEE, 2011.

[209] P. Wilkening, F. Alambeigi, R. J. Murphy, R. H. Taylor, and M. Armand. Development and experimental evaluation of concurrent control of a robotic arm and continuum manipulator for osteolytic lesion treatment. *IEEE Robotics and Automation Letters*, 2(3):1625–1631, 2017.

[210] M. S. Moses, R. J. Murphy, M. D. Kutzer, and M. Armand. Modeling cable and guide channel interaction in a high-strength cable-driven continuum manipulator. *IEEE/ASME Transactions on Mechatronics*, 20(6):2876–2889, 2015.

[211] Z. Du, W. Yang, and W. Dong. Kinematics modeling of a notched continuum manipulator. *Journal of Mechanisms and Robotics*, 7(4):041017, 2015.

[212] A. Gao, R. J. Murphy, H. Liu, I. I. Iordachita, and M. Armand. Mechanical model of dexterous continuum manipulators with compliant joints and tendon/external force interactions. *IEEE/ASME Transactions on Mechatronics*, 22(1):465–475, 2016.

[213] Boston Scientific. Fathom™ Steerable Guidewires. `https://www.bostonscientific.com/en-US/products/embolization/fathom-steerable-guidewires.html`. Accessed: 2020-10-27.

[214] J. Kim, W.-Y. Choi, S. Kang, C. Kim, and K.-J. Cho. Continuously variable stiffness mechanism using nonuniform patterns on coaxial tubes for continuum microsurgical robot. *IEEE Transactions on Robotics*, 35(6):1475–1487, 2019.

[215] S. Phee, S. Low, Z. Sun, K. Ho, W. Huang, and Z. Thant. Robotic system for no-scar gastrointestinal surgery. *The International Journal of Medical Robotics and Computer Assisted Surgery*, 4(1):15–22, 2008.

[216] L. Petruzziello, M. Campanale, C. Spada, R. Ricci, C. Hassan, G. Gullo, and G. Costamagna. Endoscopic submucosal dissection of gastric superficial neoplastic lesions: a single western center experience. *United European Gastroenterology Journal*, 6(2):203–212, 2018.

[217] Video Colonoscope EVIS EXERA (CF-2T160L/I). `https://medical.olympusamerica.com/products/colonoscope/evis-exera-cf-2t160i`. Accessed: 2019-10-17.

[218] H. Huang, H. Zheng, and G. Lim. Femtosecond laser machining characteristics of Nitinol. *Applied Surface Science*, 228(1-4):201–206, 2004.

[219] R. Pfeifer, D. Herzog, M. Hustedt, and S. Barcikowski. Pulsed Nd:YAG laser cutting of NiTi shape memory alloys—influence of process parameters. *Journal of Materials Processing Technology*, 210(14):1918–1925, 2010.

[220] J. Liu, C. Li, X. Fang, J. Jordon, and Y. Guo. Effect of wire-EDM on fatigue of nitinol shape memory alloy. *Materials and Manufacturing Processes*, 33(16):1809–1814, 2018.

[221] C. Fu, M. P. Sealy, Y. Guo, and X. Wei. Finite element simulation and experimental validation of pulsed laser cutting of nitinol. *Journal of Manufacturing Processes*, 19:81–86, 2015.

[222] N. Chernov. Circle Fit (Pratt method). `https://www.mathworks.com/matlabcentral/fileexchange/22643-circle-fit-pratt-method`. Accessed: 2020-10-04.

[223] Y. Chitalia, S. Jeong, N. Deaton, J. J. Chern, and J. P. Desai. Design and kinematics analysis of a robotic pediatric neuroendoscope tool body. *IEEE/ASME Transactions on Mechatronics*, 25(2):985–995, 2020.

Appendices

Appendix A

Computing the Multi-Needle Robot Model

This appendix provides details for computing the mechanics-based model for the multi-needle robot. In particular, it focuses on expressions for the linearized state equation matrix $\mathbf{F}(\boldsymbol{x}, s)$, which is used in Section 2.3.7 to compute the Jacobian and compliance matrices and in Section 2.4.1 for the covariance differential equation.

We define the matrix $\mathbf{F}(\boldsymbol{x}, s)$ as

$$\mathbf{F}(\boldsymbol{x}, s) = \partial \boldsymbol{f}(\boldsymbol{x}, s)/\partial \boldsymbol{x}, \tag{A.1}$$

where $\boldsymbol{f}(\boldsymbol{x}, s)$ are the differential equations describing the robot's state as defined in (2.4). Here, we see that the linearization matrix is a function of the robot's state vector $\boldsymbol{x}$ at arc length s. In order to compute $\mathbf{F}(\boldsymbol{x}, s)$, we must find the partial derivative of each state equation with respect to the states themselves.

Recall that the robot state arc length differential equations are given by

$$\boldsymbol{f}(\boldsymbol{x}, s) = \boldsymbol{x}' = \begin{bmatrix} \boldsymbol{x}_t' & \boldsymbol{x}_1' & \dots & \boldsymbol{x}_n' \end{bmatrix}^{\mathsf{T}} \tag{A.2}$$

where each flexible element has Cosserat rod states position $\boldsymbol{p}(s) \in \mathbb{R}^3$, orientation quaternion $\boldsymbol{q}(s) \in \mathbb{H}$, internal moment $\boldsymbol{m}(s) \in \mathbb{R}^3$ and internal force $\boldsymbol{n}(s) \in \mathbb{R}^3$. The Cosserat rod state equations that propagate in arc length for each flexible element are

$$\begin{aligned} \boldsymbol{p}' &= \boldsymbol{q}\boldsymbol{e}_3\boldsymbol{q}^{-1} & \boldsymbol{q}' &= \frac{1}{2}\boldsymbol{q}\boldsymbol{u} \\ \boldsymbol{m}' &= \boldsymbol{n} \times \boldsymbol{p}' - \boldsymbol{l} & \boldsymbol{n}' &= -\boldsymbol{r}. \end{aligned} \tag{A.3}$$

where $\boldsymbol{u} \in \mathbb{R}^3$ is the angular rate-of-change of the rod's body reference frame expressed in the body frame, and $\boldsymbol{r} \in \mathbb{R}^3$ and $\boldsymbol{l} \in \mathbb{R}^3$ are externally applied distributed forces

and moments per unit rod length (we assume $\boldsymbol{r} = \mathbf{0}$ and $\boldsymbol{l} = \mathbf{0}$ in this appendix).

In the remainder of this appendix, we will define the non-zero quantities of $\mathbf{F}(\boldsymbol{x}, s)$ by finding the partial derivatives of $\boldsymbol{p}'$, $\boldsymbol{q}'$, $\boldsymbol{m}'$, and $\boldsymbol{n}'$ with respect to the states $\boldsymbol{x}$. First, we denote the components of the unit quaternion as

$$\boldsymbol{q} = \begin{bmatrix} w & \boldsymbol{r} \end{bmatrix}^{\mathsf{T}} = \begin{bmatrix} w & r_1 & r_2 & r_3 \end{bmatrix}^{\mathsf{T}} \tag{A.4}$$

where w is the scalar component and $\boldsymbol{r}$ is the vector component of the quaternion. When computing partial derivatives of expressions involving quaternions, we use the quantity

$$\frac{\partial \boldsymbol{q}}{\partial \boldsymbol{q}} = \mathbf{I}_{4\times 4} - \boldsymbol{q}\boldsymbol{q}^{\mathsf{T}}, \tag{A.5}$$

to enforce the unit norm quaternion. We find the following expression for the partial derivative of the position state equation:

$$\frac{\partial \boldsymbol{p}'}{\partial \boldsymbol{q}} = \mathbf{R}(\boldsymbol{q})\boldsymbol{e}_3 = 2 \begin{bmatrix} r_2 & r_3 & w & r_1 \\ -r_1 & -w & r_3 & r_2 \\ 0 & -2r_1 & -2r_2 & 0 \end{bmatrix} \frac{\partial \boldsymbol{q}}{\partial \boldsymbol{q}}. \tag{A.6}$$

where $\boldsymbol{e}_3$ is the third standard basis vector and $\mathbf{R}(\boldsymbol{q})$ is the rotation matrix found from the quaternion $\boldsymbol{q}$.

Next, we will find the non-zero partial derivatives of $\boldsymbol{q}' = \frac{1}{2}\boldsymbol{q}\boldsymbol{u}$, which can be written as

$$\boldsymbol{q}' = \begin{bmatrix} w & -\boldsymbol{r}^{\mathsf{T}} \\ \boldsymbol{r} & \widehat{\boldsymbol{r}} + w\mathbf{I}_{3\times 3} \end{bmatrix} \begin{bmatrix} 0 \\ \boldsymbol{u} \end{bmatrix} \tag{A.7}$$

$$\boldsymbol{q}' = \begin{bmatrix} -\boldsymbol{r}^{\mathsf{T}}\boldsymbol{u} \\ \widehat{\boldsymbol{r}}\boldsymbol{u} + w\mathbf{I}_{3\times 3}\boldsymbol{u} \end{bmatrix} \tag{A.8}$$

$$\boldsymbol{q}' = \begin{bmatrix} 0 & -\boldsymbol{u}^\mathsf{T} \\ \boldsymbol{u} & \widehat{\boldsymbol{u}}^\mathsf{T} \end{bmatrix} \boldsymbol{q} \tag{A.9}$$

by using the matrix form of quaternion products. Here, the operator $\widehat{(\cdot)}$ converts a vector from $\mathbb{R}^3$ to a skew-symmetric matrix in $\mathfrak{so}(3)$ [172]. Recall that from the constitutive law (2.2), we know that $\boldsymbol{u} = \mathbf{K}_m^{-1}\mathbf{R}^\mathsf{T}\boldsymbol{m}$ if $\boldsymbol{u}^* = \mathbf{0}$, where $\mathbf{K}_m$ is the stiffness matrix for bending and torsion. We can derive the partial derivative of $\mathbf{R}^\mathsf{T}$ with respect to each component of the quaternion:

$$\frac{\partial \mathbf{R}^\mathsf{T}}{\partial w} = 2\begin{bmatrix} 0 & r_3 & -r_2 \\ -r_3 & 0 & r_1 \\ r_2 & -r_1 & 0 \end{bmatrix} \tag{A.10}$$

$$\frac{\partial \mathbf{R}^\mathsf{T}}{\partial r_1} = \left(2\begin{bmatrix} 0 & r_2 & r_3 \\ r_2 & 0 & w \\ r_3 & -w & 0 \end{bmatrix} - 4\begin{bmatrix} 0 & 0 & 0 \\ 0 & r_1 & 0 \\ 0 & 0 & r_1 \end{bmatrix} \right) \tag{A.11}$$

$$\frac{\partial \mathbf{R}^\mathsf{T}}{\partial r_2} = \left(2\begin{bmatrix} 0 & r_1 & w \\ r_1 & 0 & r_3 \\ w & r_3 & 0 \end{bmatrix} - 4\begin{bmatrix} r_2 & 0 & 0 \\ 0 & 0 & 0 \\ 0 & 0 & r_2 \end{bmatrix} \right) \tag{A.12}$$

$$\frac{\partial \mathbf{R}^\mathsf{T}}{\partial r_3} = \left(2\begin{bmatrix} 0 & w & r_1 \\ -w & 0 & r_2 \\ r_1 & r_2 & 0 \end{bmatrix} - 4\begin{bmatrix} r_3 & 0 & 0 \\ 0 & r_3 & 0 \\ 0 & 0 & 0 \end{bmatrix} \right). \tag{A.13}$$

We use these expressions to find the partial derivative of the body-frame angular velocity $\boldsymbol{u}$ with respect to the quaternion:

$$\frac{\partial \boldsymbol{u}}{\partial \boldsymbol{q}} = \mathbf{K}_m^{-1}\begin{bmatrix} \frac{\partial \mathbf{R}^\mathsf{T}}{\partial w} & \frac{\partial \mathbf{R}^\mathsf{T}}{\partial r_1} & \frac{\partial \mathbf{R}^\mathsf{T}}{\partial r_2} & \frac{\partial \mathbf{R}^\mathsf{T}}{\partial r_3} \end{bmatrix} \boldsymbol{m}. \tag{A.14}$$

Finally, we find the partial derivative of the quaternion state equation with respect

to the quaternion:

$$\frac{\partial \boldsymbol{q}'}{\partial \boldsymbol{q}} = \frac{1}{2}\left(\begin{bmatrix} -\boldsymbol{r}^{\mathsf{T}} \\ \widehat{\boldsymbol{r}} + w\mathbf{I}_{3\times 3} \end{bmatrix} \frac{\partial \boldsymbol{u}}{\partial \boldsymbol{q}} + \begin{bmatrix} 0 & -\boldsymbol{u}^{\mathsf{T}} \\ \boldsymbol{u} & \widehat{\boldsymbol{u}}^{\mathsf{T}} \end{bmatrix}\right) \frac{\partial \boldsymbol{q}}{\partial \boldsymbol{q}}. \tag{A.15}$$

Next, we find an expression for the partial derivative of the quaternion state equation with respect to the internal moment as

$$\frac{\partial \boldsymbol{q}'}{\partial \boldsymbol{m}} = \frac{1}{2}\begin{bmatrix} -\boldsymbol{r}^{\mathsf{T}} \\ \widehat{\boldsymbol{r}} + w\mathbf{I}_{3\times 3} \end{bmatrix} \mathbf{K}_m^{-1}\mathbf{R}^{\mathsf{T}}. \tag{A.16}$$

Finally, we derive the non-zero partial derivatives for the internal moment state equation as

$$\frac{\partial \boldsymbol{m}'}{\partial \boldsymbol{q}} = \widehat{\boldsymbol{n}}\frac{\partial \boldsymbol{p}'}{\partial \boldsymbol{q}} \tag{A.17}$$

$$\frac{\partial \boldsymbol{m}'}{\partial \boldsymbol{n}} = -\widehat{(\mathbf{R}\boldsymbol{e}_3)}. \tag{A.18}$$

The partial derivatives can be packed into the appropriate sub-matrix of the linearization matrix for each flexible element:

$$\mathbf{F}_i(\boldsymbol{x}_i, s) = \frac{\partial \boldsymbol{f}(\boldsymbol{x}_i, s)}{\partial \boldsymbol{x}_i} = \begin{bmatrix} \mathbf{0}_{3\times 3} & \frac{\partial \boldsymbol{p}'}{\partial \boldsymbol{q}} & \mathbf{0}_{3\times 3} & \mathbf{0}_{3\times 3} \\ \mathbf{0}_{4\times 3} & \frac{\partial \boldsymbol{q}'}{\partial \boldsymbol{q}} & \frac{\partial \boldsymbol{p}'}{\partial \boldsymbol{m}} & \mathbf{0}_{4\times 3} \\ \mathbf{0}_{3\times 3} & \frac{\partial \boldsymbol{m}'}{\partial \boldsymbol{q}} & \mathbf{0}_{3\times 3} & \frac{\partial \boldsymbol{m}'}{\partial \boldsymbol{n}} \\ \mathbf{0}_{3\times 3} & \mathbf{0}_{3\times 4} & \mathbf{0}_{3\times 3} & \mathbf{0}_{3\times 3} \end{bmatrix}. \tag{A.19}$$

When computing the Jacobian and compliance matrices, it is also necessary to find the partial derivatives of the constraint equations (2.16) with respect to the states, as explained in Section 2.3.7. Next, we will give the expressions for $\partial \boldsymbol{c}/\partial \boldsymbol{x}(s)$ in the case of several common constraints, which can then be employed to find $\mathbf{Y} = \partial \boldsymbol{c}/\partial \boldsymbol{x}_0$

using $\mathbf{X}(s) = \partial \boldsymbol{x}(s)/\partial \boldsymbol{x}_0$. These expressions are also used in the Kalman update equations (2.30)–(2.33).

The partial derivative of the load- and moment-free tip constraint (2.10) with respect to the flexible tool state is given by

$$\frac{\partial \boldsymbol{c}_t}{\partial \boldsymbol{x}_t} = \begin{bmatrix} \mathbf{0}_{6\times 7} & \mathbf{I}_{6\times 6} \end{bmatrix}. \tag{A.20}$$

Next, we will find the partial derivative for the standard grasp constraint (2.11). In this case, we have the tool quaternion $\boldsymbol{q}_t = [w_t, r_{t,1}, r_{t,2}, r_{t,3}]^\mathsf{T}$ and the snare quaternion $\boldsymbol{q}_i = [w_i, r_{i,1}, r_{i,2}, r_{i,3}]^\mathsf{T}$. First, we define the $\boldsymbol{z}$ axis of the tool and snare orientations (i.e., the tangent vector) as $\boldsymbol{p}_t' = \mathbf{R}_t \boldsymbol{e}_3$ and $\boldsymbol{p}_i' = \mathbf{R}_i \boldsymbol{e}_3$ and find the partial derivative of each vector with respect to the quaternion:

$$\frac{\partial \boldsymbol{p}_t'}{\partial \boldsymbol{q}_t} = 2 \begin{bmatrix} r_{t,2} & r_{t,3} & w_t & r_{t,1} \\ -r_{t,1} & -w_t & r_{t,3} & r_{t,2} \\ 0 & -2r_{t,1} & -2r_{t,2} & 0 \end{bmatrix} \frac{\partial \boldsymbol{q}}{\partial \boldsymbol{q}} \tag{A.21}$$

$$\frac{\partial \boldsymbol{p}_i'}{\partial \boldsymbol{q}_i} = 2 \begin{bmatrix} r_{i,2} & r_{i,3} & w_i & r_{i,1} \\ -r_{i,1} & -w_i & r_{i,3} & r_{i,2} \\ 0 & -2r_{i,1} & -2r_{i,2} & 0 \end{bmatrix} \frac{\partial \boldsymbol{q}}{\partial \boldsymbol{q}}. \tag{A.22}$$

With these expressions, we can give the partial derivative of the grasp constraint with respect to the tool state and snare state as

$$\frac{\partial \boldsymbol{c}_i}{\partial \boldsymbol{x}_t} = \begin{bmatrix} \mathbf{I}_{3\times 3} & \mathbf{0}_{3\times 4} & \mathbf{0}_{3\times 3} & \mathbf{0}_{3\times 3} \\ \mathbf{0}_{1\times 3} & \boldsymbol{z}_i^\mathsf{T} \frac{\partial \boldsymbol{z}_t}{\partial \boldsymbol{q}_t} & \mathbf{0}_{1\times 3} & \mathbf{0}_{1\times 3} \\ \mathbf{0}_{1\times 3} & \boldsymbol{m}_i^\mathsf{T} \frac{\partial \boldsymbol{z}_t}{\partial \boldsymbol{q}_t} & \mathbf{0}_{1\times 3} & \mathbf{0}_{1\times 3} \\ \mathbf{0}_{1\times 3} & \mathbf{0}_{1\times 4} & \mathbf{0}_{1\times 3} & \mathbf{0}_{1\times 3} \end{bmatrix} \tag{A.23}$$

$$\frac{\partial \boldsymbol{c}_i}{\partial \boldsymbol{x}_i} = \begin{bmatrix} -\mathbf{I}_{3\times3} & \mathbf{0}_{3\times4} & \mathbf{0}_{3\times3} & \mathbf{0}_{3\times3} \\ \mathbf{0}_{1\times3} & \boldsymbol{z}_t^\mathsf{T} \frac{\partial \boldsymbol{z}_i}{\partial \boldsymbol{q}_i} & \mathbf{0}_{1\times3} & \mathbf{0}_{1\times3} \\ \mathbf{0}_{1\times3} & \mathbf{0}_{1\times4} & \boldsymbol{z}_t^\mathsf{T} & \mathbf{0}_{1\times3} \\ \mathbf{0}_{1\times3} & \boldsymbol{m}_i^\mathsf{T} \frac{\partial \boldsymbol{z}_i}{\partial \boldsymbol{q}_i} & \boldsymbol{z}_i^\mathsf{T} & \mathbf{0}_{1\times3} \end{bmatrix}. \tag{A.24}$$

A similar derivation process can be used for other constraints, such as remote center of motion constraints, or when additional parameters are appended to the state vector $\boldsymbol{x}$, such as the heading parameter $\boldsymbol{d}$.

Appendix B

Multi-Needle Robot Estimation

This appendix lists the covariance matrices used in the multi-needle robot statistical state estimation framework (Section 2.4.1). We performed the estimation simulations and experiments with no process noise (i.e., $\mathbf{Q}_s = \mathbf{0}$). The electromagnetic tracking sensor covariance was found based on a measured standard deviation of 1 mm for the position measurement:

$$\mathbf{Z}_{EM}(o_i) = 1 \times 10^{-6}\, \mathbf{I}_{3\times 3} \quad (\mathrm{m}^2). \tag{B.1}$$

The standard grasp constraint enforces a position constraint on the tip of the snare needle coinciding with the body of the flexible tool update, an orthogonal constraint on the needle shafts, and moment-free constraints about the shaft of each needle. The covariance of this pseudo-measurement update was

$$\mathbf{Z}_{grasp}(s_i) = \begin{bmatrix} 1 \times 10^{-7}\, \mathbf{I}_{3\times 3} & (\mathrm{m}^2) \\ 1 \times 10^{-6} & (\mathrm{N/A}) \\ 1 \times 10^{-13}\, \mathbf{I}_{2\times 2} & (\mathrm{N}^2\mathrm{m}^2) \end{bmatrix}. \tag{B.2}$$

The moment- and load-free constraint at the tip of the robot is also used as a pseudo-measurement in the estimation framework. For this update, the covariance was set to

$$\mathbf{Z}_{load}(s_i) = \begin{bmatrix} 1 \times 10^{-11}\, \mathbf{I}_{3\times 3} & (\mathrm{N}^2\mathrm{m}^2) \\ 1 \times 10^{-11}\, \mathbf{I}_{3\times 3} & (\mathrm{N}^2) \end{bmatrix}. \tag{B.3}$$

It is also necessary to initialize the *posterior* state estimate $\tilde{\mathbf{P}}_{s_{\min}}$. The covariance of the base position and orientation (represented with a quaternion) for each flexible element was found using the known geometry of the acrylic fiducial disks and the

measured tracker covariance using the results of [174]. After measuring each fiducial point on a disk, we have a set of N noisy data points $\boldsymbol{p}_1, \boldsymbol{p}_2, \ldots, \boldsymbol{p}_N$ where $\boldsymbol{p}_i = \begin{bmatrix} x_i, y_i, z_i \end{bmatrix}^\mathsf{T}$ and $\boldsymbol{p}_i \sim \mathcal{N}(\mu_i, \sigma_i^2)$, which are then packed into the matrix

$$\mathbf{Y} = \begin{bmatrix} \boldsymbol{p}_1 & \boldsymbol{p}_2 & \ldots & \boldsymbol{p}_N \end{bmatrix}. \tag{B.4}$$

The locations of these data points are known in the frame of the disk due to the disk's geometry. The fiducial positions in the disk frame $\boldsymbol{c}_1, \boldsymbol{c}_2, \ldots, \boldsymbol{c}_N$ are packed into the matrix

$$\mathbf{X} = \begin{bmatrix} \boldsymbol{c}_1 & \boldsymbol{c}_2 & \ldots & \boldsymbol{c}_N \end{bmatrix}. \tag{B.5}$$

Both data sets are demeaned by computing $\mathbf{X}_{dm} = \mathbf{X} - \bar{\mathbf{X}}$ and $\mathbf{Y}_{dm} = \mathbf{Y} - \bar{\mathbf{Y}}$, allowing us to find the optimal rotation matrix $\mathbf{R}^*$ that maps $\mathbf{Y}_{dm}$ to $\mathbf{X}_{dm}$ using

$$\mathbf{A} = \mathbf{Y}_{dm}\mathbf{X}_{dm}^\mathsf{T} = \mathbf{U}\boldsymbol{\Sigma}\mathbf{V}^\mathsf{T} \tag{B.6}$$

$$\mathbf{R}^* = \mathbf{U}\mathrm{diag}\Big(1, 1, \det\big[\mathbf{U}\mathbf{V}^\mathsf{T}\big]\Big)\mathbf{V}^\mathsf{T} \tag{B.7}$$

The base position and orientation of the needle are therefore given by $\bar{\mathbf{Y}}$ and $\mathbf{R}^*$ (converted to a quaternion). Assuming that all data points are random variables with the same variance, the base position covariance is

$$\mathbf{C}_{\boldsymbol{p}} = \left(\frac{\sigma^2}{N}\right)\mathbf{I}_{3\times 3} \quad (\mathrm{m}^2), \tag{B.8}$$

where σ is the electromagnetic tracker standard deviation (1 mm in this case) and $N = 6$ is the number of data points collected on the fiducial disk. To find the initial quaternion covariance $\mathbf{C}_{\boldsymbol{q}}$), we must first find the covariance of the demeaned data, since it is used to find $\boldsymbol{q}(s_{\min})$. Each demeaned tracking data point is defined as $\boldsymbol{p}_i - \bar{\mathbf{Y}} = \boldsymbol{p}_i - \frac{1}{N}\left(\boldsymbol{p}_1, \boldsymbol{p}_2, \ldots, \boldsymbol{p}_N\right)$ for $i = 1, \ldots, N$. Therefore the variance is found to

be

$$\sigma_{dm}^2 = \left(1 - \frac{1}{N}\right)^2 \sigma_i^2 + \frac{\sigma_1^2}{N^2} + \frac{\sigma_2^2}{N^2} + \ldots + \frac{\sigma_N^2}{N^2} \tag{B.9}$$

$$\sigma_{dm}^2 = \left(1 - \frac{1}{N}\right) \sigma^2 \tag{B.10}$$

since all of the data points have the same variance. We then define the covariance matrix of the demeaned data as

$$\mathbf{C}_{\mathbf{Y}_{dm}} = \left(1 - \frac{1}{N}\right) \sigma^2 \mathbf{I}_{3\times 3}. \tag{B.11}$$

We now use methods presented by Dorst [174] for error propagation of the Procrustes method (used to find the rigid body transformation between two point clouds) in order to determine $\mathbf{C}_{\boldsymbol{q}}$. First, we use the singular value decomposition in (B.7) to define

$$\mathbf{S} = \mathbf{V}\boldsymbol{\Sigma}\mathbf{V}^{\mathsf{T}} \tag{B.12}$$

$$\mathbf{H} = \left(\mathrm{tr}\left(\mathbf{S}\right)\mathbf{I}_{3\times 3} - \mathbf{S}\right)^{-1}. \tag{B.13}$$

Dorst defines an error axis vector $\mathrm{d}\boldsymbol{a}$ which captures the error due to noise in the transformation between $\mathbf{X}_{dm}$ and $\mathbf{Y}_{dm}$. The covariance of $\mathrm{d}\boldsymbol{a}$ is given here in its simplified form because we assume $\mathbf{X}_{dm}$ (the fiducial disk geometry) has very low noise relative to $\mathbf{Y}_{dm}$ (the sensor data):

$$\begin{aligned}\mathbf{C}_{\mathrm{d}\boldsymbol{a}} = \det\left(\mathbf{C}_{\mathbf{Y}_{dm}}\right)\mathbf{R}\mathbf{H}\Big(&\mathrm{tr}\left[\mathbf{R}^{\mathsf{T}}\mathbf{C}_{\mathbf{Y}_{dm}}^{-1}\mathbf{R}\mathbf{X}_{dm}\mathbf{X}_{dm}^{\mathsf{T}}\right]\mathbf{R}^{\mathsf{T}}\mathbf{C}_{\mathbf{Y}_{dm}}^{-1}\mathbf{R} \\ &- \mathbf{R}^{\mathsf{T}}\mathbf{C}_{\mathbf{Y}_{dm}}^{-1}\mathbf{R}\mathbf{X}_{dm}\mathbf{X}_{dm}^{\mathsf{T}}\mathbf{R}^{\mathsf{T}}\mathbf{C}_{\mathbf{Y}_{dm}}^{-1}\mathbf{R}\Big)\mathbf{H}\mathbf{R}^{\mathsf{T}},\end{aligned} \tag{B.14}$$

where we use $\mathbf{R} = \mathbf{R}^*$ for clarity. Changes in the quaternion $\boldsymbol{q} = [w, \boldsymbol{r}]^{\mathsf{T}}$ can be

related to changes in d$\boldsymbol{a}$ by

$$\Delta \boldsymbol{q} = \frac{1}{2} \begin{bmatrix} 0 \\ \Delta \left(\mathrm{d}\boldsymbol{a} \right) \end{bmatrix} \boldsymbol{q} \tag{B.15}$$

$$\Delta \boldsymbol{q} = \frac{1}{2} \begin{bmatrix} -\boldsymbol{r}^{\mathsf{T}} \\ w\mathbf{I}_{3\times 3} - \widehat{\boldsymbol{r}} \end{bmatrix} \Delta \left(\mathrm{d}\boldsymbol{a} \right) \tag{B.16}$$

$$\Delta \boldsymbol{q} = \frac{1}{2} \mathbf{M} \Delta \left(\mathrm{d}\boldsymbol{a} \right) \tag{B.17}$$

where the operator $\widehat{(\cdot)}$ converts a vector from $\mathbb{R}^3$ to a skew-symmetric matrix in $\mathfrak{so}(3)$ [172]. The covariance of the quaternion is given by

$$\mathbf{C}_{\boldsymbol{q}} = E\left(\left(\boldsymbol{q} - \bar{\boldsymbol{q}} \right) \left(\boldsymbol{q} - \bar{\boldsymbol{q}} \right)^{\mathsf{T}} \right) \tag{B.18}$$

$$\mathbf{C}_{\boldsymbol{q}} = E\left(\Delta \boldsymbol{q} \Delta \boldsymbol{q}^{\mathsf{T}} \right) \tag{B.19}$$

$$\mathbf{C}_{\boldsymbol{q}} = \frac{1}{2} \mathbf{M} E\left(\Delta \left(\mathrm{d}\boldsymbol{a} \right) \Delta \left(\mathrm{d}\boldsymbol{a} \right)^{\mathsf{T}} \right) \mathbf{M} \frac{1}{2} \tag{B.20}$$

$$\mathbf{C}_{\boldsymbol{q}} = \frac{1}{4} \mathbf{M} \mathbf{C}_{\mathrm{d}\boldsymbol{a}} \mathbf{M}^{\mathsf{T}} \tag{B.21}$$

where $E\left(\cdot \right)$ represents the expected value of a random variable.

The initial covariances for the heading parameters $\boldsymbol{d}$ and external applied load $\boldsymbol{b}$ were set as

$$\mathbf{C}_{\boldsymbol{d}} = 1 \times 10^{-3} \, \mathbf{I}_{2\times 2} \quad (\mathrm{N/A}) \tag{B.22}$$

$$\mathbf{C}_{\boldsymbol{b}} = 1.44 \times 10^{-4} \, \mathbf{I}_{3\times 3} \quad (\mathrm{N}^2) \tag{B.23}$$

with the units shown. Finally, the *posterior* state estimate was initialized using

$$\tilde{\mathbf{P}}_{s_{\min}} = \mathbf{J}_{s_{\min}} \mathbf{P}_{inputs} \mathbf{J}_{s_{\min}}^{\mathsf{T}} + 1 \times 10^{-11} \mathbf{I} \tag{B.24}$$

where $\mathbf{J}_{s_{\min}}$ is the robot Jacobian at arc length $s_{\min}$, the dimensions of $\mathbf{I}$ are equal to the size of $\mathbf{J}_{s_{\min}}\mathbf{J}_{s_{\min}}^{\mathsf{T}}$, and $\tilde{\mathbf{P}}_{inputs}$ is the matrix packed with the covariances of the system inputs:

$$\mathbf{P}_{inputs} = \text{diag}\Big(\mathbf{C}_{\boldsymbol{p}_t}\ \ \mathbf{C}_{\boldsymbol{q}_t}\ \ \mathbf{C}_{\boldsymbol{p}_i}\ \ \mathbf{C}_{\boldsymbol{q}_i} \ldots \mathbf{C}_{\boldsymbol{p}_n}\ \ \mathbf{C}_{\boldsymbol{q}_n}\ \ \mathbf{C}_{\boldsymbol{d}}\ \ \mathbf{C}_{\boldsymbol{b}}\Big) \tag{B.25}$$

where n is the number of snare needles. Note that other estimated parameters can be appended to $\mathbf{P}_{inputs}$.